行政院國家科學委員會專題研究計畫結案(完整)報告

# 邊界元素法大型工程問題之運算研究（3/3）

# Boundary Element Method for the Analysis of Large Scale Engineering Problems（3/3）

計畫類別：■個別型計畫　　□整合型計畫

計畫編號：NSC90-2211-E-002-099

執行期間：90 年 08 月 01 日至 91 年 07 月 31 日
全程期間：88 年 08 月 01 日至 91 年 07 月 31 日

計畫主持人：楊德良 台大土木系教授兼
水工所特約研究員
國科會特約研究員

研究助理人員：范佳銘　碩士級專任研究助理
羅德章　博士班研究生
林昭儀　碩士班研究生

執行單位：國立台灣大學水工試驗所

中華民國九十一年十二月

# 邊界元素法大型工程問題之運算研究(3/3)

# Boundary Element Method for the Analysis of Large Scale Engineering Problems (3/3)

計畫編號：NSC-90-2111-E-002-099
執行期間：90 年 8 月 1 日至 91 年 7 月 31 日
全程期間：88 年 8 月 1 日至 91 年 7 月 31 日
主持人：楊德良　國立台灣大學土木系教授及
國立台灣大學水工試驗所研究員及
國科會特約研究員

## 一. 中文摘要(關鍵字：邊界元素法、工程計算、計算流體力學、大型工程問題)

邊界元素法對解大型工程計算問題來說是一種效率比較高的方法，這個方法較傳統的有限元素法及有限差分法來得靈活。這原因是在邊界元素法只需要在問題幾何形狀的邊界上做一些網格，比較起來，其他的數值方法需要體內打網格。雖說邊界元素法的效率較高，同時電算機的速度和內容日新月異，工程界上總是有更大及更新的問題，現有的方法不能有效的解決。所以在推導數值方法上面，我們還沒到達止境。

對於大型工程問題之運算，諸如進水之渦流及捲氣問題、颱風受地形之影響等三維又非線性及時變的複雜流力問題，一直是工程問題頗具挑戰性的研發題材。當問題過於複雜，因離散法而造成大量未知數儲存及求解，即便對於今日的高效率電算機也會造成困難。近年來，邊界元素法藉著降低維度的優勢，已可用於三維及時變性之複雜問題上。然而因爲解滿矩陣的現制，當問題的難度推到某一個限度也會遭到困難。

本計劃因此提出幾個創新的構想來更進一步推動邊界元素法的解題能力，我們首先提出以疊代收斂法來解邊界元素法，如此矩陣完全不用形成。我們又準備利用特殊解邊界元素法與數學上新發展的薄板曲線軸向函數的內差法來解決體內積分的問題，如此一來，即便是非線性及非均質的問題也不需要體內積分。對於計算流體力學問題，我們把 Navier-Stokes 方程式表成速度-渦度的公式，並進一步分解成聯立的 Poisson 公式以使用邊界元素法來處理。當這數種方法結合在一起，我們計畫去解一些如前述的大型流體力學在工程上應用的問題。本研究想借三年的時間來研究這一套解題的技術，以提升我國在此方面的國際競爭能力，並盼能實際解決工程上所遭遇之大量計算之分析與設計問題。

## 二. 英文摘要 (Keywords: Boundary element method, Engineering

computation, Computational fluid dynamics)

Boundary Element Method (BEM) is an efficient numerical method for solving engineering problems. It is more efficient than the traditional Finite Element Method (FEM) and Finite Difference Method (FDM) because normally only boundary geometry needs to be defined and discretized. This provides not only a higher flexibility in dealing with complex geometry and moving boundaries, but also a more efficient solution algorithm.

Despite the rapid advancement in computer technology, the application of computational fluid dynamics to three-dimensional, nonlinear and transient flow problems remains a great challenge to the engineering community. Problems such as vorticity dynamics and air entrainment in hydraulic inlet, and large scale air motion and ground topography interaction, require a fine mesh and a huge number of discrete unknowns that may tax even the capacity of present-day supercomputers. In recent years, the boundary element method (BEM) has gained a reputation in solving large scale, three-dimensional, nonlinear and transient problems due to its ability to reduce the dimensionality of spatial discretization. However, when the problem gets really complex, even the reduced solution system can be too large for the computer to handle, particularly concerning the storage and the solution of the matrix system.

In this project we propose an iterative BEM that does not assemble the matrix, thus greatly alleviate the storage problem. Because the integral formula that is used for iteration integrates around the entire boundary, the propagation of the correction of each iteration is much more effective than that of the conventional finite difference iteration. Very fast convergence has been observed. In computation fluid dynamics, for the solution of Navier-Stokes equations, we use the velocity-vorticity formulation to decompose the governing equations to a system of Poisson equations with transient and nonlinear right-hand-side. The right-hand-side is to be iterated together with the iterative BEM scheme. Furthermore, we shall utilize the particular solution BEM (as known as dual reciprocity BEM) combined with the thin-plate spline radial basis function to interpolate and to solve the right-hand-side. The resultant BEM is completely free from domain integration, despite the nonlinear terms. We intend to combine the above innovative techniques to solve large scale fluid mechanics problems in engineering, as far as massive analysis and design procedure are concerned.

## 三、計畫的原由與目的

在工程界中有許多問題需要用計算流體力學來模擬。這其中包括水力學的

問題及空氣動力學的問題。雖然說我們兩者都準備研究，但是我們將以水力問題（不可壓縮流）爲主。我們研究的方向將針對一些大型問題。當離散後的系統變成太大，傳統的數值方法沒有辦法解決的時候，我們便可應用這一連串的創新方法，包括使用邊界元素法以減少離散空間度，疊代方法以避免大型矩陣的形成，由邊界元素法公式性質所造成的快速收斂，以及最優化的薄板曲線軸向函數來內插體內值，來繼續往前推進來解越來越大的系統。

四.研究方法

(1) 測試疊代邊界元素法：我們將用較簡單的控制方程式，好比 Laplace 方程式來測試。我們尤其對這方法的收斂性及可否加速收斂會嚴謹的研究。
(2) 測試特殊解邊界元素法：我們將以測試 Poisson 方程式爲主。對各種不同的方程式右項值，我們會一一檢查這方法的有效性。我們將比較傳統雙轉換邊界元素法所用的軸向基本函數及我們現在所提出的薄板曲線軸向基本函數的精度及收斂率。
(3) 解非時變性及線性的問題：我們將用速度-渦度數學模式來解非時變的低雷諾數問題。
(4) 解非時變性及非線性的問題：我們將測試用疊代法解非線性問題的有效性。
(5) 解時變性及非線性的問題：我們將解 Navier-Stokes 方程式。這時候我們將把所有上述發展的方法組合起來。

五.研究成果

本計畫在三年研究期間，總共發表 8 篇期刊論文：7 篇會議論文：2 篇研究技術報告及完成 6 篇碩士論文及 1 篇博士論文，詳細之數值模擬結果，分別附在總結研究之報告中，這些論文及研究報告分列於下列之參考文獻用。

參考文獻

(A) 期刊論文


1. Young, D.L., Chang, T.J., Eldho, T.I., , 2002, The Riemann Complex Boundary Element Method for the Solutions of Two-Dimensional Elliptic Equations, Applied Mathematical Modeling, Vol.26, pp.893-911. (SCI)
2. Fan, C.M., Young, D.L., 2002, Analysis of the 2D Stokes Flows by the Non-Singular Boundary Integral Equation Method, International Mathematical Journal, Vol.2, No.12, pp.1199-1215.
3. Young, D.L., Wang, Y.F., Eldho, T.I., 2002, Three-dimensional Transient Shallow Water Flow Simulation Using a Boundary Integral Equation Model, The Journal of Hydraulic Research, IAHR, Vol.40, pp.403-412. (SCI)
4. Young, D.L., Huang, J.L., and Eldho, T.I., 2001, Simulation of Laminar Vortex Shedding Flow Past Cylinders

Using a Coupled BEM and FEM Model, Compt. Methods Appl. Mech. Engrg.,Vol. 192,pp.5975-5998.(SCI)

5. Young, D.L., Huang, J.L., and Eldho T.I., 2001, Numerical Simulation of High-Reynolds Number Flow around Circular Cylinders by a Three-step FEM-BEM Model, Int. J. Numer. Mech. Fluids, Vol.37, pp. 657-689.(SCI)
6. Young, D.L., Chang, J.T., Eldho, T.I., 2001,A Coupled BEM and Arbitrary Lagrangian-Eulerian FEM Model for the Solution of Two-dimensional Laminar Flow in External Flow Fields , International Journal for Numerical Methods in Engineering . Vol.51, pp.1053-1077.(SCI)
7. Young, D.L., Wang, Y.F., Eldho, T.I.,2000, Solution of the Advection-Diffusion Equation Using the Eulerian-Lagrangian Boundary Element Method, International Journal of Engineering Analysis with Boundary Elements, Vol. 24/6, pp. 449-457.(SCI)
8. Cheng, A.H.-D., Young, D.L., and Tsai, C.C. , 2000,Solution of Poisson's Equation by Iterative DRBEM Using Compactly Supported, Positive Definite Radial Basis Function, International Journal of Engineering Analysis with Boundary Elements, 24/7, pp.549-557 (SCI).

(B) 研討會論文

1. Young,D.L., 2002, "FEM-BEM Analysis of Vortex –induced Oscillation of circular Cylinder",The 2nd International Conference on Structural Stability and Dynamics, Singapore, 16-18 December, 2002.(invited paper)
2. Fan,C.M.,andYoung,D.L.,2001, "Analysis of the Stokes Flow by the NSBIE for the Laplace Equation and Biot-Savart Law", CD-ROM Proceedings of the 25th National Conference on Mechanics, Taichung,Vol.1, pp.415-426.
3. Young, D.L., Tsai, C.C. and Cheng, A.H.-D. , 2001, An Iterative DRBEM for Three-dimensional Poisson's Equation, paper in BETECH, XIV, pp. 323-332, Florida, USA
4. Tsai, C. C. ,Young, D. L. ,and Cheng, A.H.-D,2001,"Meshless BEM for steady Three-dimensional Stokes Flows", CD-ROM Proceedings of the International Conference on Computational Engineering and Science 2001, Puerto Vallarta, Mexico.
5. Young,D.L., 2001, "Large Eddy Simulation of Turbulent Flow over Surface-mounted Obstacles using Three-Step FEM-BEM Method", Proceedings of the Two-strait Conference on Computational Fluid Dynamics,pp121-138, Taiwan.
6. Eldho, T.I., and Young D. L., 2000, "Solution of the Velocity-vorticity Navier-Stokes Equations using Dual Reciprocity Boundary Element Method", CD_ROM Proceedings of 14th Engineering Mechanics Conference, ASCE, Austion,Texas,2000.

7. D., Chen, C.S., Golberg, M.A., and Young, D.L., 2000, Radial Basis Functions Polynomial Basis Functions, Particular Solutions, and DRBEM, CD-ROM Proceedings of 14th Engineering Mechanics Conference, ASCE, Austin, Texas, 2000.

(C) 技術報告

1. 楊德良等,2001,邊界元素大型工程問題之運算研究(2/3),行政院國科會專題計畫期中成果報告,2001年5月,NSC89-2211-E-002-138。

2. 楊德良等, 2000,邊界元素大型工程問題之運算研究(1/3),行政院國科會專題計畫其中報告,2000年4月,NSC 89-EPA-E002-013。

(D) 博碩士論文

1. The Non-Singular Boundary Integral Equation Analysis to the Stokes Flow，呂鴻烈碩士論文，國立台灣大學土木工程學研究所，2000年7月。

2. 必歐沙伐定理與速度-渦度及邊界元素法解二維史托克斯流場，梁恩維碩士論文，國立台灣大學土木工程學研究所，2001年6月。

3. Application of 3D Helmholtz Equation by the Boundary Element Method to the Wave Propagation Problems，林詠欽碩士論文，國立台灣大學土木工程學研究所，2001年6月。

4. The Non-Singular Boundary Integral Equations Analysis to Some Engineering Problems，范佳銘碩士論文，國立台灣大學土木工程學研究所，2001年6月。

5. Application of Helmholtz Equation by the Boundary Element Method to the Waveguide and Scattering Propagation Problems，陳國清碩士論文，國立台灣大學土木工程學研究所，2002年6月。

6. Non-Singular Boundary Integral Equation for the Analysis of the Electromagnetic Problems，邱家麟碩士論文，國立台灣大學土木工程學研究所，2002年6月。

7. Messless Numerical Methods and their Engineering Applications，蔡加正博士論文，國立台灣大學土木工程學研究所，2002年6月。

ELSEVIER

Applied Mathematical Modelling 26 (2002) 893–911

APPLIED MATHEMATICAL MODELLING

www.elsevier.com/locate/apm

# The Riemann complex boundary element method for the solutions of two-dimensional Elliptic equations

D.L. Young *, T.J. Chang [1], T.I. Eldho [2]

*Department of Civil Engineering and Hydrotech Research Institute, National Taiwan University, Taipei 10617, Taiwan*

Received 4 July 2000; received in revised form 2 January 2002; accepted 1 March 2002

**Abstract**

In this paper, a new boundary integral equation model Riemann complex boundary element method (RCBEM), is proposed based on the boundary element method (BEM) and the theory of Vekua and its modification as well as complex Riemann function as the fundamental solution. The RCBEM method is used to solve the linear, second order, elliptical partial differential equations in the fluid flow problems. In comparison to the generally used BEM, for RCBEM, there are two distinct differences. First one is that, RCBEM applies complex Riemann function as the fundamental solution of the adjoint operator while in direct BEM, on the other hand Green function is used. The second one is that the governing equations should be transformed into complex domain because there exist two characteristics in complex plane for elliptic systems, while in the direct BEM is not, since the Green function is adopted instead. The singular problem occurring in direct BEM can be avoided in RCBEM, especially for regular domain problems. The efficiency and accuracy of the RCBEM depends on the complex variable integration. To verify the feasibility and accuracy of RCBEM, the model is applied to different case studies of potential flows, Helmholtz equation problem and advection–diffusion problem and results are compared with analytical solutions and other numerical models. The results are satisfactory and prove the applicability of RCBEM for various two-dimensional elliptic equation problems.
© 2002 Elsevier Science Inc. All rights reserved.

*Keywords:* Riemann complex functions; Boundary element method; Fluid flow problems

* Corresponding author. Tel./fax: +886-2-23626114.
*E-mail address:* dlyoung@hy.ntu.edu.tw (D.L. Young).
[1] Present address: Department of Agricultural Engineering, National Taiwan University.
[2] Present address: Department of Civil Engineering, IIT Bombay, India.

0307-904X/02/$ - see front matter © 2002 Elsevier Science Inc. All rights reserved.
PII: S0307-904X(02)00048-3

## 1. Introduction

Boundary element method (BEM) has been established as a powerful numerical tool in the solution of various fluid flow problems [1]. In BEM, the computational domain becomes the enclosing boundary and the effective dimensions of the problem considered will be reduced by one. Hence it is much easier in discretization and data preparation for the problem considered. These advantages make BEM more suitable for the solution of various fluids flow problems.

BEM are usually derived from the Green's theorem with an appropriate free-space Green's function [2] using real variables. In recent times, a boundary element approach using complex variables for boundary integration, known as complex variable boundary element method (CVBEM) has been introduced [3]. The CVBEM is a generalization of the Cauchy integral formula into a boundary integral equation method, followed by formulation into a workable computer algorithm for effective mathematical simulation. This generalization allows an immediate and valuable transfer of the modeling technique and makes the process simpler and more efficient than using the real variables. But this limits its application to two-dimensional harmonic (Laplace) problems [3].

Generally an integral equation is solved by a numerical model that assumes the boundary of the problem domain is discretized into piecewise-polynomial curves, and the known and the unknown boundary values are approximated as piecewise-continuous functions along the boundary. Unlike the Green's function formulations, the complex variable method does not depend on the shape of the contour between nodes [3,4]. Most of the complex variable boundary element methods adopt piecewise-linear representations of the complex functions that result in a second order accurate integration and normally give second-order accurate solutions for the boundary element solutions as well [4]. In complex BEM, the simplicity and elegance of complex analysis carries over to the computations as well. While the Green's function formulation and the complex method are not directly compared here, studies by Dold and Peregrine [5] and Hromadka and Lai [3] indicate that the latter method is clearly superior to others in many fluid flow problems.

In the present study, a new complex boundary element method called Riemann Complex Boundary Element Method (RCBEM) is proposed. In RCBEM, the solutions of two-dimensional fluid flow problems are developed based on the theory of Vekua [6] and it's modification and, thereby Riemann function [7] is taken as the fundamental solution to solve the linear second order elliptic equations.

In comparison with the generally used direct BEM, there are two major differences in RCBEM. In direct BEM, Greens functions are employed as solutions of adjoint operator while in RCBEM complex Riemann functions are used as the fundamental solutions of the adjoint operators. Secondly in RCBEM, the governing equations must be transformed into a complex domain because there exist two characteristics in complex plane for elliptic systems (it should be noted that hyperbolic systems remain in real plane), while the direct BEM is solved in real planes, since the Green function is adopted instead. The main difference of RCBEM with the CVBEM [3] is, while in RCBEM, the Riemann functions are used as the fundamental solutions, in CVBEM, Cauchy's functions are used as the fundamental solutions which will restrict the applications of more engineering problems beyond the harmonic functions.

In RCBEM, since the generic meaning of Riemann function is a characteristic boundary value problem, and the characteristic curves are closely associated with the propagation of certain types

of singularities, we can infer that the Riemann function used is a regular solution, meaning that the singularities are far behind infinite. Some of the important features offered by RCBEM are: (1) the Riemann functions used are regular solutions and hence they satisfy the governing equations throughout the region enclosed by the problem boundary, the approximation is made only at the boundary; (2) the integration of the boundary integrals along each boundary element are carried out exactly; (3) mathematical means can be devised to evaluate approximation errors; and (4) substantial modeling simplification are possible resulting from the complex variable application and the boundary element approach. However, it should be noted that the present theory of RCBEM is for two-dimensional problems only.

In this paper, the RCBEM is applied for the solutions of various fluid flow problems governed by Laplace equation, Helmholtz equation and steady state advection–diffusion equations. The feasibility and accuracy of the RCBEM has been shown by solving a variety of problems governed by the above mentioned equations. RCBEM solutions are verified by comparing with available exact solutions and direct BEM solutions. Good agreements are observed in all the cases.

## 2. Complex Riemann boundary integral equations

### 2.1. Riemann function in complex variables

Initially, let us take account of some results of the theory of solutions of linear second order elliptic differential equations essentially based on the complex Riemann function and the Volterra type integral equation described by Vekua [6]. Consider a second order linear elliptic differential equation in two independent variables $x$ and $y$,

$$L[u] = \frac{\partial^2 u}{\partial x^2} + \frac{\partial^2 u}{\partial y^2} + a(x,y)\frac{\partial u}{\partial x} + b(x,y)\frac{\partial u}{\partial y} + c(x,y)u = f(x,y) \tag{2.1}$$

where the coefficients $a, b, c$ and $f$ are functions of the variables $x$ and $y$, are analytic and continuous in a domain $D$. Let the coordinate transformation of the complex variables be represented as $z = x + \mathrm{i}y$, $\bar{z} = x - \mathrm{i}y$ and the differential operators as,

$$\frac{\partial}{\partial z} = \frac{1}{2}\left(\frac{\partial}{\partial x} - \mathrm{i}\frac{\partial}{\partial y}\right), \qquad \frac{\partial}{\partial \bar{z}} = \frac{1}{2}\left(\frac{\partial}{\partial x} + \mathrm{i}\frac{\partial}{\partial y}\right)$$

Now using the new complex variables, Eq. (2.1) can be transformed into,

$$M[u] = \frac{\partial^2 u}{\partial z \partial \bar{z}} + A(z,\bar{z})\frac{\partial u}{\partial z} + B(z,\bar{z})\frac{\partial u}{\partial \bar{z}} + C(z,\bar{z})u = F(z,\bar{z}) \tag{2.2}$$

which is a complex form of hyperbolic partial differential equation. $A$, $B$, $C$ and $F$ are defined as,

$$A(z,\bar{z}) = \frac{1}{4}\left[a\left(\frac{z+\bar{z}}{2}, \frac{z-\bar{z}}{2\mathrm{i}}\right) + \mathrm{i}b\left(\frac{z+\bar{z}}{2}, \frac{z-\bar{z}}{2\mathrm{i}}\right)\right], \quad C(z,\bar{z}) = \frac{1}{4}c\left(\frac{z+\bar{z}}{2}, \frac{z-\bar{z}}{2\mathrm{i}}\right)$$

$$B(z,\bar{z}) = \frac{1}{4}\left[a\left(\frac{z+\bar{z}}{2},\frac{z-\bar{z}}{2\mathrm{i}}\right) - \mathrm{i}b\left(\frac{z+\bar{z}}{2},\frac{z-\bar{z}}{2\mathrm{i}}\right)\right], \quad F(z,\bar{z}) = \frac{1}{4}f\left(\frac{z+\bar{z}}{2},\frac{z-\bar{z}}{2\mathrm{i}}\right)$$

Eq. (2.2) is the complex form of (2.1), and the coefficients $A$, $B$, $C$ and $F$ are holomorphic with respect to variables $z$ and $\bar{z}$ in a domain $z \in D$ and $\bar{z} \in D_1$ where $D$ and $D_1$ are simply connected domains.

Now the Riemann function can be expressed in two alternative forms [6],

$$R(t,\bar{z};t,\tau) = \exp\left[\int_{\tau}^{\bar{z}} A(t,\eta)\,\mathrm{d}\eta\right] \quad \text{on } z = t \tag{2.3}$$

$$R(z,\tau;t,\tau) = \exp\left[\int_{t}^{z} B(\xi,\tau)\,\mathrm{d}\xi\right] \quad \text{on } \bar{z} = \tau \tag{2.4}$$

where $t$ and $\tau$ are fixed parameters. The Riemann function $R$ satisfies the following normalized condition,

$$R(z,\tau;t,\tau) = 1 \quad \text{on } z = t,\ \bar{z} = \tau \tag{2.5}$$

By taking the adjoint of Eq. (2.2), using the Riemann functions and integrating with respect $z$, $\bar{z}$, we have the Volterra type integral equation of second kind [6],

$$R(z,\bar{z};t,\tau) - \int_{\tau}^{\bar{z}} A(z,\eta)R(z,\eta;t,\tau)\,\mathrm{d}\eta - \int_{t}^{z} B(\xi,\bar{z})R(\xi,\bar{z};t,\tau)\,\mathrm{d}\xi + \int_{t}^{z}\int_{\tau}^{\bar{z}} C(\xi,\eta)R(\xi,\eta;t,\tau)\,\mathrm{d}\xi\,\mathrm{d}\eta = 1 \tag{2.6}$$

As described in Vekua [6], using the adjoint property of Eq. (2.2) and using the Riemann functions, exchanging the pairs of $(z,\bar{z})$ and $(t,\tau)$ and integrating with respect to $t$ in the interval $(z_0,z)$, $\tau$ in $(\bar{z}_0,\bar{z})$, one can obtain

$$u(z,\bar{z}) = u(z_0,\bar{z}_0)R(z,\bar{z};z_0,\bar{z}_0) + \int_{z_0}^{z} \Phi_1(t)R(z,\bar{z};t,\bar{z}_0)\,\mathrm{d}t + \int_{\bar{z}_0}^{\bar{z}} \Phi_2(\tau)R(z,\bar{z};z_0,\tau)\,\mathrm{d}\tau + \int_{z_0}^{z}\int_{\bar{z}_0}^{\bar{z}} F(t,\tau)R(z,\bar{z};t,\tau)\,\mathrm{d}\tau\,\mathrm{d}t \tag{2.7}$$

where $\Phi_1(z) = \dfrac{\partial u(z,\bar{z}_0)}{\partial z} + B(z,\bar{z}_0)u(z,\bar{z}_0)$; $\Phi_2(z) = \dfrac{\partial u(z_0,\bar{z})}{\partial \bar{z}} + A(z_0,\bar{z})u(z_0,\bar{z})$.

It should be noted that the coefficients of Eq. (2.1) are real functions and $u$ is also a real function and hence after taking integration by parts, the solution of (2.1) can be written as,

$$u(x,y) = \mathrm{Re}\left[H_0(z)\phi(z) + \int_{z_0}^{z} H(z,t)\phi(t)\,\mathrm{d}t + \int_{z_0}^{z}\int_{\bar{z}_0}^{\bar{z}} R(z,\bar{z};t,\tau)F(t,\tau)\mathrm{d}\tau\,\mathrm{d}t\right] \tag{2.8}$$

where Re means real part and

$$H_0(z) = R(z,\bar{z};z_0,\bar{z}_0) \tag{2.9}$$

$$H(z,t) = -\frac{\partial}{\partial t}R(z,\bar{z};t,z_0) + B(z,\bar{z}_0)R(z,\bar{z};t,z_0) \tag{2.10}$$

$$\phi(z) = 2u(z,\bar{z}) - u(z_0,\bar{z}_0)R(z,\bar{z}_0;z_0,\bar{z}_0) \tag{2.11}$$

$\phi(z)$ is an arbitrary holomorphic function in $D$ determined by the boundary condition. Assuming without loss of generality that $z_0 = 0$ lying inside the region $D$ and also $A(0,\bar{z}) = B(z,0) = 0$, we get,

$$H(z,t) = -\frac{\partial}{\partial t}R(z,\bar{z};t,0) \tag{2.12}$$

$$\phi(z) = 2u(z,0) - u(0,0)R(z,0;0,0) \tag{2.13}$$

The detailed procedure of the derivation of Eq. (2.8) is given in Vekua [6], which is not repeated here.

### 2.2. Riemann functions for the elliptic differential equations

Before the application of boundary element procedure for the concerned elliptic differential equations using RCBEM, we have to find the fundamental solutions (Riemann functions in RCBEM). The fundamental solution is derived from the general Eq. (2.6). In this section, we consider some important elliptic equations in different forms, such as Laplace equation, modified Helmholtz equation and Helmholtz equation. Equations like steady-state advection–diffusion equation are solved after converting it into the modified Helmholtz equation.

#### 2.2.1. Laplace equation

Considering the Laplace equation,

$$\nabla^2 u = 0 \tag{2.14}$$

Comparing with the Eq. (2.2), the coefficients $A(z,\eta) = B(\xi,\bar{z}) = C(\xi,\eta) = 0$. From Eq. (2.6), the fundamental solution (Riemann function) for the Laplace equation is obviously,

$$R(z,\bar{z};t,\tau) = 1 \tag{2.15a}$$

Hence the Eqs. (2.9) and (2.12) for potential flow problems can be written as,

$$H_0(z) = 1 \tag{2.15b}$$

$$H(z,t) = -\frac{\partial}{\partial t}R(z,\bar{z};t,o) = 0 \tag{2.15c}$$

#### 2.2.2. Modified Helmholtz equation

Consider the modified Helmholtz equation,

$$\nabla^2 u - \lambda^2 u = 0 \tag{2.16}$$

where $\lambda$ is assumed a constant. In comparison with Eq. (2.2), the coefficients $A(z,\eta) = B(\xi,\bar{z}) = 0$, and $C(\xi,\eta) = -\lambda^2/4$. Now Eq. (2.6) can be expressed as,

$$R(z,\bar{z};t,\tau)-\frac{1}{4}\lambda^2\int_t^z\int_\tau^{\bar{z}}R(\xi,\eta;t,\tau)\,\mathrm{d}\xi\,\mathrm{d}\eta=1 \tag{2.17}$$

By the methods of successive approximations [8], the solution is,

$$R(z,\bar{z};t,\tau)=1+\int_t^z\int_\tau^{\bar{z}}\Gamma_0(z,\bar{z};\xi,\eta;t,\tau)\,\mathrm{d}\eta\,\mathrm{d}\xi \tag{2.18}$$

where $\Gamma_0(z,\bar{z};\xi,\eta;t,\tau)=\sum_{v=1}^{\infty}N_0^{(v)}(z,\bar{z};\xi,\eta;t,\tau)$

$$N_0^{(v)}(z,\bar{z};\xi,\eta;t,\tau)=\int_\xi^z\int_\eta^{\bar{z}}N_0^{(v-1)}(s,\sigma;\xi,\eta;t,\tau)N_0\,\mathrm{d}\sigma\,\mathrm{d}s;\quad N_0^{(1)}=N_0=-C(\xi,\eta)$$

$$\text{since } N_0^{(1)}=-C(\xi,\eta)=\lambda^2/4,\ N_0^{(2)}=\int_\xi^z\int_\eta^{\bar{z}}\left(\frac{1}{4}\lambda^2\right)\left(\frac{1}{4}\lambda^2\right)\mathrm{d}\sigma\,\mathrm{d}s=\frac{\lambda^4}{16}(z-\xi)(\bar{z}-\eta)$$

$$N_0^{(3)}=\int_\xi^z\int_\eta^{\bar{z}}\left(\frac{1}{4}\lambda^2\right)\left[\frac{\lambda^4}{16}(z-\xi)(\bar{z}-\eta)\right]\mathrm{d}\sigma\,\mathrm{d}s=\frac{\lambda^6}{64}(z-\xi)^2(\bar{z}-\eta)^2\ldots$$

Now we have,

$$\begin{aligned}R(z,\bar{z};t,\tau)&=1+\int_t^z\int_\tau^{\bar{z}}\Gamma_0(z,\bar{z};\xi,\eta;t,\tau)\,\mathrm{d}\eta\,\mathrm{d}\xi=1+\int_t^z\int_\tau^{\bar{z}}\left[\sum_{v=1}^{\infty}N_0^{(v)}(z,\bar{z};\xi,\eta,t,\tau)\right]\mathrm{d}\eta\,\mathrm{d}\xi\\&=1+\int_t^z\int_\tau^{\bar{z}}\left[\frac{1}{4}\lambda^2+\frac{\lambda^4}{16}(z-\xi)(\bar{z}-\eta)+\frac{\lambda^6}{64}(z-\xi)^2(\bar{z}-\eta)^2+\cdots\right]\mathrm{d}\eta\,\mathrm{d}\xi\\&=\sum_{k=1}^{\infty}[(z-t)(\bar{z}-\tau)/2]^{2k}/k!\Gamma(k+1)=I_0\left(\lambda\sqrt{(z-t)(\bar{z}-\tau)}\right)\end{aligned} \tag{2.19a}$$

where $I_0$ is the modified Bessel function of the first kind of order zero which also shows the regular behavior in the defined domain.

Hence the Eqs. (2.9) and (2.12) can be written as,

$$H_0(z)=I_0(\lambda r),\quad r=\sqrt{x^2+y^2} \tag{2.19b}$$

$$H(z,t)=\frac{1}{2}\lambda\sqrt{\bar{z}}\frac{I_1\left(\lambda\sqrt{\bar{z}(z-t)}\right)}{\sqrt{z-t}} \tag{2.19c}$$

where $I_j$ is the modified Bessel function of the first kind of order one which is a regular function for the defined domain.

*2.2.3. Helmholtz equation*

For the Helmholtz equation ($\lambda$ is constant),

$$\nabla^2u+\lambda^2u=0 \tag{2.20}$$

In comparison with Eq. (2.2), the coefficients $A(z,\eta) = B(\xi,\bar{z}) = 0$, and $C(\xi,\eta) = \lambda^2/4$. Using the successive approximation as mentioned above, we obtain

$$R(z,\bar{z};t,\tau) = J_0\left(\lambda\sqrt{(z-t)(\bar{z}-\tau)}\right) \tag{2.21a}$$

where $J_0$ is the Bessel function of the first kind of order zero, which is also a regular function for the defined domain.

Hence the Eqs. (2.9) and (2.12) can be written as,

$$H_0(z) = J_0(\lambda r), \quad r = \sqrt{x^2+y^2} \tag{2.21b}$$

$$H(z,t) = -\frac{\partial}{\partial t}R(z,\bar{z};t,0) = -\frac{1}{2}\lambda\sqrt{\bar{z}}\frac{J_1\left(\lambda\sqrt{\bar{z}(z-t)}\right)}{(\sqrt{z-t})} \tag{2.21c}$$

where $J_1$ is the Bessel function of the first kind of order one, which shows the regular behavior in the defined domain.

### 2.3. Boundary conditions

In this section, the application of two types of boundary conditions, Dirichlet boundary conditions and mixed boundary conditions, are illustrated with reference to the RCBEM model development.

#### 2.3.1. Dirichlet boundary conditions

Let $D$ be a simply connected domain bounded by a contour $\Gamma$. Considering the function $u(x,y)$ satisfying the real boundary condition,

$$u(x,y) = g(x,y) = g(s) \quad s \in \Gamma \tag{2.22}$$

Assuming that $g(s)$ satisfies the Hölder condition on boundary $\Gamma$ and the boundary value $\phi(t)$ of Eq. (2.13) also satisfies the Hölder condition which can be expressed in the form of double layer (or the Cauchy kernel integral),

$$\phi(z) = \frac{1}{2\pi\mathrm{i}}\int_\Gamma \frac{\phi(t)}{t-z}\,\mathrm{d}t \tag{2.23}$$

for harmonic function [6] and

$$\phi(z) = \frac{1}{2\pi\mathrm{i}}\int_\Gamma \frac{\mu(t)}{t-z}\,\mathrm{d}t \tag{2.24}$$

for the other functions [6] where $\mu(t)$ is a real density function of the dipole.

Substituting Eq. (2.24) into Eq. (2.8), the Fredholm integral equation of the first kind can be obtained as,

$$u(x,y) = \int_\Gamma \mu(t)M(z,t)\,\mathrm{d}s \tag{2.25}$$

where

$$M(z,t) = \mathrm{Re}\left[\frac{H_0(z)\mathrm{d}t/\mathrm{d}s}{2\pi\mathrm{i}(t-z)} + \frac{\mathrm{d}t/\mathrm{d}s}{2\pi\mathrm{i}}\int_0^z \frac{H(z,t_1)}{t-t_1}\,\mathrm{d}t_1\right] \tag{2.26}$$

Let an interior point $z$ approaches to an arbitrary point $t_0$, and satisfies the boundary condition Eq. (2.22), the Fredholm type integral equation of second kind can be obtained,

$$\left(1-\frac{\bar{\alpha}}{2\pi}\right)\mu(t_0) + \int_\Gamma M(t_0,t)\mu(t)\,\mathrm{d}s = g(t_0) \tag{2.27}$$

for the unknown function $\mu$, ($\bar{\alpha}$ is contour angle, $0 \leqslant \bar{\alpha} \leqslant 2\pi$) [6], where,

$$M(t_0,t) = \mathrm{Re}\left[\frac{H_0(t_0)\mathrm{d}t/\mathrm{d}s}{2\pi\mathrm{i}(t-t_0)} + \frac{\mathrm{d}t/\mathrm{d}s}{2\pi\mathrm{i}}\int_0^{t_0} \frac{H(t_0,t_1)}{t-t_1}\,\mathrm{d}t_1\right] \tag{2.28}$$

Eqs. (2.25)–(2.28) are convenient to evaluate in numerical methods since the integral equations are all regular.

*2.3.2. Mixed boundary conditions*

Considering the following more general mixed type boundary condition,

$$p(s)\frac{\partial u}{\partial x} + q(s)\frac{\partial u}{\partial y} + r(s)u = g(s) \quad s \in \Gamma \tag{2.29}$$

and the fact that

$$\frac{\partial}{\partial x} = \frac{\partial}{\partial z} + \frac{\partial}{\partial \bar{z}}, \qquad \frac{\partial}{\partial y} = \mathrm{i}\left(\frac{\partial}{\partial z} - \frac{\partial}{\partial \bar{z}}\right),$$

Eq. (2.29) can be written as

$$A(s)\frac{\partial u}{\partial z} + \overline{A}(s)\frac{\partial u}{\partial \bar{z}} + r(s)u = g(s) \tag{2.30}$$

where $A(s) = p(s) + \mathrm{i}q(s)$, $\overline{A}(s) = p(s) - \mathrm{i}q(s)$.

Substituting Eq. (2.30) into Eq. (2.8) yields,

$$\mathrm{Re}\left[L(t_0)\phi'(t_0) + M(t_0)\phi(t_0) + \int_0^{t_0} N(t_0,t_1)\phi(t_1)\,\mathrm{d}t\right] = g(t_0) \tag{2.31}$$

where $L(t_0) = A(t_0)H_0(t_0)$ and

$$M(t_0) = A(t_0)\frac{\partial H_0(t_0)}{\partial t_0} + A(t_0)H(t_0,t) + \overline{A}(t_0)\frac{\partial H_0(t_0)}{\partial \bar{t}_0} + r(t_0)H_0(t_0) \tag{2.32}$$

$$N(t_0,t_1) = A(t_0)\frac{\partial H_0(t_0,t_1)}{\partial t_0} + \overline{A}(t_0)\frac{\partial H(t_0,t_1)}{\partial \bar{t}_0} + r(t_0)H(t_0,t_1) \tag{2.33}$$

Assuming that the boundary values $\phi(z)$ and $\phi'(z)$ satisfy the Hölder condition on boundary $\Gamma$, we can use an integral representation of the following,

$$\phi(z) = \frac{1}{2\pi i}\int_{\Gamma} \mu(t)\ln(t-z)\,dt \quad z \in D \tag{2.34}$$

With the help of Eqs. (2.34), (2.31) can be written as,

$$\mathrm{Re}\left\{ -\left(1-\frac{\bar{\alpha}}{2\pi}\right)L(t_0)\mu(t_0) - \int_{\Gamma}\left[\frac{L(t_0)}{t_0-t} - E_0(t_0,t)\right]\mu(t)\,dt\right\} = g(t_0) \tag{2.35}$$

where,

$$E(t_0,t) = \frac{1}{2\pi i}\int_0^{t_0} N(t_0,t)\ln(t-t_1)\,dt_1 + M(t_0)\ln(t-t_0) \tag{2.36}$$

Eqs. (2.34)–(2.36) are convenient to evaluate in numerical methods since the integral equations are all regular. The above equations can be used in the evaluation of mixed type and Neuman type boundary conditions in the RCBEM procedure.

## 3. Boundary integral procedure

Using the results described in Section 2, RCBEM is developed to solve the singular integral equation. The first step in the RCBEM procedure is that the boundary of the domain of the problem considered is divided into piecewise smooth elements as shown in Fig. 1. On any one of the elements considered, the boundary conditions are of the same kind, say Dirichlet, Neumann or mixed etc. Assuming $t_0$ as a base point (as in Fig. 1), we have

$$t - t_0 = re^{i\alpha} \tag{3.1}$$

$$dt = e^{i\theta}\,ds \tag{3.2}$$

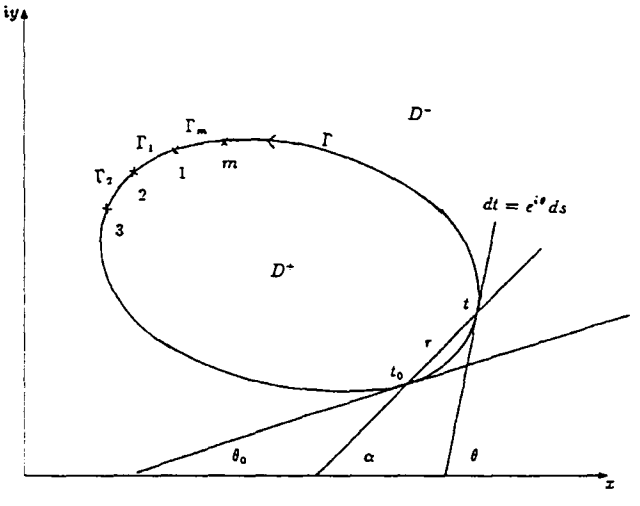


Fig. 1. Domain and boundary for complex plane.

Then the kernel of Eq. (2.27) or (2.28) can be expressed as,

$$M(t_0,t) = \frac{1}{2\pi}\mathrm{Im}\left[\frac{H_0(t_0)e^{i(\theta-\alpha)}}{r} + e^{i\theta}\int_0^{t_0}\frac{H(t_0,t_1)}{t-t_1}\,dt_1\right]$$
$$= \frac{1}{2\pi}\frac{H_0(t_0)\sin(\theta-\alpha)}{r} + \frac{1}{2\pi}\mathrm{Im}\left[e^{i\theta}\int_0^{t_0}\frac{H(t_0,t_1)}{t-t_1}\,dt_1\right] \tag{3.3}$$

The first term of Eq. (3.3) is regular as $t$ approaches to $t_0$ [8].

Our aim is to finally devise a method that will convert Eq. (2.27) into a series of algebraic equations. For convenience, considering a linear element, the unknowns of Eq. (2.27) can be represented as follows [9],

$$\mu(t) = \sum_{i=1}^{2} N_i\mu_i = \frac{(\mu_{j+1}-\mu_j)\xi + \xi_{j+1}\mu_j - \xi_j\mu_{j+1}}{(\xi_{j+1}-\xi_j)} \quad \xi_j \leqslant \xi \leqslant \xi_{j+1} \tag{3.4}$$

in which $\xi$ is the distance along the element (see Fig. 2), $N_i$ is the shape function of the linear element and,

$$r_i = (\xi^2 + \eta_i^2)^{1/2} \tag{3.5}$$

$$\alpha_i = \tan^{-1}\left(\frac{\xi\sin\theta + \eta_i\cos\theta}{\xi\cos\theta - \eta_i\sin\theta}\right) \tag{3.6}$$

are used in the integration.

The last term of Eq. (3.3) is the imaginary part of complex variable integration, which can be evaluated using the simple trapezoidal rule, Simpson 3/8 rule or by Gaussian quadrature. Here the implementation using Gaussian quadrature is explained briefly.

In the Gaussian quadrature method, the complex variable integration is done by separating the real and imaginary parts, and integrating each separately. For example, consider the Helmholtz equation,

$$H(t_0,t_1) = -\frac{\lambda}{2}\sqrt{t_0}\frac{J_1\left(\lambda\sqrt{t_0(t_0-t_1)}\right)}{\sqrt{t_0-t_1}} \tag{3.7}$$

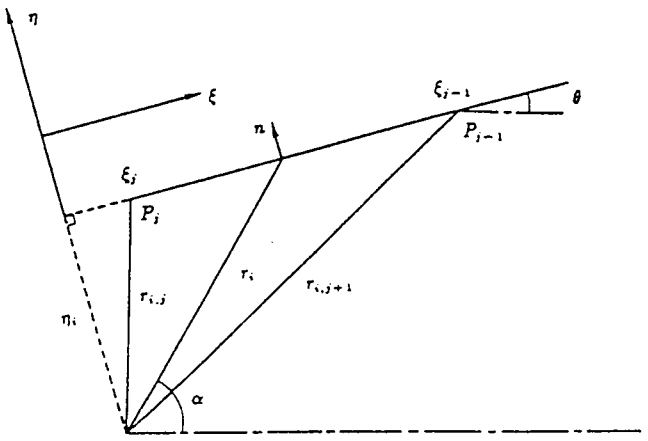


Fig. 2. Local $\xi-\eta$ coordinate system for RCBEM.

Substituting Eq. (3.7) into Eq. (2.28), the complex integration can be expressed as,

$$\int_0^{t_0} \frac{J_1(\lambda\sqrt{t_0(t_0-t_1)})}{(t_j-t_1)\sqrt{t_0-t_1}}\,\mathrm{d}t_1 \quad 0\leqslant t_1\leqslant t_0, \quad t_0 = x_0 + \mathrm{i}y_0 \tag{3.8}$$

Since Eq. (3.8) is independent of path, a straight-line integration can be chosen between 0 and $t_0$. Let

$$t_1(s) \equiv x(s) + \mathrm{i}y(s) = s + \mathrm{i}\frac{y_0}{x_0}s \quad 0\leqslant s\leqslant x_0 \tag{3.9}$$

$$\mathrm{d}t_1 = \left(1 + \mathrm{i}\frac{y_0}{x_0}\right)\mathrm{d}s \tag{3.10}$$

Substituting Eqs. (3.9) and (3.10) into Eq. (3.8), the integral can be separated into real part and imaginary part and the Gaussian quadrature can be applied for numerical integration.

The last term of Eq. (3.3) can be written as follows after the numerical discretization for each $\mu_i$

$$\frac{1}{2\pi}\mathrm{Im}\left[\mathrm{e}^{\mathrm{i}\theta}\int_0^{t_0}\frac{H(t_0,t_1)N_j}{t_i-t_1}\,\mathrm{d}t_1\right]\mu_j = B_{ij}\mu_j, \quad i = 1,2,\ldots N \tag{3.11}$$

The integral on the first term of Eq. (3.3) can be integrated over the element between $p_j$ and $p_{j+1}$ with respect to the base point $p_i$, by omitting the constant of $H_0(t_0)$.

$$I^{\mathrm{e}} = \int_{\xi_j}^{\xi_{j+1}} \frac{\sin(\theta_j-\alpha_i)}{r_i}\mu(\xi)\,\mathrm{d}\xi = [K^{\mathrm{e}}]\begin{pmatrix}\mu_j\\ \mu_{j+i}\end{pmatrix} \tag{3.12}$$

where

$$|K^{\mathrm{e}}| = |(K^{\mathrm{e}})_{i,j}, (K^{\mathrm{e}})_{i,j+1}| = |\xi_{j+1}I_{11} - I_{12}, I_{12} - \xi_j I_{11}| \tag{3.13}$$

in which

$$I_{11} = (\sin\theta_i I_1 - \cos\theta_j I_2)\frac{1}{2\pi}; \quad I_{12} = (\sin\theta_j I_3 - \cos\theta_j I_4)\frac{1}{2\pi} \tag{3.14}$$

$$I_1 = \frac{1}{(\xi_{j+1}-\xi_j)}\int_{\xi_j}^{\xi_{j+1}}\frac{\cos\alpha_i}{r_i}\,\mathrm{d}\xi = \frac{1}{(\xi_{j+1}-\xi_j)}\left[\frac{1}{2}\cos\theta_j \ln\left(\frac{\xi_{j+1}^2+\eta_i^2}{\xi_j^2+\eta_i^2}\right) - \sin\theta_j\left(\tan^{-1}\frac{\xi_{j+1}}{\eta_i} - \tan^{-1}\frac{\xi_j}{\eta_i}\right)\right] \tag{3.15}$$

$$I_2 = \frac{1}{(\xi_{j+1}-\xi_j)}\int_{\xi_j}^{\xi_{j+1}}\frac{\sin\alpha_i}{r_i}\,\mathrm{d}\xi = \frac{1}{(\xi_{j+1}-\xi_j)}\left[\frac{1}{2}\sin\theta_j \ln\left(\frac{\xi_{j+1}^2+\eta_i^2}{\xi_j^2+\eta_i^2}\right) - \cos\theta_j\left(\tan^{-1}\frac{\xi_{j+1}}{\eta_i} - \tan^{-1}\frac{\xi_j}{\eta_i}\right)\right] \tag{3.16}$$

$$I_3 = \frac{1}{(\xi_{j+1}-\xi_j)}\int_{\xi_j}^{\xi_{j+1}} \frac{\cos\alpha_i}{r_i}\xi\,d\xi$$
$$= \frac{1}{(\xi_{j+1}-\xi_j)}\left\{\cos\theta_j\left[(\xi_{j+1}-\xi_j)-\eta_i\left(\tan^{-1}\frac{\xi_{j+1}}{\eta_i}-\tan^{-1}\frac{\xi_j}{\eta_i}\right)\right]-\frac{\eta_j}{2}\sin\theta_j\ln\left(\frac{\xi_{j+1}^2+\eta_i^2}{\xi_j^2+\eta_i^2}\right)\right\} \tag{3.17}$$

$$I_4 = \frac{1}{(\xi_{j+1}-\xi_j)}\int_{\xi_j}^{\xi_{j+1}} \frac{\sin\alpha_i}{r_i}\xi\,d\xi$$
$$= \frac{1}{(\xi_{j+1}-\xi_j)}\left\{\sin\theta_j\left[(\xi_{j+1}-\xi_j)-\eta_i\left(\tan^{-1}\frac{\xi_{j+1}}{\eta_i}-\tan^{-1}\frac{\xi_j}{\eta_i}\right)\right]+\frac{\eta_i}{2}\cos\theta_j\ln\left(\frac{\xi_{j+1}^2+\eta_i^2}{\xi_j^2+\eta_i^2}\right)\right\} \tag{3.18}$$

Finally, the algebraic Eq. (2.27) can be expressed as,

$$\sum_{j=1}^{N}(A_{ij}+B_{ij})\mu_j = g_i \quad i=1,2,\ldots N \tag{3.19}$$

where

$$A_{ij} = \left|(K^e)_{ij}+\left(1-\frac{\bar{\alpha}}{2\pi}\right)\delta_{ij}\right| \qquad \delta_{ij}=\begin{cases}1 & i=j\\ 0 & i\neq j\end{cases} \tag{3.20}$$

Eq. (3.20) is used only in the case of interior problems. For the exterior problems, Eq. (3.20) is written as,

$$A_{ij} = \left|(K^e)_{ij}-\frac{\bar{\alpha}}{2\pi}\delta_{ij}\right| \qquad \delta_{ij}=\begin{cases}1 & i=j\\ 0 & i\neq j\end{cases} \tag{3.21}$$

It should be noted that for exterior problem, the normal vector is in opposite direction.

## 4. Numerical applications

To test the feasibility and accuracy of the RCBEM model, here three numerical applications are presented. Initially, we consider the potential flow problems in which interior and exterior problems are considered. Secondly, a fluid flow problem governed by the Helmholtz equation is considered and finally a steady-state advection–diffusion problem is solved by transforming the governing equation into the modified Helmholtz equation. The RCBEM results in all the cases are compared with analytical and other numerical solutions.

### *4.1. Potential flow problems*

The governing equation for the potential flow problems is the Laplace equation. Here the potential flows are considered with interior problems and exterior problems. In the case of po-

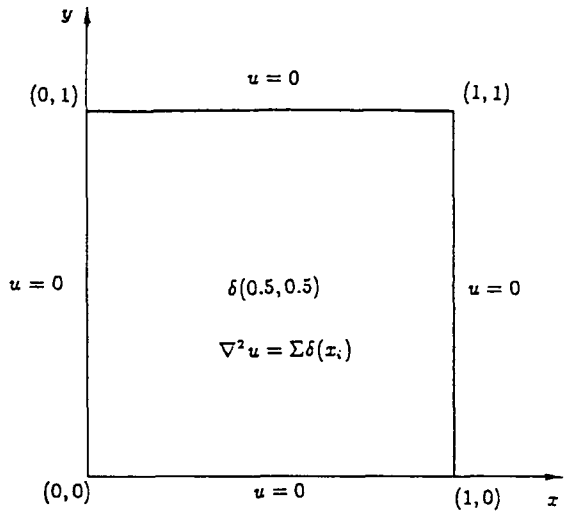


Fig. 3. Study domain and boundary conditions for the groundwater flow problem.

tential flow problems, we consider the solution of two problems using the RCBEM. Initially an interior problem of groundwater flow is considered and then an exterior problem of source outside a circular cylinder is considered.

*4.1.1. Groundwater flow problem*

Here we consider a two-dimensional groundwater flow problem in a homogeneous, isotropic porous media with a pumping well. The problem is a bounded square region, $0 \leqslant x \leqslant 1$ and $0 \leqslant y \leqslant 1$ with zero potential on all the sides as shown in Fig. 3. There is a pumping well at the middle of the domain with unit discharge. In the RCBEM model, the boundary of the domain is discretized with 40 linear elements. Fig. 4 shows the potential variation with respect to the $x$-axis at $y = 0.5$ from the well position. The results are compared with exact solution and a BEM model [2]. Good agreement is observed between the results. A sensitivity study with different mesh discretization showed that RCBEM yields comparable results with other models even with 8 linear boundary elements. This case study shows the feasibility of the RCBEM model for the interior type problems.

*4.1.2. Exterior flow problem*

Here we consider the two-dimensional flow field past a circular cylinder of radius $r = 1$ due to a source at $x = 2$ with strength $m = 2\pi$. The aim is to find the stream function distribution over the circular cylinder due to the source effects. The problem domain with discretization is shown in Fig. 5. The boundary conditions of the stream function along the cylinder are assumed to be zero. Since the problem is exterior in nature, a sensitivity study of the mesh showed that a finer discretization is necessary [2]. In the RCBEM model, the total boundary of the domain is discretized with 160 linear elements. The problem can be simplified by considering the symmetry and discretizing half of the domain.

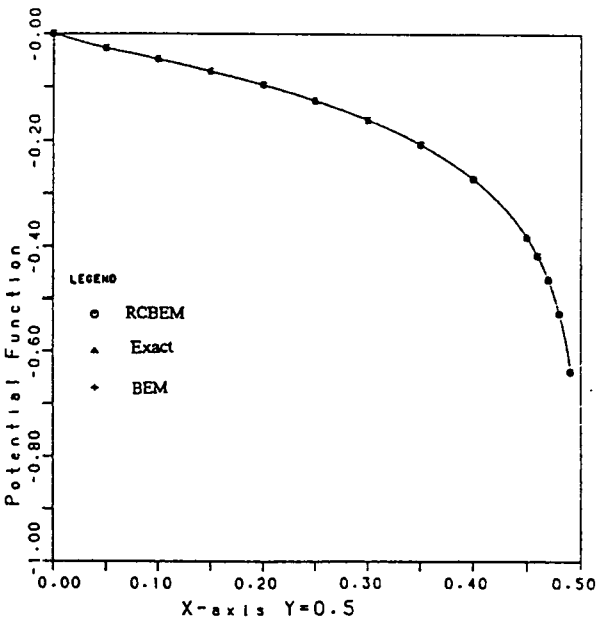


Fig. 4. Comparison of potential for groundwater flow problem.

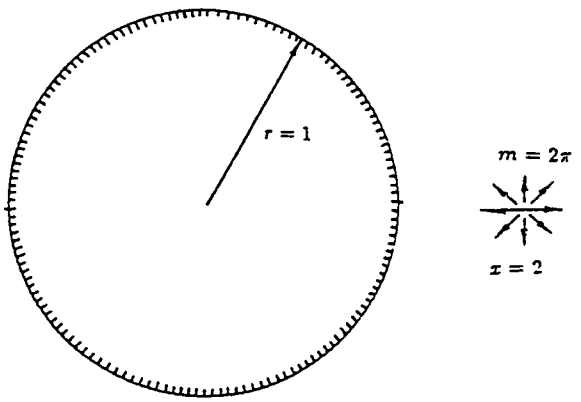


Fig. 5. Study domain for the exterior potential flow problem with source outside a circular cylinder.

In this problem, the influence of the point source can be directly taken into account or it can be separated into the perturbed part and the potential flow part and the solution can be combined [2]. In the present analysis, as the problem considered is linear in nature, it is convenient to separate the stream function ($\psi$) into two parts, $\psi = \psi_U + \psi_P$, where $\psi_U$ defines the stream function due to potential flow and $\psi_P$ is a perturbed stream function owing to the influence of the source. Fig. 6 shows the stream function variation around the circular cylinder. The results are compared with exact solution. Good agreement is observed between the results. This case study shows the feasibility of the RCBEM model for the exterior type problems.

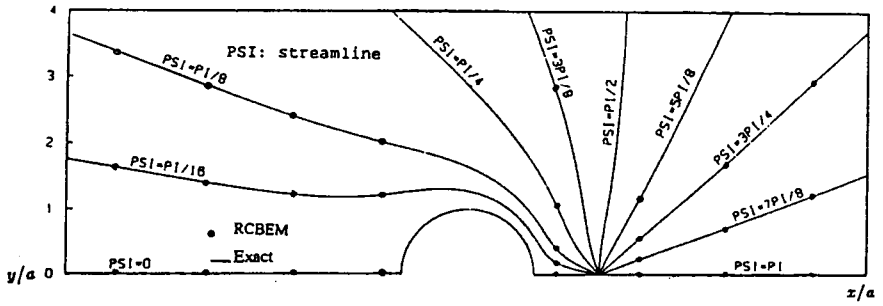


Fig. 6. Streamlines for the exterior potential flow problem: comparison of RCBEM and exact solution.

### 4.2. Helmholtz equation problem

The governing equation of the reduced wave problem is the Helmholtz equation. To illustrate the application of the Helmholtz equation problem, here we consider an interior problem in which the potential is propagated from a point source of unit strength. For the demonstration purpose, the value of $\lambda$ is assumed as 1. The problem domain with discretization is shown in Fig. 7. The point source is located at the center of the domain. All over the boundary of the domain, a Dirichlet boundary condition $u(1,\theta) = 1$ is assumed. The boundary of the domain is discretized with 120 elements. The exact solution for the problem considered is given by,

$$u = \frac{J_0(\lambda r)}{J_0(\lambda a)} \tag{4.1}$$

Fig. 8 shows the propagation of potential for $a = 1$ along the axis using the RCBEM. The results are compared with the exact solution and a BEM model [2]. The results are almost identical. A sensitivity study with different mesh discretization showed that RCBEM yields

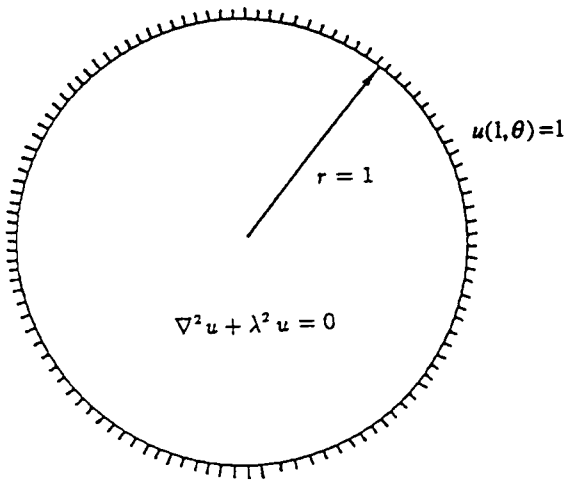


Fig. 7. Study domain and boundary conditions for the Helmholtz equation problem.

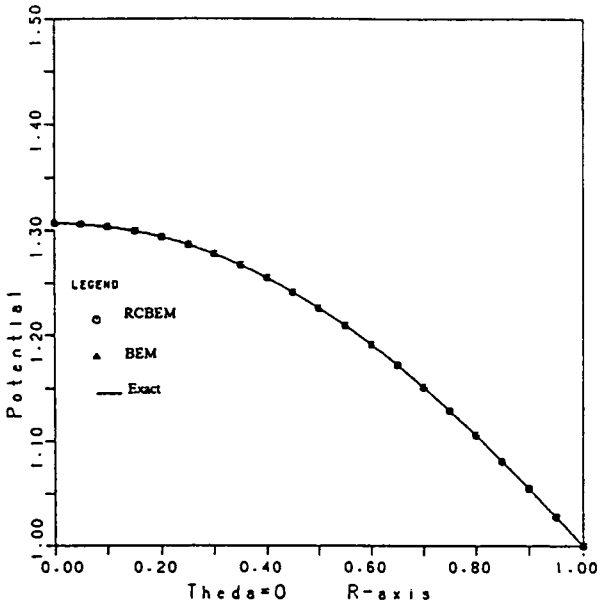


Fig. 8. Comparison of potential for the Helmholtz equation problem.

comparable results with other models even with 40 linear boundary elements. This case study shows the feasibility of the RCBEM model for the Helmholtz equation type problems.

### 4.3. Advection–diffusion problem

Here the steady-state advection–diffusion problem is solved, by converting the governing equation into the modified Helmholtz equation. The governing equation of steady-state advection–diffusion problem is,

$$\nabla \cdot ([k]\nabla u) - (\overline{V} \cdot \nabla)u = f \tag{4.2}$$

where $k$ is the diffusivity coefficient, $\overline{V}$ is the convective velocity and $f$ is the source or sink term. The governing equation is made dimensionless using the following variables,

$$\bar{x}^* = \frac{\bar{x}}{L}, \quad \nabla^* = L\nabla, \quad [k^*] = \frac{[k]}{K}, \quad \overline{V}^* = \frac{\overline{V}}{U}, \quad u^* = \frac{u}{u_0} \tag{4.3}$$

where $L$ is the characteristic length, $K$ is the characteristic diffusivity and $U$ is the characteristic velocity. Assuming $f = 0$, the non-dimensional form of Eq. (4.2) can be written as,

$$\nabla^* \cdot ([k^*]\nabla^* u^*) - Pe(\overline{V}^* \cdot \nabla^*)u^* = 0 \tag{4.4}$$

where $Pe = UL/K$ is the Peclet number. Using the following transformation [10],

$$u^{**} = e^{-g}u^*; \quad \nabla^{**} g = \frac{1}{2} Pe[k^*]^{-1}\overline{V} \tag{4.5}$$

into Eq. (4.4), we can obtain the transformed modified Helmholtz equation as the following equation after omitting the superscript ** for brevity,

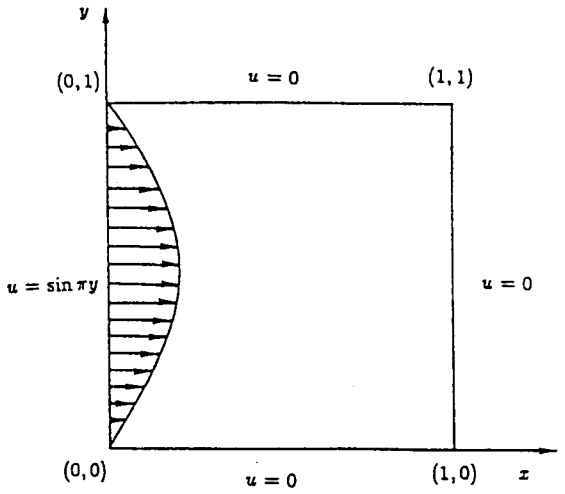


Fig. 9. Study domain and boundary conditions for the advection–diffusion problem.

$$\nabla \cdot ([k]\nabla u) - \lambda^2 u = 0 \tag{4.6}$$

where

$$\lambda^2 = \frac{1}{4} Pe^2 \overline{V} [k]^{-1} \overline{V} + \frac{1}{2} Pe \nabla \cdot \overline{V} \tag{4.7}$$

There are two limitations for this transformation viz. $\lambda^2$ have to be positive and the flow field should be irrotational. Here we consider an advection–diffusion problem in two-dimensional domain. The problem is a bounded square domain. A boundary condition with $\sin(\pi y)$ concentration profile is imposed on the boundary $(0, y)$ and zero concentration is assumed on all other boundaries. Fig. 9 depicts the studied domain with associated boundary conditions. The RCBEM simulates the flow field with constant $V_x = 1$, $V_y = 0$, $[k] = [I]$, and different Peclet numbers from diffusion (low $Pe$) to advection (high $Pe$) dominated flows. The boundary of the domain is discretized into 40 linear elements. The computations are carried out for Peclet numbers of 0, 1, 10, 40 and 80. For this problem, an exact solution can be derived as,

$$u = \frac{\sin \pi y}{e^a - e^b} [e^{a+bx} - e^{ax+b}] \tag{4.8}$$

where

$$a = \frac{Pe + \sqrt{4\pi^2 + Pe^2}}{2}, \qquad b = \frac{Pe - \sqrt{4\pi^2 + Pe^2}}{2} \tag{4.9}$$

Using RCBEM, for all the Peclet numbers, very stable and comparable results with analytical solutions are obtained. Fig. 10 shows the concentration along $(x, 0.5)$ compared with exact solution for various Peclet numbers. Good agreement is observed between the solutions and the results show that RCBEM is stable for higher Peclet number problems, which are more difficult and challengable to other numerical methods. This case study shows the effectiveness of the RCBEM model for the two-dimensional steady-state advection–diffusion problems.

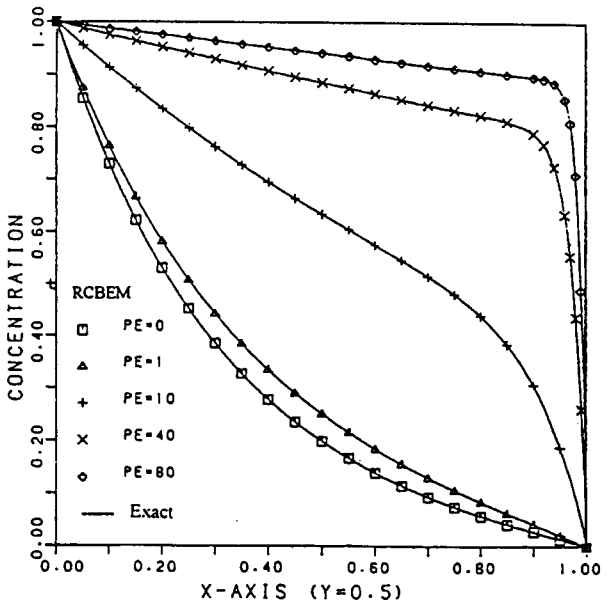


Fig. 10. Comparison of concentration for the advection–diffusion problem.

## 5. Concluding remarks

A new boundary integral equation model, RCBEM, is proposed based on the (BEM) and the theory of Vekua and its modification as well as complex Riemann function as the fundamental solution. The RCBEM method is used to solve the linear, second order, elliptical partial differential equations in the fluid flow problems. Compared to the generally used BEM, RCBEM applies complex Riemann function as the solution of the adjoint operator and the governing equations should be transformed into complex domain. The singular problem occurring in direct BEM can be avoided in RCBEM, especially for regular domain problems. The efficiency and accuracy of the RCBEM depends on the complex variable integration and the presented methodology applies only to two-dimensional problems. The simulations of various numerical examples presented demonstrated the accuracy and feasibility of RCBEM model.

## Acknowledgements

The work reported in this paper was supported by the National Science Council, Taiwan. It is greatly appreciated.

## References

[1] H. Power, L.C. Wrobel, Boundary Integral Methods in Fluid Mechanics, Computational Mechanics Publications, Southampton, 1995.

[2] C.A. Brebbia, J.C.F. Telles, L.C. Wrobel, Boundary Element Techniques—Theory and Applications in Engineering, Springer, Berlin, 1984.
[3] T.V. Hromadka II, C. Lai, The Complex Variable Boundary Element Method in Engineering Analysis, Spinger, New York, 1986.
[4] W.W. Schultz, S.W. Hong, Solution of potential problems using an over determined complex boundary integral method, J. Comp. Phys. 84 (1988) 414–440.
[5] J.W. Dold, D.H. Peregrine, Steep unsteady water waves: an efficient computational scheme, in: Proceedings of the 19th International Conference On Coastal Engineering, Houston, TX, USA, 1984.
[6] I.N. Vekua, New Methods for Solving Elliptic Equations, North-Holland Publishing Company, Amsterdam, 1967.
[7] R. Courant, D. Hilbert, Methods of Mathematical Physics, vol. 1, Interscience, New York, 1953.
[8] F.G. Tricomi, Integral Equations, Interscience, New York, 1957.
[9] V.V. Ivanov, The Theory of Approximate Methods and their Application to the Numerical Solution of Singular Integral Equation, Nordhoff Publishing Co., Leyden, 1976.
[10] M. Ikeuchi, M. Sakakihara, Boundary elements in steady convective diffusion problems, J. Comput. Appl. Math. 12/13 (1985) 381–389.

Vol. 2, no. 12, 2002

ISSN 1311 – 6797

# INTERNATIONAL MATHEMATICAL JOURNAL

Editorial Board

M. Amamiya ( Japan )
J. M. Ash ( USA )
T. Colding ( USA )
M. Fliess ( France )
A. Fokas ( UK )
K. Fuller ( USA )
J. Glimm ( USA )
W. Goldman ( USA )
F. C. Graham ( USA )
T. Hall ( Australia )
D. Hong ( USA )
S. Kichenassamy ( France )
F. – H. Lin ( USA )
J. Lyness ( USA )
K. Ono ( USA )
I. Prigogine ( Belgium )
L. Reichel ( USA )
P. C. Sabatier ( France )
M. Tang ( USA )
W. Veech ( USA )
J. Vigo – Aguiar ( Spain )
X. Zhou ( USA )

Managing Editor: Emil Minchev

International Scientific Publications

## *International Mathematical Journal*

Aims and scopes: The journal will publish carefully selected original research papers in the area of pure and applied mathematics as follows: combinatorics, order, lattices, ordered algebraic structures, general mathematical systems, number theory, field theory and polynomials, commutative rings and algebras, algebraic geometry, linear and multi linear algebra, matrix theory, associative and nonassociative rings, category theory, homological algebra, K – theory, group theory, Lie algebras, real functions, measure and integration, functions of complex variables, potential theory, special functions, ordinary differential equations, partial differential equations, finite difference and functional equations, approximation and expansion, Fourier analysis, abstract harmonic analysis, integral transforms, operational calculus, integral equations, functional analysis, operator theory, calculus of variation and optimal control, optimization, geometry, differential geometry, topology, manifolds, probability theory and stochastic processes, statistics, numerical analysis, computer science, mechanics, thermodynamics, quantum theory, relativity, economics, programming, games, mathematical biology, information and communication, circuits.

Call for papers: The authors are cordially invited to submit papers in triplicate to the Managing Editor: Emil Minchev. Manuscripts submitted to this journal will be considered for publication with the understanding that the same work has not been published and is not under consideration for publication elsewhere.

Managing Editor: Dr. Emil Minchev, Department of Mathematics, Faculty of Education, Chiba University, Yayoi – cho 1 –33, Inage – ku, Chiba 263 – 8522, Japan

e – mail: eminchev@hotmail.com

Intern. Math. Journal, Vol. 2, no. 12, 2002, 1199 – 1215

# Analysis of the 2D Stokes Flows by the Non-Singular Boundary Integral Equation Method

Chia-Ming Fan , Der-Liang Young*

Department of Civil Engineering & Hydrotech Research Institute
National Taiwan University, Taipei, Taiwan, Republic of China
*correspond to: D.L. Young Fax:+886-2-23639258
E-mail:dlyoung@hy.ntu.edu.tw

## Abstract

The non-singular boundary integral equation for the Laplace (Poisson) equation, the Biot-Savart law and the velocity-vorticity formulation will be used to solve some typical flow field problems, such as the 2D Stokes flows in a square cavity and a circular cavity. The conventional treatment of singularity for the boundary element method is circumvented by the introduction of Gauss flux theorem and other iterative analytic schemes, which will be elaborated in detail in this paper. We have computed the 2D Stokes flows in a circular cavity and a square cavity, which are compared with the solutions with those of both analytic and some other numerical results, such as finite difference, finite element, and conventional boundary element methods available in literature. The present study demonstrates that the non-singular boundary element method gives very good results as comparing with analytic or other numerical solutions, even in a very coarse grid.
Keywords: Non-singular boundary integral equation, Laplace (Poisson) equation, Biot-Savart law, velocity-vorticity formulation, 2D Stokes flows, cavity flows

## Introduction

Boundary element method(BEM) is a very powerful numerical technique for the solution of boundary value problems. Only the boundary needs to

be discretized, the domain integration is not required and the flux term is obtained directly. Although the boundary element method was developed widely and quickly, there still exist some problems. How to deal with the integration of singularities in BEM still confused many researchers.

The boundary element method has been known for its difficulty of numerical integration of singularities in the kernel of boundary integral equation. In order to avoid solving these types of singularity, many methodologies are investigated such as mapping method[1], and other types of desingularity formulations are proposed by researchers[2] [3]. This technique was developed originally by Landweber and Macagno[4].

There are two kinds of desingularity techniques in general. One is to move the singular points away from the boundary and outside the problem domain[5]. And the other general way of treating the non-singular boundary integral equation is to consider the singular points which are still on the boundary but the singular behavior is removed by a mathematical technique via the Gauss flux theorem and other analytic schemes [6][7]. The non-singular boundary equation method in this paper belongs to the second method.

The viscous incompressible flow is governed by the Navier-Stokes equations. There are three general formulations for numerical analysis of the viscous flows which are governed by the Navier-Stokes equations. They are the primitive variable approach, the vorticity-stream function approach and the velocity-vorticity approach. The primitive variable approach and the vorticity-stream function approach have been investigated by many researchers such as Anderson et al (1984)[8]. The velocity-vorticity formulation also has been implemented in numerical calculations by some researchers like Giannatasio and Napolitano (1996)[9]. The most advantage of the velocity-vorticity formulation is to separate the kinematic and kinetic aspects of the pressure from the incompressible fluid flow computation.

The Stokes flow problem is a subproblem of the Navier-Stokes flow problems. The non-linear convective terms are considered very small and neglected. The governing equations of the Stokes flow are changed to a linear equation system of the Laplace equation for the vorticity and the Poisson equation for the velocity. According to the Biot-Savart law, the governing equations of velocities are transformed to the Laplace equation and the velocity field can be determined by the vorticity field from the principle of the linear superposition. Liang (2000)[10] has successfully used the conventional BEM and the Biot-Savart law to simulate the Stokes flow in a 2D circular cavity

and a square cavity.

## Mathematical Models

### 1.Derivation of the Velocity-Vorticity Formulation

The non-dimensional Navier-Stokes equations which are the governing equations for incompressible Newtonian fluid can be written as

$$\frac{\partial \vec{u}}{\partial t} + (\vec{u} \cdot \nabla)\vec{u} = -\nabla p + \frac{1}{Re}\nabla^2 \vec{u} \quad (1)$$

where $\vec{u}$ is the velocity vector, $p$ is the pressure, $Re$ is the Reynolds number, and $t$ is the time.
Another governing equation of the flow field is the continuity equation.

$$\nabla \cdot \vec{u} = 0 \quad (2)$$

The vorticity vector can be expressed as

$$\vec{\omega} = \nabla \times \vec{u} \quad (3)$$

By taking the curl of both sides of eq(1) and using eq(2) and eq(3) , we can get the vorticity transport equation as

$$\frac{\partial \vec{\omega}}{\partial t} + (\vec{u} \cdot \nabla)\vec{\omega} = (\vec{\omega} \cdot \nabla)\vec{u} + \frac{1}{Re}\nabla^2 \vec{\omega} \quad (4)$$

By taking the curl of eq(3) and using eq(2) and some vector identity formula, we are able to obtain a vector form of the Poisson equation for the velocity

$$\nabla^2 \vec{u} = -\nabla \vec{\omega} \quad (5)$$

For two-dimensional problems, the governing equations, eq(4) and eq(5), are simplified to the followings:

$$\frac{\partial \omega}{\partial t} + u\frac{\partial \omega}{\partial x} + v\frac{\partial \omega}{\partial y} = \frac{1}{Re}\nabla^2 \omega \, (6)$$

$$\nabla^2 u = -\frac{\partial \omega}{\partial y} \, (7)$$

$$\nabla^2 v = \frac{\partial \omega}{\partial x} \quad (8)$$

When the Reynolds number approach to zero, the flow field is the so-called Stokes flow. Then eq(6) will become the form of the Laplace equation.

$$\nabla^2 \omega = 0 \quad (9)$$

In 1820 , the French scientists Jean-Baptiste Biot and Fe'lix Savart derived the Biot-Savart law based on experiments . By the Biot-Savart law and the principle of linear superposition , the Poisson equation , eq(7) and eq(8) , can be simplified to the following equations. That is, the homogeneous and the particular solutions.

$$u = u_h + u_p \quad (10)$$

$$v = v_h + v_p \quad (11)$$

$$\nabla^2 u_h = 0 \quad (12)$$

$$\nabla^2 v_h = 0 \quad (13)$$

$$u_p = \iint_a \frac{-\omega(x', y')}{2\pi} \left( \frac{y - y'}{(x - x')^2 + (y - y')^2} \right) dx'dy' \quad (14)$$

$$v_p = \iint_a \frac{\omega(x', y')}{2\pi} \left( \frac{x - x'}{(x - x')^2 + (y - y')^2} \right) dx'dy' \quad (15)$$

where $u_p$ and $v_p$ are the particular solutions of eq(7) and eq(8), respectively. $u_h$ and $v_h$ are the homogeneous solutions of eq(7) and eq(8), respectively, and $\omega$ is the vorticity located at$(x', y')$. It is noted that when we solve the homogeneous solution $u_h$, the original boundary condition of $u$ has to be subtracted from the particular solution $u_p$ on the boundary.

Eq(14) and eq(15) can be discretized numerically at any $i$ point of $(x, y)$ in the domain and on the boundary as

$$(u_p)_i = \sum_{\substack{j=1 \\ i \neq j}}^{N} \frac{-\omega_j}{2\pi} \left( \frac{y_i - y_j}{(x_i - x_j)^2 + (y_i - y_j)^2} \right) a_j \quad (16)$$

$$(v_p)_i = \sum_{\substack{j=1 \\ i \neq j}}^{N} \frac{\omega_j}{2\pi} \left( \frac{x_i - x_j}{(x_i - x_j)^2 + (y_i - y_j)^2} \right) a_j \quad (17)$$

where $\omega_j$ is the corresponding vorticity associated with a small area $a_j$.

## 2.Formulation of Non-Singular Boundary Integral Equation for Laplace Equation

The vorticity transport equation as well as homogeneous solution of the velocity equation in the Stokes flow are the Laplace equations. If we want to find the solutions of this kind of problems by boundary integral equation method , we need to derive the non-singular boundary integral equation first. In conventional boundary element method, we get the boundary integral equation for the Laplace equation as follows.

$$\varepsilon(\vec{x})\,\phi(\vec{x}) = \oint_{\Gamma} \left[ G(\vec{x}, \vec{x}') \frac{\partial \phi(\vec{x}')}{\partial n_{\vec{x}'}} - \phi(\vec{x}') \frac{\partial G(\vec{x}, \vec{x}')}{\partial n_{\vec{x}'}} \right] d\Gamma(\vec{x}') \quad (18)$$

The coefficient $\varepsilon(\vec{x})$ is equal to $1/2$ when $\vec{x}$ is on the smooth boundary. The coefficient $\varepsilon(\vec{x})$ is equal to 1 when $\vec{x}$ is inside the domain, and 0 when $\vec{x}$ is outside the domain. The Green's function $G(\vec{x}, \vec{x}')$ indicates the potential at the field point $\vec{x}$ induced by the source(base) point $\vec{x}'$. In two dimensional domain, the fundamental solution of the Laplace equation $G(\vec{x}, \vec{x}')$ can be written as

$$G(\vec{x}, \vec{x}') = \frac{-1}{2\pi} \ln(r) \quad (19)$$

in which $r$ of the above equation is the distance between field point $\vec{x}$ and base point $\vec{x}'$. The eq(18) then can be written as followings after an addition and subtraction of singularity process[11].

$$\varepsilon(\vec{x})\phi(\vec{x}) + \oint_{\Gamma} [\phi(\vec{x}') - \phi(\vec{x})] \frac{\partial G(\vec{x},\vec{x}')}{\partial n_{\vec{x}'}} d\Gamma(\vec{x}') + \oint_{\Gamma} \phi(\vec{x}) \frac{\partial G(\vec{x},\vec{x}')}{\partial n_{\vec{x}'}} d\Gamma(\vec{x}')$$

$$= \oint_{\Gamma} \left[ \frac{\partial \phi(\vec{x}')}{\partial n_{\vec{x}'}} - \left( \frac{\partial \phi(\vec{x})}{\partial n_{\vec{x}}} \right) \left( \frac{\sigma(\vec{x}')}{\sigma(\vec{x})} \right) \right] G(\vec{x},\vec{x}')\, d\Gamma(\vec{x}')$$

$$+ \left( \frac{\partial \phi(\vec{x})}{\partial n_{\vec{x}}} \right) \left( \frac{1}{\sigma(\vec{x})} \oint_{\Gamma} \sigma(\vec{x}')\, G(\vec{x},\vec{x}')\, d\Gamma(\vec{x}') \right) \quad (20)$$

where $\sigma(\vec{x})$ and $\sigma(\vec{x}')$ are the source functions at $\vec{x}$ and $\vec{x}'$, respectively. The source function satisfies a homogeneous boundary integral equation and the derivation can be referenced in Jason and Symm [12]. The source function will be found by an iterative method.

$$\sigma^{m+1}(\vec{x}) = \sigma^{m}(\vec{x}) - \int_{\Gamma} \left[ \sigma^{m}(\vec{x}') \left( \frac{\partial G(\vec{x},\vec{x}')}{\partial n_{\vec{x}}} \right) - \sigma^{m}(\vec{x}) \left( \frac{\partial G(\vec{x},\vec{x}')}{\partial n_{\vec{x}'}} \right) \right] d\Gamma(\vec{x}') \quad (21)$$

where $m$ is the iterative number.
The Gauss flux theorem in potential theory will reduce the normal derivative type singularities in integral equations. The Gauss flux theorem can be written as

$$-\varepsilon(\vec{x}) = \oint_{\Gamma} \frac{\partial G(\vec{x},\vec{x}')}{\partial n_{\vec{x}'}} d\Gamma(\vec{x}') \quad (22)$$

The concept of equipotential function $\Phi_e$ is required to be introduced to solve the singular kernel of $\ln(r)$. The $\Phi_e$ is defined by

$$\Phi_e = \oint_{\Gamma} \sigma(\vec{x}')\, G(\vec{x},\vec{x}')\, d\Gamma(\vec{x}') \quad (23)$$

where $\Phi_e$ is a constant in the interior of an equipotential surface.
By substituting eq(22) and eq(23) into eq(20), then eq(20) will become

$$\oint_{\Gamma} \left[\phi\left(\vec{x}'\right) - \phi\left(\vec{x}\right)\right] \frac{\partial G\left(\vec{x}, \vec{x}'\right)}{\partial n_{\vec{x}'}} d\Gamma\left(\vec{x}'\right)$$

$$= \oint_{\Gamma} \left[\frac{\partial \phi\left(\vec{x}'\right)}{\partial n_{\vec{x}'}} - \left(\frac{\partial \phi\left(\vec{x}\right)}{\partial n_{\vec{x}}}\right) \frac{\sigma\left(\vec{x}'\right)}{\sigma\left(\vec{x}\right)}\right] G\left(\vec{x}, \vec{x}'\right) d\Gamma\left(\vec{x}'\right) + \left(\frac{\partial \phi\left(\vec{x}\right)}{\partial n_{\vec{x}}}\right) \frac{\Phi_e}{\sigma\left(\vec{x}\right)} \quad (24)$$

The eq(24) is the Non-Singular Boundary Integral Equation for the Laplace equation. The numerical singularities is eliminated when $r$ approaches to zero.

## Numerical Methods

For computational purpose, the boundary should be divided into finite nodes. The integral equation, eq(24), will be discretized as follows.

$$\sum_{j=1}^{N} \{A_{ij}\phi_j\} - \sum_{j=1}^{N} \{A_{ij}\}\phi_i$$

$$= \sum_{j=1}^{N} \left\{ B_{ij} \left(\frac{\partial \phi}{\partial n}\right)_j \right\} - \sum_{j=1}^{N} \left\{ \frac{\sigma_j}{\sigma_i} B_{ij} \right\} \left(\frac{\partial \phi}{\partial n}\right)_i + D_i \left(\frac{\partial \phi}{\partial n}\right)_i$$

$$i = 1 \sim N \quad (25)$$

Through eq(25), we can establish the following algebraic system.

$$[A]_{N\times N} \{\phi\}_{N\times 1} = [B]_{N\times N} \left\{\frac{\partial \phi}{\partial n}\right\}_{N\times 1} \quad (26)$$

The matrices [A] and [B] are the coefficient matrices, their components of [A] and [B] are obtained from eq(25).

$$A_{ij} = \int \frac{\partial G\left(\vec{x}_i, \vec{x}'\right)}{\partial n_j} N_j\left(\vec{x}'\right) d\Gamma\left(\vec{x}'\right) \quad (27)$$

$$B_{ij} = \int G\left(\vec{x}_i, \vec{x}'\right) N_j\left(\vec{x}'\right) d\Gamma\left(\vec{x}'\right) \quad (28)$$

$$D_i = \frac{\Phi_e}{\sigma_i} \quad (29)$$

where

$$\frac{\partial G\left(\vec{x}, \vec{x}'\right)}{\partial n_j} = \frac{\partial G}{\partial r}\frac{\partial r}{\partial n_j} = \frac{\partial G}{\partial r}\left(\frac{\partial r}{\partial x_j}\frac{\partial x_j}{\partial n_j} + \frac{\partial r}{\partial y_j}\frac{\partial y_j}{\partial n_j}\right) = \frac{1}{2\pi}\frac{\vec{r} \bullet \vec{n}}{r^2}$$

$$r = \sqrt{\left(x - x'_j\right)^2 + \left(y - y'_j\right)^2}$$

The solutions of velocity-vorticity formulation can be obtained by an iterative technique and it is stated briefly as follows: 1. Establish geometry and compute the source functions, equipotential functions. 2.Solve the particular solutions and homogeneous solutions of velocity $u, v$ separately by the Biot-Savart law and the nonsingular boundary integral equation. 3.From step 2 obtain the boundary condition of vorticity $\omega$ and solve the vorticity by nonsingular boundary integral equation. 4.Check the convergences of $u, v$ and $\omega$ until the convergences are reached. The details of the numerical procedures can be referred to Fan[11].

## Numerical Results

The first test problem is the 2-D circular cavity. The velocity $v_\theta = 1$ and $v_r = 0$ on the upper half side and $v_\theta = v_r = 0$ on the others are imposed. The radius $R$ is chosen to be equal to 10. Figure 1 illustrates the geometry of the circular cavity.

The velocity vector for Stokes flow in a circular cavity is shown in Figure 2. Figure 3, 4 and 5 are the distributions of the contours of vorticity ($\omega$), velocity ($u$), and velocity ($v$), respectively. The numerical solutions are symmetric with respective to the y-axis and almost the same with those of Liang(2000)[10]. Liang used the conventional boundary element method to solve the Laplace type equation. The no-slip boundary condition by the viscosity induces the sharp velocity gradient near the boundaries and also the corner singularities of the vorticity.

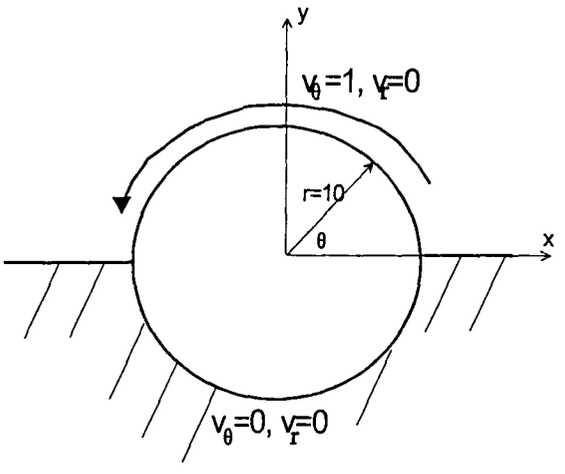


Figure 1: Schematic diagram of a circular cavity

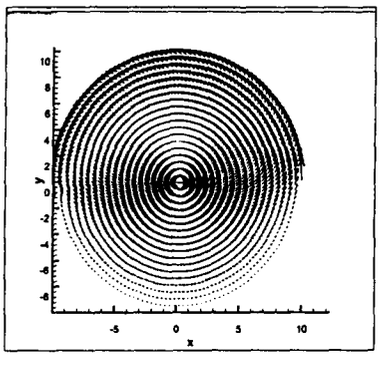


Figure 2: Velocity vectors for Stokes flow in a circular cavity

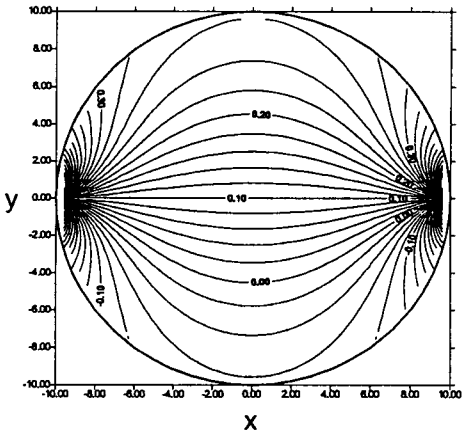


Figure 3: Vorticity $\omega$ contour for a circular cavity

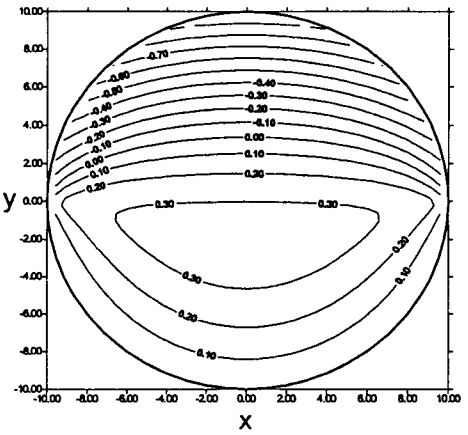


Figure 4: Velocity $u$ contour for a circular cavity

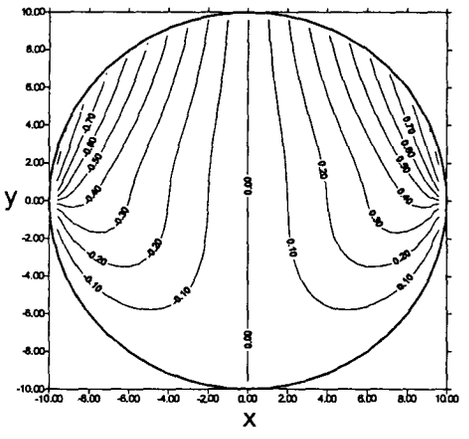


Figure 5: Velocity $v$ contour for a circular cavity

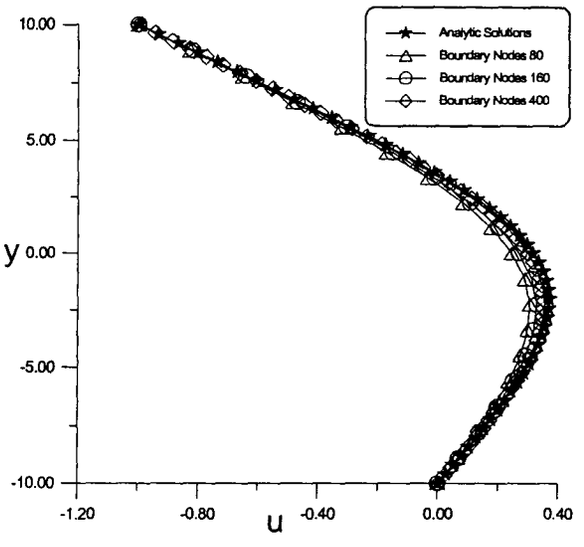


Figure 6: Comparison of $u$ velocity profiles along $x = 0$ at different meshes for a circular cavity

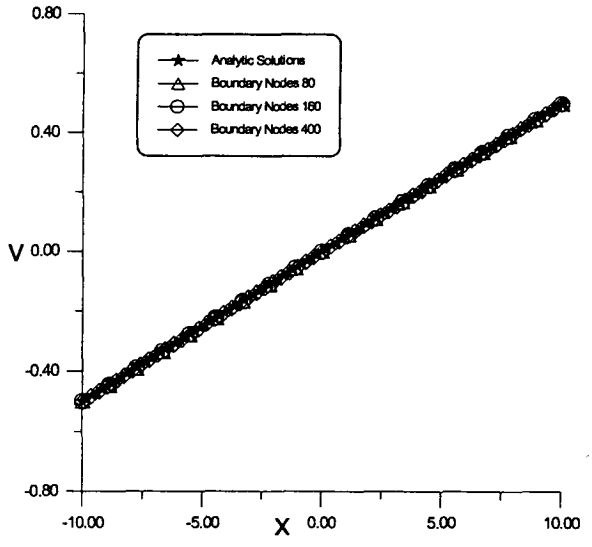


Figure 7: Comparison of $v$ velocity profiles along $y = 0$ at different meshes for a circular cavity

According to the principle of linear superposition, Figure 4 and 5 depict the combination of the particular solution and the homogeneous solution for velocity components $u$ and $v$.

Figure 6 is the profile of velocity component $(u)$ along $x = 0$ and Figure 7 is the profile of velocity component $(v)$ along $y = 0$ for different meshes. The numerical solutions with 80, 160 and 400 boundary nodes are compared with the exact solution which is derived by Hwu et al [13]. From this observation, it is concluded that the 400 boundary nodes are fine enough as far as numerical accuracy is concerned. Even the very coarse mesh of 80 will also render reasonable accuracy.

Figure 8 depicts the geometry of the square cavity. The velocity vector for Stokes flow in a square cavity is shown in Figure 9. The distributions of vorticity $(\omega)$ contours are illustrated in Figure 10. According to Figure

10, the distributions of vorticity are symmetric with respective to the $x = 0.5$ axis. The distributions of vorticity and velocity are the same with those obtained by Lo(2000)[14] which were computed by the finite element method(FEM). The singularities occurring on the upper two corners can be found conspicuously in Figure 10. This kind of corner singularity is due to the discontinuous boundary conditions of $u$ velocity at both corners.

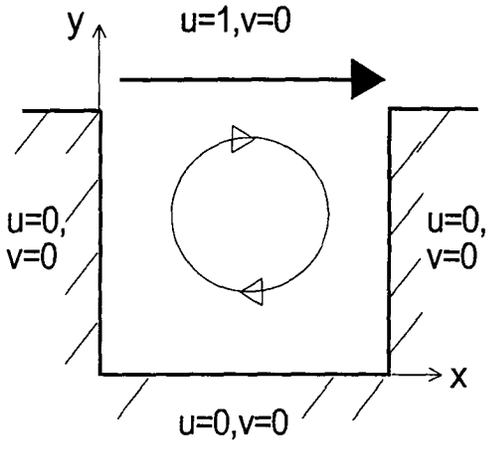


Figure 8: Schematic diagram of a square cavity

Figure 11 is the profile of velocity component $u$ along $x = 0.5$ and Figure 12 is the profile of velocity component $v$ along $y = 0.5$. The motion of fluid in the square cavity is clockwise. The results are compared with a series solution[15], two FEM solutions[14][16], a conventional BEM solution[17] and an iterative dual reciprocity boundary element method(DRBEM) solution[18]. The figure reveals that all the solutions are very close, and therefore it is convinced that the present nonsingular boundary element method is feasible to solve the 2D Stokes flows in a square cavity too. However, the numerical integration of singularity is observed to be much easier as comparing with the conventional boundary element method, which needs special algorithms to perform the singular integration.

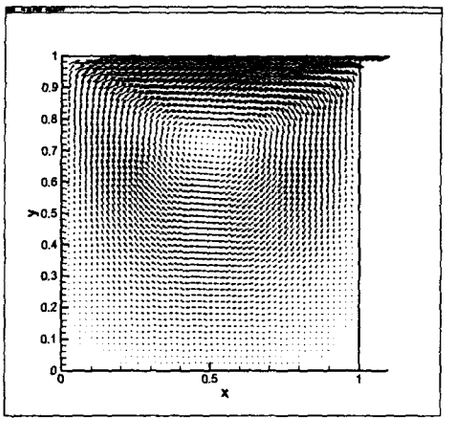


Figure 9: Velocity vectors for Stokes flow in a square cavity

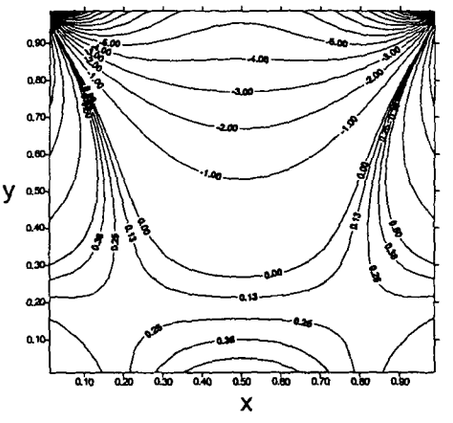


Figure 10: Vorticity $\omega$ contour for a square cavity

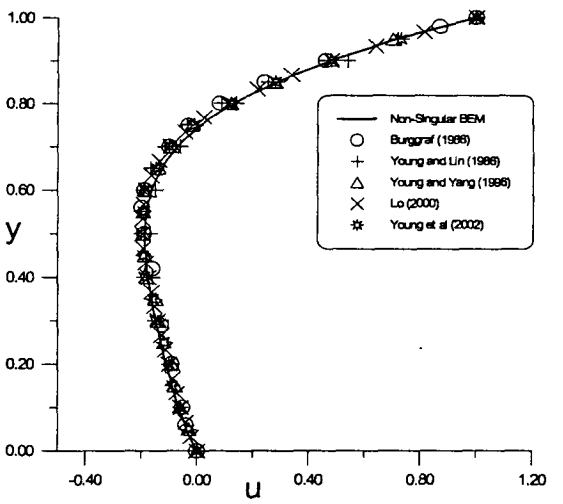


Figure 11: Comparison of $u$ velocity profiles along $x = 0.5$ for a square cavity

## Concluding Remarks

A truly non-singular boundary element method has been implemented for solving the 2D Stokes flow problems. The numerical solutions of the Stokes flow in a circular and a square cavity are almost identical in comparing with those by exact or other numerical methods. Comparisons with analytic solutions for a circular cavity and series solutions for a square cavity are also very agreeable, too. The simulations of circular cavity problem are performed for different mesh sizes and the results show good agreements as comparing with exact solutions. Both circular and square cavities show the efficiency of the non-singular boundary integral equation and the reliability of the velocity-vorticity formulation. It also demonstrates that combination of the Biot-Savart law to solve the particular solution can be used together with the principle of linear superposition of homogeneous solution of Laplace equation to obtain the velocity field. And the fact that the vorticity induces

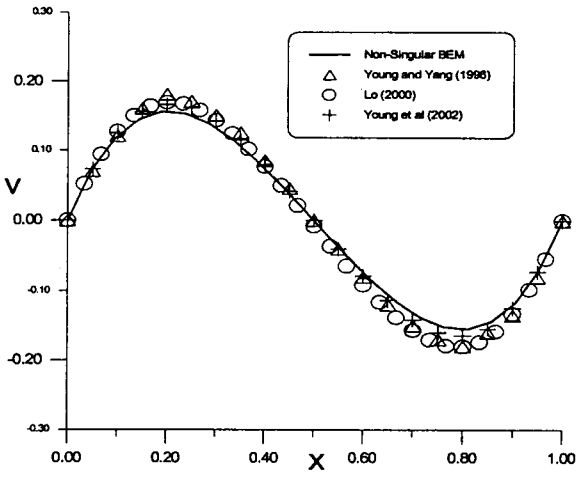


Figure 12: Comparison of $v$ velocity profiles along $y = 0.5$ for a square cavity

the velocity is obviously confirmed. The extension to 3D Stokes flow is a straightforward task and will be reported in another paper in the future.

## Acknowledgement

This work was supported by the grant from the National Science Council, Taiwan. It is greatly appreciated.

## References

[1] Y.L. Zang, Y.M. Cheng, and W. Zhang, A higher-order boundary element method for three-dimensional potential problems, Int. J. Numer. Methods Fluids, 21(1995), 331-321.
[2] Y. Cao,W.W. Schultz, and R.F. Beck, Three-dimensional desingularized boundary integral methods for potential problems, Int. J. Numer. Methods Fluids, 12(1991), 785-803.
[3] W.S. Hwang and Y.Y. Huang, Non-singular direct formulation of boundary integral equations for potential flow, Int. J. Numer. Methods Fluids, 26(1998), 627-635.

[4] L. Landweber and A. Macagno, Irrotational flow about ship forms, IHHR report, Iowa, 123(1969).
[5] M.A. Golberg, The method of fundamental solution for Poisson's equation, Engineering Analysis with Boundary Elements, 16(1995), 205-213.
[6] W.S. Hwang, A boundary integral method for acoustic radiation and scattering, J. Acoust. Soc. America, 101(1997), 3330-3335.
[7] Y.Y. Huang, The study on potential flow by nonsingular boundary methods, Ph.D. thesis, National Taiwan University, 1998.
[8] D.A. Anderson, J.C. Tannehill and R.H. Fletcher, Computational Fluid Mechanics and Heat Transfer, McGraw-Hill, New York, 1984 .
[9] P. Giannattasio and M. Napolitano, Optimal vorticity conditions for the node-centered finite-difference discretization of the second-order velocity-vorticity equations, J. Comput. Phy., 127(2000), 208-217.
[10] E.W. Liang, Velocity-vorticity formulation for the 2D Stokes flows by Biot-Savart law and boundary element method, MS Thesis, National Taiwan University, 2000.
[11] C.M. Fan, The non-singular boundary integral equations analysis to some engineering problems, MS Thesis, National Taiwan University, 2001.
[12] M.A. Jason and G.T. Symm , Integral Equation Methods in Potential Theory and Elastostatics , Academic , London ,1977.
[13] T. Y. Hwu , D. L. Young and Y. Y. Chen, Chaotic advections for Stokes flows in circular cavity, J. Engineering Mech., ASCE, 123(1997), 774-782.
[14] D.C. Lo, Two-dimensional velocity-vorticity formulation for incompressible flows with free surfaces by the finite element method, MS Thesis, National Taiwan University, 2000.
[15] O.R. Burggraf, Analytic and numerical studies of structure of steady separated flows, J. Fluid Mechanics, 24(1966) , 131-151.
[16] D.L. Young and Q.H. Lin, Application of finite element method to 2-D flows , In Proc. Third National Conf. on Hydraulic Engineering, Taipei, 223-242, 1986.
[17] D.L. Young and S.K. Yang, Simulation of two-dimensional steady Stokes flow by the velocity-vorticity boundary element method, In Proc. $20^{th}$Nat. Mechanics Conference,Taipei, 422-429, 1996.
[18] D.L. Young, C.C. Tsai, T.I. Eldho, and A.H.-D. Cheng, Solution of Stokes flow using an iterative DRBEM based on compactly-supported, positive-definite radial basis function, Computers and Mathematics with Applications, 43(2002), 607-619.

**Received: August 8, 2002**

International Mathematical Journal, Vol. 2, no. 12, 2002

## Contents

# Three-dimensional transient shallow water flow simulation using a boundary integral equation model

# Simulation des écoulements peu profonds non permanents à l'aide d'un modèle d'équations intégrales de frontières.

D.L. YOUNG, *Department of Civil Engineering & Hydrotech Research Institute, National Taiwan University, Taipei, Taiwan 10617, Te/Fax: +886-2-23626114, Email: dlyoung@hy.ntu.edu.tw*

Y.F. WANG, *Department of Civil Engineering & Hydrotech Research Institute, National Taiwan University, Taipei, Taiwan 10617*

T. I. ELDHO, *Department of Civil Engineering & Hydrotech Research Institute, National Taiwan University, Taipei, Taiwan 10617, Current affiliation: Dept. of Civil Engg., Indian Institute of Technology, Khragpur, India 721 302*

**ABSTRACT**

This paper describes the applications of a model based on the boundary integral equation method (BIEM) for the analysis of three-dimensional (3-D) transient flow in large-scale shallow water flow fields. Under the assumption of hydrostatic pressure distribution and non-stratification, Ekman type linear barotropic models are adopted in the development of the BIEM model. The BIEM model has been compared with analytical solutions and other numerical schemes and found to be feasible and accurate. The circulation structures in hypothetical shallow-water flow fields are simulated under long-duration, intermittent and periodic wind blowing with various kinds of bottom configurations. The computed results for large-scale hypothetical shallow water flow fields are a good realization of actual behaviors at least in terms of qualitative aspects.

**RÉSUMÉ**

Cet article décrit les applications d'un modèle basé sur la méthode des équations intégrales de frontières (BIEM), pour analyser les écoulements tridimensionnels non permanents sur de grandes étendues en eau peu profonde. Sous l'hypothèse d'une pression hydrostatique et en l'absence de stratification, le modèle BIEM est développé en adoptant les modèles barotropiques linéaires de type Eckman. Le modèle BIEM par comparaison avec des solutions analytiques et d'autres schémas numériques, se trouve être consistant et précis. Les circulations de fluide dans des champs de courant peu profonds hypothétiques, sont simulées sous l'effet de vents de longue durée, intermittents, et périodiques, avec différentes configurations des fonds. Les résultats calculés pour des champs de courant hypothétiques à grande échelle donnent une bonne idée des comportements réels au moins en termes qualitatifs.

## 1 Introduction

Important issues pertaining to water quantity and quality have led to an increasing interest in the large-scale motion of shallow water flow fields like lakes, estuaries, coastal oceans and reservoirs. The complex hydrodynamic process of mass momentum transport and circulation pattern in shallow water include: free surface velocity driven by wind shear stress, momentum mixing propagated downward to the bottom through the turbulent shear stress, Ekman spiral-type velocity distortion due to the Coriolis effect and inertial currents and Coriolis force. Only an appropriate 3-D numerical model can include various shallow water parameters and effectively simulate the hydrodynamics of a large shallow water flow field like a lake or an ocean.

In the literature, even though a large number of 2-D numerical schemes for the simulation of shallow water flow fields can be found, only a few 3-D numerical models are available for the analyses of various shallow water flow parameters. Most of these hydrodynamic models are based on either the finite difference method (FDM) or the finite element method (FEM). Almost all of the available hydrodynamics models are derived either from Ekman's theory or Navier-Stokes equations with convective effects (Liggett, 1994). Mathematical models based on Ekman's model (Ekman, 1905) are widely used to describe the phenomena of the hydrodynamic circulation of lakes and oceans (Welander 1957; Liggett 1969; Gallagher et al. 1973; Young and Liggett 1977 etc.).

Using the analytical solutions of Welander (1957), Liggett and Hadjitheodorou (1969) presented an algorithm of a depth-averaged stream function using the FDM for steady-state lake circulation. This method was further extended by Gallagher et al. (1973) for steady state conditions using the FEM and by Young and Liggett (1977) for transient flow problems using the FEM in Laplace transform space. Though the stream function approach can evaluate the 3-D flow field in horizontal two- dimensional computational domain, there are several disadvantages. For the flow fields with lateral flows or islands, the boundary conditions will be too difficult to implement. The stream function defined by depth averaged velocity, also introduces some simplifications of physical properties in the vertical direction, such as the rigid-lid assumption to neglect the effect of free surface flow conditions. Besides the aforementioned approaches, the finite Fourier transforms approach (Liggett, 1969) and the eigen-function approach (Davies 1983, Lardner and Song 1992) were also applied to linear barotropic hydrodynamic equations. The eigen-function approach requires the solution of a series of equation systems, and it is difficult to determine the optimal number of eigen-function expan-

Revision received January 19, 2001. Open for discussion till December 31, 2002.

the hydrostatic assumption and the implicit finite difference scheme, one can derive the partial differential equation with finite difference formation for the time domain as:

$$S\,u^{n+1} - v^{n+1} - E_k\left(\frac{\partial^2 u}{\partial z^2}\right)^{n+1} = -\left(\frac{\partial \eta}{\partial x}\right)^{n+1} + S\,u^n \tag{9}$$

$$S\,v^{n+1} + u^{n+1} - E_k\left(\frac{\partial^2 v}{\partial z^2}\right)^{n+1} = -\left(\frac{\partial \eta}{\partial y}\right)^{n+1} + S\,v^n \tag{10}$$

$$0 = -\left(\frac{\partial p}{\partial z}\right)^{n+1} - 1 \tag{11}$$

$$\left(\frac{\partial u}{\partial x}\right)^{n+1} + \left(\frac{\partial v}{\partial y}\right)^{n+1} + \left(\frac{\partial w}{\partial z}\right)^{n+1} = 0 \tag{12}$$

in which $S=1/\Delta t$, $\Delta t$ is the time interval, $n$ is the present time level, and $n+1$ is the advanced time level. The variables of the $n^{th}$ time step are known, while the $n+1$ step variables are unknown.

### 3 Boundary Integral Formulation

The governing equations (9)~(10) can be converted into boundary integral equations by using Green's theorem and integration-by-parts (Wang ,1994;Young et al., 2000b) as:

$$\begin{aligned} u^{n+1}(\bar{x}) = {} & \int_{\Omega_o} \hat{u}_x \left[ -\left(\frac{\partial \eta}{\partial x}\right)^{n+1} + Su^n \right] + \hat{v}_x \left[ -\left(\frac{\partial \eta}{\partial y}\right)^{n+1} + Sv^n \right] d\Omega_o - \\ & \int_{\Gamma_o} u^{n+1} \left[ \left( E_k \frac{\partial \hat{u}_x}{\partial z} \bar{k} \right) \cdot \bar{n} \right] + v^{n+1} \left[ \left( E_k \frac{\partial \hat{v}_x}{\partial z} \bar{k} \right) \cdot \bar{n} \right] d\Gamma_o + \\ & \int_{\Gamma_o} \hat{u}_x \left[ \left( E_k \frac{\partial u^{n+1}}{\partial z} \bar{k} \right) \cdot \bar{n} \right] + \hat{v}_x \left[ \left( E_k \frac{\partial v^{n+1}}{\partial z} \bar{k} \right) \cdot \bar{n} \right] d\Gamma_o \end{aligned} \tag{13}$$

$$\begin{aligned} v^{n+1}(\bar{x}) = {} & \int_{\Omega_o} \hat{u}_y \left[ -\left(\frac{\partial \eta}{\partial x}\right)^{n+1} + Su^n \right] + \hat{v}_y \left[ -\left(\frac{\partial \eta}{\partial y}\right)^{n+1} + Sv^n \right] d\Omega_o - \\ & \int_{\Gamma_o} u^{n+1} \left[ \left( E_k \frac{\partial \hat{u}_y}{\partial z} \bar{k} \right) \cdot \bar{n} \right] + v^{n+1} \left[ \left( E_k \frac{\partial \hat{v}_y}{\partial z} \bar{k} \right) \cdot \bar{n} \right] d\Gamma_o + \\ & \int_{\Gamma_o} \hat{u}_y \left[ \left( E_k \frac{\partial u^{n+1}}{\partial z} \bar{k} \right) \cdot \bar{n} \right] + \hat{v}_y \left[ \left( E_k \frac{\partial v^{n+1}}{\partial z} \bar{k} \right) \cdot \bar{n} \right] d\Gamma_o \end{aligned} \tag{14}$$

where $\Omega_0$ is the domain and $\Gamma_0$ is the boundary of the domain for the base point in which the point force or the point source acts, $\hat{u}_x$, $\hat{v}_x$, $\hat{u}_y$, $\hat{v}_y$ are the fundamental solutions or free space Green's functions.

The advanced time level flow variables on the left-hand side of the integral equations are influenced by the effects of free surface fluctuations and the inertial effect contained in the volume integral term. The boundary integral parts that include the velocity boundary condition effect and shear stress boundary condition effects.

To obtain the fundamental solutions of the equations (13) and (14), here a Fourier transform method is used (Bracewell 1986; Wang 1994; Young et al. 2000b). The coupled differential adjoint operators are transformed into a symbolic algebraic system in the Fourier space first, which are solved by the matrix inversion. Each element of the inverse matrix illustrates the resulting influence of velocity components and pressure due to a point force and point source in the Fourier space. Then the inverse Fourier- transforms are derived by the Cauchy's integral formula, the residue theorem, the convolution law and the mathematical tables for elementary parts of inverse matrix. The derived fundamental solutions due to the contribution of the $x$-directional point force are,

$$\hat{u}_x = \frac{\delta\ (x-x_o)\delta\ (y-y_o)}{2\sqrt{2E_k(S^2+1)}} e^{-C_1}[C_3\cos C_2 - C_4 \sin C_2] \tag{15}$$

$$\hat{v}_x = \frac{\delta\ (x-x_o)\delta\ (y-y_o)}{2\sqrt{2E_k(S^2+1)}} e^{-C_1}[C_4\cos C_2 + C_3 \sin C_2] \tag{16}$$

and the derived fundamental solutions due to the contributions of the y-directional point force are,

$$\hat{u}_y = -\frac{\delta\ (x-x_o)\delta\ (y-y_o)}{2\sqrt{2E_k(S^2+1)}} e^{-C_1}[C_4\cos C_2 + C_3 \sin C_2] \tag{17}$$

$$\hat{v}_y = \frac{\delta\ (x-x_o)\delta\ (y-y_o)}{2\sqrt{2E_k(S^2+1)}} e^{-C_1}[C_3\cos C_2 - C_4 \sin C_2] \tag{18}$$

The parameters $C_1$, $C_2$, $C_3$ and $C_4$ are defined as,

$$C_1 = C_3\frac{|z-z_o|}{\sqrt{2E_k}},\ C_2 = C_4\frac{|z-z_o|}{\sqrt{2E_k}},\ C_3 = \sqrt{S+\sqrt{1+S^2}},\ C_4 = \sqrt{-S+\sqrt{1+S^2}} \tag{19}$$

The variables ($x_0$, $y_0$, $z_0$) are coordinates of base point in which point force or point source acts. Variables ($x$,$y$,$z$) are the coordinates of any field point in which the effect of point action is concerned. $\delta$ is the Dirac-delta function, indicating point action and $S=1./\Delta t$.

As well known, the fundamental solution is the influence function of the physical system. Within the obtained solutions (15)~(18), the exponential functions exhibit the decaying behavior caused by the turbulent shear stress. The trigonometric functions indicate the spiral-like property caused by the Coriolis force. The Dirac-delta functions express the un-propagated momentum transport due to the fundamental assumption of Ekman's model for the neglect of horizontal momentum transport. For solutions of transient problems, the role of the time interval $\Delta t$ is of interest. For various time intervals, the $z$- directional distributions show that the influence region extends and the peak increases as the time interval is increased. The properties of fundamental solutions all satisfy the mathematical requirement of Green's function (Wang 1994, Young et al. 2000b).

The BIEM model is formulated by substituting fundamental solu-

tions into boundary integral equations. The velocity distribution in the vertical direction ($w$) is found from the continuity equation after solving the $u$ and $v$ components. The problem is solved by letting the base point approach to each boundary node in sequence, finding the unknown variables at each boundary node, and then determining the field point from the solved boundary variables.

## 4 Model Development and Verification

Inserting the fundamental solutions (15) ~ (18) into the integral equations of horizontal velocity (13) and (14), the expressions for the integral equation model for the velocity component $u$ and $v$ can be obtained (Young et al., 2000b). The expressions are in a point-by-point sense in the horizontal direction due to the existence of the Dirac-delta function in the fundamental solutions. The flow velocity at any concerned field point is represented by a function of free surface gradients, free surface velocity, free surface wind stresses, bottom velocity and bottom stresses, which have the same horizontal position with the field point. Again, moving the field point to the free surface and bottom boundary and imposing the boundary condition on the free surface and the bottom, the following linear system is derived for any field points:

$$[KU]_{4\times4}\begin{Bmatrix}(u,v)_{un}\\(\tau_x,\tau_y)_{un}\end{Bmatrix}_{4\times1}=[KN]_{4\times4}\begin{Bmatrix}(u,v)_{kn}\\(\tau_x,\tau_y)_{kn}\end{Bmatrix}_{4\times1}+\{SV\}_{4\times1}+\{SP\}_{4\times1} \tag{20}$$

where subscripts $un$ and $kn$ indicate, respectively the unknown and known flow variables given by the boundary conditions. $KU$ is the coefficient matrix obtained from the derived velocity equations for $u$ and $v$ associated with unknown variables, and $KN$ is the coefficient matrix with known values. $SV$ is the vector resulting from the volume integral of the initial effect known for this time step. $SP$ is the vector resulting from the volume integral of the pressure gradient. Since the pressure gradient is a function of free surface elevation and the free surface is unknown for this time step, $SP$ is an unknown vector. An implicit treatment with Picard's iteration method of evaluating the free surface fluctuation is considered in the present model. The implicit approach needs iterations but a large time interval is allowed. The vertical velocity component is evaluated by integrating the continuity equation directly.

The free surface kinematic boundary condition and continuity equation are combined for free surface evaluation and derived as:

$$\frac{\partial\eta}{\partial t}=-\frac{1}{F_r^2}\left[\frac{\partial}{\partial x}\int_{-h}^{\eta}u\ dz+\frac{\partial}{\partial y}\int_{-h}^{\eta}v\ dz\right] \tag{21}$$

Using a finite-difference scheme, the free surface position for the advanced $(n+1)$ step can be calculated from,

$$\eta^{n+1}=\eta^{n}-(\Delta t)\frac{1}{F_r^2}\left[\frac{\partial}{\partial x}\int_{-h}^{\eta}u^{n+1}\ dz+\frac{\partial}{\partial y}\int_{-h}^{\eta}v^{n+1}\ dz\right] \tag{22}$$

The boundary condition on the shoreline is the usual no-flux condition.

Since the unknown free surface position is contained in the integrals of equation (22), and is necessary for the evaluation of the velocity for the advanced step, a Picard's iteration method in the implicit scheme is used here, with the following steps.

Step 1: Evaluate the flow field, $u_i^{n+1}$, $v_i^{n+1}$, for the $i^{th}$ iteration using the velocity and free surface elevation of the previous $(i\text{-}1)^{th}$ iteration.

Step 2: Compute the free surface elevation for this iteration.

$$\eta^{n+1}=\eta^{n}+(\Delta t/2)\left[F(u_{i-1}^{n+1},v_{i-1}^{n+1})+F(u_i^{n+1},v_i^{n+1})\right] \tag{23}$$

$$F(u,v)=-\frac{1}{F_r^2}\left[\frac{\partial}{\partial x}\int_{-h}^{\eta}u\ dz+\frac{\partial}{\partial y}\int_{-h}^{\eta}v\ dz\right] \tag{24}$$

Step 3: Compute the maximum Euclidean norm of the velocity field.

$$E=\max\ (|u_i^{n+1}-u_{i-1}^{n+1}|^2+|v_i^{n+1}-v_{i-1}^{n+1}|^2)^{1/2} \tag{25}$$

Step 4: If $E<\varepsilon$, then stops iteration, else repeats the steps 1 to 3 for the next cycle of the iteration. The symbol $\varepsilon$ is used for the convergence criterion for iterative procedure.

The depth- averaged velocities and stream function can be obtained from,

$$U(h+\eta)=\frac{\partial\Psi}{\partial y}=\int_{-h}^{\eta}u\ dz \tag{26}$$

$$V(h+\eta)=-\frac{\partial\Psi}{\partial x}=\int_{-h}^{\eta}v\ dz \tag{27}$$

where $U$ is the $x$- directional depth-averaged velocity, $V$ is the $y$-directional depth-averaged velocity and $\psi$ is the stream function. The transient shallow-water flow problem is an initial value problem. If the initial state of a flow field and the attendant boundary conditions of bottom, free surface and shoreline are given, then it is possible to simulate any instant of the flow field. By the above numerical scheme, simulation can be proceeded in the following steps,

[1] Input the initial conditions and boundary conditions.

[2] Compute the initial effect $SV$, boundary condition effect $KN$ and the pressure effect $SP$ on the right hand side of equation (20).

[3] Solve the linear system (20), to find the unknown velocity and shear stress on boundary node.

[4] Calculate field (or interior) velocities $u$, $v$ through the integral equations (13) and (14).

[5] Compute the vertical velocity component by the continuity equation.

[6] Compute the free surface elevation from equation (22) for this time step, use Picard's iteration if necessary.

[7] Evaluate the depth-averaged stream function and the total velocity for this time step.

[8] Repeat steps [2] to [7] for the next cycle of computation.

Figure 1 shows a schematic flow chart of the transient BIEM model developed.

The generally used boundary conditions in the present study are described in section 2. Depending upon the problem considered, the inflow and outflow boundary conditions also can be prescribed. Generally in shallow water bodies like lakes, estuaries and reservoirs, the inflow and outflow conditions are caused from river discharge, topographic currents, tidal flow and interaction among them. In the case of discharge or currents in the shallow water body considered, the inflow and outflow boundary conditions are prescribed in terms of discharge or velocities. In the case of tidal flow, the boundary condition can be prescribed in terms of surface elevation or wind shear stress. All these inflow and outflow boundary conditions can be easily included in the present BIEM model.

The present BIEM model has been verified with analytical and other numerical schemes like FDM and FEM (Wang 1994; Young and Wang 1995a; Young and Wang 1995b; Young et al. 2000b). To demonstrate the accuracy of the model, here a comparison with an analytical Ekman's spiral solution (Ekman 1905; Welander 1957) for an infinite extensive hypothetical ocean having a finite depth is briefly described. The shallow-water flow field to be simulated is driven by uniform, southern wind blowing from rest over the whole ocean. The simulation is carried out until a steady state has been achieved. Initially, the velocity field is assumed to be zero throughout the domain. The boundary conditions prescribed are: no slip bottom condition, $\Delta_x = 0$ and $\Delta_y = fL\tau/\upsilon g$. It is assumed that the characteristic depth of the ocean D=80m; characteristic length $L=1.25\times10^5$ m; g=980 cm/sec$^2$;$\upsilon$=200 cm$^2$/sec; $f$=0.0001 rad/sec; $\Delta t$=0.02 and wind shear stress $\tau$=1cm$^2$/sec$^2$. Analyses have been carried out for various dimensionless depths h=1.0, 0.8 and 0.4 and the solutions at steady state have been found. Table 1 shows a comparison of the free surface velocities of the BIEM solutions with the analytical solutions (Ekman 1905; Welander 1957). Good agreement is observed between the results. More detailed comparisons of the present BIEM model with other analytical solutions and numerical solutions of FDM and FEM are described in Young and Wang (1995a, 1995b) and Young et al. (2000b).

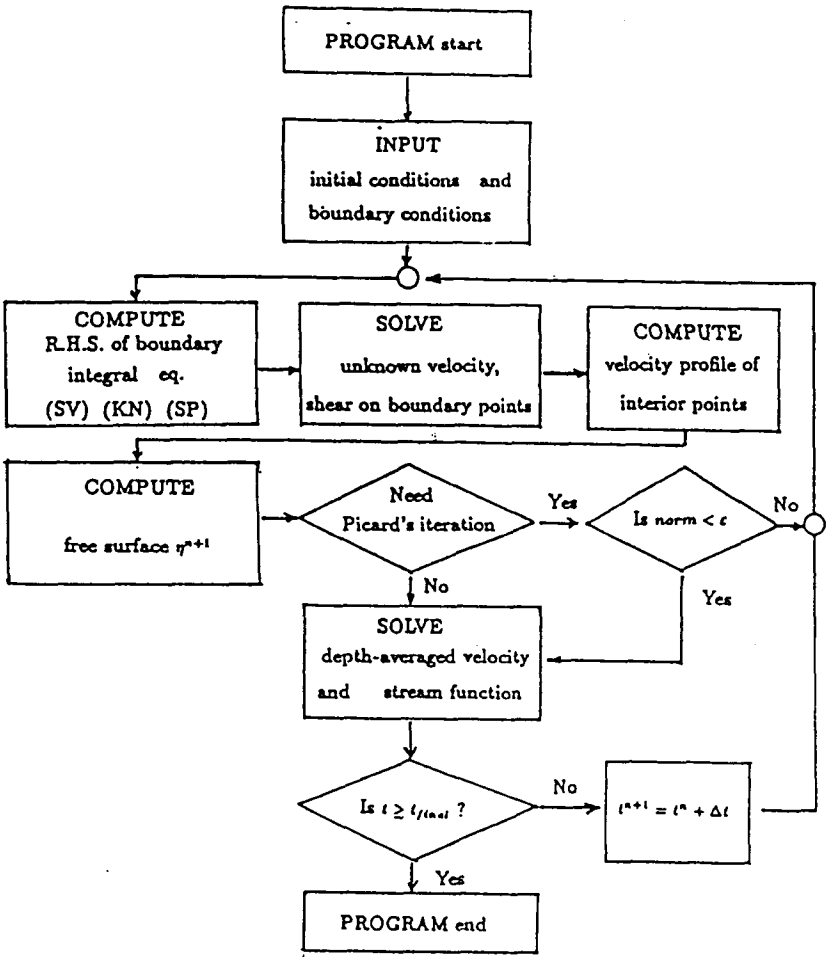


Fig. 1. A schematic flow chart of the transient BIEM model

Table 1. Comparison of BIEM solutions and analytical solutions of free surface velocities for Ekman's spiral problem with various depths

| Depth $h$ | Analytical $u$ | BIEM $u$ | Relative error(%) |
|---|---|---|---|
| 1.0 | 0.00079674 | 0.00079698 | 0.03 |
| 0.8 | 0.00079426 | 0.00079346 | 0.10 |
| 0.4 | 0.00086894 | 0.00086841 | 0.06 |
| Depth $h$ | Analytical $v$ | BIEM $v$ | Relative error(%) |
| 1.0 | 0.00079780 | 0.00079890 | 0.14 |
| 0.8 | 0.00079487 | 0.00079567 | 0.10 |
| 0.4 | 0.00086069 | 0.00086105 | 0.04 |

## 5 Results and Discussion

To demonstrate the applications of the BIEM model in the large-scale shallow water modeling, three examples are presented and various hydrodynamic parameters are illustrated. Initially the hydrodynamics in a rectangular basin with the bottom sloping at a corner is simulated and then the flow pattern in a shallow water flow field with bottom slope and lateral flow is computed, followed by simulation of a shallow water basin with transient blowing wind.

### *5.1 Simulation of Rectangular Shallow Water Basin with Sloping Bottom*

The BIEM model has been used in the hydrodynamics simulation of an idealized lake with a length four times its width and oriented in a north-south direction. The configuration and the parameters used are approximately the case of Lake Michigan (Harleman et al. 1962; Liggett and Hadjitheodorou 1969) but no attempt was made to reproduce the shape or bottom topography. In the present case, the shape of the lake is rectangular with a sloping bottom plane at the northwestern corner as shown in Figure 2. This gradually sloping bottom descends uniformly from the northwestern corner to the maximum depth of h=1.0 in the southwestern direction. For simulation purpose, a southwestern wind is introduced. The boundary conditions are: $u= v= w= 0$ as no-slip bottom condition and $\Delta_x=0$, $\Delta_y = fL\tau/\upsilon g$ and moving free surface assumption is used for the free surface. It is assumed that the characteristic depth of the lake $D$=8000 cm; characteristic length $L$=12500000 cm; $g$=980 cm/sec$^2$;$\upsilon$=200 cm$^2$/sec; $f$=0.0001 rad/sec and $\tau$=1 cm$^2$/sec$^2$. The basin geometry and its BIEM discretization with 11x41 mesh are shown in Figure 2.

Figure 3 shows the horizontal velocities for the basin at steady state due to the effect of a southwestern wind at the free surface z=0, z= –0.2 and z= –0.4 depth, respectively. The velocity flow field is compared with the FDM results of Liggett and Hadjitheodorou (1969) and generally fairly agreement is observed. A strong circulating current is observed within the sloping corner near the free surface. In Figure 3, blank areas for –0.2-depth and –0.4-depth show that the floor of the basin would be exposed at that depth. As obvious from the Figure 3, the smaller depths near the northwestern corner of the lake tend to align the

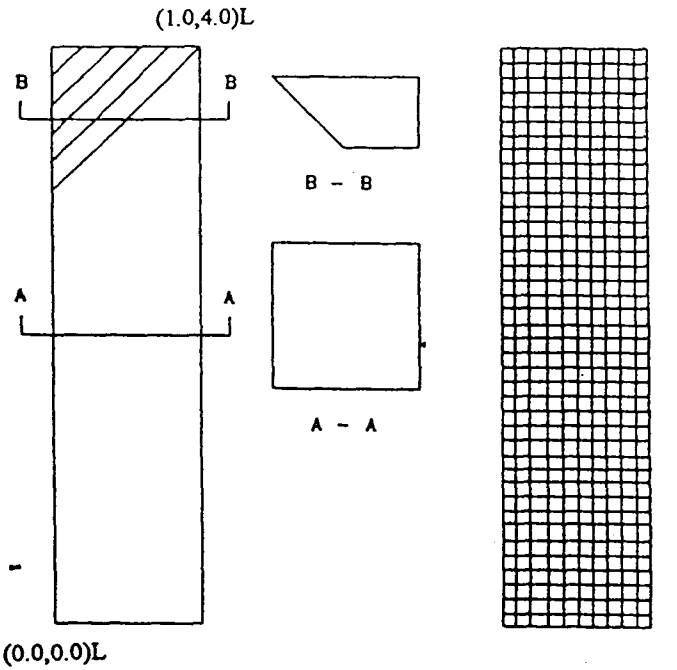


Fig. 2. Boundary configuration and mesh for a rectangular basin with sloping corner

velocity with the wind direction. As the depth of the lake becomes small, the friction term in the governing equation of motion tends to predominate and being balanced by the pressure gradient. The predominant force balance for small depth is between the viscous forces and wind stress, while the Coriolis force playing a minor role.

Dynamic responses of the free-surface velocity and bottom shear stresses are presented in Figures 4a and 4b, respectively for posi-

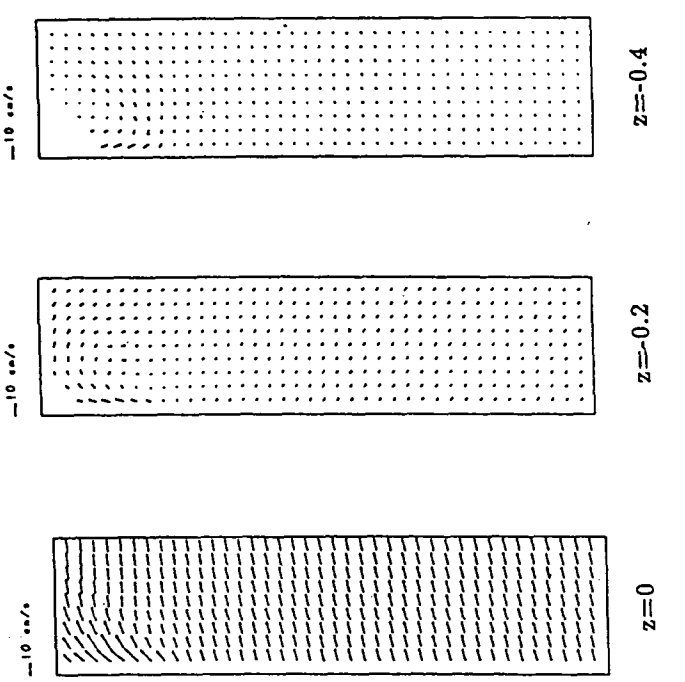


Fig. 3. Horizontal velocity field on various depths of rectangular basin with sloping corner

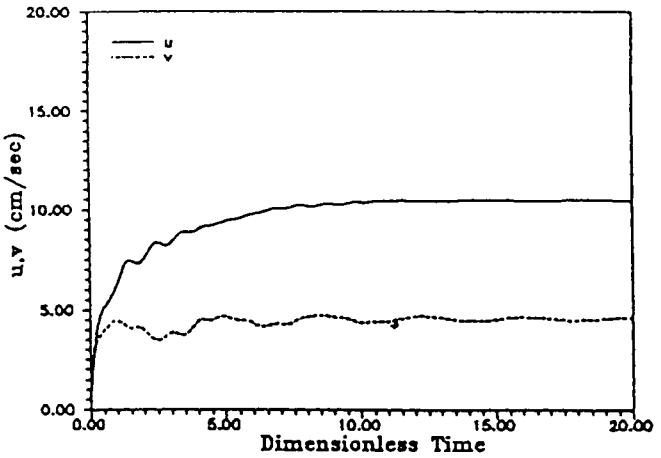


Fig. 4a. Response of velocity components at free surface for rectangular basin at (0.3,3.7)L

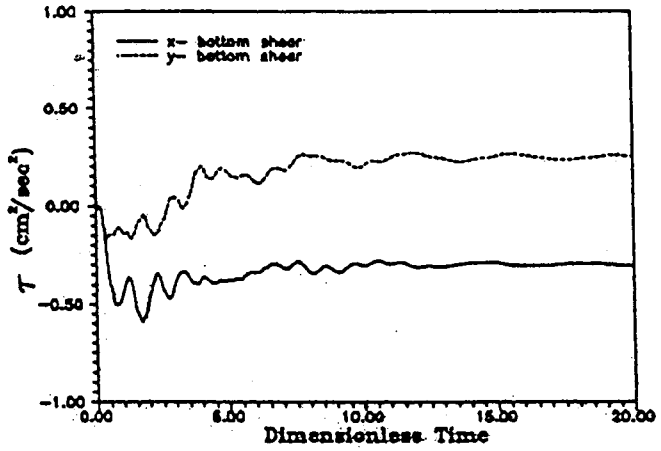


Fig. 4b. Response of bottom shear stresses for rectangular basin at (0.3,3.7)L

tion (0.3,3.7)L with $h$=0.6. In comparison to other domain oriented numerical models, as the BIEM model is boundary oriented, computational domain can be easily moved about to follow the free surface variations and the flow on the free surface is simulated satisfactorily here.

### 5.2 *Simulation of Sloping Shallow Water Flow Field with Lateral Flow*

To test the effectiveness of BIEM to investigate the effect of the lateral inflow and outflow, the circulation of a rectangular basin with sloping bottom is simulated. The dimensions of the lake and the flow field with its initial boundary value problem and physical parameters are the same as in Section 5.1 with a difference of both sides and two ends slope uniformly towards the center, as in Figure 5. The side slopes meet the end slopes at $45^0$ from the corners. The central part of lake is triangular in cross section. For simulation purpose, a south wind is introduced. As shown in Figure 5, a steady flux with a magnitude of 0.005 ($cm^2/sec$), flows into the basin at (0.0,0.5)L and flows out of the basin at (1.0,3.5)L, at the surface level.

The transient processes of the free-surface velocity and bottom

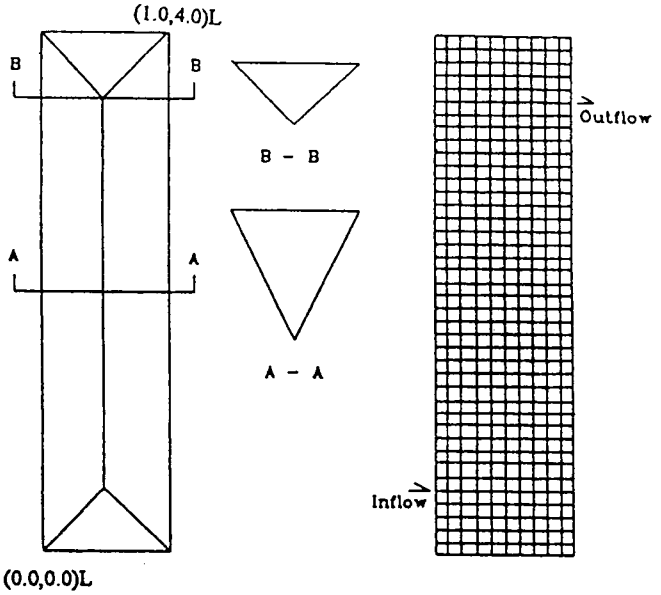


Fig. 5. Shoreline configuration and mesh for a sloping rectangular basin with lateral flows

shear stresses are sketched in Figures 6a and 6b for the point (0.3,2.0)L, respectively. Small fluctuations are observed in the initial stage, they are caused by the sudden-start of lateral inflow and outflow. The dynamic response of the free-surface fluctuation

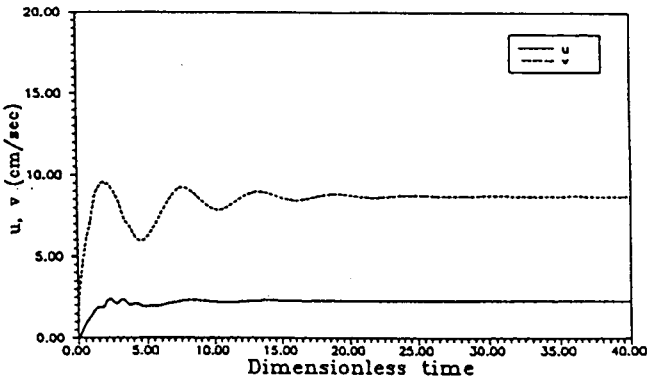


Fig. 6a. Response of free surface velocity components for lateral flow problem at (0.3,2)L

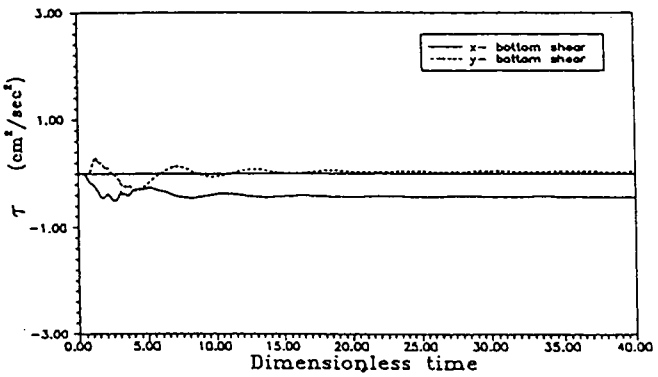


Fig. 6b. Response of bottom shear stresses for lateral flow problem at (0.3,2)L

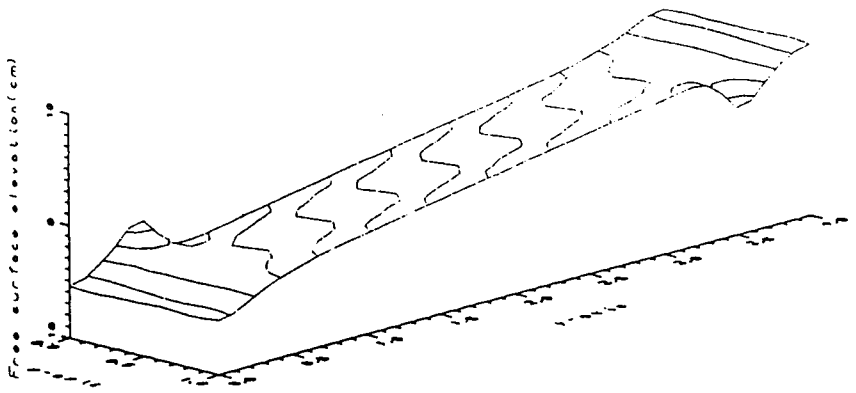

Fig. 7. Distributions of free surface elevation for lateral flow problem

also shows small variations, of the order of less than 1 cm at the initial stage (up to time t=15) and then the fluctuations stabilizes. The distribution of free-surface elevation is shown in Figure 7. The convex free surface due to the inflow and the concave free surface due to the outflow are clearly depicted in Figure 7.

Figure 8 shows the horizontal velocities for the basin at steady state due to the effect of the south wind at the free surface z=0, z=-0.2 and z=-0.4, respectively. The lateral inflow and outflow changes the flow field near the inlet and outlet, but the oscillation motion still exists. In Figure 8, blank areas for –0.2-depth and –0.4-depth show that the floor of the basin would be exposed at that depth. As obvious, the smaller depths near the coasts of the lake tend to align the velocity with the wind direction and influenced by the inflow and outflow. In this case study, even though a quantitative comparison with other model results has not been made, the computed results are a good realization of actual behaviors expected in terms of qualitative aspects. This case study also illustrates the effectiveness of BIEM to model a flow basin with changing bathymetry and inflow and outflow conditions.

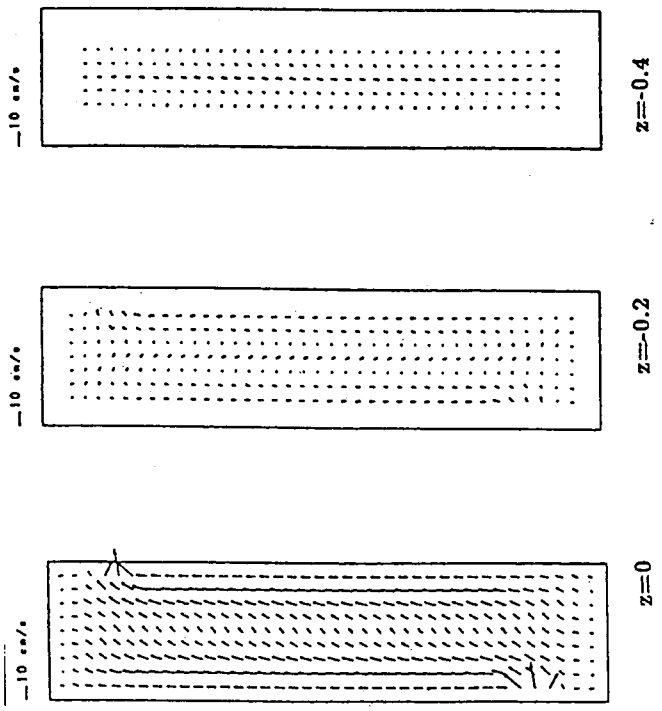


Fig. 8. Horizontal velocity field on various depths for lateral flow problem

### 5.3 *Simulations of Shallow Waters with Transient Blowing Wind*

To investigate the effect of various types of blowing wind on the shallow-water surface, the sudden-stop wind and the periodic wind are applied to simulate flows in the rectangular basin with sloping bottom presented in Section 5.2 without any inflow or outflow. The wind is blowing in the south direction. The flow motions for both the seiche and surge models are rather realistically simulated and illustrated in the followings.

To simulate the seiche motion, consider the blowing wind suddenly stops at $t$=9.5 (dimensionless). The transient processes of the free-surface velocity and bottom shear stresses are sketched in Figures 9a and 9b, respectively. The dynamic response of the free-surface fluctuation is illustrated in Figure 10. The maximum free surface fluctuation is of an order of 1cm. Solutions by the BIEM indicate that the initial oscillation has started in the initial stage, and the periodic motion of the seiche type has occurred after the wind has stopped. The sudden-stop wind plays a role of negative impulse for the shallow water. With a time lag, the computed bottom shear stress is suddenly raised at the measured point (0.3,2.0)L, after the wind stops, to balance the negative impulse. To simulate the shallow water flows during the wind blowing

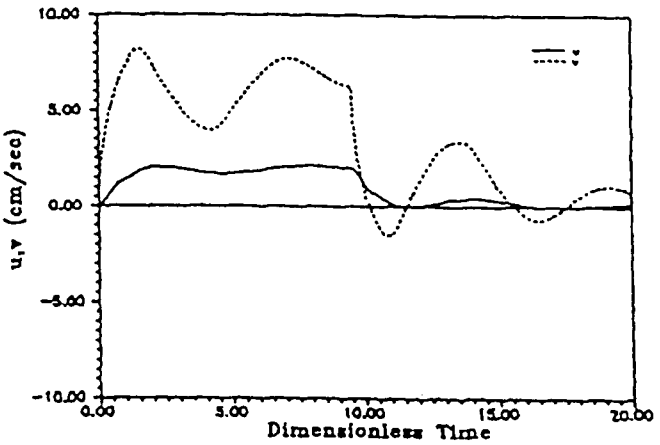


Fig. 9a. Responses of free surface velocity components at (0.3,2)L with intermittent wind

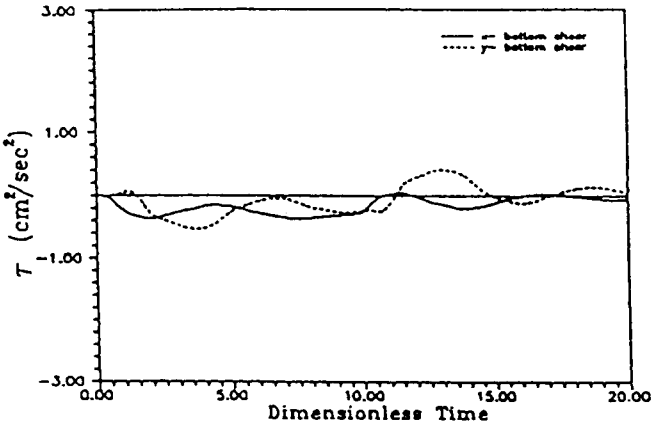


Fig. 9b. Responses of bottom shear stresses at (0.3,2)L with intermittent wind

phase, the application of the BIEM model to calculate the periodic wind of $\Delta_y$ is simulated. Dynamic responses of free surface velocity ($v$) and bottom shear stresses at the center of flow field due to the sinusoidal wind are shown in Figures 11a and 11b. The dynamic response of the free surface velocity component ($u$) is very similar to that of $v$ component, but the maximum variation is to very lesser extent of 2.5 cm/sec. Figure 12 presents the transient behavior of free surface fluctuation in the order of 2cm at center. After a long time simulation, a periodic surge type motion is obtained from the BIEM model without numerical dispersion. The numerical oscillatory period is 6.2857 (dimensionless time) which is almost the same as the wind period $2\pi$. Because the circulation is driven by the south wind, the oscillatory behavior of surface velocity has occurred much earlier for the $v$ component. The time lag of propagation downward also retards the periodic motion due to the bottom shear to take place later than the free surface motion. This case study shows the efficacy of BIEM to deal with various free surface conditions and to simulate the free surface position effectively.

## 6 Concluding Remarks

A three-dimensional boundary integral (BIEM) model is presented to simulate the hydrodynamics in homogeneous shallow water flow field. The BIEM model effectively reduces the computational dimension by one, thus solving a three- dimensional problem in two dimensions. In the three-dimensional BIEM model, the free surface variations are accurately simulated as the computational domain can be easily moved about to follow the free surface fluctuations. Some of the other advantages of the model include, ease of discretization and data preparation, flexibility to deal with infinite domain problems, ease of dealing with the irregular boundaries and direct solution of flux at the boundaries. Numerical simulations of the model for various examples have shown good agreement with some analytical and other numerical solutions. The presented case studies of shallow water flow problems with different bathymetry and boundary conditions show the feasibility of the model in the three-dimensional transient analysis of large-scale shallow water flow fields like lakes, estuaries and oceans.

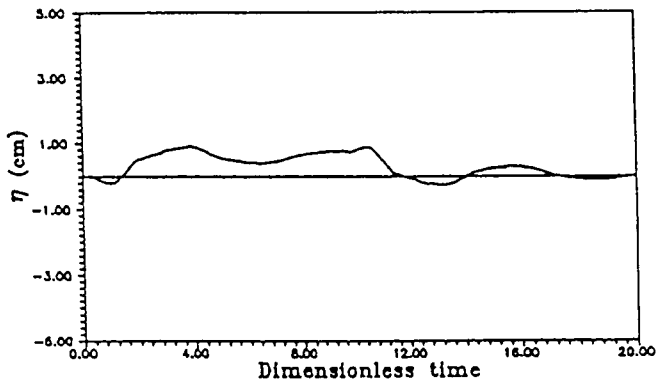


Fig. 10. Response of free surface fluctuation (0.3,2)L with intermittent wind

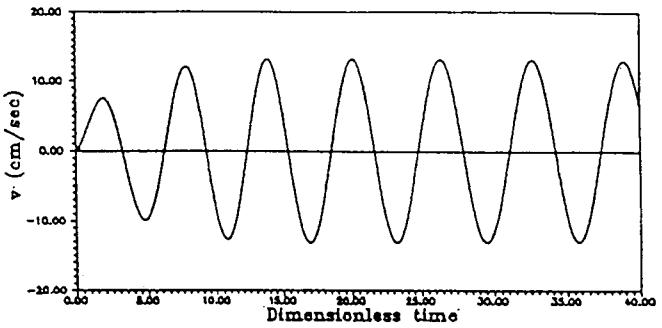


Fig. 11a. Response of $v$ velocity at free surface for the point (0.3,2)L with sinusoidal wind

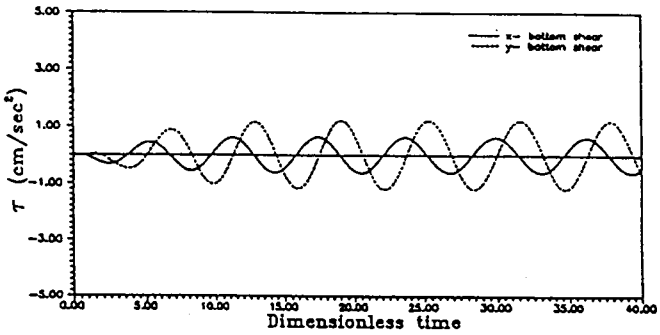


Fig. 11b. Responses of bottom shear stresses for the point (0.3,2)L with sinusoidal wind

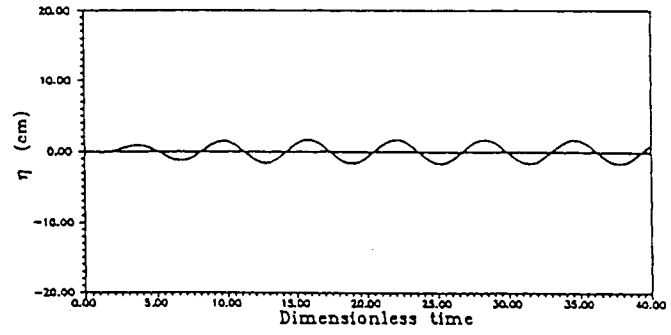


Fig. 12. Response of free surface fluctuation for the point (0.3,2)L with sinusoidal wind

## Acknowledgements

The work reported in this paper was supported by the National Science Council, Taiwan. It is greatly appreciated.

## References

BRACEWELL, R.N. (1986) *The Fourier Transform and Its Applications*, 2nd Edition, McGraw-Hill, New York.

DAVIES, A.M. (1983) "Formulation of a linear three-dimensional hydrodynamic sea model using a Galerkin-eigenfunction method." *Int. J. Numer. Meth. Fluids*, 3, 33-60.

EKMAN, V.W. (1905) "On the influence of the earth's rotation on ocean currents." *Arkiv Met. Astr. Fysik.*, 2, 1-53.

GALLAGHER, R.H., LIGGETT J.A. and CHAN S.T.K. (1973) "Finite element shallow lake circulation analysis." *J. Hydr. Div., ASCE, 99*, HY7, 1083-1096.

HARLEMAN, D.R.F., HOLLEY E.R. JR., HOOPES J.A. and RUMER R.R. JR. (1962) "The feasibility of a dynamic model of Lake Michigan". *Pub. No. 9*, Great Lakes Research Division, Institute of Science and Technology, University of Michigan.

IWASA,Y., and TADA, A.A. (1988) "Numerical simulation of wind-induced currents in the southern part of Lake Biwa." *Proc. 6th Con. APD-IAHR* , Kyoto, Japan, 201-208.

LARDNER, R.W., and SONG, Y.A. (1992) "A comparison of spatial grids for numerical modeling of flow near coastal seas." *Int. J. Numer. Meth. Fluids*, 14, 109-124.

LIGGETT, J.A. and HADJITHEODOROU C. (1969) "Circulation in shallow homogeneous lakes." *J. Hydr. Div., ASCE,* 95, HY2, 609-620.

LIGGETT, J.A. (1969) "Unsteady circulation in shallow homogeneous lakes." *J. Hydr. Div., ASCE.*, 95, HY4, 1273-1288.

LIGGETT, J.A. (1994) *Fluid Mechanics.*, McGraw-Hill Inc., New York.

WANG, Y.F. (1994) "Fundamental solutions and boundary integral equation methods for 3D shallow homogeneous bodies of water." *Ph.D. Thesis*, Department of Civil Engineering, National Taiwan University, Taipei, Taiwan.

WELANDER, P. (1957) "Wind action on shallow sea: Some generalizations of Ekman's theory." *Tellus*, 9, 45-52.

YOUNG, D.L., and LIGGETT, J.A. (1977) "Transient finite element shallow lake circulation." *J. Hydr. Div., ASCE*, 103, HY2, 109-121.

YOUNG, D.L., and WANG, Y.F. (1995a) "Boundary element computations of transient 3D shallow water circulation.", *Proc. 1st Int. Conf. On Water Resources Engineering*, San Antonio, Texas, USA, *Water Resources Engineering*, Vol. 2, 1303-1307, W.H. Espey, Jr. and P.G. Combs (ed.) ASCE, New York.

YOUNG, D.L., and WANG, Y.F. (1995b) "Fundamental solutions and boundary integral equation method of 3D shallow waters.", *Proc. 1st Asian CFD. Conf.* Hong Kong, 623-628, Hong Kong Univ. of Science and Technology, Hong Kong.

YOUNG, D.L., WANG, Y.F., and ELDHO, T.I. (2000a) "Boundary integral solutions for three- dimensional shallow water equations: Part I – Steady state analysis.", Communicated to *J. of Fluid Mech.*

YOUNG, D.L., WANG, Y.F., and ELDHO, T.I. (2000b) "Boundary integral solutions for three- dimensional shallow water equations: Part II – Transient analysis.", Communicated to *J. of Fluid Mech.*

## Notations

D = typical depth
$f$ = Coriolis parameter
g = acceleration due to gravity
h = local depth
L = typical length of the domain
n = unit outward normal
p = pressure
t = time
u, v, w = velocity vectors in x, y, z- directions
$\rho$ = fluid density
$\upsilon$ = eddy viscosity
$\theta$ = latitude of fluid element
$\eta$ = free surface
$\tau$ = wind shear stress

ELSEVIER

Comput. Methods Appl. Mech. Engrg. 190 (2001) 5975–5998

Computer methods in applied mechanics and engineering

www.elsevier.com/locate/cma

# Simulation of laminar vortex shedding flow past cylinders using a coupled BEM and FEM model

D.L. Young *, J.L. Huang, T.I. Eldho

*Department of Civil Engineering and Hydrotech Research Institute, National Taiwan University, Taipei 10617, Taiwan, ROC*

Received 17 May 2000; received in revised form 27 July 2000

**Abstract**

This paper describes a novel computational model developed to simulate laminar vortex-shedding flows past circular cylinders in 2D incompressible viscous flows in external flow fields. The model based on unsteady 2D Navier–Stokes equations in primitive variables is able to solve the infinite boundary value problems by extracting the boundary effects on a specified finite computational domain, using the projection method. The external flow field is simulated using the boundary element method (BEM) by solving a pressure Poisson equation that assumes the pressure as zero at the infinite boundary. The momentum equation of the flow motion is solved using the three-step finite element method (FEM). The present model is applied to simulate vortex-shedding flow past a single circular cylinder and flow past two cylinders in which one act as a control cylinder, for low Reynolds number flows. For both the cases, the time development of the flow towards periodic vortex shedding, are illustrated by streamline pictures. The simulation results are compared with experimental data and other numerical models and found to be very reasonable and satisfactory. © 2001 Elsevier Science B.V. All rights reserved.

*Keywords:* Navier–Stokes equations; Vortex-shedding; Boundary elements; Finite elements

## 1. Introduction

The studies of vortex shedding and suppression of the fluid forces behind bluff bodies exposed to uniform flow have been the focus of numerous investigations. These studies have been motivated by the desire to understand the fundamental physics of such flows as well as their practical importance in various industries. The occurrences of these flow phenomena are due to instabilities and depend on Reynolds number and geometry of the bluff body.

The phenomena of vortex shedding associated with the external flow problems are visible everywhere around our living environments such as: the variation of flow field arisen by the wind across the high-rise building, the drag force induced by the driving car accelerating in the wind and also the ocean current interaction with the offshore structures. The major difficulty in simulating these flows lies in setting the boundary conditions of the computational domain to simulate the external flow that has infinite domain. There are three typical boundary conditions namely inflow, outflow and two side virtual boundaries. The inflow boundary is the forced flow into the computational domain. As far as the outflow boundary is concerned, the flow phenomenon in the downstream affected by the wake shall be taken into account.

A large number of experimental studies have been reported on vortex shedding flows (for example, Bearman [1], Strykowsky and Sreenivasan [2]), but detailed investigations in unsteady flow field is rather

* Corresponding author. Tel.: +886-2-2362-6114; fax: 886-2-2362-6114.
*E-mail address:* dlyoung@hy.ntu.edu.tw (D.L. Young).

0045-7825/01/$ - see front matter © 2001 Elsevier Science B.V. All rights reserved.
PII: S0045-7825(01)00208-0

limited due to the difficulties involved in unsteady flow measurements. Vortex shedding flow past bluff bodies has also attracted the attention of numerous numerical investigators. With the advent of very powerful computers, numerical methods like finite volume (FVM), finite difference (FDM), finite elements (FEM) and boundary elements (BEM) have become widely used to investigate various fluid dynamics problems.

Braza et al. [3] used a second-order FVM and analyzed the vortex shedding past circular cylinders in laminar flow regime. Franke et al. [4] used FVM to solve 2D unsteady Navier–Stokes equations and analyzed laminar vortex shedding flows past circular and square cylinders. Lecointe and Piquet [5] calculated the flow around circular cylinders using the stream function-vorticity approach with a FDM. Jackson [6] used a Galerkin FEM approach to study vortex shedding in flow past variously shaped bodies by solving steady-state equations. For the last two decades, FEM and BEM have been widely in use for the solution of various fluid dynamics problems. The theoretical potentials of FEM [7,8] and BEM [9] have been adequately exposed for the solution of different forms of Navier–Stokes equations by various researchers.

Various forms of finite element formulations are available in literature for the solution of incompressible viscous flows. As the most commonly used Galerkin formulation is not able to cope with the convective effects efficiently, other forms like Petrov–Galerkin formulations [10] and Taylor–Galerkin [11] schemes were developed. Based on Taylor–Galerkin schemes, Jiang and Kawahara [12] recently developed a three-step finite element scheme for the unsteady incompressible viscous flows. Different forms of BEMs like direct BEM, indirect BEM [9] are in use for the solution of fluid dynamics problems.

In the present study, a novel computational procedure is developed to solve the vortex shedding flow past bluff bodies in external flow fields. The model is based on the projection method [13–15] of the Navier–Stokes equations in primitive variables. A three-step explicit FEM is used to solve the momentum equations of the flow domain. The pressure Poisson equation for the external field is treated by the BEM and then coupled with the three-step FEM scheme. The robustness and accuracy of the developed numerical scheme in the application of vortex shedding flow past single circular cylinder and two circular cylinders in which one acts as a control cylinder have been verified by comparing with experimental and other numerical results available in literature.

Use of BEM for the solution of the pressure Poisson equation helps to handle the infinite domain of the external flow problem from a finite discrete domain efficiently, as the fundamental solutions used in the BEM formulations automatically satisfy the conditions at infinity. The use of three-step FEM for the solution of the Navier–Stokes equations helps to deal with the convective effects efficiently.

After presenting the governing equations, the numerical formulation using coupled BEM and three-step FEM are briefly described. Then the solution procedure and numerical results for two case studies of vortex-shedding flow past a single cylinder and flow past two cylinders in which one acts as a control cylinder, for low Reynolds number flows are presented, followed by a few concluding remarks.

## 2. Governing equations

The motion of an incompressible viscous fluid flow in two dimensions, is governed by the following Navier–Stokes equations and continuity equation written as [16]:

$$\frac{\partial u}{\partial x}+\frac{\partial v}{\partial y}=0, \tag{1}$$

$$\frac{\partial u}{\partial t}+u\frac{\partial u}{\partial x}+v\frac{\partial u}{\partial y}=-\frac{1}{\rho}\frac{\partial p}{\partial x}+\upsilon\left(\frac{\partial^2 u}{\partial x^2}+\frac{\partial^2 u}{\partial y^2}\right)+f_x, \tag{2}$$

$$\frac{\partial v}{\partial t}+u\frac{\partial v}{\partial x}+v\frac{\partial v}{\partial y}=-\frac{1}{\rho}\frac{\partial p}{\partial y}+\upsilon\left(\frac{\partial^2 v}{\partial x^2}+\frac{\partial^2 v}{\partial y^2}\right)+f_y, \tag{3}$$

where $u$ is the velocity in $x$-direction and $v$ is the velocity in $y$-direction, $p$ is the pressure, $\upsilon$ is the kinematic viscosity, $t$ is the time, $\rho$ is the mass density, $f_i=\rho g l_i$ is the body forces in $x$-, $y$-directions, $g$ is the gravitational acceleration and $l_i$ direction cosines in $x$- and $y$-directions. Using the following dimensionless forms of the variables:

$$x^* = x/D, \quad y^* = y/D, \quad u^* = u/u_0, \quad v^* = v/u_0, \quad t^* = tu_0/D, \quad p^* = p/\rho u_0^2. \tag{4}$$

Eqs. (1)–(3) can be written as:

$$\frac{\partial u^*}{\partial x^*} + \frac{\partial v^*}{\partial y^*} = 0, \tag{5}$$

$$\frac{\partial u^*}{\partial t^*} + u^*\frac{\partial u^*}{\partial x^*} + v^*\frac{\partial u^*}{\partial y^*} = -\frac{\partial p^*}{\partial x^*} + \frac{1}{Re}\left(\frac{\partial^2 u^*}{\partial x^{*2}} + \frac{\partial^2 u^*}{\partial y^{*2}}\right) + \frac{l_x}{Fr^2}, \tag{6}$$

$$\frac{\partial v^*}{\partial t^*} + u^*\frac{\partial v^*}{\partial x^*} + v^*\frac{\partial v^*}{\partial y^*} = -\frac{\partial p^*}{\partial y^*} + \frac{1}{Re}\left(\frac{\partial^2 v^*}{\partial x^{*2}} + \frac{\partial^2 v^*}{\partial y^{*2}}\right) + \frac{l_y}{Fr^2}, \tag{7}$$

where $Re = u_0 D/v$ is the Reynolds number and $Fr = u_0/(gD)^{1/2}$ is the Froude number. Dropping the asterisk from the dimensionless variables in the following equations for brevity and putting the body force terms into the pressure field for neglecting the free surface effects, the non-dimensionalized governing equations for (1)–(3) can be written as:

$$\frac{\partial u}{\partial x} + \frac{\partial v}{\partial y} = 0, \tag{8}$$

$$\frac{\partial u}{\partial t} + u\frac{\partial u}{\partial x} + v\frac{\partial u}{\partial y} = -\frac{\partial p}{\partial x} + \frac{1}{Re}\left(\frac{\partial^2 u}{\partial x^2} + \frac{\partial^2 u}{\partial y^2}\right), \tag{9}$$

$$\frac{\partial v}{\partial t} + u\frac{\partial v}{\partial x} + v\frac{\partial v}{\partial y} = -\frac{\partial p}{\partial y} + \frac{1}{Re}\left(\frac{\partial^2 v}{\partial x^2} + \frac{\partial^2 v}{\partial y^2}\right). \tag{10}$$

For the solution of external flow problems, appropriate initial and boundary conditions should be prescribed. At the initial time, some known values of velocities can be prescribed as initial conditions.

Generally used boundary conditions are the prescribed velocities

$$u = u_0, \qquad v = v_0 \tag{11}$$

or velocity gradient and the non-slip boundary conditions on the solid wall surface.

As far as external flows are concerned, the outer boundaries are located at the infinity. In numerical computations, due to the limitations of computational facilities, it is assumed that the computational domain is limited to the finite region. Outside the finite region, we assume that flow is uniform (constant velocity), continuity equation is valid, convective acceleration can be neglected and the pressure gradient in the flow direction as zero. Hence in the present analysis we assume that

$$\nabla^2 p = 0 \tag{12}$$

is valid out of the finite computational domain. As a consequence, only the inflow boundary condition is needed as the boundary requirement of the computational domain. A sample computational domain for the type of problems that will be considered in the present study is shown in Fig. 1, with boundary conditions. The boundary condition of the fixed body in the flow is set as no-slip boundary.

The coefficient of drag and the coefficient of lift on the solid body and the Strouhal number $St$ are found from the following equations:

$$C_d = \frac{F_d}{1/2\rho u_0^2 D}, \quad C_l = \frac{F_l}{1/2\rho u_0^2 D}, \quad St = \frac{fD}{u_0}, \tag{13}$$

$$F_d = \oint_s p_s n_y \, ds - \oint_s \tau_s n_x \, ds, \tag{14}$$

$$F_l = \oint_s p_s n_x \, ds + \oint_s \tau_s n_y \, ds, \tag{15}$$

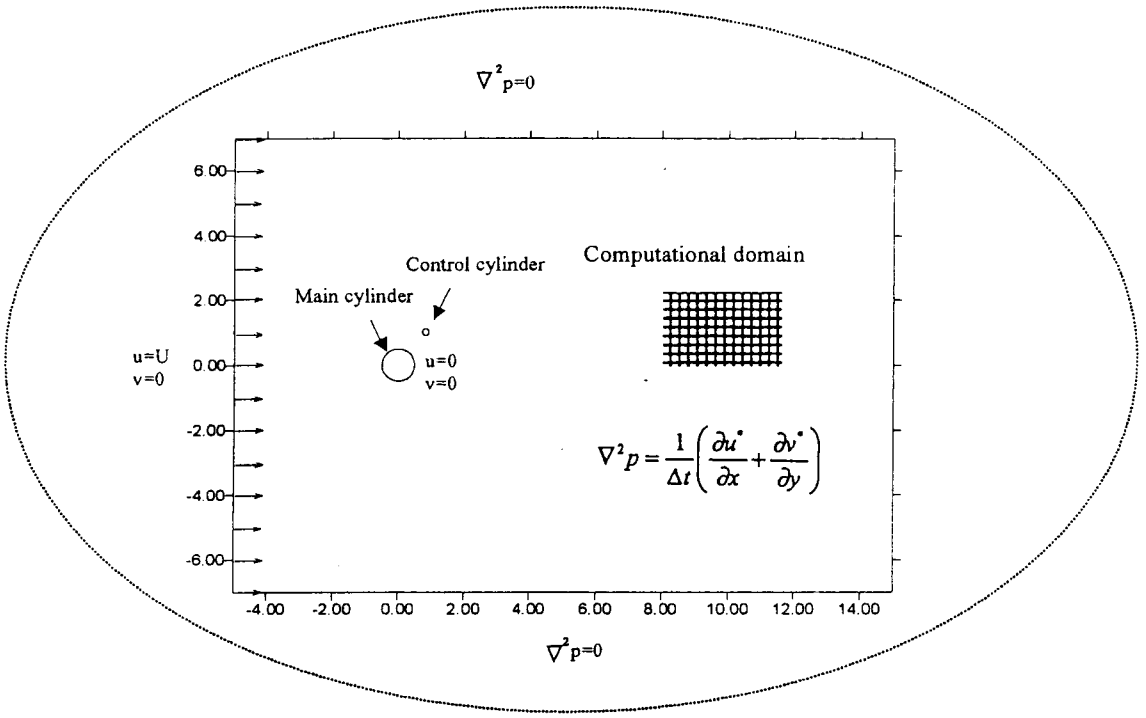


Fig. 1. Computational domain and boundary conditions.

where $u_0$ is the fluid velocity, $F_d$ is the drag force, $\rho$ is the mass density, $D$ is the characteristic dimension, $F_l$ is the lift force, $f$ is the frequency of the oscillation, $\tau_s$ is the shear force acting on the body, $p_s$ is the pressure acting on the body, and $n_x$ and $n_y$ are the direction cosines in the $x$- and $y$-coordinates, respectively.

## 3. Numerical formulation

As mentioned earlier, in the present model, a coupled BEM–FEM approach is used in the solution of the governing differential equations. In this section, the numerical formulation is briefly described.

### 3.1. Three-step FEM formulation for the Navier–Stokes equations

In the present model, the momentum Navier–Stokes equations are approximated using an explicit three-step FEM based on a Taylor series expansion in time [12]. From Taylor's series, a function $f$ in time can be represented as

$$f(t+\Delta t) = f(t) + \Delta t\frac{\partial f(t)}{\partial t} + \frac{\Delta t^2}{2}\frac{\partial^2 f(t)}{\partial t^2} + \frac{\Delta t^3}{6}\frac{\partial^3 f(t)}{\partial t^3} + O(\Delta t^4). \tag{16}$$

Approximating Eq. (16) upto third-order accuracy, the three-step formulation can be written as:

$$f\left(t+\frac{\Delta t}{3}\right) = f(t) + \frac{\Delta t}{3}\frac{\partial f(t)}{\partial t}, \tag{17}$$

$$f\left(t+\frac{\Delta t}{2}\right) = f(t) + \frac{\Delta t}{2}\frac{\partial f(t+\Delta t/3)}{\partial t}, \tag{18}$$

$$f(t+\Delta t) = f(t) + \Delta t\frac{\partial f(t+\Delta t/2)}{\partial t}. \tag{19}$$

When Eqs. (17)–(19) are discretized using the standard Galerkin FEM and the resulting finite element equations are solved using the Jacobi iteration, the three-step FEM is obtained [12]. This method has all the advantages of Taylor–Galerkin method.

From the above scheme, using a projection method of the Navier–Stokes equations [13–15], we can convert Eqs. (9) and (10) in the following steps:

*Step* 1

$$\frac{u^{n+1/3}-u^n}{\Delta t/3} = -\left[u^n\frac{\partial u^n}{\partial x}+v^n\frac{\partial u^n}{\partial y}\right]-\frac{\partial p^n}{\partial x}+\frac{1}{Re}\nabla^2 u^n, \tag{20}$$

$$\frac{v^{n+1/3}-v^n}{\Delta t/3} = -\left[u^n\frac{\partial v^n}{\partial x}+v^n\frac{\partial v^n}{\partial y}\right]-\frac{\partial p^n}{\partial y}+\frac{1}{Re}\nabla^2 v^n. \tag{21}$$

*Step* 2

$$\frac{u^{n+1/2}-u^n}{\Delta t/2} = -\left[u^{n+1/3}\frac{\partial u^{n+1/3}}{\partial x}+v^{n+1/3}\frac{\partial u^{n+1/3}}{\partial y}\right]-\frac{\partial p^n}{\partial x}+\frac{1}{Re}\nabla^2 u^{n+1/3}, \tag{22}$$

$$\frac{v^{n+1/2}-v^n}{\Delta t/2} = -\left[v^{n+1/3}\frac{\partial v^{n+1/3}}{\partial x}+u^{n+1/3}\frac{\partial v^{n+1/3}}{\partial y}\right]-\frac{\partial p^n}{\partial y}+\frac{1}{Re}\nabla^2 v^{n+1/3}. \tag{23}$$

*Step* 3

$$\frac{u^*-u^n}{\Delta t} = -\left[u^{n+1/2}\frac{\partial u^{n+1/2}}{\partial x}+v^{n+1/2}\frac{\partial u^{n+1/2}}{\partial y}\right]+\frac{1}{Re}\nabla^2 u^{n+1/2}, \tag{24}$$

$$\frac{v^*-v^n}{\Delta t} = -\left[u^{n+1/2}\frac{\partial v^{n+1/2}}{\partial x}+v^{n+1/2}\frac{\partial v^{n+1/2}}{\partial y}\right]+\frac{1}{Re}\nabla^2 v^{n+1/2}, \tag{25}$$

where $u^*$ and $v^*$ are the apparent velocities. Combining the continuity equation (8) and take gradient of (24) and (25), the pressure Poisson equation is derived to correct the velocity equation as

$$\nabla^2 p^{n+1} = \frac{1}{\Delta t}\left(\frac{\partial u^*}{\partial x}+\frac{\partial v^*}{\partial y}\right). \tag{26}$$

Now the end-of-step velocity can be derived as:

$$u^{n+1} = u^* - \Delta t\frac{\partial p^{n+1}}{\partial x}, \tag{27}$$

$$v^{n+1} = v^* - \Delta t\frac{\partial p^{n+1}}{\partial y}. \tag{28}$$

Spatial discretization of Eqs. (20)–(25) are performed by the standard Galerkin method using four-point bilinear elements [17]. The resulting finite element equations for Eqs. (20) and (21) can be expressed as:

$$M_{ij}\frac{u_j^{n+1/3}-u_j^n}{\Delta t/3} = -A_{ij}^n u_j^n - B_{ij}p_j^n - \frac{1}{Re}S_{ij}u_j^n + \int_{\partial\Omega} N_i\frac{1}{Re}\left(\frac{\partial u^n}{\partial n}\right)\mathrm{d}S, \tag{29}$$

$$M_{ij}\frac{v_j^{n+1/3}-v_j^n}{\Delta t/3} = -A_{ij}^n v_j^n - D_{ij}p_j^n - \frac{1}{Re}S_{ij}v_j^n + \int_{\partial\Omega} N_i\frac{1}{Re}\left(\frac{\partial v^n}{\partial n}\right)\mathrm{d}S. \tag{30}$$

In a similar way, Eqs. (22)–(25) can be discretized and finite element equations can be formed.

Eqs. (27) and (28) can be discretized as

$$M_{ij}u_j^{n+1} = M_{ij}u_j^* - \Delta t B_{ij}p_j^{n+1}, \tag{31}$$

$$M_{ij}v_j^{n+1} = M_{ij}v_j^* - \Delta t D_{ij}p_j^{n+1}, \tag{32}$$

where

$$M_{ij} = \int_\Omega N_i N_j \, d\Omega, \quad A_{ij}^n = \int_\Omega N_i \left( N_k u_k^n \frac{\partial N_j}{\partial x} + N_k v_k^n \frac{\partial N_j}{\partial y} \right) d\Omega,$$

$$B_{ij} = \int_\Omega N_i \frac{\partial N_j}{\partial x} d\Omega, \quad D_{ij} = \int_\Omega N_i \frac{\partial N_j}{\partial y} d\Omega, \quad S_{ij} = \int_\Omega \left( \frac{\partial N_i}{\partial x} \frac{\partial N_j}{\partial x} + \frac{\partial N_i}{\partial y} \frac{\partial N_j}{\partial y} \right) d\Omega,$$

in which $N_i$ and $N_j$ are the shape functions. After assembling the system and applying the boundary conditions, the system of equations are solved using the Jacobi iteration scheme.

In the present model, the pressure Poisson equation (26) is solved using the BEM formulation, given in the following section using the boundary conditions derived from the solution of Eq. (12) on the infinite domain from the finite discrete domain. As obvious, the solution of the pressure Poisson equation is implicit using the velocities obtained from the solution of Eqs. (24) and (25) and hence an iterative procedure is necessary between the solutions of $u^{n+1}, v^{n+1}$ and $p^{n+1}$.

### 3.2. BEM formulation for Poisson equation

Consider the Poisson-type pressure equation in $p$, $u$ and $v$, Eq. (26),

$$\nabla^2 p = \frac{1}{\Delta t} \left( \frac{\partial u^*}{\partial x} + \frac{\partial v^*}{\partial y} \right) = b \tag{33}$$

with appropriate pressure boundary conditions.

In the present model, an iterative scheme is used such that the velocity $u^*$ and $v^*$ are known in the current iteration and time-step from the previous step by solving the Navier–Stokes equations.

A weighting function $p^*$ can now be introduced such that it has continuous first derivatives within the domain. The following weighted residual statement can now be written:

$$\int_\Omega (\nabla^2 p - b) p^* \, d\Omega = \int_{\Gamma 2} (q - \bar{q}) p^* \, d\Gamma - \int_{\Gamma 1} (p - \bar{p}) q^* \, d\Gamma, \tag{34}$$

where $q = \partial p / \partial n$ and $q^* = \partial p^* / \partial n$.

Let $p^*$ be the fundamental solution of the Laplace equation in two dimensions, represented as $p^* = (-\ln(r)/2\pi)$, where $r$ is the distance from the collocation point $(k)$ to other field points $(i)$ given as:

$$r = \sqrt{(x_k - x_i)^2 + (y_k - y_i)^2}. \tag{35}$$

Now applying Green's second identity theorem to Eq. (33) and using the standard boundary element procedure [18], we can get the boundary integral equation as:

$$C_i p_i + \int_\Gamma p q^* \, d\Gamma + \int_\Omega b p^* \, d\Omega = \int_\Gamma q p^* \, d\Gamma, \tag{36}$$

where $C_i$ is the Green's constant which can be calculated by surrounding the boundary point $i$ by a small circle of radius $\varepsilon$ and taking each term in Eq. (36) in the limit as $\varepsilon \to 0$. Generally $C_i$ can be represented as $\theta/2\pi$, where $\theta$ is the internal angle at point $i$ in radians.

In Eq. (36), we have boundary integrals and domain integrals. In the present model, the domain integration is carried out by subdividing the domain into a series of internal cells, on each of which a numerical integration is performed. Here linear elements are used for the boundary discretization and 2D isoparametric quadrilateral cells are used for the internal discretization. The details of the element properties, shape functions, coordinate transformation and numerical integration used here are described in [18] which is not repeated here.

If the domain is discretized into $M$ internal cells, then the domain integral can be written as:

$$D_i = \int_\Omega b p^* \, d\Omega = \sum_{e=1}^{M} \left[ \sum_{k=1}^{\mathrm{NI}} w_k (b p^*)_k \right] \Omega_e, \tag{37}$$

where the integral has been approximated by a summation over different cells ($e$ varies from 1 to $M$), $w_k$ are the Gauss integration weights, the function $(bp^*)_k$ needs to be evaluated at integration points $k$ on each cell ($k$ varies from 1 to NI, where NI is the total number of integration points on each cell) and $\Omega_e$ is the area of cell $e$. The term $D_i$ is the result of the numerical integration and is different for each position $i$ of the boundary nodes.

Assuming that the boundary of the domain is discretized into NE linear elements with $N$ nodes, Eq. (36) can be discretized and written in matrix form as

$$C_i p_i + \sum_{j=1}^{N} \bar{H}_{ij} p_j + D_i = \sum_{j=1}^{N} G_{ij} q_j. \tag{38}$$

Combining the effect of the constant term $C$ with the $\bar{H}$ matrix, we can write the system of matrix as

$$Hp + D = Gq. \tag{39}$$

In Eq. (39), the boundary conditions are introduced and the known values are taken to the right-hand side to form a system of linear equations of the form

$$Ag = F, \tag{40}$$

where $g$ is a vector of unknown boundary values of $p$ and $q$, and $F$ is a known vector. Eq. (40) is solved using Gauss elimination scheme and all the boundary values will be then known. Once this is done, it is possible to calculate internal values of $p$ or its derivatives from Eq. (36).

It should be noted that the same BEM formulation without any domain integral given above (Eq. (36)) is valid for the solution of the Laplace equation given in Eq. (12). Eq. (12) is solved for the infinite domain using the same discretization from the discrete finite domain.

Here the main advantage of using BEM in the solution of the pressure Poisson equation, is the effectiveness of BEM to deal with the infinite domain of the external flow problem from a finite discrete domain. The boundary condition of pressure on the infinite computational domain is only known which is used to solve the finite domain problem. Other numerical methods like FDM or FEM are not so efficient as BEM to solve the pressure Poisson equation in infinite domain from a finite discrete domain. In BEM, the fundamental solutions used in the formulations automatically satisfy the conditions at infinity and hence very efficient to solve the infinite domain problem from the finite discrete domain [18].

## 4. Computational procedure

As mentioned earlier, here an iterative scheme is used in the solution of the Navier–Stokes equations. In most of the incompressible viscous flow problems solved using Navier–Stokes equations, the most natural boundary conditions arise when the velocity is prescribed all over the boundaries of the problem. As shown in Fig. 1, the boundary condition of the fixed body in the flow is set as non-slip boundary. The computational procedure adopted here includes the following iterative steps:

For the time step $n = 1$

1. Assume at infinite domain, pressure $p = 0$ and solve the pressure Laplace equation (Eq. (12)) outside the computational domain and the pressure Poisson equation (Eq. (26)) inside the computational domain and get the pressure boundary conditions on the boundaries of the computational domain. These equations are solved simultaneously by utilizing the compatibility and equilibrium conditions of continuity of pressure and flux at the common boundary as described in [18].
2. Solution of the Navier–Stokes equations using three-step FEM and pressure projection method.
   - Solve for the unknown apparent velocity values (Eqs. (24) and (25)).
   - Calculate the pressure distribution for the current time-step from the pressure Poisson (Eq. (26)) using BEM.
   - Determine the new velocity values by solving Eqs. (27) and (28).

3. Check for convergence of the velocity and pressure components in the present iteration, for example

$$\frac{|v_k^{n+1} - v_k^n|}{|v_k^n|} \leqslant 0.001. \tag{41}$$

If convergence criterion is satisfied, then proceed to the next step, otherwise go to step 1.

4. In the successive time-step, use the velocity and pressure components from the previous time-step as initial conditions and the new boundary flow conditions and use the iterative procedure, steps 1–3. The procedure is repeated until the prescribed time-step is reached.

## 5. Model applications

The proposed BEM–three-step FEM model has been applied on two test problems to verify the accuracy and feasibility of the model. The present model has been used to simulate the vortex shedding flow past a cylinder and in the case of vortex shedding and suppression of fluid forces on two circular cylinders in which one act as a control cylinder, in the range of Reynolds number 50–140.

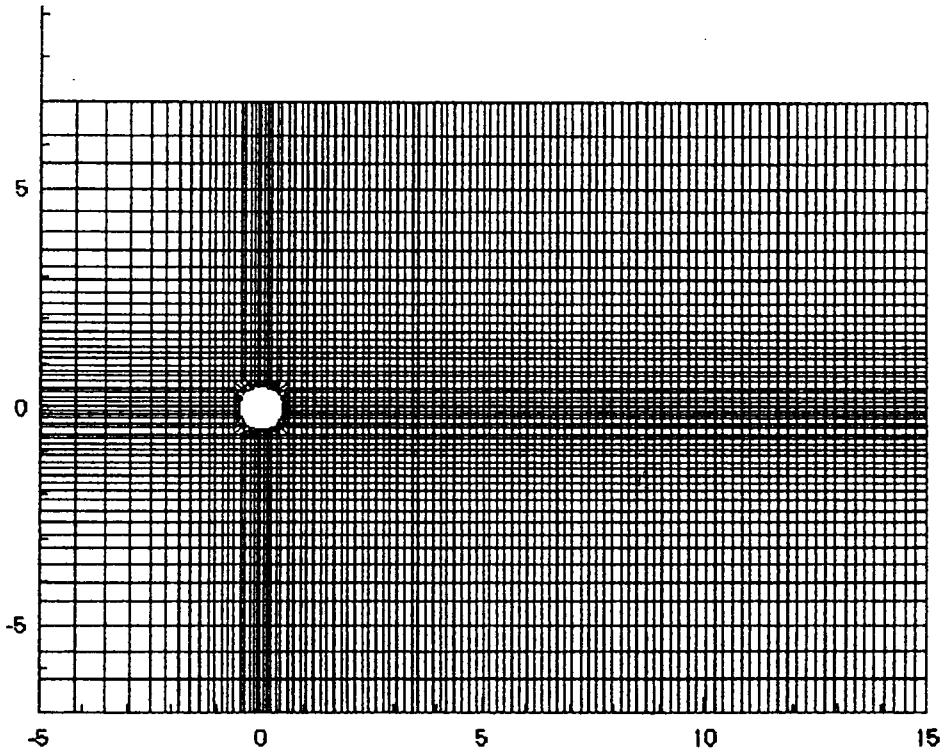


Fig. 2. Mesh for the computational domain – case 1.

Table 1
Comparison of numerical results for the flow across a circular cylinder

| *Re* | Grid | $C_d$ | *St* | Author |
|---|---|---|---|---|
| 100 | 13 530 | 1.28 | 0.16 | Braza et al. [3] |
| | 1852 | 1.76 | 0.18 | Gresho et al. [19] |
| | 826 | 1.33 | 0.163 | Li et al. [20] |
| | 5750 | 1.29 | 0.168 | Present |
| | 1802 | 1.25 | 0.165 | Present |

### 5.1. Vortex shedding flow past a single circular cylinder

A large number of experimental and numerical studies have been carried out on the vortex shedding flow that is produced by the flow across a fixed circular cylinder [1–6,20,21]. Initially, the flow across a cylinder phenomenon has been simulated here to compare the results with the existing studies. The present model was tested by simulating flow past a circular cylinder for $Re = 100$. Fig. 1 shows the computational domain with boundary conditions (in this case, no control cylinder). It was 20 units long (cylinder diameter is unity) and 14 units wide approximately. The discretization of the domain using 5568 elements and 5750 nodes is

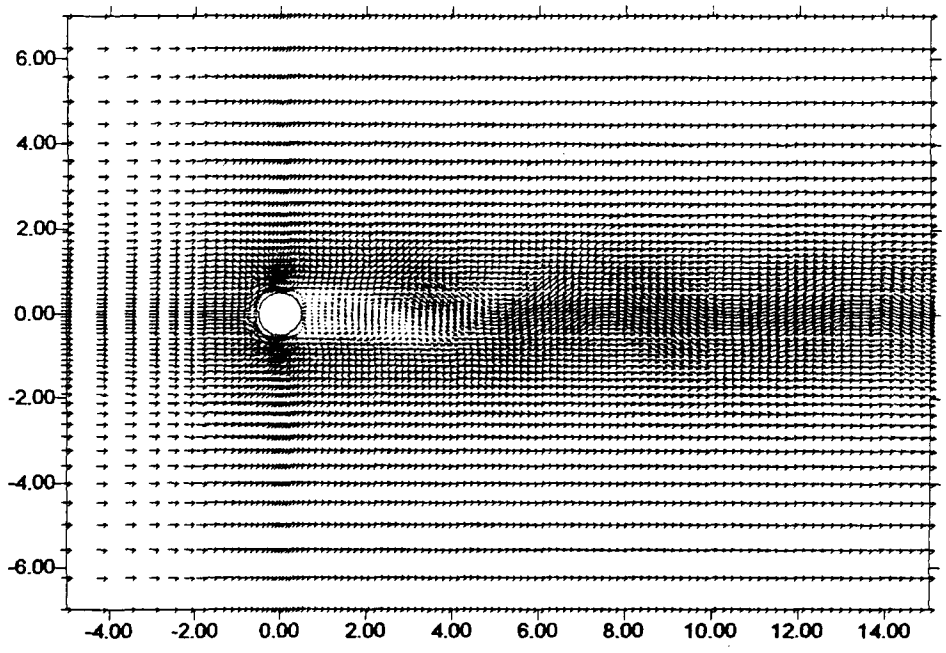


Fig. 3. Velocity field for flow across a circular cylinder, $Re = 80$, $t = 200$ s.

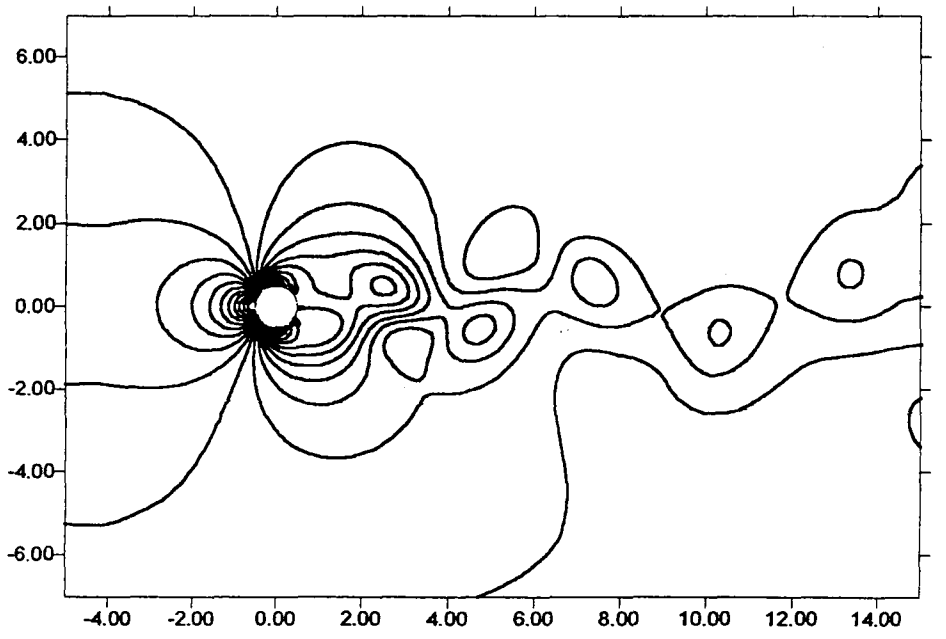


Fig. 4. Pressure field for flow across a circular cylinder, $Re = 80$, $t = 200$ s.

shown in Fig. 2. The domain of computation was wide enough to encompass the range of the vortex shedding. A time-step of 0.0125 s is used in the computation. The boundary conditions were chosen as $u = 1$, $v = 0$ at the inlet and a non-slip boundary $u = 0$, $v = 0$ on the cylinder surface.

The model was run in unsteady condition and the coefficient of drag and Strauhal number were calculated using Eq. (13). Table 1 shows a comparison of the coefficient of drag and Strauhal number at $Re = 100$, between the results of Braza et al. [3], Gresho et al. [19] and Li et al. [20]. Good agreement is observed between the results.

The time marching calculation of vortex shedding for the problem is carried out at Reynolds number of 80 for comparison purpose [2]. Before analyzing the time-dependent vortex shedding for a cycle, the

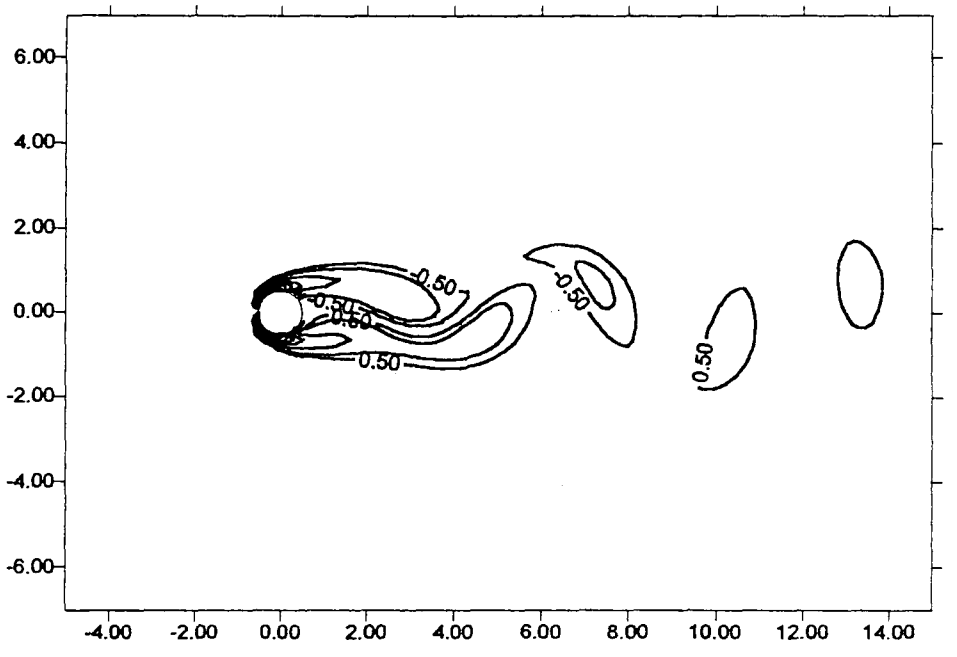


Fig. 5. Vorticity distribution for flow across a circular cylinder, $Re = 80$, $t = 200$ s.

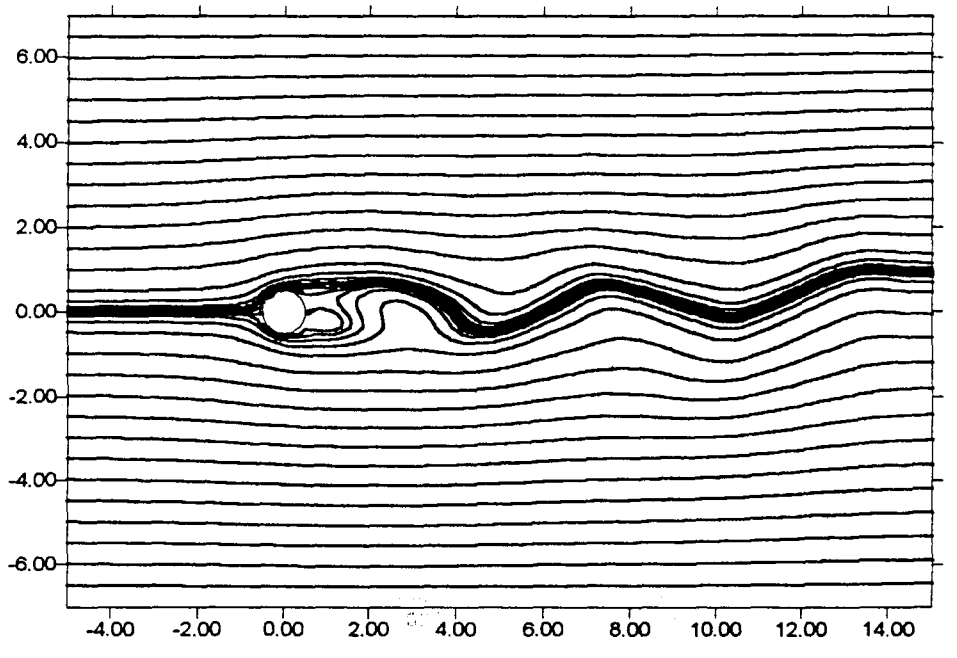


Fig. 6. Streamline distribution for flow across a circular cylinder, $Re = 80$, $t = 200$ s.

velocity, pressure and vorticity are estimated at time $t = 200$ s. Fig. 3 shows the velocity field and Fig. 4 shows the pressure field for the Reynolds number 80 at time equal to 200 s. The vorticity distribution around the cylinder is depicted in Fig. 5. Fig. 6 shows the streamlines for the circular cylinder. These figures show the salient features of the flow across the cylinder at $Re = 80$. As the above figures depict, the numerical simulations with the present model have rendered very reasonable and satisfactory results in comparison with the previous studies.

To analyze the time-dependent vortex shedding for a cycle, the streamlines are calculated for a cycle of 6.4 s. Fig. 7 shows the periodic vortex shedding at various time intervals between $t = 0$ and $t = 6.4$ s. The

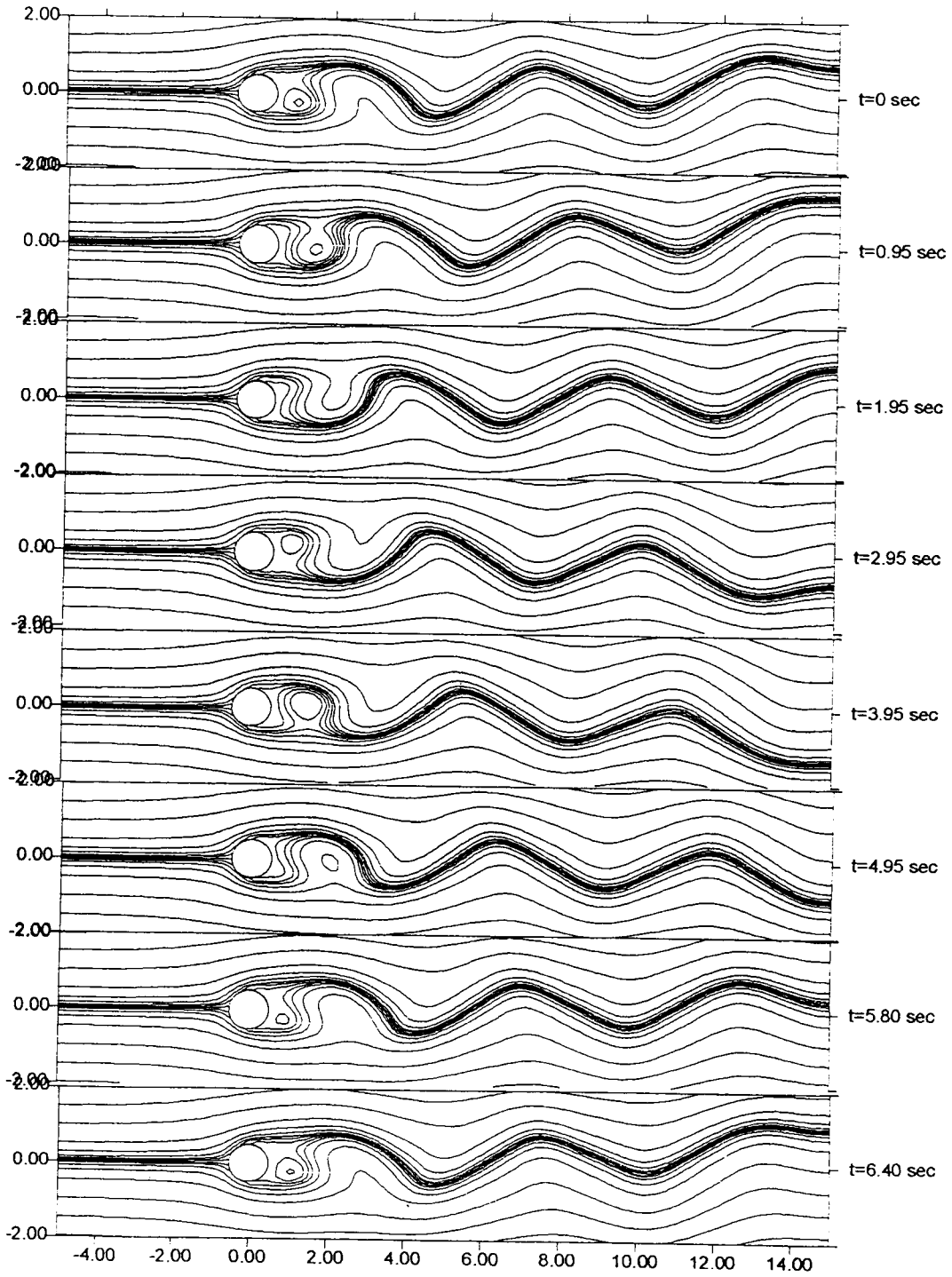


Fig. 7. Time development of vortex shedding streamlines past a circular cylinder, $Re = 80$.

dynamics of the flow behind the cylinder and the changes in the vortex shedding pattern within a cycle can be easily observed from Fig. 7. Fig. 8 shows the coefficient of lift calculated for the time 200 s. Fig. 9 shows the dimensionless shedding frequency for various Reynolds numbers in the range of 50–140. The results are compared with the experimental results of Strykowski and Sreenivasan [2] and Wang and Chang [21]. Good agreement is observed between the results. The vortex shedding analysis in the case of the single circular cylinder is used further in the vortex shedding and suppression in the next case study by introducing a control cylinder.

### 5.2. *Vortex shedding and suppression flow past a circular cylinder with a control cylinder*

In this case study, the model is applied to investigate the effect of a control cylinder in the vicinity of a main circular cylinder in a uniform flow field, which suppresses the vortex shedding by the main circular

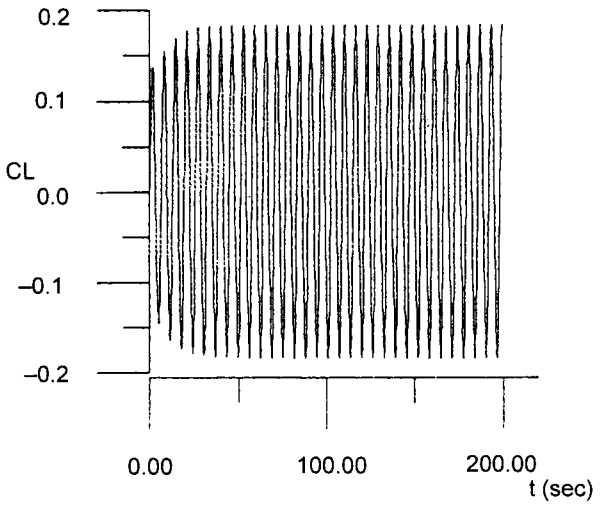


Fig. 8. Time behavior of lift coefficient for flow across a circular cylinder, $Re = 80$.

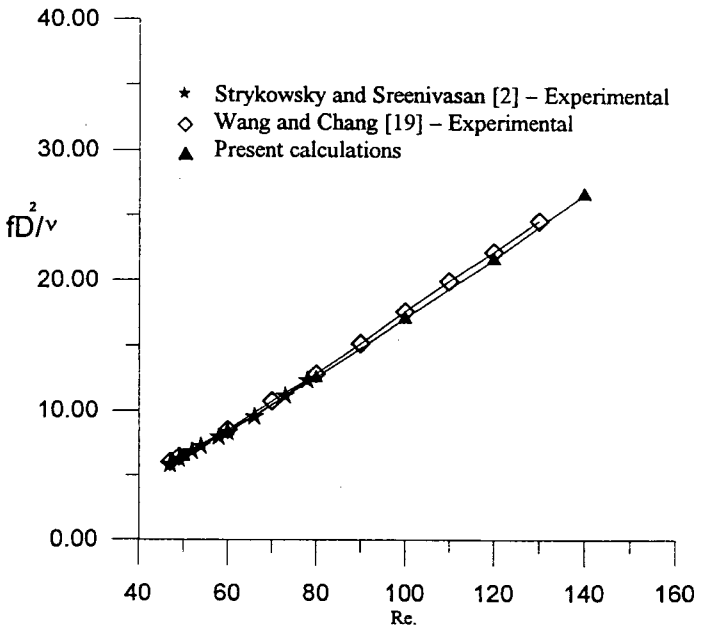


Fig. 9. Dimensionless shedding frequency for flow across a circular cylinder.

cylinder. Recently Strykowski and Sreenivasan [2] experimentally proved that the vortex shedding behind circular cylinders can be altered and suppressed altogether (or controlled) over a limited range of Reynolds number (below 120) using a small control cylinder in the near wake of the main cylinder. Sakamoto and Haniu [22] also showed experimentally that the vortex shedding behind circular cylinder can be suppressed at high Reynolds numbers using appropriately placing a small control cylinder. In this case study, the vortex alteration and suppression are investigated numerically using BEM–three-step FEM model at a low Reynolds number of 80.

Here the same problem described in previous case study (Section 5.1), is used but a small circular cylinder (of size $D/d = 5$, $D/d = 4$ $D/d = 3$, where $D$ is the diameter of main cylinder and $d$ is the diameter of control cylinder) is placed at various positions and its effects on the vortex shedding is numerically analyzed. The domain with the main cylinder and control cylinder with discretization is shown in Fig. 10. The domain is discretized using 5572 elements and 5757 nodes and time-step of 0.0125 s is used in the analysis. Initially the effects of a control cylinder of size $D/d = 5$, placed at $x = 1.53D$ and $y = 1.1D$ (assuming the position of the center of the main cylinder at $(0.0, 0.0)$) is analyzed. Before analyzing the time-dependent vortex shedding, the velocity, pressure and vorticity of the main cylinder in the presence of control cylinder are estimated at time $t = 200$ s. Fig. 11 shows the velocity field and Fig. 12 shows the pressure field for the Reynolds number 80 at time equal to 200 s. The vorticity distribution around the cylinder is depicted in Fig. 13. Fig. 14 shows the streamlines for the circular cylinder. These figures show the salient features of the effect of a control cylinder in the flow regime of the main circular cylinder in comparison with the flow field described in the first case (Section 5.1).

To analyze the time-dependent vortex shedding, for the same position of the control cylinder mentioned above, the streamlines are calculated at various time steps up to 150 s, in which the vortex shedding without control cylinder is the initial condition. Fig. 15 shows the periodic vortex shedding at various time intervals between $t = 0$ (before introduction of control cylinder) and $t = 150$ s. Fig. 16 shows the vorticity variations for different time-steps. From these figures, it can be easily observed that there is a significant change in the vortex shedding and control due to the influence of the control cylinder. The dynamics of the flow behind the cylinders and the changes in the vortex shedding pattern with time change can also be easily observed from Fig. 15.

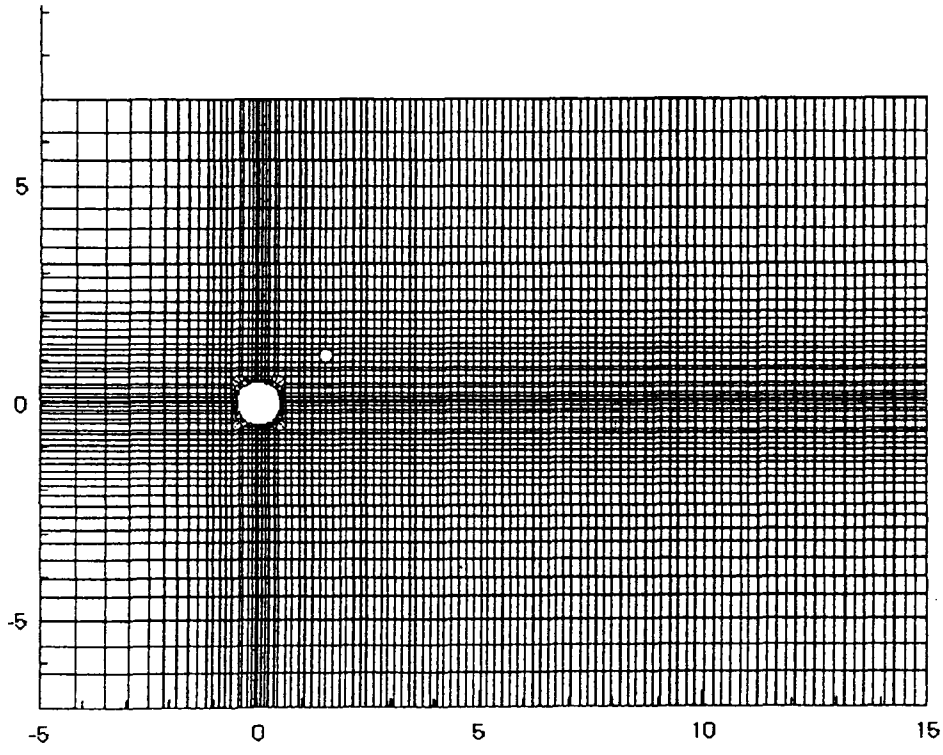


Fig. 10. Discretization of the computational domain with cylinders – case 2.

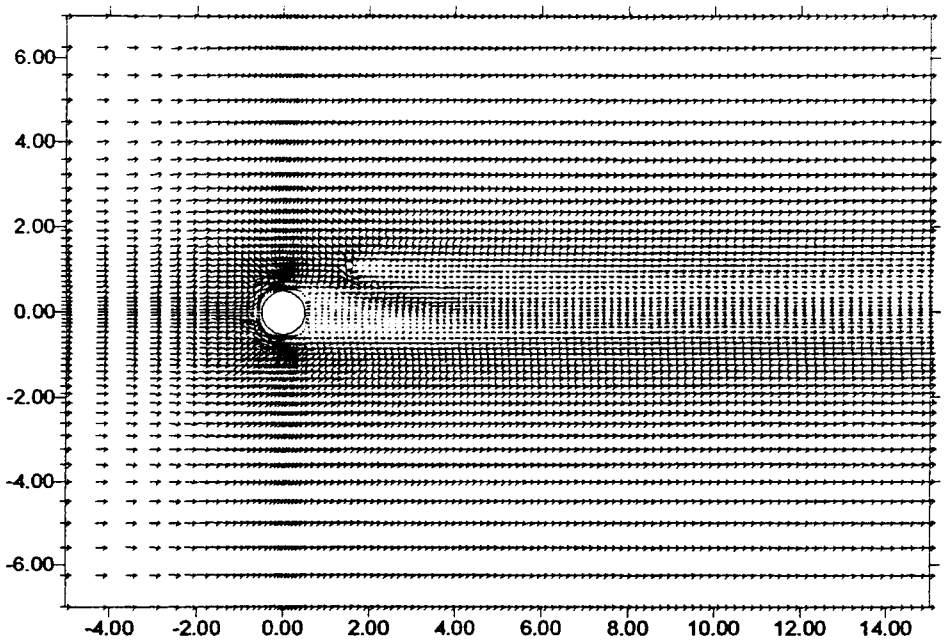


Fig. 11. Velocity field for flow across a circular cylinder with control cylinder, $Re = 80$, $t = 200$ s, $D/d = 5$.

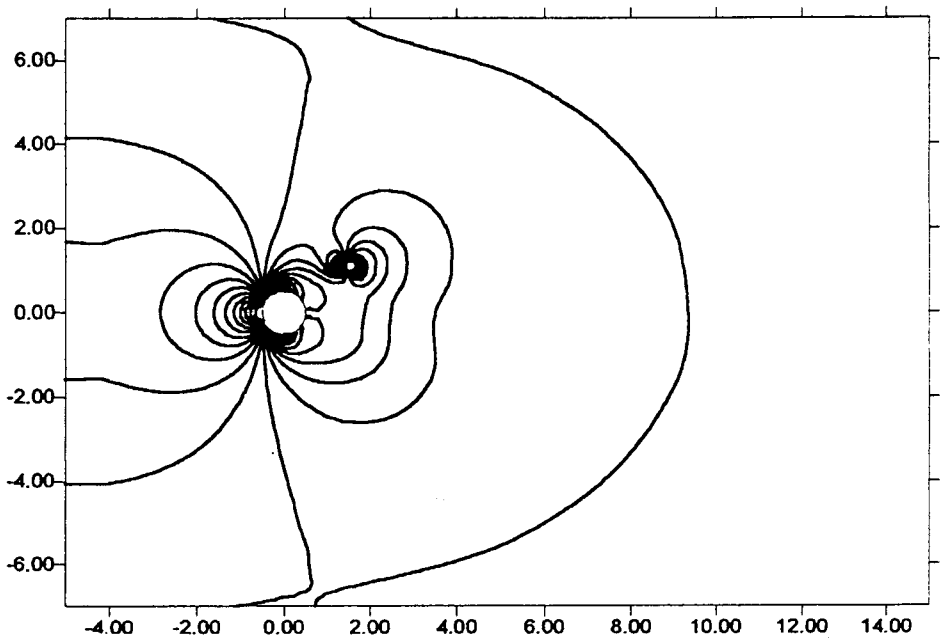


Fig. 12. Pressure field for flow across a circular cylinder with control cylinder, $Re = 80$, $t = 200$ s, $D/d = 5$.

To investigate the effects of various positions of the control cylinder on the vortex shedding, numerical analysis has been carried out by placing the control cylinder ($D/d = 5$) at $x = 1.53D$ and at various depths. Figs. 17 and 18 show the vortex shedding streamlines and the vorticity distribution at various depths of the control cylinder at time 200 s. It is very clear that the vortex shedding pattern considerably changes with the variation in the position of the control cylinder. To show the effect of the size of the control cylinder on the vortex shedding, analyses are carried out for two other sizes of control cylinder of $D/d = 4$ and $D/d = 3$. Figs. 19 and 20 show the vortex shedding streamlines for the control cylinders of sizes $D/d = 4$ and $D/d = 3$, respectively, at $x = 1.53D$ and at various $y$-positions, at $t = 200$ s. As can be seen from Figs. 17, 19 and 20, when the size of the control cylinder changes, the vortex shedding pattern changes drastically.

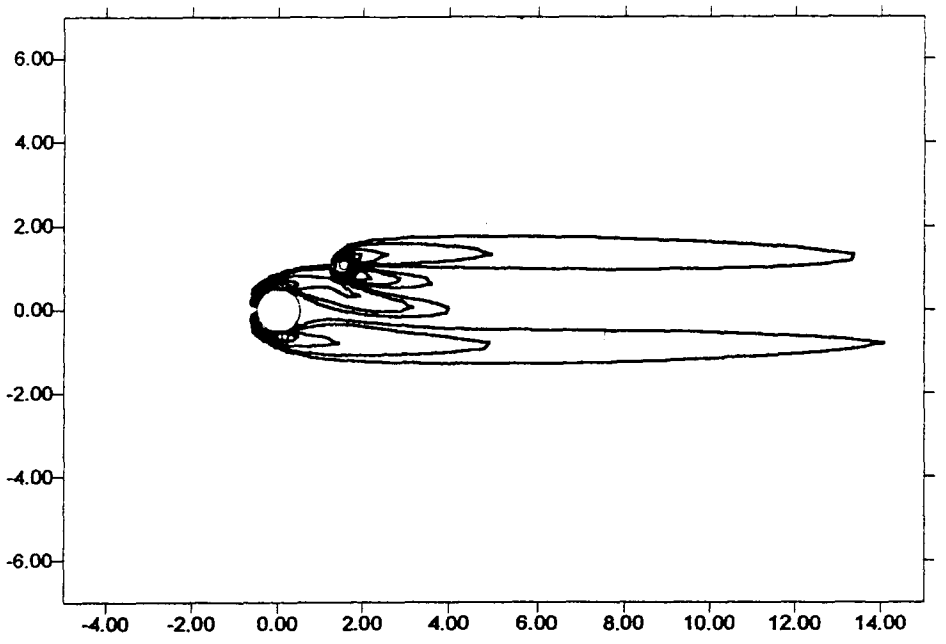


Fig. 13. Vorticity distribution for flow across a circular cylinder with control cylinder, $Re = 80$, $t = 200$ s, $D/d = 5$.

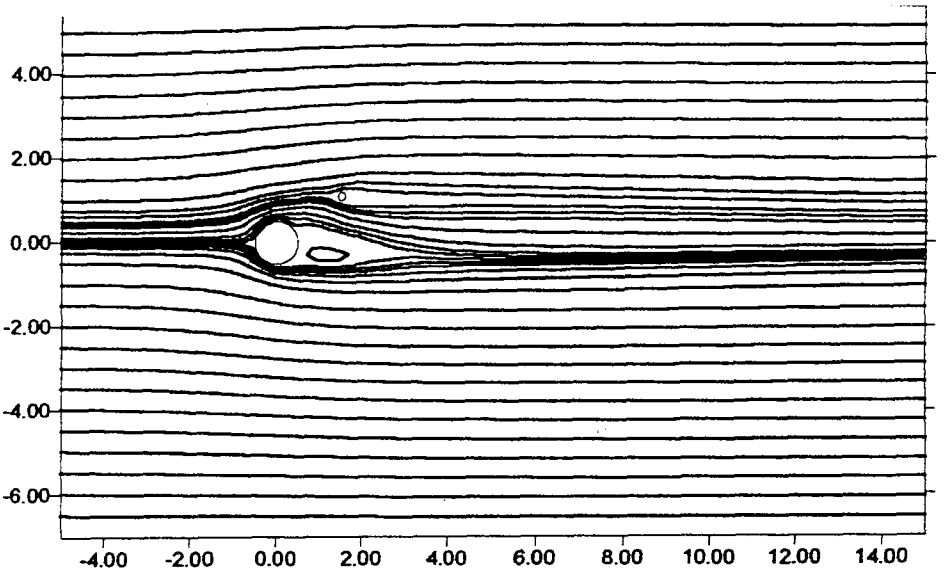


Fig. 14. Streamline distribution for flow across a circular cylinder with control cylinder, $Re = 80$, $t = 200$ s, $D/d = 5$.

The way of quantifying the changes occurring due to the introduction of control cylinder in the wake is by monitoring the vortex shedding frequency [2]. The vortex shedding frequency data were taken for $D/d = 10$ and at the position of $x/D = 1.2$ and $y/D = 1$. Fig. 21 shows the dimensionless shedding frequency for various Reynolds numbers in the range of 50–140 without the control cylinder and with control cylinder. The results are compared with the experimental results of Strykowski and Sreenivasan [2] as well as Wang and Chang [21]. The experimental investigation of Strykowski and Sreenivasan [2] reported that the critical Reynolds number for the control cylinder to suppress the vortex shedding at the position of $x/D = 1.2$ and $y/D = 1$ for $D/d = 10$ is 80. However the numerical simulations of the present study indicates a little high value of critical Reynolds number of 100. This difference may be attributed to the differences of the level of disturbance, specific end conditions and 3D effects [2]. As a matter of fact, if the location of the control cylinder is changed, we will get the vortex shedding, even at $Re = 80$, as illustrated in Figs. 17, 19 and 20.

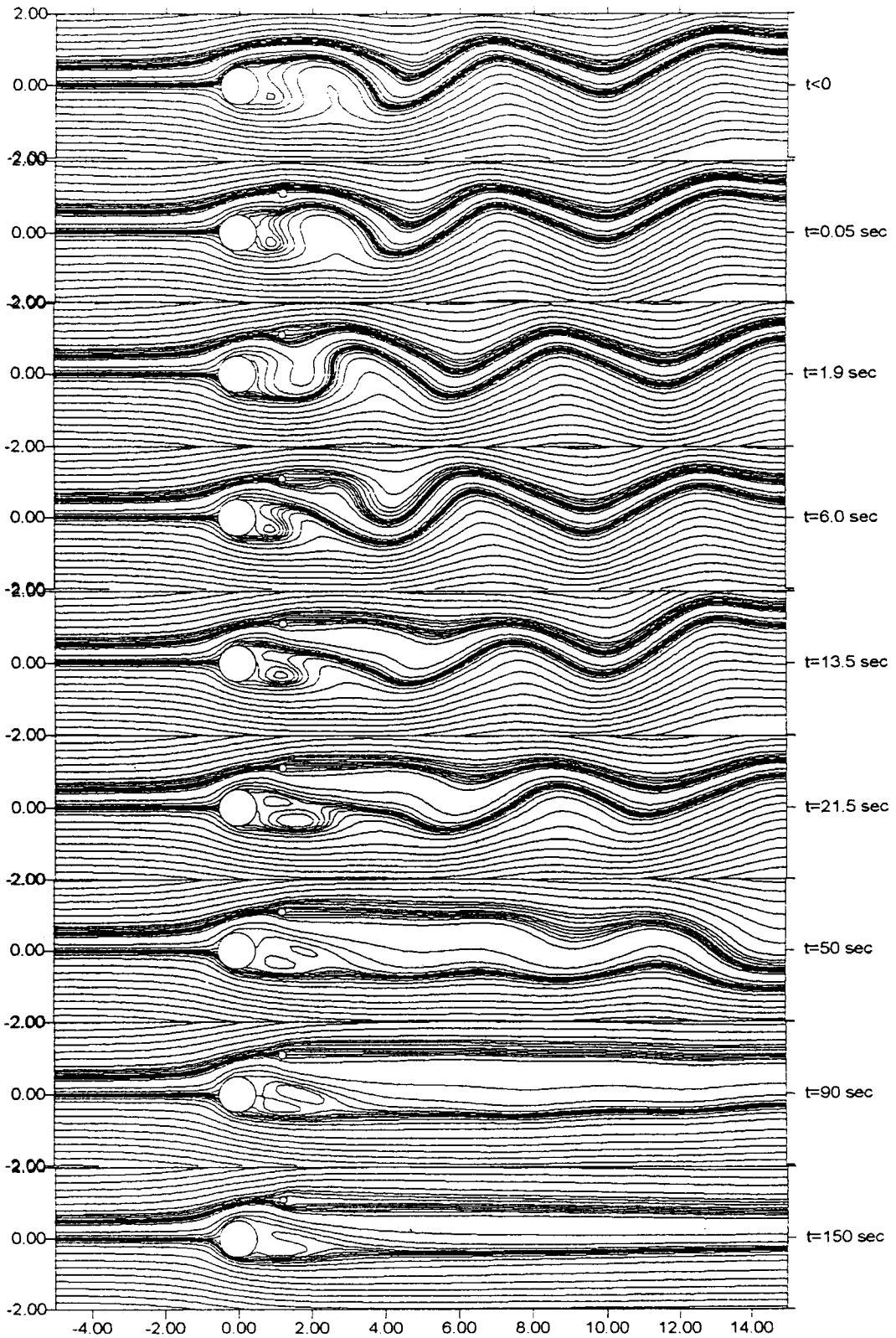


Fig. 15. Time development of vortex shedding streamlines for flow past a circular cylinder with control cylinder, $Re = 80$, $D/d = 5$.

Fig. 22 shows the coefficient of lift calculated for the time 200 s for a control cylinder of size $D/d = 4$ at $x = 1.53D$ and for various $y$-positions. It clearly depicts the effect of the control cylinder in the flow regime in comparison without control cylinder. The coefficient of lift drastically changes with the position of the

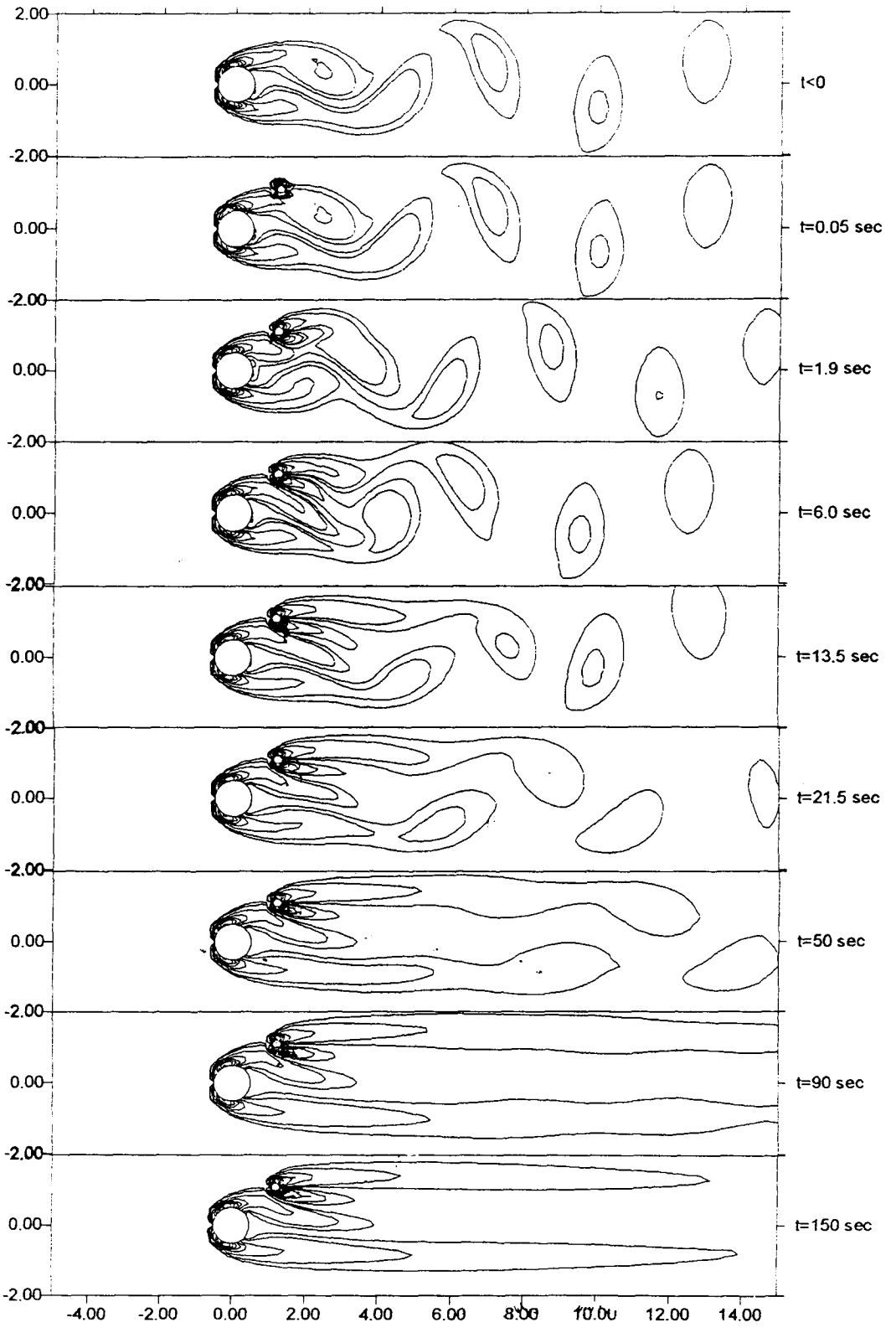


Fig. 16. Time development of vorticity for flow past a circular cylinder with control cylinder, $Re = 80$, $D/d = 5$.

control cylinder. As can be seen in Fig. 22, when the control cylinder is introduced at a depth of $1.72D$ (from center line of control cylinder), there is a drastic oscillation in lift coefficient which reduces and become constant at $y = 0.84D$ position of the control cylinder. If the depth of the control cylinder again reduced, again there is oscillation in the lift coefficient.

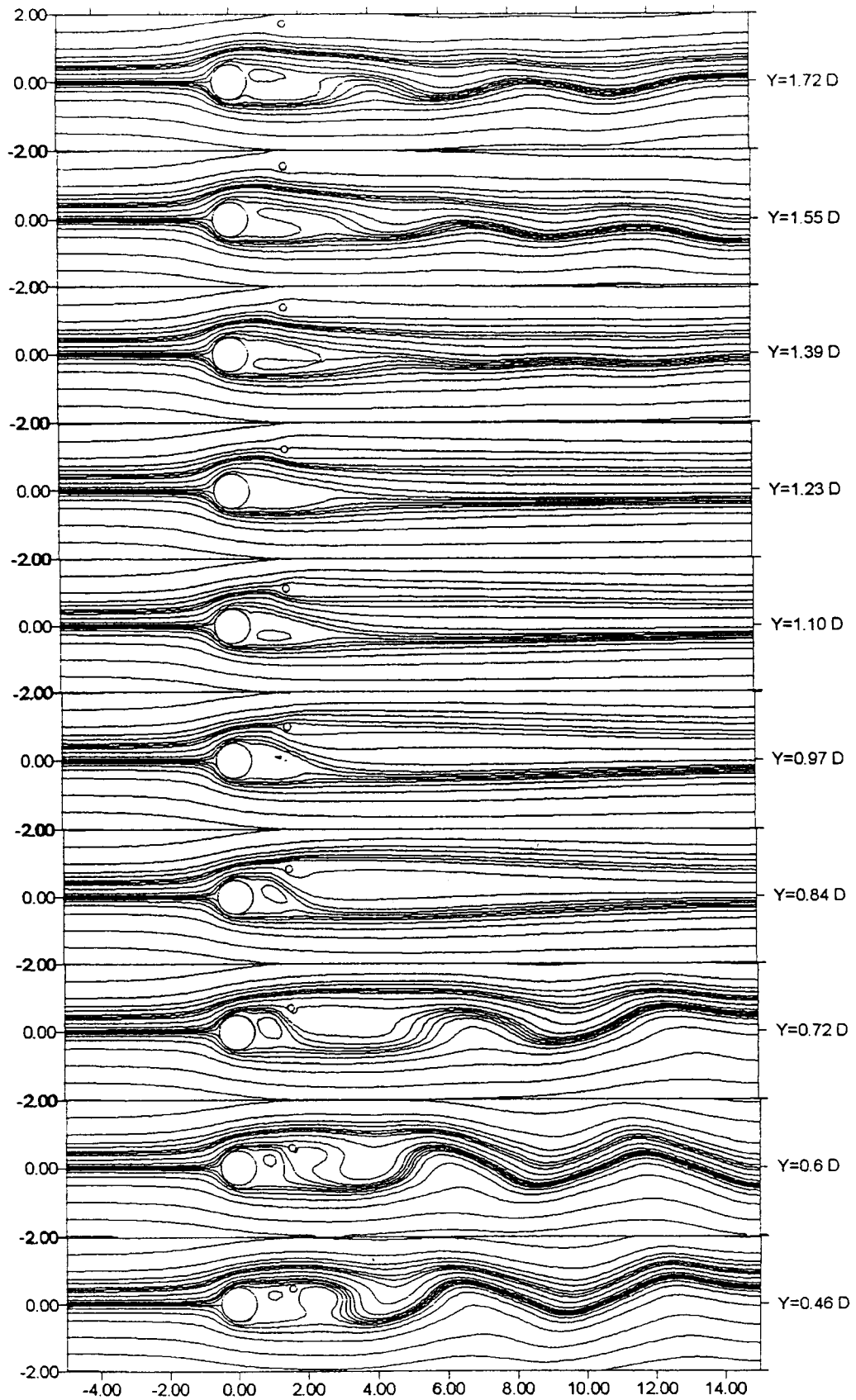


Fig. 17. Vortex shedding streamlines for flow past a circular cylinder with control cylinder at various depths, $t = 200$ s, $x = 1.53D$, $Re = 80$, $D/d = 5$.

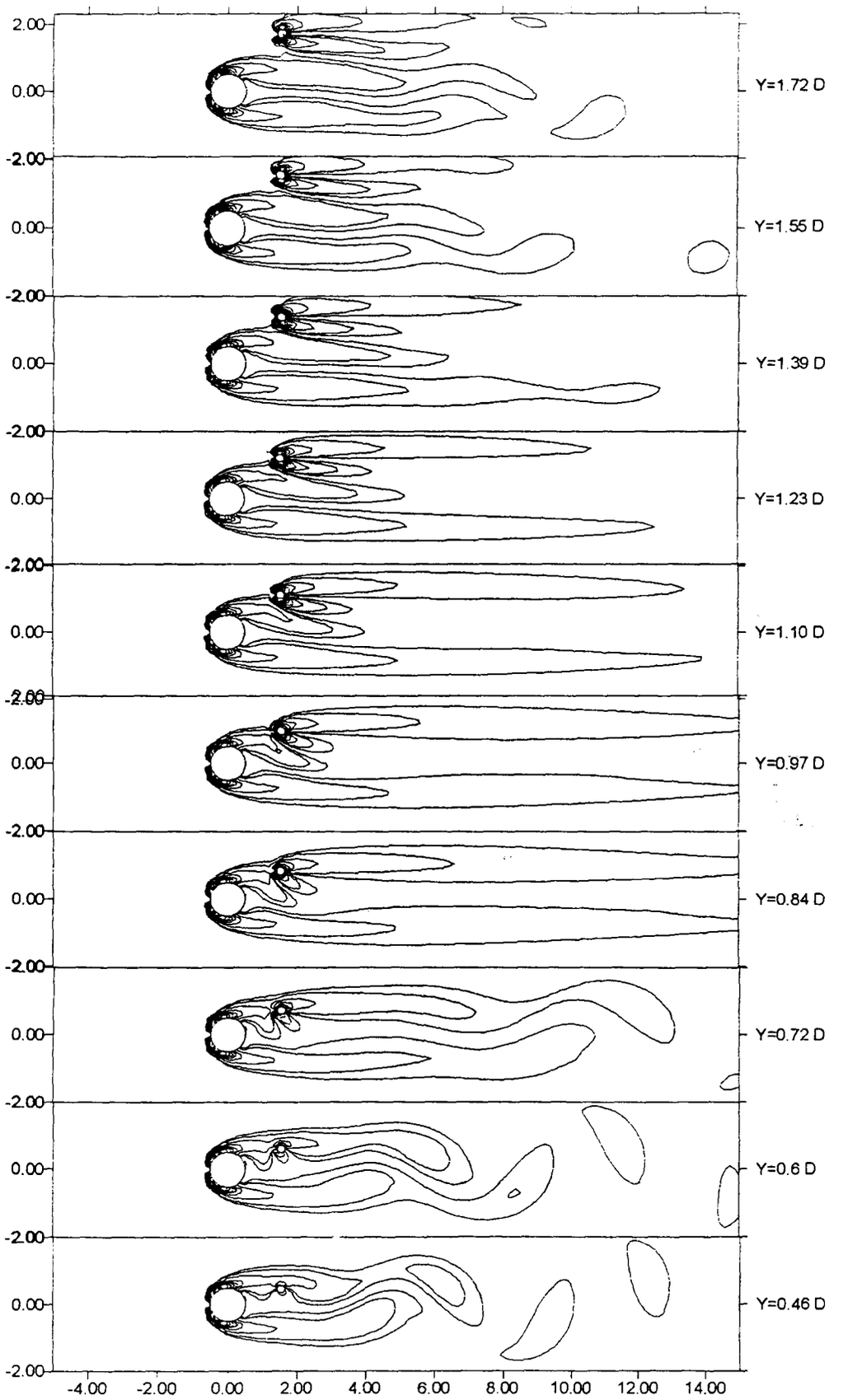


Fig. 18. Vorticity distribution for flow past a circular cylinder with control cylinder at various depths, $t = 200$ s, $x = 1.53D$, $Re = 80$, $D/d = 5$.

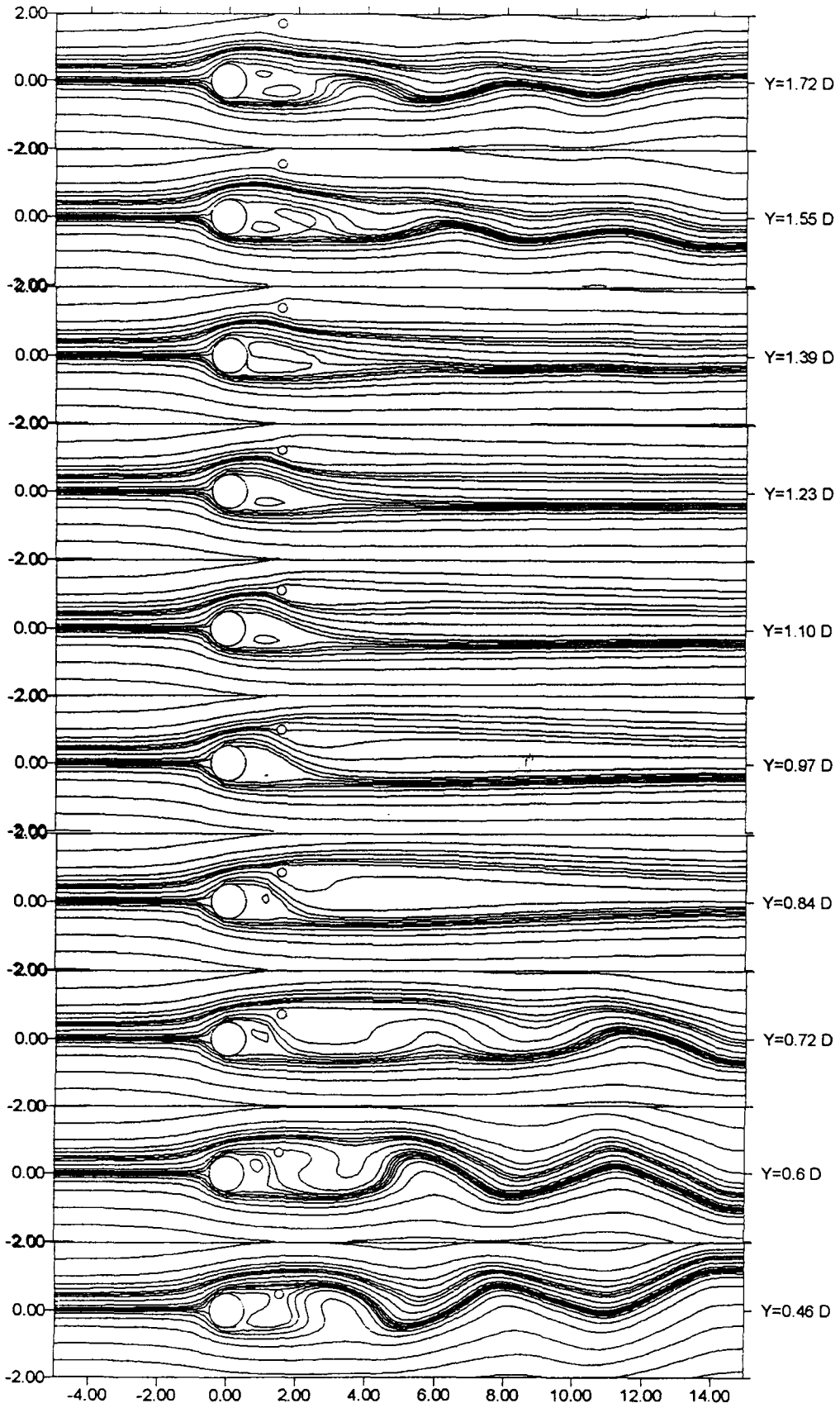


Fig. 19. Vortex shedding streamlines for flow past a circular cylinder with control cylinder of size $D/d = 4$, $t = 200$ s, $x = 1.53D$, $Re = 80$.

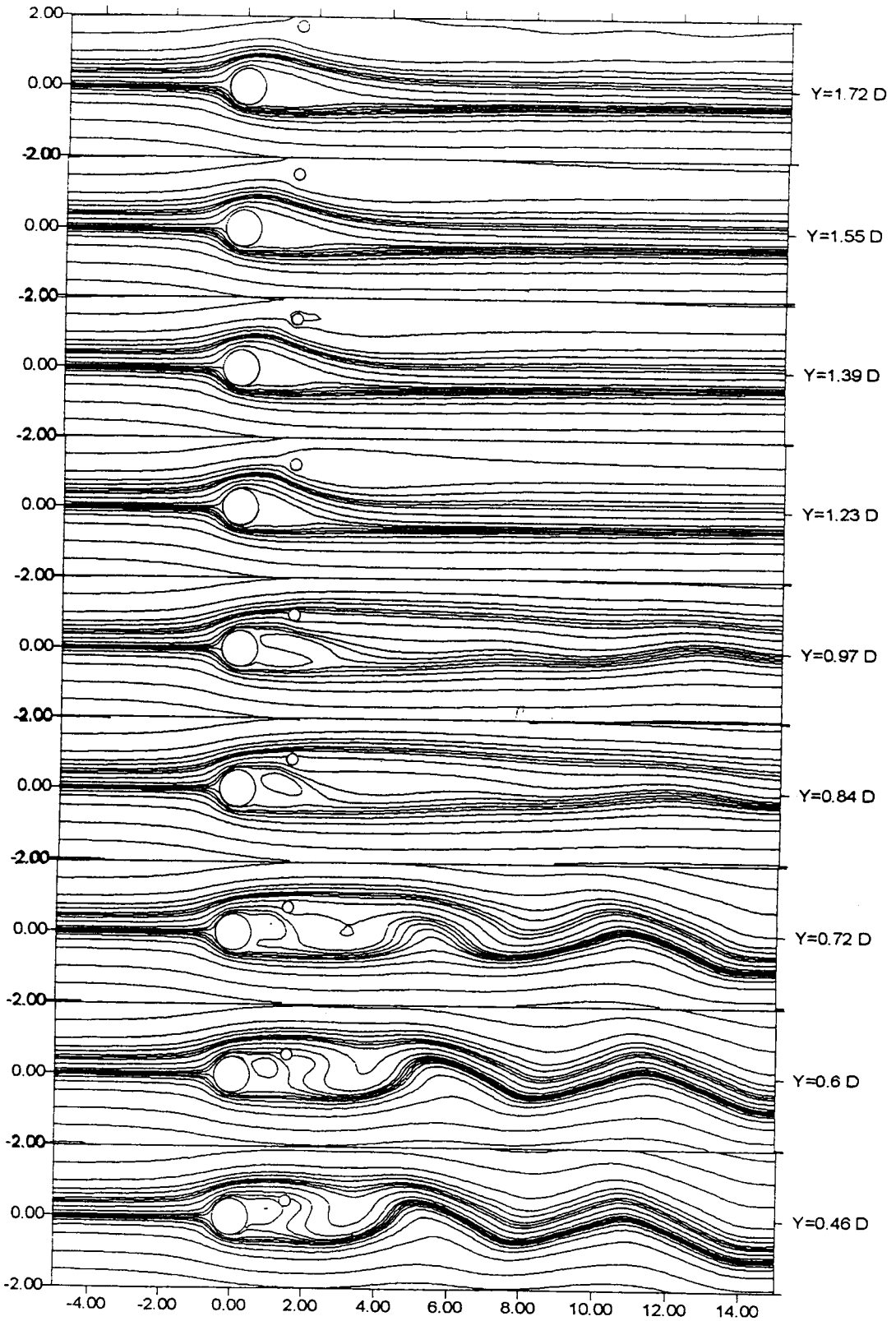


Fig. 20. Vortex shedding streamlines for flow past a circular cylinder with control cylinder of size $D/d = 3$, $t = 200$ s, $x = 1.53D$, $Re = 80$, $D/d = 5$.

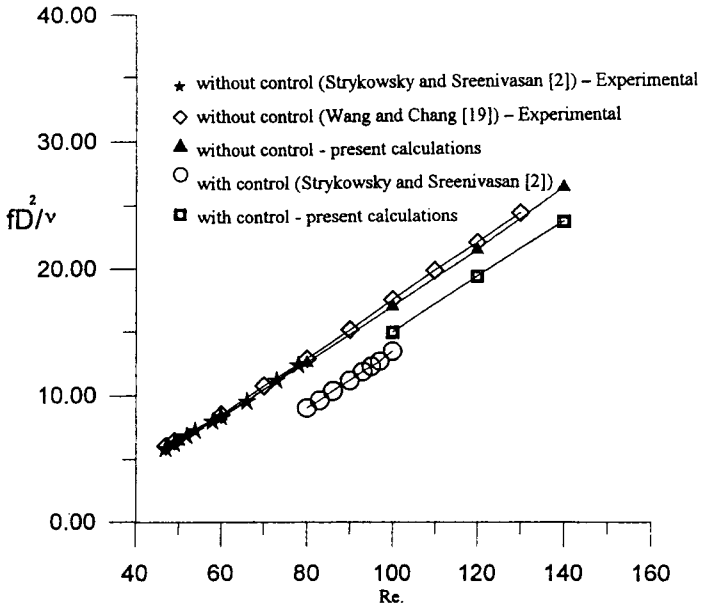


Fig. 21. Dimensionless shedding frequency for flow past a circular cylinder without and with control cylinder located at $x/D = 1.2$, and $y/D = 1$, $D/d = 10$.

This numerical study further explains the study of Strykowski and Sreenivasan [2] on the effect of a small control cylinder in the wake of a main circular cylinder. The temporal vortex shedding streamlines plotted reveal that the presence of the smaller cylinder reduces the growth rate of the disturbances and its suppression accompanied by the disappearance of the sharp spectral peaks, coincides with negative temporal growth rates. The presence of the control cylinder alters the stability of the flow and diverts small amount of fluid into the wake of the main cylinder. The position and size of the control cylinder are very important factors in the vortex shedding and suppression, for the given Reynolds number of the flow regime.

The reasons for the suppression of vortex shedding by a proper placement of a small control (second) cylinder in the near wake of the main cylinder are attributed to the redistribution of the vorticity in the shear layer, the fluid diversion between main and control cylinders to reduce the velocity gradients, as well as the pressure change between the two cylinders, as pointed out by Strykowsky and Sreenivasan [2]. Figs. 5 and 13 show the vorticity distributions without the control cylinder and with control cylinder, respectively. The concentrated vorticity in the shear layer behind the main cylinder is smeared and diffused by the proper placement of the control cylinder. The pressure distribution without the control cylinder and with control cylinder are shown in comparison in Figs. 4 and 12, respectively. The drastic reduction of pressure in the wake of main cylinder by the introduction of control cylinder suggests the mechanism for the suppression of vortex shedding.

## 6. Concluding remarks

A novel computational model has been developed to solve 2D incompressible viscous flow problems by the coupling of three-step FEM and BEM and used in the analysis of vortex shedding past circular cylinders at low Reynolds numbers. The model based on unsteady Navier–Stokes equations in primitive variables, is able to solve the infinite boundary value problems by extracting the boundary effects on a specified finite computation domain, using the projection method. In the model, the Navier–Stokes equations are solved using a three-step FEM and the Poisson-type pressure equations are solved using BEM. By coupling the FEM and BEM, the model is able to handle infinite domain problems efficiently.

The model has been efficiently applied to simulate vortex-shedding flow past a single circular cylinder and vortex shedding and suppression of flow past two circular cylinders in which one acts as a control cylinder, at low Reynolds number flow regime. Both the applications gave reasonable and satisfactory

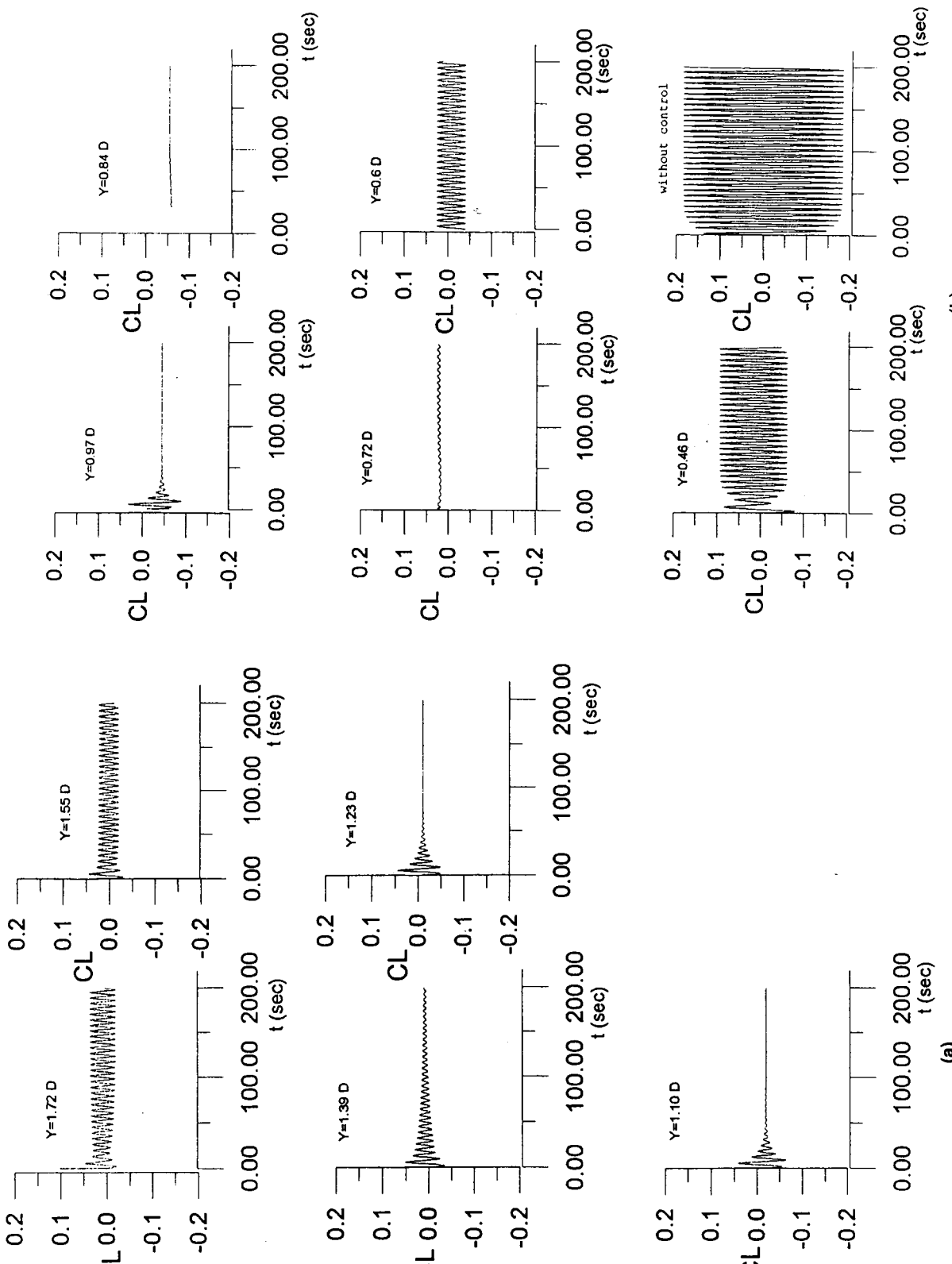


Fig. 22. (a) Variation of lift coefficient with various position of the control cylinder, $D/d = 4$, $x = 1.53D$, $Re = 80$. (b) Variation of lift coefficient with various position of the control cylinder, $D/d = 4$, $x = 1.53D$, $Re = 80$.

results comparable with the available experimental and numerical results in literature and show the feasibility and robustness of the present model.

## Acknowledgements

The support of the National Science Council, Taiwan, which made this research possible, is deeply appreciated.

## References

[1] P.W. Bearman, Vortex shedding from oscillating bluff bodies, Ann. Rev. Fluid Mech. 16 (1984) 195–222.
[2] P.J. Strykowski, K.R. Sreenivasan, On the formation and suppression of vortex shedding at low Reynolds numbers, J. Fluid Mech. 218 (1990) 71–107.
[3] M. Braza, P. Chassaing, H.H. Minh, Numerical study and physical analysis of the pressure and velocity fields in the near wake of a circular cylinder, J. Fluid Mech. 165 (1986) 79–139.
[4] R. Franke, W. Rodi, B. Schonung, Numerical calculation of laminar vortex shedding flow past cylinders, J. Wind Engrg. Ind. Aerodynamics 35 (1990) 237–257.
[5] Y. Lecointe, J. Piquet, Flow structure in the wake of an oscillating cylinder, J. Fluids Engrg., Trans. ASME 111 (1989) 139–148.
[6] C.P. Jackson, A finite-element study of the onset of vortex shedding in flow past variously shaped bodies, J. Fluid Mech. 182 (1987) 23–45.
[7] J.N. Reddy, D.K. Gartling, The Finite Element Method in Heat Transfer and Fluid Dynamics, CRC Press, London, 1992.
[8] C. Taylor, T.G. Hughes, Finite Element Programming of The Navier–Stokes Equations, Pineridge, Swansea, 1981.
[9] H. Power, L.C. Wrobel, Boundary Integral Methods in Fluid Mechanics, Computational Mechanics Publications, Southampton, 1995.
[10] T.E. Tezduyar, D.K. Ganjoo, Petrov–Galerkin formulations with weighting functions dependent upon spatial and temporal discretization: applications to transient convection-diffusion problems, Comput. Methods Appl. Mech. Engrg. 59 (1985) 249–271.
[11] J.A. Donea, Taylor–Galerkin method for convective transport problems, Int. J. Numer. Methods Fluids 20 (1984) 101–119.
[12] C.B. Jiang, M. Kawahara, The analysis of unsteady incompressible flows by a three-step finite element method, Int. J. Numer. Methods Fluids 16 (1993) 793–811.
[13] A.J. Chorin, Numerical solution of Navier–Stokes equations, Math. Comput. 22 (1968) 745–762.
[14] R. Temam, The Navier–Stokes Equations, Elsevier, Amsterdam, 1984.
[15] D.L. Young, C.B. Liao, H.J. Sheen, Computations of recirculation zones of a confined annular swirling flow, Int. J. Numer. Methods Fluids 29 (1999) 791–810.
[16] J.A. Liggett, Fluid Mechanics, McGraw-Hill, New York, 1994.
[17] J.N. Reddy, Finite Element Method, McGraw-Hill, New York, 1993.
[18] C.A. Brebbia, J.C.F. Telles, L.C. Wrobel, Boundary Element Techniques – Theory and Applications in Engineering, Springer, Berlin, 1984.
[19] P.M. Gresho, S.T. Chan, R.L. Lee, C.D. Upson, A modified finite element method for solving the time-dependent, incompressible Navier–Stokes equations part 2: application, Int. J. Numer. Methods Fluids 4 (1984) 619–640.
[20] J. Li, M. Chambarel, M. Donneaud, R. Martin, Numerical study of laminar flow past one and two circular cylinders, Comput. Fluids 19 (2) (1991) 155–170.
[21] A.B. Wang, Y.C. Chang, Experimental investigations of suppression of vortex shedding from a circular cylinder, Trans. Aeronaut. Astronaut. Soc. Republic of China 28 (3) (1996) 249–254.
[22] H. Sakamoto, H. Haniu, Optimum suppression of fluid forces acting on a circular cylinder, J. Fluids Engrg., Trans. ASME 116 (1994) 221–227.

INTERNATIONAL JOURNAL FOR NUMERICAL METHODS IN FLUIDS
*Int. J. Numer. Meth. Fluids* 2001; **37**: 657–689 (DOI: 10.1002/fld.187)

# Numerical simulation of high-Reynolds number flow around circular cylinders by a three-step FEM–BEM model

D. L. Young*[,1], J. L. Huang and T. I. Eldho

*Department of Civil Engineering and Hydrotech Research Institute, National Taiwan University, Taipei, Taiwan, ROC*

## SUMMARY

An innovative computational model, developed to simulate high-Reynolds number flow past circular cylinders in two-dimensional incompressible viscous flows in external flow fields is described in this paper. The model, based on transient Navier–Stokes equations, can solve the infinite boundary value problems by extracting the boundary effects on a specified finite computational domain, using the projection method. The pressure is assumed to be zero at infinite boundary and the external flow field is simulated using a direct boundary element method (BEM) by solving a pressure Poisson equation. A three-step finite element method (FEM) is used to solve the momentum equations of the flow. The present model is applied to simulate high-Reynolds number flow past a single circular cylinder and flow past two cylinders in which one acts as a control cylinder. The simulation results are compared with experimental data and other numerical models and are found to be feasible and satisfactory. Copyright © 2001 John Wiley & Sons, Ltd.

KEY WORDS: boundary elements; finite elements; incompressible viscous flow; Navier–Stokes equations; vortex shedding suppression

## 1. INTRODUCTION

The vortex shedding phenomena from bluff bodies like circular cylinders are commonly considered as the main source that causes the flow induced vibrations, noises, and even collapse of a body in an external flow. The study of the vortex shedding over a circular cylinder and suppression of fluid forces has received much attention, since practical applications are expected in various areas of engineering such as high-rise buildings analysis, wind engineering, aeronautics, etc. The major difficulty in simulating the vortex shedding and fluid force on the bluff bodies in external flow fields lies in setting the boundary conditions of the computational domain to simulate the external flow that has infinite domain.

* Correspondence to: Department of Civil Engineering, National Taiwan University, Taipei, Taiwan 10617, ROC.
[1] E-mail: dlyoung@hy.ntu.edu.tw

Copyright © 2001 John Wiley & Sons, Ltd.

*Received July 2000*
*Accepted February 2001*

Even though a large number of experimental studies have been reported on laminar vortex shedding flows (for example, Reference [1]) at low Reynolds number, investigations in unsteady flow field at high Reynolds number are rather limited due to the difficulties involved in unsteady flow measurements, with rare exceptions such as the works of Cantwell and Coles [2] and Sakamato and Haniu [3]. Many methods have been developed to suppress vortex shedding and to reduce the fluid forces over circular cylinders [4]. Recently, Strykowsky and Sreenivasan [1] reported that vortex shedding can be suppressed by introducing small diameter control cylinders at a low Reynolds number flow regime, and Sakamato and Haniu [3] succeeded in reducing the fluid forces acting on a circular cylinder at comparatively large Reynolds numbers with the introduction of a control cylinder near the main cylinder. The aim of the present work is the numerical investigation of the flow around a main cylinder and the reduction of the fluid forces around the main cylinder by introducing a control cylinder at various positions, using an innovative numerical scheme.

Numerical simulations of vortex shedding flow past bluff bodies have been performed by many researchers with the use of the finite volume method (FVM), finite difference method (FDM), finite element method (FEM) or the boundary element method (BEM). Braza *et al.* [5] and Franke *et al.* [6] used the FVM and analyzed the vortex shedding past circular cylinders and square cylinders in a laminar flow regime. Using FDM, Lecointe and Piquet [7] calculated the flow around circular cylinders using the stream function–vorticity approach. A Galerkin FEM has been used by Jackson [8] to study vortex shedding in flow past variously shaped bodies by solving steady state equations. FEM and BEM have been widely in use for the solution of various fluid dynamics problems in the last two decades. For the solution of different forms of Navier–Stokes equations, the use of FEM [9,10] and BEM [11] has been described by various researches.

In FEM, it is well known that the conventional Galerkin finite element scheme leads to spurious oscillatory solutions for fluid dynamics problems at high Reynolds numbers. To overcome such oscillation and numerical dissipation, various upwind schemes have been successfully presented by researchers. In the finite element approximation, the upwind schemes have been developed by the use of schemes based on the Petrov–Galerkin [12–14] or the Taylor–Galerkin methods [15]. Jiang and Kawahara [16] recently developed a three-step finite element scheme for the unsteady incompressible viscous flows, based on the Taylor–Galerkin schemes.

In this paper, a new computational model is presented to solve the high-Reynolds number flow past bluff bodies in external flow fields. The model, based on transient Navier–Stokes equations, can solve the infinite boundary value problems by extracting the boundary effects on a specified finite computational domain, using the projection method [17]. A three-step FEM is used to solve the momentum equations of the flow. The pressure Poisson equation for the external flow field is treated by the BEM and then coupled with the three-step FEM scheme. The feasibility of the developed numerical scheme in the application of high-Reynolds number flows has been illustrated by applying the model to simulate high-Reynolds number flow past a single circular cylinder, and flow past two cylinders in which one acts as a control cylinder. The simulation results are compared with some experimental data and other numerical models and are found to be feasible and satisfactory.

Copyright © 2001 John Wiley & Sons, Ltd. 

After presenting the governing equations, the numerical formulation using coupled BEM and three-step FEM are briefly described. Then the solution procedure and numerical results for two case studies of high-Reynolds number flow around a single circular cylinder and flow around two cylinders in which one acts as a control cylinder, are presented and followed by a few concluding remarks.

## 2. GOVERNING EQUATIONS

The governing equations of the motion of an incompressible viscous fluid flow can be expressed by the Navier–Stokes equations and continuity equation and written in Cartesian tensor notation as follows:

$$\frac{\partial u_i}{\partial x_i} = 0 \tag{1}$$

$$\frac{\partial u_i}{\partial t} + \frac{u_j \partial u_i}{\partial x_j} = -\frac{1}{\rho}\frac{\partial p}{\partial x_i} + \nu \frac{\partial^2 u_i}{\partial x_j \partial x_j} + f_i \tag{2}$$

where $u_i$, $i = 1, 2$, are two components of the velocity vector in the $x$-, $y$-directions, $p$ is pressure, $\nu$ is kinematic viscosity, $t$ is time, $\rho$ is mass density, $f_i = \rho g l_i$ are body forces in the $x$-, $y$-directions, $g$ is gravitational acceleration and $l_i$ are direction cosines in the $x$- and $y$-directions. Using the following dimensionless forms of the variables:

$$x^* = x/D, \quad y^* = y/D, \quad u^* = u/u_0, \quad v^* = v/u_0, \quad t^* = tu_0/D, \quad p^* = p/\rho u_0^2 \tag{3}$$

where $D$ is a characteristic length and $u_0$ is a characteristic velocity. Now Equations (1) and (2) can be written as

$$\frac{\partial u_i^*}{\partial x_i^*} = 0 \tag{4}$$

$$\frac{\partial u_i^*}{\partial t^*} + \frac{u_j^* \partial u_i^*}{\partial x_j^*} = -\frac{\partial p^*}{\partial x_i^*} + \frac{1}{Re}\frac{\partial^2 u_i^*}{\partial x_j^* \partial x_j^*} + \frac{l_i}{Fr^2} \tag{5}$$

where $Re = u_0 D/\nu$ is the Reynolds number and $Fr = u_0/(gD)^{1/2}$ is the Froude number. Dropping the asterisk from the dimensionless variables in the following equations for brevity and putting the body force terms into the pressure field for neglecting the free surface effects, the non-dimensionalized governing equations for (1) and (2) can be written as

$$\frac{\partial u_i}{\partial x_i} = 0 \tag{6}$$

Copyright © 2001 John Wiley & Sons, Ltd.

$$\frac{\partial u_i}{\partial t}+\frac{u_j\,\partial u_i}{\partial x_j}=-\frac{\partial p}{\partial x_i}+\frac{1}{Re}\left(\frac{\partial^2 u_i}{\partial x_j\,\partial x_j}\right) \tag{7}$$

Generally used boundary conditions are the prescribed velocities

$$u=u_0, \qquad v=v_0 \tag{8}$$

and the non-slip boundary conditions. At the initial time, some known values of velocities and pressure can be prescribed as initial conditions.

As far as external flows are concerned, the outer boundaries are located at the infinity. In numerical computations, due to the limitations of computational facilities, it is assumed that the computational domain is limited to the finite region. In the present analysis we assume that

$$\nabla^2 p=0 \tag{9}$$

is valid out of the finite computational domain. As a consequence, only the inflow boundary condition is needed as the boundary requirement of the computational domain. A sample computational domain for the type of problem that will be considered in the present study is shown in Figure 1 with boundary conditions. The boundary condition of the fixed body in the flow is set as a no-slip boundary.

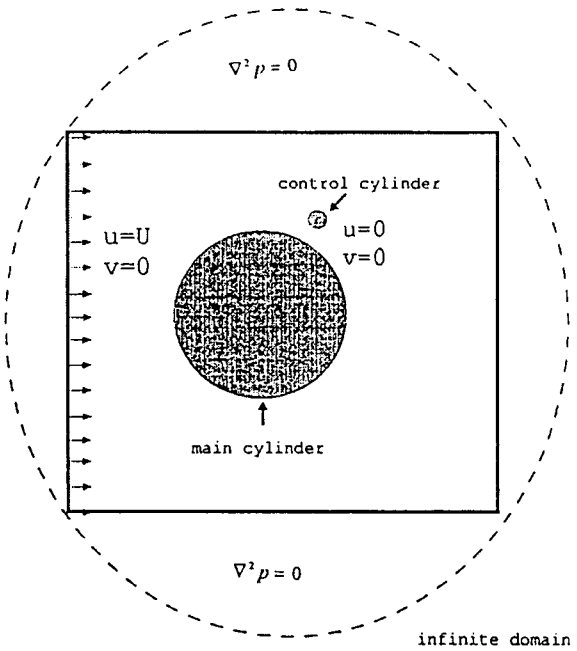


Figure 1. Computational domain and boundary conditions for a typical problem.

Copyright © 2001 John Wiley & Sons, Ltd.

## 3. NUMERICAL FORMULATION

As mentioned earlier, in the present model, a coupled three-step FEM–BEM approach is used in the solution of the governing differential equations. In this section, the numerical formulation is briefly described.

### *3.1. Three-step FEM formulation for momentum equations*

In the present model, the mass–momentum Navier–Stokes equations are approximated using an explicit three-step FEM based on a Taylor series expansion in time [16]. From Taylor's series, a function $h$ in time can be represented as

$$h(t+\Delta t) = h(t) + \Delta t \frac{\partial h(t)}{\partial t} + \frac{\Delta t^2}{2}\frac{\partial^2 h(t)}{\partial t^2} + \frac{\Delta t^3}{6}\frac{\partial^3 h(t)}{\partial t^3} + O(\Delta t^4) \tag{10}$$

Approximating Equation (10) up to third-order accuracy, the three-step formulation can be written as

$$h\left(t+\frac{\Delta t}{3}\right) = h(t) + \frac{\Delta t}{3}\frac{\partial h(t)}{\partial t} \tag{11}$$

$$h\left(t+\frac{\Delta t}{2}\right) = h(t) + \frac{\Delta t}{2}\frac{\partial h(t+\Delta t/3)}{\partial t} \tag{12}$$

$$h(t+\Delta t) = h(t) + \Delta t \frac{\partial h(t+\Delta t/2)}{\partial t} \tag{13}$$

When Equations (11)–(13) are discretized using the standard Galerkin FEM and the resulting finite element equations are solved using the Jacobian iteration, the three-step FEM is obtained [16]. This method has all the advantages of the Taylor–Galerkin method and is stable while solving the convective transport equations.

From the above scheme, using a projection method of the Navier–Stokes equations [17], one can convert Equation (7) in the following steps:

Step 1

$$\frac{u_i^{n+1/3} - u_i^n}{\Delta t/3} = -u_j^n \frac{\partial u_i^n}{\partial x_j} - \frac{\partial p^n}{\partial x_i} + \frac{1}{Re}\nabla^2 u_i^n \tag{14}$$

Step 2

$$\frac{u_i^{n+1/2} - u_i^n}{\Delta t/2} = -u_j^{n+1/3} \frac{\partial u_i^{n+1/3}}{\partial x_j} - \frac{\partial p^n}{\partial x_i} + \frac{1}{Re}\nabla^2 u_i^{n+1/3} \tag{15}$$

Copyright © 2001 John Wiley & Sons, Ltd.

Step 3

$$\frac{u_i^* - u_i^n}{\Delta t} = -u_j^{n+1/2}\frac{\partial u_i^{n+1/2}}{\partial x_j} + \frac{1}{Re}\nabla^2 u_i^{n+1/2} \tag{16}$$

where $u_i^*$ is the apparent velocity. Combining the continuity equation (6) and taking the gradient of Equation (16), the pressure Poisson equation is derived to correct the velocity equation as

$$\nabla^2 p^{n+1} = \frac{1}{\Delta t}\left(\frac{\partial u_i^*}{\partial x_i}\right) \tag{17}$$

Now the present velocity can be derived as

$$u_i^{n+1} = u_i^* - \Delta t\frac{\partial p^{n+1}}{\partial x_i} \tag{18}$$

Spatial discretization of Equations (14)–(16) are performed by the standard Galerkin method using four-point bilinear elements [9]. The resulting finite element equations can be expressed as

For step 1

$$M_{ij}\frac{\vec{u}_j^{n+1/3} - \vec{u}_j^n}{\Delta t/3} = -A_{ij}^n\vec{u}_j^n - \vec{B}_{ij}p_j^n - \frac{1}{Re}S_{ij}\vec{u}_j^n + \int_{\partial\Omega}\frac{N_i}{Re}\left(\frac{\partial\vec{u}^n}{\partial n}\right)\mathrm{d}S \tag{19}$$

For step 2

$$M_{ij}\frac{\vec{u}_j^{n+1/2} - \vec{u}_j^n}{\Delta t/2} = -A_{ij}^{n+1/3}\vec{u}_j^{n+1/3} - \vec{B}_{ij}p_j^n - \frac{1}{Re}S_{ij}\vec{u}_j^{n+1/3} + \int_{\partial\Omega}\frac{N_i}{Re}\left(\frac{\partial\vec{u}^{n+1/3}}{\partial n}\right)\mathrm{d}S \tag{20}$$

For step 3

$$M_{ij}\frac{\vec{u}_j^* - \vec{u}_j^n}{\Delta t} = -A_{ij}^{n+1/2}\vec{u}_j^{n+1/2} - \frac{1}{Re}S_{ij}\vec{u}_j^{n+1/2} + \int_{\partial\Omega}\frac{N_i}{Re}\left(\frac{\partial\vec{u}^{n+1/2}}{\partial n}\right)\mathrm{d}S \tag{21}$$

Equations (18) can be discretized as

$$M_{ij}\vec{u}_n^{n+1} = M_{ij}\vec{u}_j^* - \Delta t\vec{B}_{ij}p_j^{n+1} \tag{22}$$

where

$$M_{ij} = \int_\Omega N_i N_j\,\mathrm{d}\Omega$$

Copyright © 2001 John Wiley & Sons, Ltd. 

$$A_{ij}^n = \int_\Omega N_i \left( u_k^n \frac{\partial N_j}{\partial x_k} \right) \mathrm{d}\Omega$$

$$\vec{B}_{ij} = \int_\Omega N_i \frac{\partial N_j}{\partial x_k} \mathrm{d}\Omega$$

$$S_{ij} = \int_\Omega \left( \frac{\partial N_i}{\partial x_k} \frac{\partial N_j}{\partial x_k} \right) \mathrm{d}\Omega$$

in which $N_i$ and $N_j$ are the shape functions and arrows stand for the two components associated with the $x$- and $y$-directions.

After assembling the system and applying the boundary conditions, the system of equations are solved using the Jacobian iterative scheme.

### *3.2. BEM formulation for pressure Poisson equation*

Consider the Poisson type pressure equation in $p$ and $u_i^*$, Equation (17)

$$\nabla^2 p = \frac{1}{\Delta t} \left( \frac{\partial u_i^*}{\partial x_i} \right) = b \tag{23}$$

with pressure boundary conditions as

$$\bar{p} = p_0 \quad \text{on } \Gamma_1, \qquad \bar{q} = \frac{\partial p_o}{\partial n} \quad \text{on } \Gamma_2 \tag{24}$$

where $n$ is the unit outward normal vector. In the present model, an iterative scheme is used such that the velocity $u_i^*$ is known in the current iteration and time step from the previous step by solving the Navier–Stokes equations.

A weighting function $p^*$ can now be introduced such that it has continuous first derivatives within the domain. The following weighted residual statement can now be written:

$$\int_\Omega (\nabla^2 p - b) p^* \, \mathrm{d}\Omega = \int_{\Gamma 2} (q - \bar{q}) p^* \, \mathrm{d}\Gamma - \int_{\Gamma 1} (p - \bar{p}) q^* \, \mathrm{d}\Gamma \tag{25}$$

where $q = \partial p / \partial n$ and $q^* = \partial p^* / \partial n$.

Let $p^*$ be the fundamental solution of the Laplace equation in two dimensions, represented as $p^* = -\ln r/(2\pi)$, where $r$ is the distance from the collocation point $(k)$ to other field points $(i)$ given as

$$r = \sqrt{(x_k - x_i)^2 + (y_k - y_i)^2} \tag{26}$$

Copyright © 2001 John Wiley & Sons, Ltd.

Now applying Green's second identity theorem to Equation (25) and using the standard boundary element procedure [18], we can get the boundary integral equation as

$$C_i p_i + \int_\Gamma pq^* \, d\Gamma + \int_\Omega bp^* \, d\Omega = \int_\Gamma qp^* \, d\Gamma \tag{27}$$

where $C_i$ is the Green's constant which can be calculated by surrounding the boundary point $i$ by a small circle of radius $\varepsilon$ and taking each term in Equation (27) in the limit as $\varepsilon \to 0$. Generally, $C_i$ can be represented as $\theta/(2\pi)$ where $\theta$ is the internal angle at point $i$ in radians.

In Equation (27), we have boundary integrals and domain integrals. In the present model, the domain integration is carried out by subdividing the domain into a series of internal cells, on each of which a numerical integration is performed. Here, linear elements are used for the boundary discretization and two-dimensional isoparametric quadrilateral cells are used for the internal discretization. The details of the element properties, shape functions, coordinate transformation and numerical integration used here are described in Brebbia *et al.* [18] which is not repeated here.

If the domain is discretized into $M$ internal cells, then the domain integral can be written as

$$D_i = \int_\Omega bp^* \, d\Omega = \sum_{e=1}^{M} \left[ \sum_{k=1}^{NI} w_k (bp^*)_k \right] \Omega_e \tag{28}$$

where the integral has been approximated by a summation over different cells ($e$ varies from 1 to $M$), $w_k$ are the Gauss integration weights, the function $(bp^*)_k$ needs to be evaluated at integration points $k$ on each cell ($k$ varies from 1 to $NI$, where $NI$ is the total number of integration points on each cell) and $\Omega_e$ is the area of cell $e$. The term $D_i$ is the result of the numerical integration and is different for each position $i$ of the boundary nodes.

Assuming that the boundary of the domain is discretized into NE linear elements with $N$ nodes, Equation (27) can be discretized and written in matrix form as

$$C_i p_i + \sum_{j=1}^{N} \bar{H}_{ij} p_j + D_i = \sum_{j=1}^{N} G_{ij} q_j \tag{29}$$

Combining the effect of the constant term $C$ with the $\bar{H}$ matrix, we can write the matrix system as

$$Hp + D = Gq \tag{30}$$

In Equation (30), the boundary conditions are introduced and the known values are taken to the right-hand side to form a system of linear equations of the form

$$Ab = F \tag{31}$$

Copyright © 2001 John Wiley & Sons, Ltd.

where $b$ is a vector of unknown boundary values of $p$ and $q$, and $F$ is a known vector. Equation (31) is solved using Gauss elimination scheme and all the boundary values will be then known. Once this is done, it is possible to calculate internal values of $p$ or its derivatives. The values of $p$ are calculated at any internal point using the Equation (27) that can be written in condensed form as

$$p_i = \int_\Gamma qp^* \, d\Gamma - \int_\Gamma pq^* \, d\Gamma - \int_\Omega bp^* \, d\Omega \tag{32}$$

The same discretization is used for the boundary integrals, that is

$$p_i = \sum_{j=1}^{N} G_{ij} q_j - \sum_{j=1}^{N} \bar{H}_{ij} p_j - D_i \tag{33}$$

where $i$ is an internal point.

The main advantage of using BEM in the solution of the pressure Poisson equation is the effectiveness of BEM to deal with infinite domain problems. Here, only the boundary conditions of pressure on the finite computational domain are known which is used to solve the infinite domain problem.

## 4. COMPUTATIONAL PROCEDURE

As mentioned earlier, here an iterative scheme is used in the solution of the Navier–Stokes equations. In most of the incompressible viscous flow problems solved using Navier–Stokes equations, the most natural boundary conditions arise when the velocity is prescribed all over the boundaries of the problem. As shown in Figure 1, the boundary condition of the fixed body in the flow is set as non-slip boundary. The computational procedure adopted here includes the following iterative steps:

For the time step $n = 1$,

1. Assume at infinite domain, pressure $p = 0$ and solve the pressure Laplace equation (Equation (9)) outside the computational domain and the pressure Poisson equation (Equation (17)) inside the computational domain together and get the pressure boundary conditions on the boundaries of the computational domain.
2. Solution of the Navier–Stokes equations using three-step FEM and projection method.
   - Solve for the unknown apparent velocity values (Equation (16)).
   - Calculate the pressure distribution for the current time step from the pressure Poisson equation (17) using BEM.
   - Determine the new velocity values by solving Equation (18).
3. Check for convergence of the velocity and pressure components in the present iteration, for example

$$\frac{|p_n^{k+1} - p_n^k|}{|p_n^k|} \leq 0.0001 \quad \text{and} \quad \frac{|u_n^{k+1} - u_n^k|}{|u_n^k|} \leq 0.0001$$

Copyright © 2001 John Wiley & Sons, Ltd.

If convergence criterion is satisfied, then proceed to the next step, otherwise go to step 1.

4. In the successive time step, use the velocity and pressure components from the previous time step as initial conditions and the new boundary flow conditions and use the iterative procedure, steps 1–3. The procedure is repeated until the prescribed time step is reached.

The coefficient of drag and the coefficient of lift on the solid body are found from the following equations

$$C_d = \frac{F_d}{\frac{1}{2}\rho u_o^2 D}, \qquad C_l = \frac{F_l}{\frac{1}{2}\rho u_o^2 D} \tag{34}$$

$$F_d = \oint_s p_s n_y \, ds - \oint_s \tau_s n_x \, ds \tag{35}$$

$$F_l = \oint_s p_s n_x \, ds + \oint_s \tau_s n_y \, ds \tag{36}$$

where $u_o$ is the fluid velocity, $F_d$ is the drag force, $\rho$ is the mass density, $D$ is the characteristic dimension, $F_l$ is the lift force, $\tau_s$ is the shear force acting on the body, $p_s$ is the pressure acting on the body, and $n_x$ and $n_y$ are the direction cosines in the $x$- and $y$-coordinates respectively.

## 5. MODEL APPLICATIONS

The proposed three-step FEM–BEM model has been applied on two test problems to verify the accuracy and feasibility of the model. The present model has been used to simulate the high-Reynolds number flow past a cylinder, and also in the case of suppression of fluid forces on two circular cylinders in which one acts as a control cylinder, in the range of Reynolds number 65000 to $10^7$.

### *5.1. High-Reynolds number flow past a single circular cylinder*

Even though a large number of experimental and numerical studies have been reported on the flow across a fixed circular cylinder in the laminar flow regime [1,5,8,15,19], only a few studies have been reported on the high-Reynolds number flow across a circular cylinder [2,3,13,14]. Here, the present three-step FEM–BEM model has been applied for the simulation of high-Reynolds number flow past a fixed circular cylinder and the results are compared with the available experimental and numerical results. The present model was tested by simulating flow past a circular cylinder at a large range of Reynolds numbers of $Re = 65000$, $10^6$ and $10^7$. Figure 1 shows the computational domain with boundary conditions (in this case, no control cylinder). It is 20 units long (cylinder diameter is unity) and 14 units wide approximately.

Copyright © 2001 John Wiley & Sons, Ltd. 

Four different meshes are used in the analysis depending on the Reynolds number. The meshes used are: mesh A, with 5568 elements and 5750 nodes; mesh B, with 4056 elements and 4186 nodes; mesh C, with 5784 elements and 5914 nodes (size of element near to the cylinder is 0.00875); mesh D, with 5784 elements and 5914 nodes (size of element near to the cylinder is 0.00027). A zoomed view of the typical mesh near to the cylinder (mesh D) is shown in Figure 2. The domain of computation was wide enough to encompass the range of the vortex shedding and fluid forces. The boundary conditions were chosen as $u = 1$, $v = 0$ at the inlet and a non-slip boundary $u = 0$, $v = 0$ on the cylinder surface. The model was run in unsteady condition.

Initially, a simulation has been performed at a high Reynolds number of 65000. For this simulation, mesh B described earlier is used and a time step of 0.02 is used. The velocity, pressure and vorticity are estimated at time $t = 200$. Figure 3(a) shows the velocity field and Figure 3(b) shows the pressure field for the Reynolds number 65000 at $t = 200$. The vorticity distribution around the cylinder is depicted in Figure 3(c). Figure 3(d) shows the streamlines for the circular cylinder. The time evolution of the coefficients of drag and lift are plotted in Figures 4 and 5 respectively. Further analysis has been carried out for flow at $Re = 10^6$ and $10^7$. For the simulation with $Re = 10^6$, mesh C described earlier is used and a time step of 0.0001 is adopted. For the simulation with $Re = 10^7$, mesh D described earlier is used and a time step of 0.00001 is used. Figure 6(a)–(c) shows the pressure field, vorticity distribution and

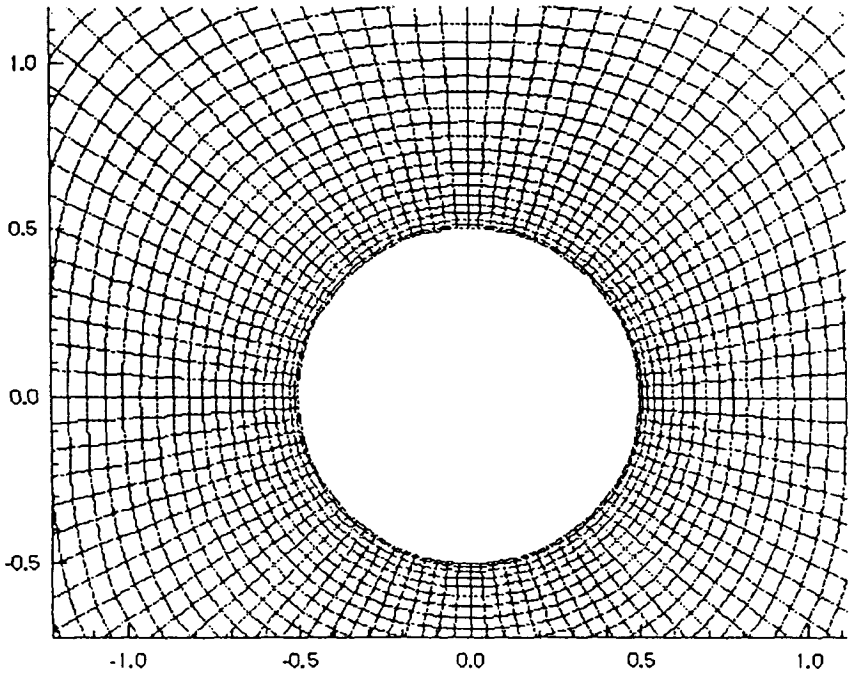


Figure 2. Zoomed view of the mesh for the computational domain—case 1.

Copyright © 2001 John Wiley & Sons, Ltd.

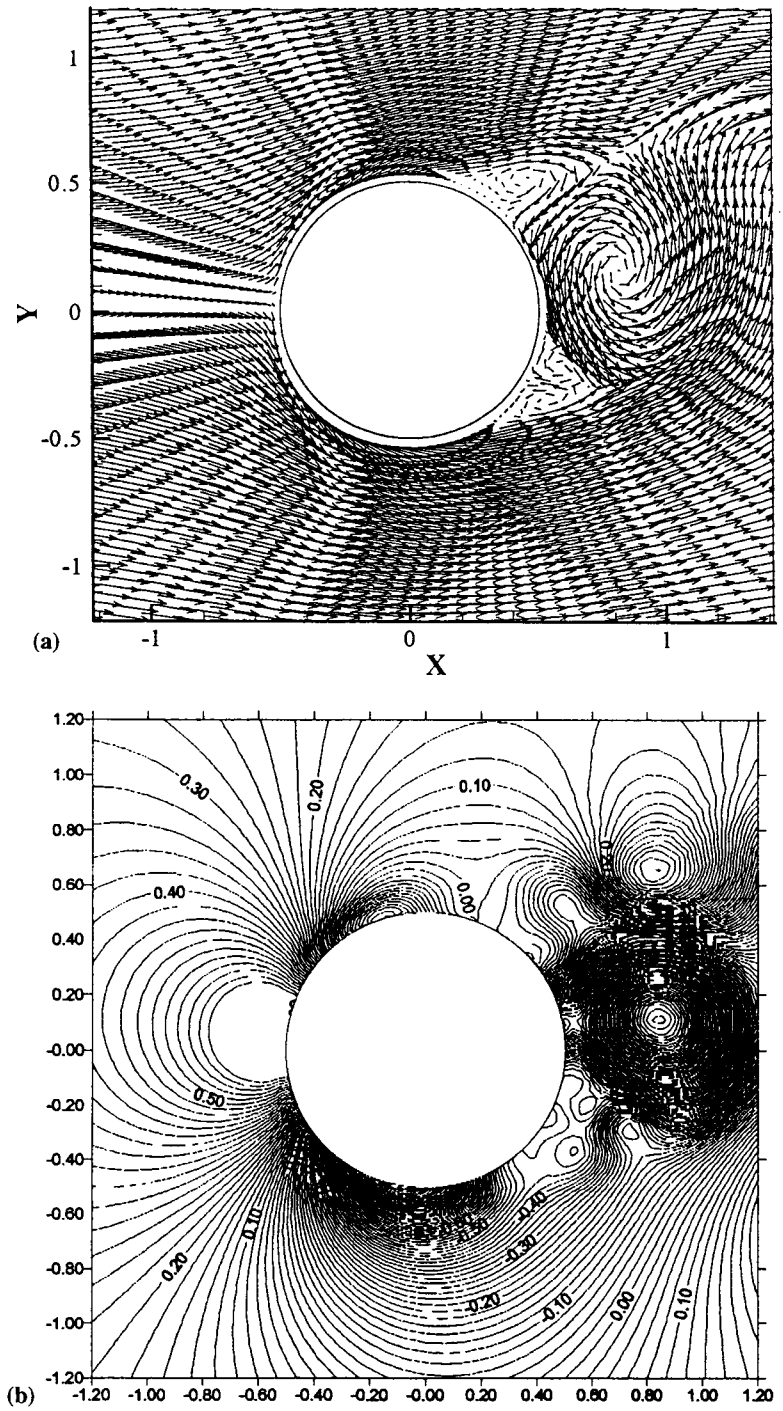


Figure 3. (a) Velocity field for flow around a circular cylinder, $Re = 6.5 \times 10^4$, $t = 200$. (b) Pressure field for flow around a circular cylinder, $Re = 6.5 \times 10^4$, $t = 200$. (c) Vorticity distribution for flow around a circular cylinder, $Re = 6.5 \times 10^4$, $t = 200$. (d) Streamline distribution for flow around a circular cylinder, $Re = 6.5 \times 10^4$, $t = 200$.

Copyright © 2001 John Wiley & Sons, Ltd.

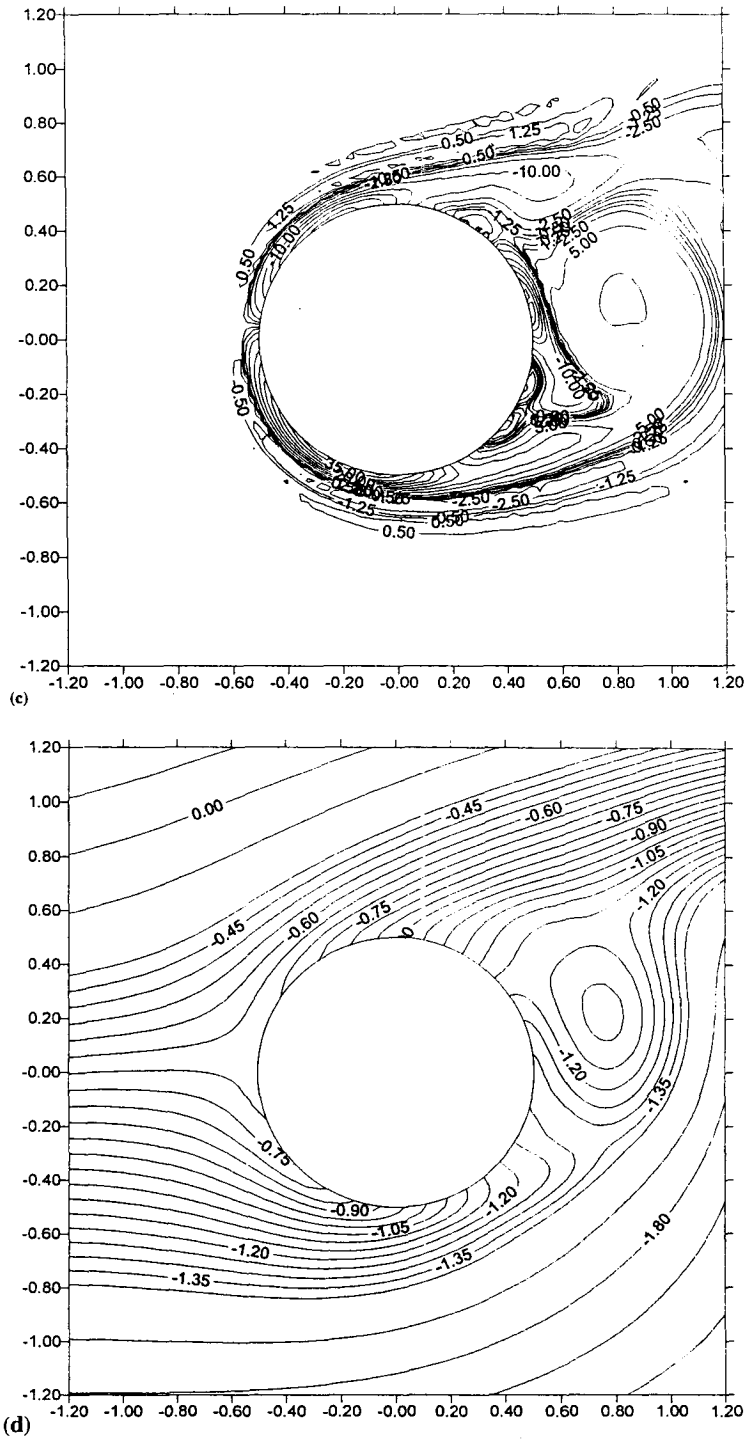


Figure 3 (*Continued*)

Copyright © 2001 John Wiley & Sons, Ltd.

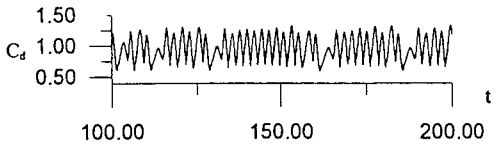


Figure 4. Time behavior of drag coefficient for flow across a circular cylinder, $Re = 6.5 \times 10^4$.

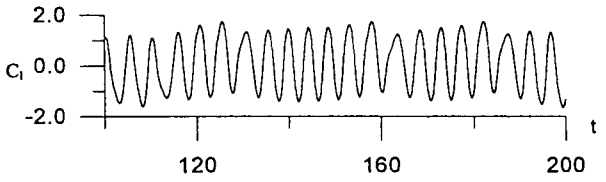


Figure 5. Time behavior of lift coefficient for flow across a circular cylinder, $Re = 6.5 \times 10^4$.

streamlines respectively for the Reynolds number $10^6$ at time $t = 22$. Figure 7(a)–(c) shows the pressure field, vorticity distribution and streamlines respectively for the Reynolds number $10^7$ at time $t = 0.4$. These figures clearly show the effect of increase in Reynolds number in the flow regime and the applicability of the present model to simulate flow past a circular cylinder at very high Reynolds numbers.

Figure 8 shows the variation of the coefficient of drag with respect to Reynolds numbers for various meshes mentioned earlier. The results are compared with the experimental results of Cantwell and Coles [2] and numerical results of Kakuda and Tosaka [13], Kondo [14], Tamura and Kuwahara [20] and Chang [21]. The results from the present model are generally in fairly good agreement with the other model results. The vortex shedding and fluid forces analysis in the case of the single circular cylinder is used further in the fluid force suppression analysis in the next case study by introducing a control cylinder.

For very high-Reynolds number flows past a smooth boundary such as a cylinder, the flow becomes a very interesting and challenging one, namely, the triple-deck like phenomena, as discussed by Stevertson [22] for flat plates and by Smith *et al.* [23] for smooth humps. There are three distinct decks (if we consider a cross section through the center of the cylinder), the inviscid irrotational upper deck, the inviscid rotational middle deck and the viscous rotational low deck [22]. Physically, the flow phenomena in the three decks could be analyzed by solving the potential, Euler and Navier–Stokes equations respectively. As pointed out by Smith *et al.* [23], the distinction between these three decks are rather difficult in reality. However, by using the Navier–Stokes equations solver of the present study, it is possible to observe the triple-deck like phenomena around a cylinder at very high Reynolds number. Combining Figures 6 and 7 for $Re = 10^6$ to $10^7$, especially the vorticity distributions of Figures 6(b) and 7(b), and streamlines of Figures 6(c) and 7(c), the middle and lower decks are almost confined to the boundary of the cylinder, leaving the upper deck behaving like a potential flow.

Copyright © 2001 John Wiley & Sons, Ltd.

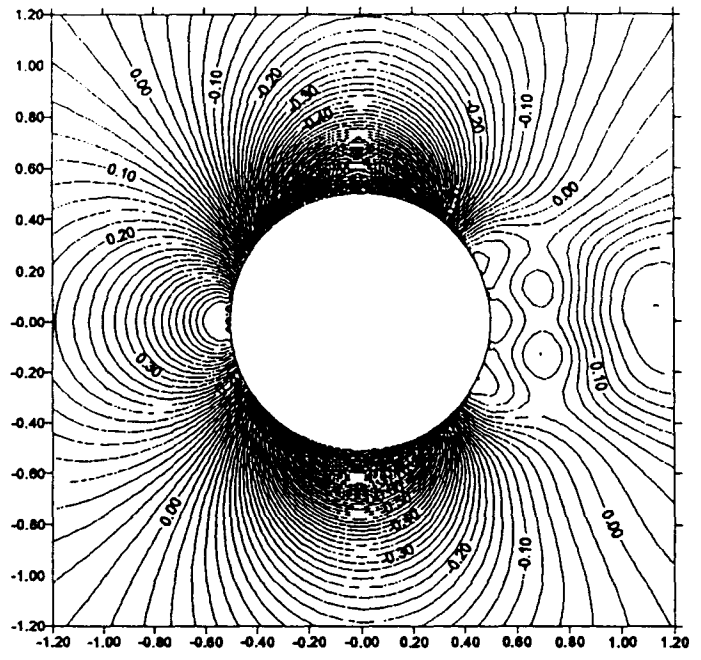


(a)

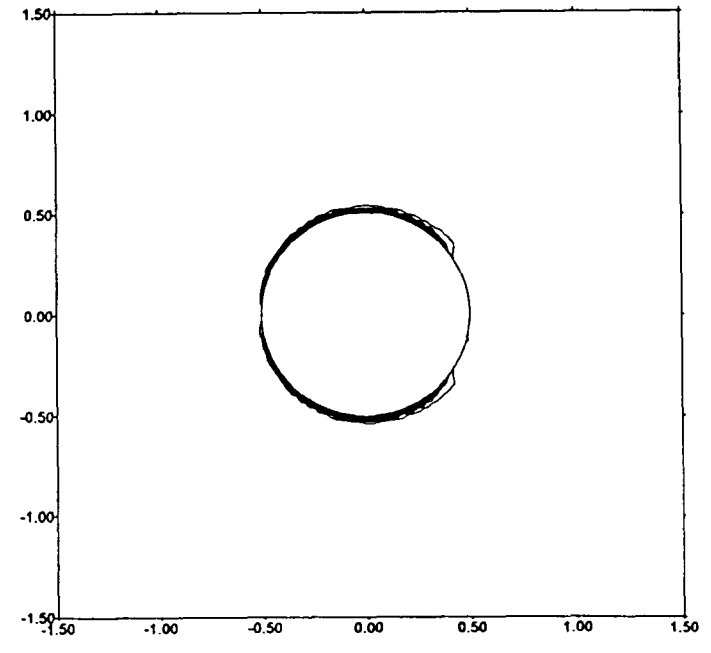


(b)

Figure 6. (a) Pressure field for flow around a circular cylinder, $Re = 10^6$, $t = 22$. (b) Vorticity distribution for flow around a circular cylinder, $Re = 10^6$, $t = 22$. (c) Streamline distribution for flow around a circular cylinder, $Re = 10^6$, $t = 22$.

Copyright © 2001 John Wiley & Sons, Ltd.

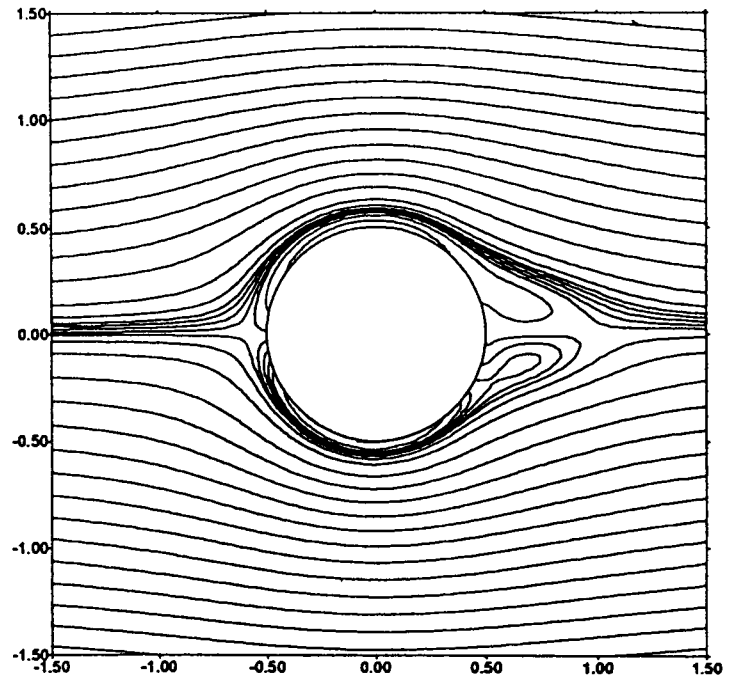

(c)

Figure 6 (*Continued*)

*5.2. Suppression of flow past a circular cylinder with a control cylinder at high Reynolds numbers*

In this case study, the model is applied to investigate the effect of a control cylinder in the vicinity of a main circular cylinder in a uniform flow field, which suppresses the fluid forces by the main circular cylinder. Recently, Sakamoto and Haniu [3] showed experimentally that the vortex shedding behind a circular cylinder can be suppressed at high Reynolds numbers using an appropriately placed small control cylinder. In this case study, the vortex alteration and suppression are investigated numerically using the three-step FEM–BEM model at a high Reynolds number of 65000.

Here, the same problem described in previous case study (Section 5.1) is used but a small circular cylinder (of size $d/D = 0.06$, where $D$ is the diameter of the main cylinder and $d$ is the diameter of the control cylinder) is placed at various positions, and its effects on the fluid forces on the main cylinder are numerically analyzed. A sample of zoomed discretization near the circular cylinders with the main cylinder and control cylinder is shown in Figure 9. The domain is discretized using 4060 elements and 4193 nodes. Figure 10 shows the definition of the coordinate system used in the present study. The control cylinder is placed at a position of $G/d = 2$ (refer to Figure 10) above the middle centerline of the main cylinder with $\alpha$ angles (0°–180°) and its effect on the fluid flow at an interval of 15° is investigated. The diameter of the control cylinder and the $G/d$ position are chosen according to the values used by Sakamoto and Hainu [3].

Copyright © 2001 John Wiley & Sons, Ltd. 

Initially, the effect of the control cylinder placed at 30° is analyzed. The velocity, pressure and vorticity of the main cylinder in the presence of the control cylinder are estimated at time $t = 200$ ($\Delta t = 0.02$). Figure 11(a) shows the velocity field and Figure 11(b) depicts the pressure field at time $t = 200$. The vorticity distribution around the cylinder is depicted in Figure 11(c). Figure 11(d) shows the streamlines for the circular cylinder. These figures show the salient features of the effect of the control cylinder in the flow regime of the main circular cylinder in comparison with the flow field described in the first case (Section 5.1). From these figures, it can be easily observed that there is a significant change in the vortex shedding and fluid forces due to the influence of the control cylinder.

To investigate the effects of various positions of the control cylinder on the vortex shedding for the selected size of the control cylinder and $G/d = 2$, numerical analyses have been carried out by placing the control cylinder at various positions. Figure 12(a)–(d) shows the velocity field, pressure distribution, vorticity distribution and streamlines for a 45° position of the control cylinder at time $t = 70$ ($\Delta t = 0.005$). Figure 13 illustrates the pressure distribution for a 90° position of the cylinder at time $t = 100$ ($\Delta t = 0.01$). Figure 14(a)–(d) exhibits the velocity field, pressure distribution, vorticity distribution and stream lines for a 120° position of the control cylinder at time $t = 100$ ($\Delta t = 0.01$), and Figure 15 shows the pressure distribution for

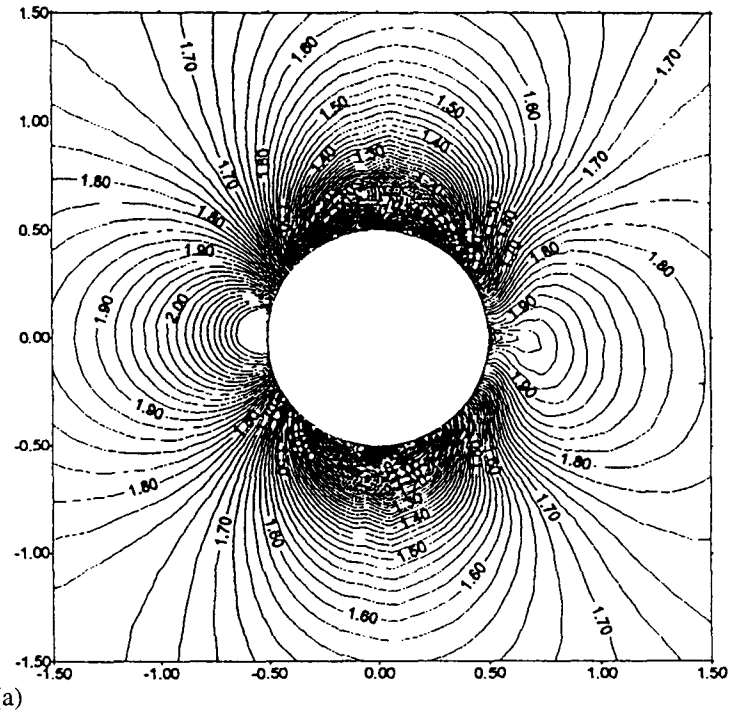


(a)

Figure 7. (a) Pressure field for flow around a circular cylinder, $Re = 10^7$, $t = 0.4$. (b) Vorticity distribution for flow around a circular cylinder, $Re = 10^7$, $t = 0.4$. (c) Streamline distribution for flow around a circular cylinder, $Re = 10^7$, $t = 0.4$.

Copyright © 2001 John Wiley & Sons, Ltd.

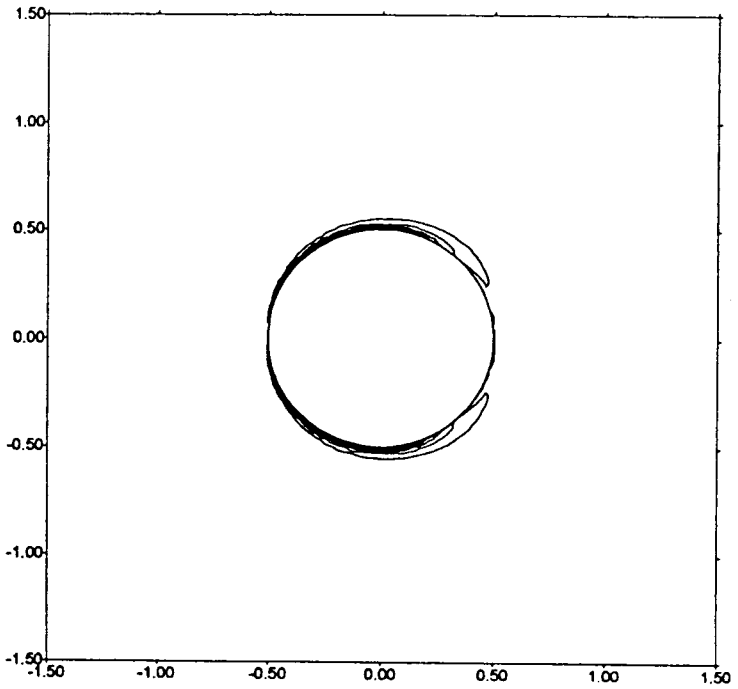


(b)

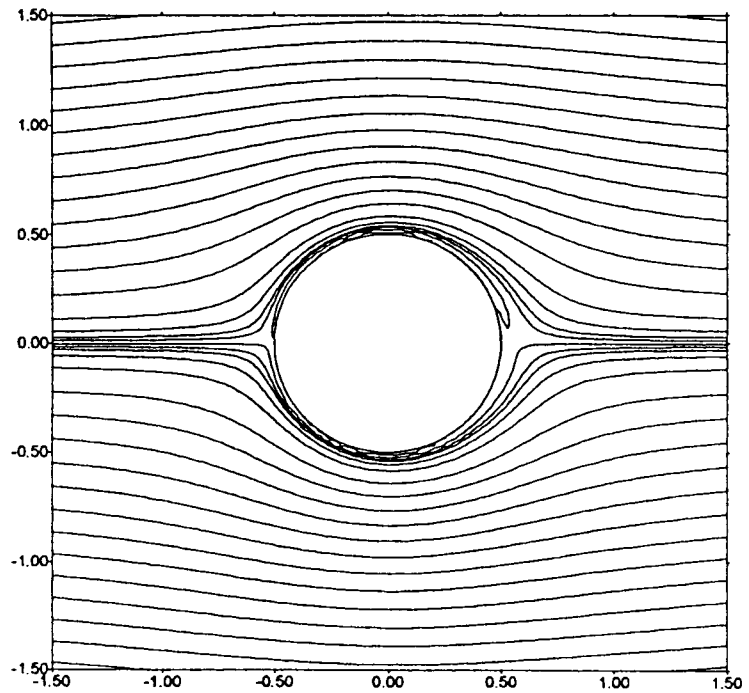


(c)

Figure 7 (*Continued*)

Copyright © 2001 John Wiley & Sons, Ltd.

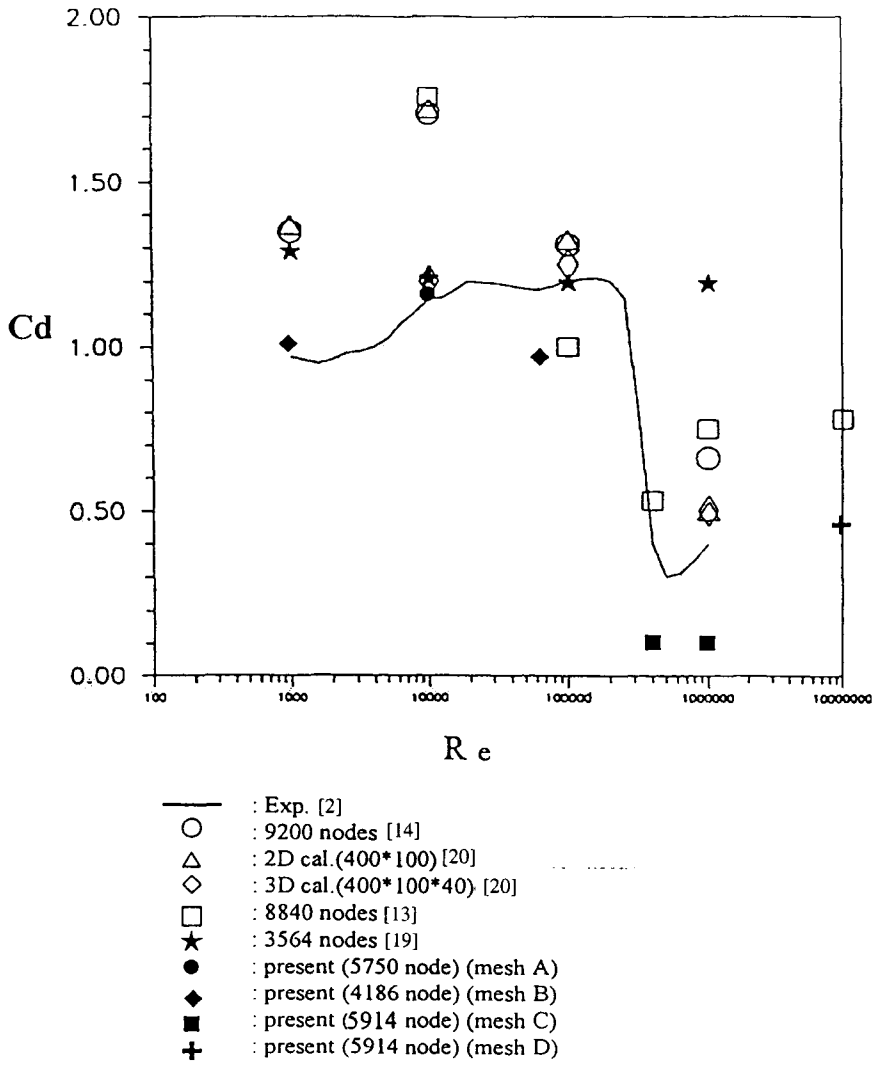


Figure 8. Drag coefficient variation with reference to Reynolds number.

a 150° position of the control cylinder at time $t = 100$ ($\Delta t = 0.01$). It is very clear that the vortex-shedding pattern considerably changes with the variation in the position of the control cylinder.

The method of quantifying the changes in fluid forces occurring due to the introduction of the control cylinder in the wake is by monitoring the drag and lift forces on the main cylinder. Figure 16 shows the ratio of coefficient of drag ($C_{dc}$) due to the control cylinder to the drag coefficient ($C_{dn}$) without the control cylinder for various positions of the control cylinder. Figure 17 shows the ratio of the root mean square (r.m.s.) value of the coefficient of lift ($C_{lfc}$)

Copyright © 2001 John Wiley & Sons, Ltd.

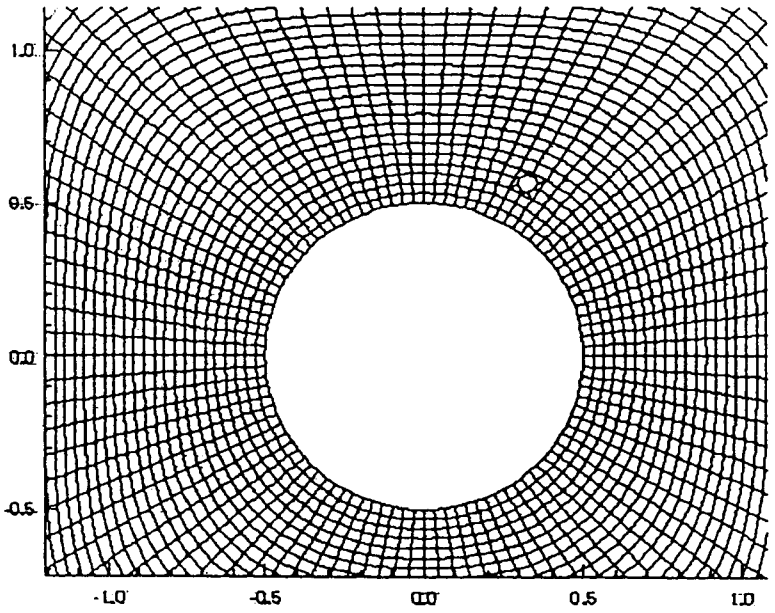


Figure 9. Zoomed view of the mesh for the computational domain—case 2.

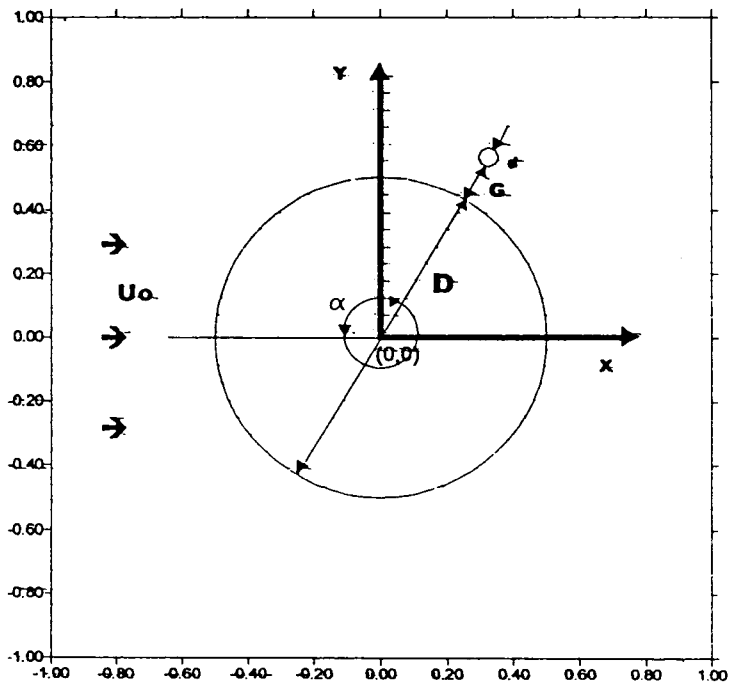


Figure 10. Definition sketch and coordinate position of the main and control cylinders.

Copyright © 2001 John Wiley & Sons, Ltd.

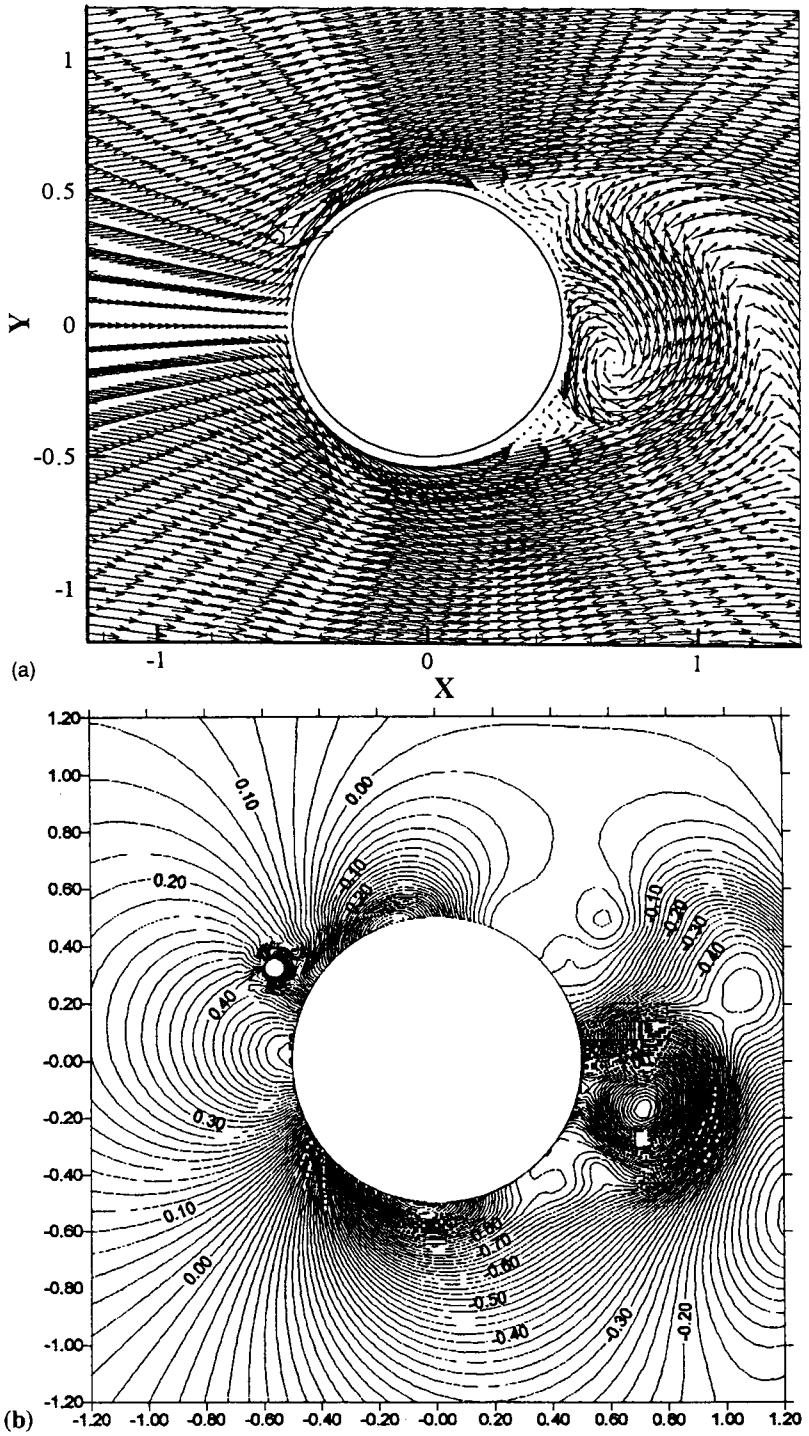


Figure 11. (a) Velocity field for flow around a circular cylinder with control cylinder, $Re = 6.5 \times 10^4$, $t = 200$, $\alpha = 30°$. (b) Pressure field for flow around a circular cylinder with control cylinder, $Re = 6.5 \times 10^4$, $t = 200$, $\alpha = 30°$. (c) Vorticity distribution for flow around a circular cylinder with control cylinder, $Re = 6.5 \times 10^4$, $t = 200$, $\alpha = 30°$. (d) Streamline distribution for flow around a circular cylinder with control cylinder, $Re = 6.5 \times 10^4$, $t = 200$, $\alpha = 30°$.

Copyright © 2001 John Wiley & Sons, Ltd.

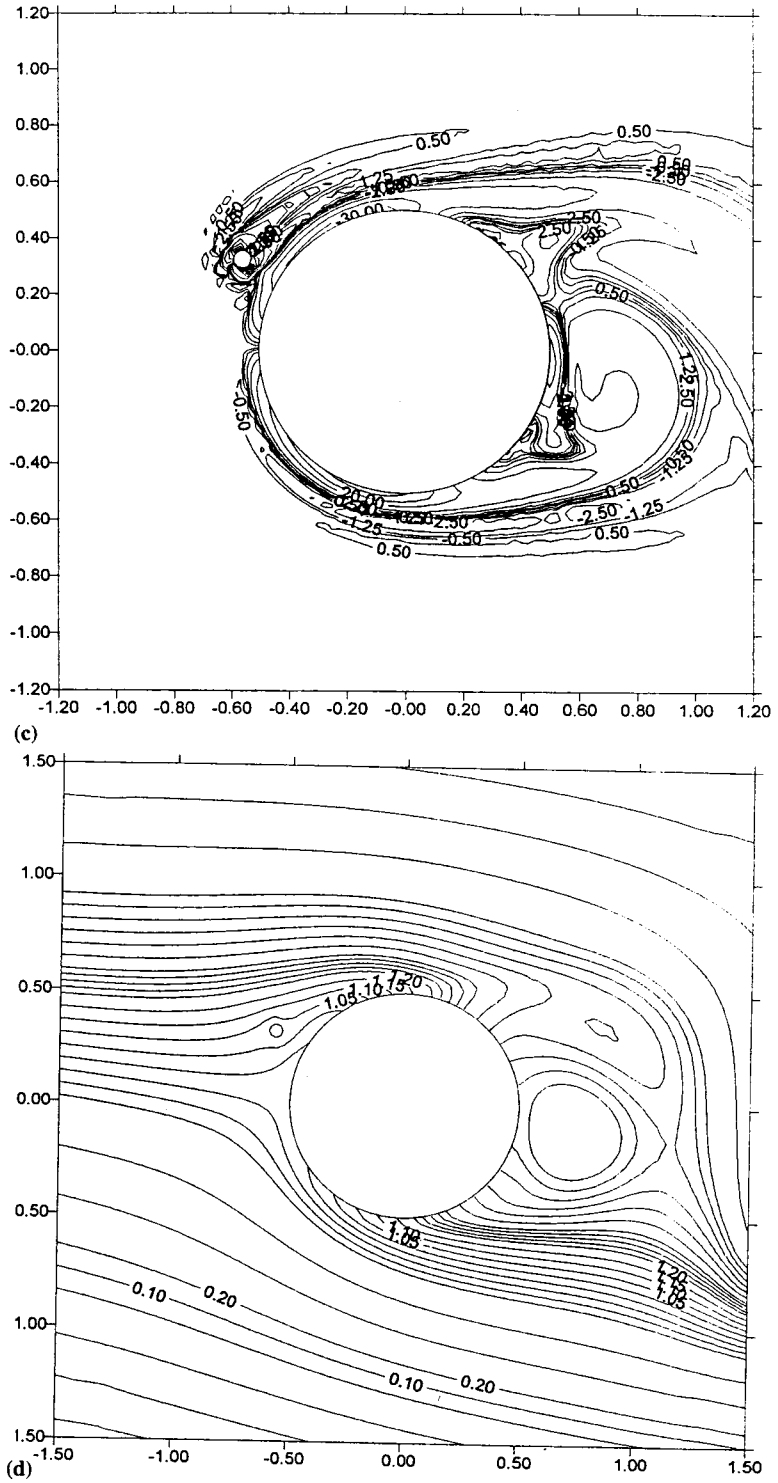


Figure 11 (*Continued*)

Copyright © 2001 John Wiley & Sons, Ltd.

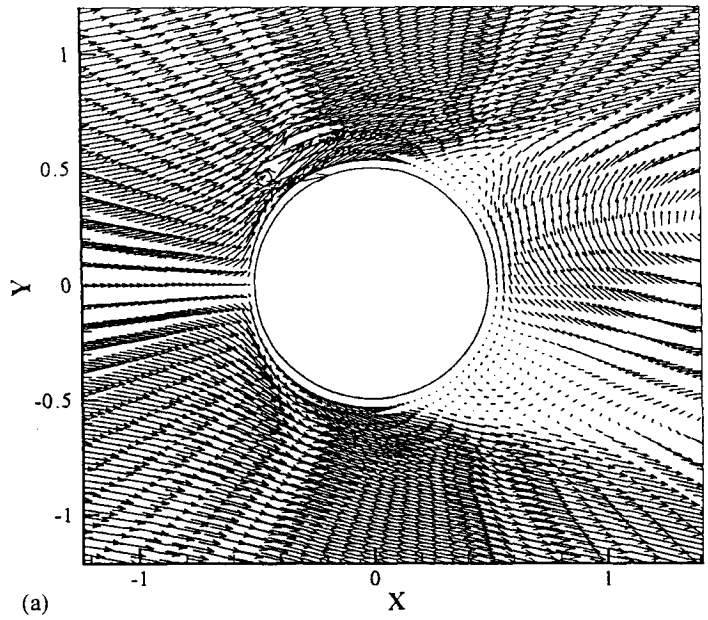


(a)

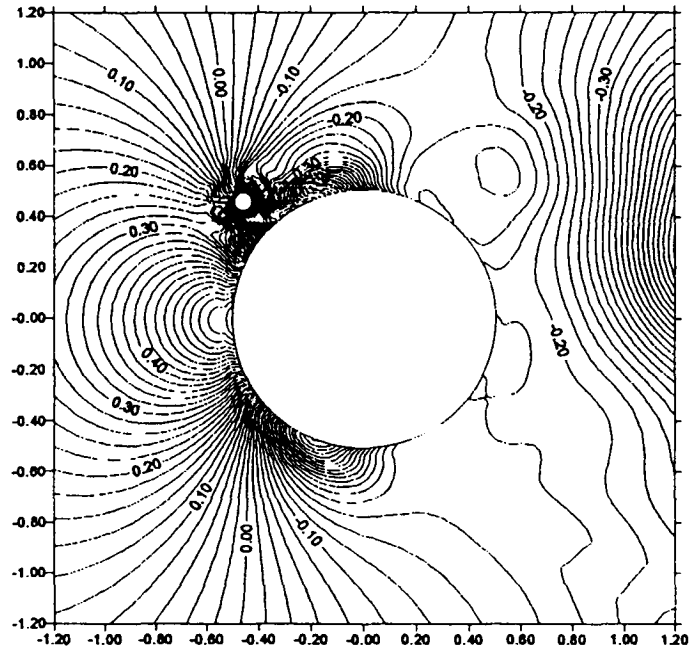


(b)

Figure 12. (a) Velocity field for flow around a circular cylinder with control cylinder, $Re = 6.5 \times 10^4$, $t = 70$, $\alpha = 45°$. (b) Pressure field for flow around a circular cylinder with control cylinder, $Re = 6.5 \times 10^4$, $t = 70$, $\alpha = 45°$. (c) Vorticity distribution for flow around a circular cylinder with control cylinder, $Re = 6.5 \times 10^4$, $t = 70$, $\alpha = 45°$. (d) Streamline distribution for flow around a circular cylinder with control cylinder, $Re = 6.5 \times 10^4$, $t = 70$, $\alpha = 45°$.

Copyright © 2001 John Wiley & Sons, Ltd.

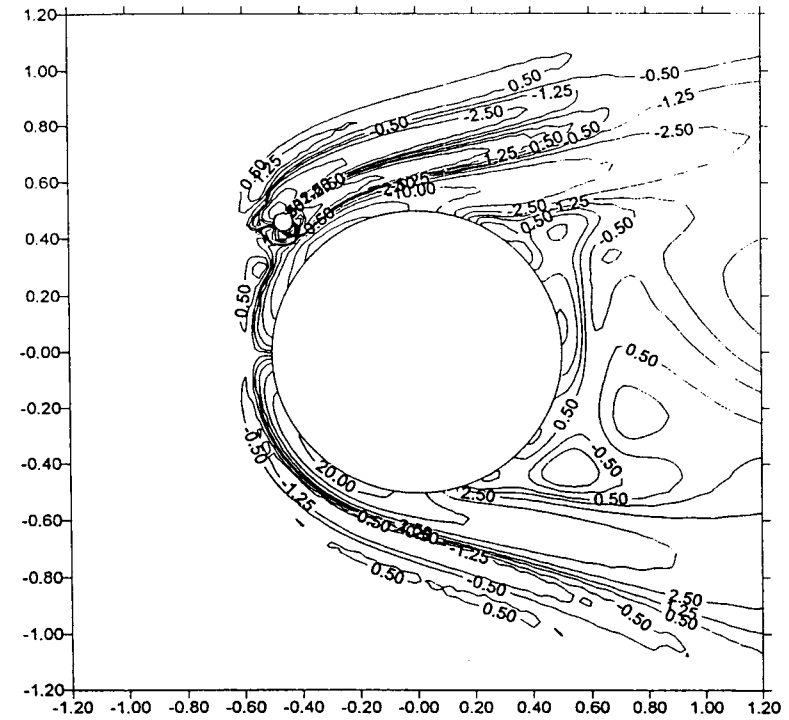


(c)

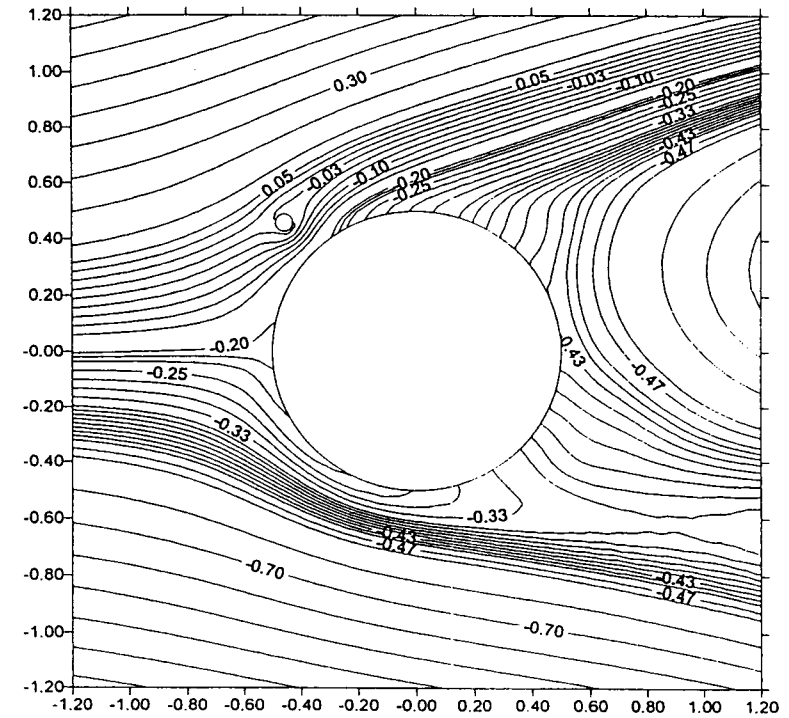


(d)

Figure 12 (*Continued*)

Copyright © 2001 John Wiley & Sons, Ltd.

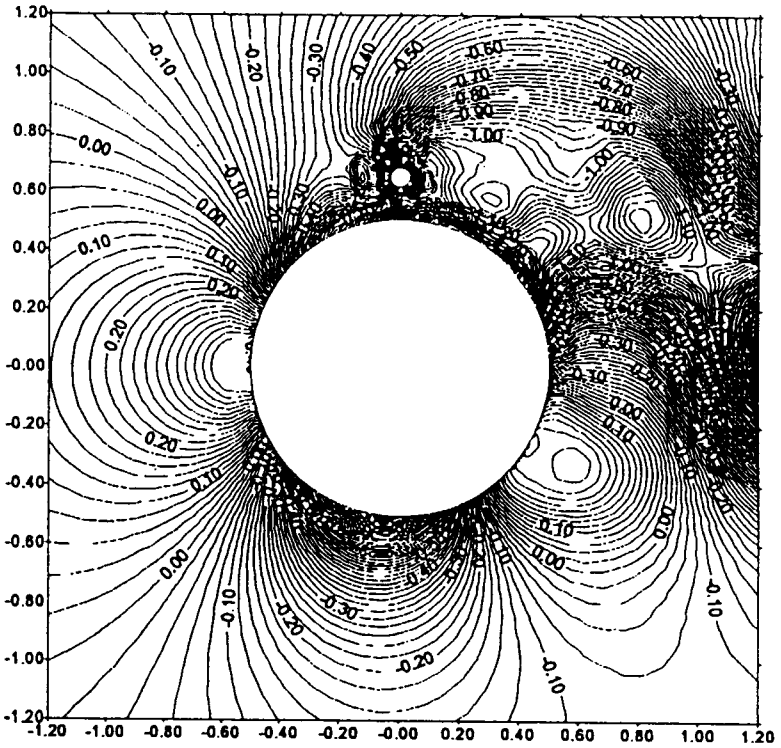


Figure 13. Pressure field for flow around a circular cylinder with control cylinder, $Re = 6.5 \times 10^4$, $t = 100$, $\alpha = 90°$.

due to the control cylinder to the lift coefficient ($C_{\text{lfn}}$) without the control cylinder for the various positions of the control cylinder. The results are compared with the experimental results of Sakamoto and Haniu [3] as well as Chang [19]. The experimental investigation of Sakamoto and Haniu [3] reported that the critical position for the control cylinder to suppress the fluid forces is near 60° and near 120°. However, the numerical simulations of the present study indicate a slightly different value of near 50° and near 120°. This difference may be attributed to the differences of the level of disturbance, specific end conditions and three-dimensional effects.

Figures 18 and 19 show respectively the coefficients of drag and lift calculated with reference to the various positions of the control cylinder. Figure 20 displays the corresponding power spectrum of the fluctuating drag coefficient for various positions of the control cylinder. These figures clearly depict the effect of the control cylinder in the flow regime in comparison to the case without the control cylinder. The coefficients of drag and lift drastically change with the position of the control cylinder. As is obvious, large reductions in the time-averaged drag is due to the displacement of the separation points, which are very conspicuous in the cases of $\alpha = 45°$ and 120°.

Copyright © 2001 John Wiley & Sons, Ltd.

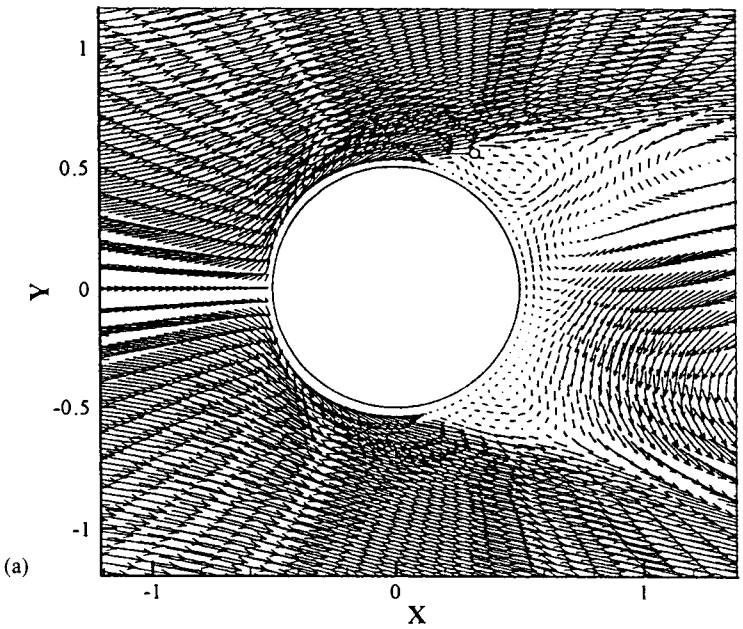


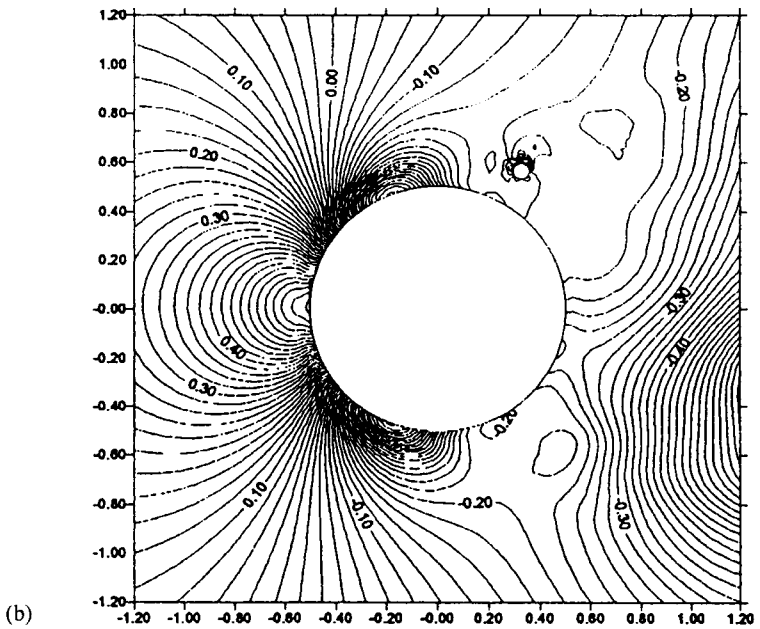


Figure 14. (a) Velocity field for flow around a circular cylinder with control cylinder, $Re = 6.5 \times 10^4$, $t = 100$, $\alpha = 120°$. (b) Pressure field for flow around a circular cylinder with control cylinder, $Re = 6.5 \times 10^4$, $t = 100$, $\alpha = 120°$. (c) Vorticity distribution for flow around a circular cylinder with control cylinder, $Re = 6.5 \times 10^4$, $t = 100$, $\alpha = 120°$. (d) Streamline distribution for flow around a circular cylinder with control cylinder, $Re = 6.5 \times 10^4$, $t = 100$, $\alpha = 120°$.

Copyright © 2001 John Wiley & Sons, Ltd.

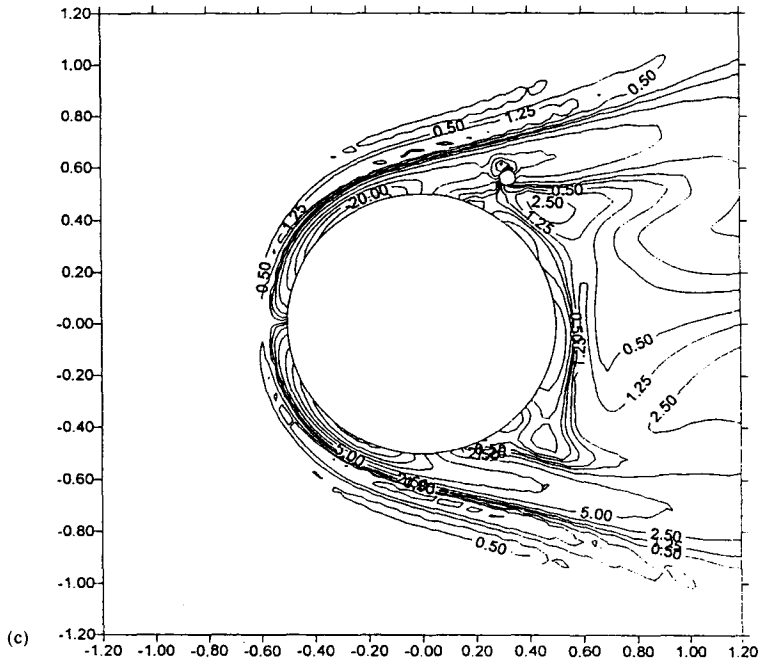


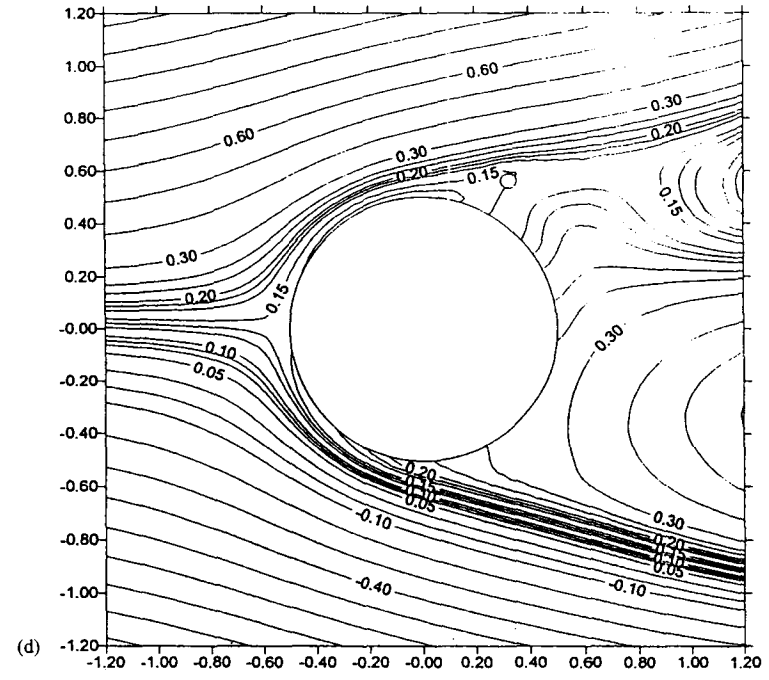


Figure 14 (*Continued*)

Copyright © 2001 John Wiley & Sons, Ltd.

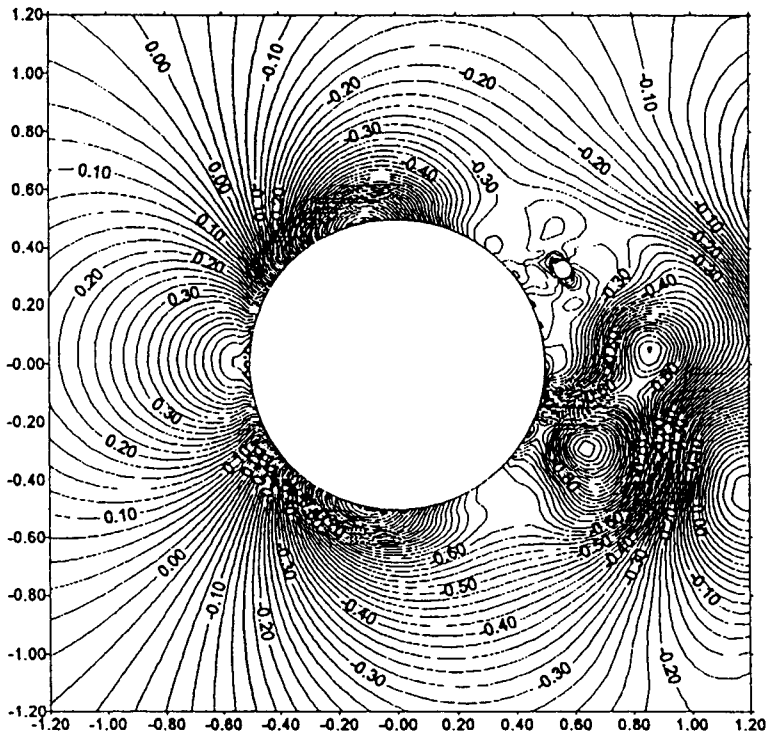


Figure 15. Pressure field for flow around a circular cylinder with control cylinder, $Re = 6.5 \times 10^4$, $t = 100$, $\alpha = 150°$.

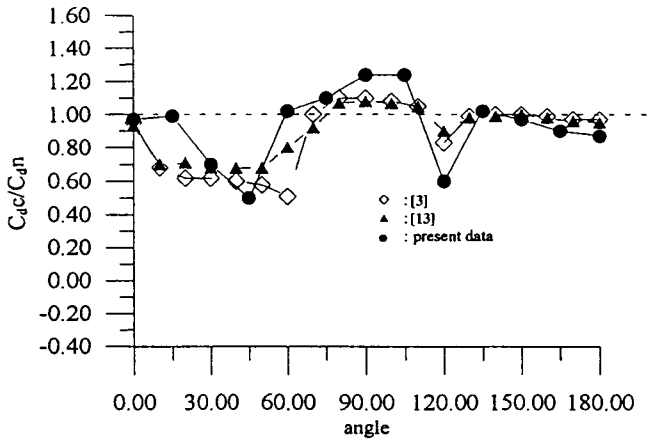


Figure 16. Comparison of the ratio of drag coefficient of cylinder with and without control cylinder for various $\alpha$ angles.

Copyright © 2001 John Wiley & Sons, Ltd. 

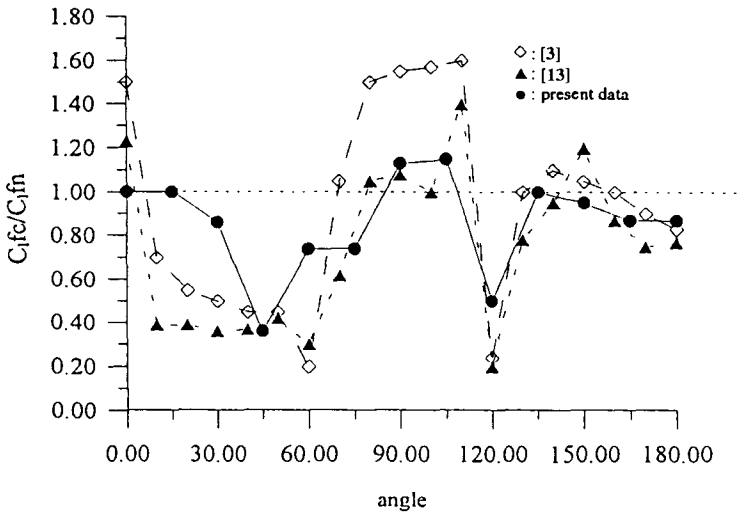


Figure 17. Comparison of the ratio of r.m.s. value of lift coefficient of cylinder with and without control cylinder for various $\alpha$ angles.

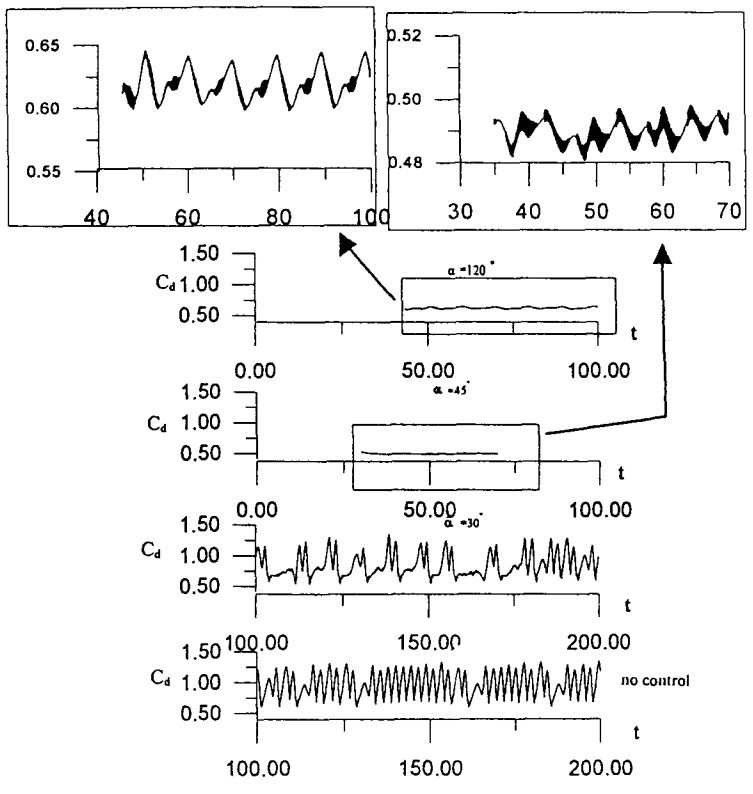


Figure 18. Drag coefficient of cylinder with and without control cylinder for various $\alpha$ angles.

Copyright © 2001 John Wiley & Sons, Ltd.

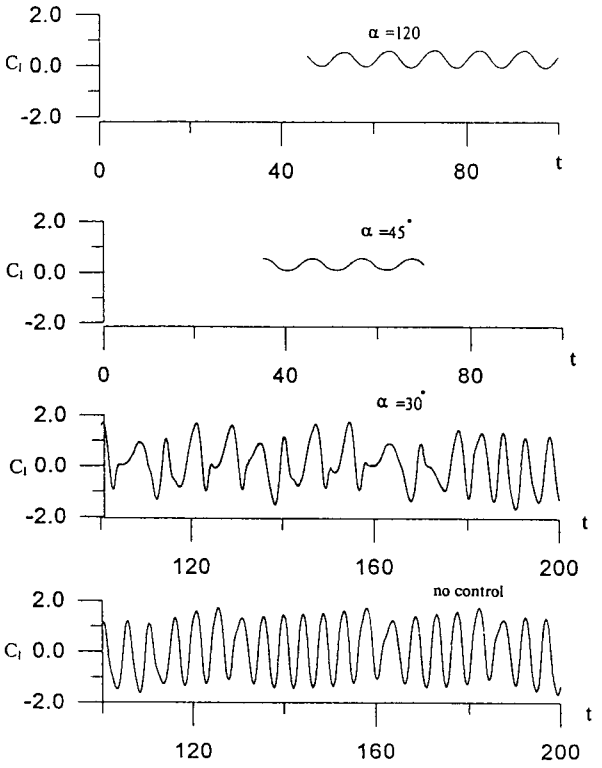


Figure 19. Lift coefficient of cylinder with and without control cylinder for various $\alpha$ angles.

This numerical study further explains the study of Sakamato and Haniu [3] on the effects of a small control cylinder, in the wake of a main circular cylinder at a high Reynolds number. The pressure fields and vorticity distributions plotted reveal that the presence of the smaller cylinder reduces the growth rate of the disturbances and its suppression accompanied by the disappearance of the sharp spectral peaks, coincides with negative temporal growth rates. The presence of the control cylinder alters the stability of the flow and diverts small amounts of fluid into the wake of the main cylinder. The position and size of the control cylinder are very important factors in the vortex shedding and suppression, for the given Reynolds number of the flow regime [3], even though in the present analysis the effect of the size of the control cylinder is not considered.

The reasons for the suppression of fluid forces by the proper placement of a small control cylinder in the near wake of the main cylinder, are attributed to the redistribution of the vorticity in the shear layer, the fluid diversion between main and control cylinders to reduce the velocity gradients, as well as the pressure change between the two cylinders, as pointed out by Sakamoto and Haniu [3]. Figures 3(c), 12(c) (at 45°) and 14(c) (at 120°) respectively show the vorticity distributions without the control cylinder and with the

Copyright © 2001 John Wiley & Sons, Ltd.

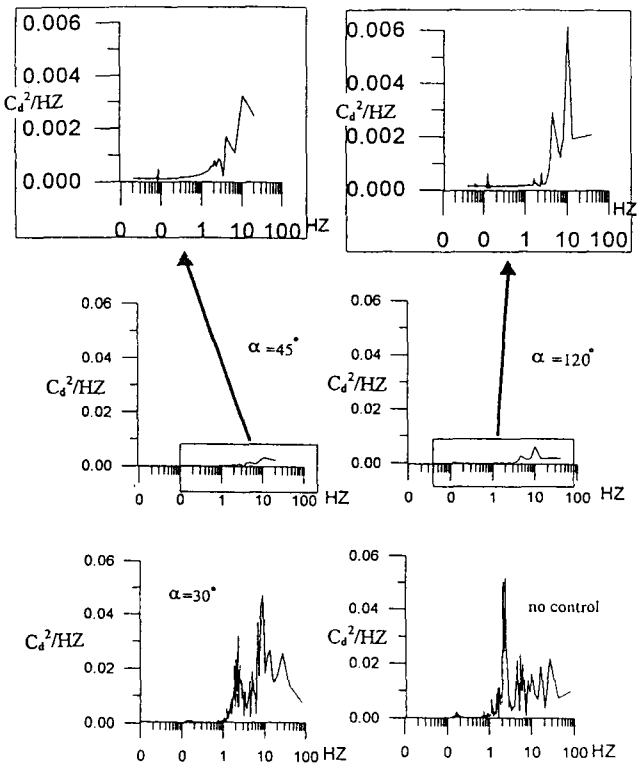


Figure 20. Power spectrum of fluctuating drag coefficient of cylinder with and without control cylinder for various $\alpha$ angles.

control cylinder at $Re = 65000$. The concentrated vorticity in the shear layer behind the main cylinder is smeared and diffused by the proper placement of the control cylinder. The suppression of vortex shedding as a consequence will reduce the magnitudes of the drag and lift forces as well as the oscillating frequencies. The pressure distributions without the control cylinder and with the control cylinder are shown for comparison in Figures 3(b), 12(b) (at 45°) and 14(b) (at 120°) respectively. The drastic reduction of pressure in the wake of the main cylinder by the introduction of the control cylinder suggests the mechanism for the suppression of vortex shedding and fluid forces.

## 6. CONCLUDING REMARKS

In this paper a novel computational model is presented to solve high-Reynolds number incompressible viscous flow problems. In the model, the transient Navier–Stokes equations in primitive variables are solved by a three-step FEM using a projection method, and the Poisson type pressure equations are solved using BEM. By coupling the three-step FEM

Copyright © 2001 John Wiley & Sons, Ltd.

and BEM, the model is able to handle infinite domain problems efficiently. The infinite boundary value problems are solved by extracting the boundary effects on a specified finite computational domain using the projection method.

The present model is applied to simulate high-Reynolds number flow past a single circular cylinder, and flow past two cylinders in which one acts as a control cylinder. The simulation results are compared with some experimental data and other numerical models and found to be feasible and satisfactory. Even though two-dimensional problems are presented here, the model can be easily extended to three-dimensional problems and also turbulence models can be incorporated.

## REFERENCES


1. Strykowski PJ, Sreenivasan KR. On the formation and suppression of vortex shedding at low Reynolds numbers. *Journal of Fluid Mechanics* 1990; **218**: 71–107.
2. Cantwell B, Coles D. A experimental study of entrainment and transport in the turbulent near wake of a circular cylinder. *Journal of Fluid Mechanics* 1983; **136**: 321–374.
3. Sakamoto H, Haniu H. Optimum suppression of fluid forces acting on a circular cylinder. *Journal of Fluids Engineering, Transactions of ASME* 1994; **116**: 221–227.
4. Zdravkovich MM. Review and classification of various aerodynamic and hydrodynamic means for suppressing vortex shedding. *Journal of Wind Engineering and Industrial Aerodynamics* 1981; 7(2): 145–189.
5. Braza M, Chassaing P, Minh HH. Numerical study and physical analysis of the pressure and velocity fields in the near wake of a circular cylinder. *Journal of Fluid Mechanics* 1986; **165**: 79–139.
6. Franke R, Rodi W, Schonung B. Numerical calculation of laminar vortex shedding flow past cylinders. *Journal of Wind Engineering and Industrial Aerodynamics* 1990; **35**: 237–257.
7. Lecointe Y, Piquet J. Flow structure in the wake of an oscillating cylinder. *Journal of Fluids Engineering, Transactions of ASME* 1989; **111**: 139–148.
8. Jackson CP. A finite-element study of the onset of vortex shedding in flow past variously shaped bodies. *Journal of Fluid Mechanics* 1987; **182**: 23–45.
9. Reddy JN. *Finite Element Method.* McGraw-Hill: New York, 1993.
10. Taylor C, Hughes TG. *Finite Element Programming of The Navier–Stokes Equations.* Pineridge Press Limited: Swansea, 1981.
11. Power H, Wrobel LC. *Boundary Integral Methods in Fluid Mechanics.* Computational Mechanics Publications: Southampton, 1995.
12. Brooks A, Hughes TJR. Streamline upwind/Petrov–Galerkin formulations for convection dominated flow with particular emphasis on the incompressible Navier–Stokes equations. *Computer Methods in Applied Mechanics and Engineering* 1982; **32**: 199–259.
13. Kakuda K, Tosaka N. Numerical simulation of high Reynolds number flows by Petrov–Galerkin finite element method. *Journal of Wind Engineering and Industrial Aerodynamics* 1993; **46/47**: 339–347.
14. Kondo N. Direct third-order upwind finite element simulation of high Reynolds number flows around a circular cylinder. *Journal of Wind Engineering and Industrial Aerodynamics* 1993; **46/47**: 349–356.
15. Donea JA. Taylor–Galerkin method for convective transport problems. *International Journal for Numerical Methods in Fluids* 1984; **20**: 101–119.
16. Jiang CB, Kawahara M. The analysis of unsteady incompressible flows by a three-step finite element method. *International Journal for Numerical Methods in Fluids* 1993; **16**: 793–811.
17. Young DL, Liao CB, Sheen HJ. Computations of recirculation zones of a confined annular swirling flow. *International Journal for Numerical Methods in Fluids* 1999; **29**: 791–810.
18. Brebbia CA, Telles JCF, Wrobel LC. *Boundary Element Techniques—Theory and Applications in Engineering.* Springer-Verlag: Berlin, 1984.
19. Chang YC. Experimental investigations on the control of vortex shedding behind a circular cylinder. MS thesis, Institute of Applied Mechanics, National Taiwan University, 1996.
20. Tamura T, Kuwahara K. Direct finite difference computation of turbulent flow around a circular cylinder. *Numerical Methods in Fluid Dynamics* 1989; **2**: 645–650.


Copyright © 2001 John Wiley & Sons, Ltd. 

21. Chang JT. Numerical simulation of wind flows over structures. PhD thesis, Graduate Institute of Civil Engineering, National Taiwan University, 1995.
22. Stewartson K. Multi-structured boundary layers on flat plates and related bodies. In *Advances in Applied Mechanics*, vol. 14, Yih CS (ed.). Academic Press: New York, 1974; 146–239.
23. Smith FT, Brighton PWM, Jackson PS, Hunt JCR. On boundary-layer flow past two-dimensional obstacles. *Journal of Fluid Mechanics* 1981; **113**: 123–152.

Copyright © 2001 John Wiley & Sons, Ltd.

INTERNATIONAL JOURNAL FOR NUMERICAL METHODS IN ENGINEERING
*Int. J. Numer. Meth. Engng* 2001; **51**:1053–1077

# A coupled BEM and arbitrary Lagrangian–Eulerian FEM model for the solution of two-dimensional laminar flows in external flow fields

D. L. Young*,†, J. T. Chang and T. I. Eldho

*Department of Civil Engineering and Hydrotech Research Institute, National Taiwan University, Taipei, 10617, Taiwan*

SUMMARY

This paper describes a new computational model developed to solve two-dimensional incompressible viscous flow problems in external flow fields. The model based on the Navier–Stokes equations in primitive variables is able to solve the infinite boundary value problems by extracting the boundary effects on a specified finite computational domain, using the pressure projection method. The external flow field is simulated using the boundary element method by solving a pressure Poisson equation that assumes the pressure as zero at the infinite boundary. The momentum equation of the flow motion is solved using the three-step finite element method. The arbitrary Lagrangian–Eulerian method is incorporated into the model, to solve the moving boundary problems. The present model is applied to simulate various external flow problems like flow across circular cylinder, acceleration and deceleration of the circular cylinder moving in a still fluid and vibration of the circular cylinder induced by the vortex shedding. The simulation results are found to be very reasonable and satisfactory. Copyright © 2001 John Wiley & Sons, Ltd.

KEY WORDS: Navier–Stokes equations; external flow; arbitrary Lagrangian–Eulerian method; boundary elements; finite elements

## 1. INTRODUCTION

The two-dimensional laminar viscous flow problems in external flow fields have been the focus of numerous investigations. These studies have been motivated by the desire to understand the fundamental physics of such flows as well as their practical importance in various industries. The phenomena of external flow problems are visible everywhere around our living environments such as: the variation of flow field arisen by the wind across the high-rise building, the drag force induced by driving car accelerating in the wind and also the

*Correspondence to: Der-Liang Young, Department of Civil Engineering and Hydrotech Research Institute, National Taiwan University, Taipei, 10617, Taiwan.
†E-mail: dlyoung@hy.ntu.edu.tw

Contract/grant sponsor: National Science Council of Taiwan

*Received 6 December 1999*
*Revised 9 October 2000*

Copyright © 2001 John Wiley & Sons, Ltd.

ocean current interaction with the offshore structures. The major difficulty in simulating these flows lies in setting the boundary conditions of the computational domain to simulate the external flow that has infinite domain. There are three typical boundary conditions namely inflow, outflow and two-side virtual boundaries. The inflow boundary is the forced flow into the computational domain. As far as the outflow boundary is concerned, the flow phenomenon in the downstream affected by the wake shall be taken into account.

With the advent of very powerful computers, numerical methods like finite differences (FDM), finite elements (FEM) and boundary elements (BEM) have become widely used to investigate fluid flow problems [1]. The numerical simulation of unsteady incompressible Navier–Stokes equations using FDM has been reported in numerous studies (for example, Jordan and Fromm [2] using ADI method). Braza *et al.* [3] used a second-order finite-volume method and analysed the dynamical characteristics of the pressure and velocity fields of the unsteady, incompressible laminar flows. For the last two decades, FEM and BEM have been used widely for the solution of various fluid dynamics problems. The theoretical potentials of FEM [4, 5] and BEM [6] have been adequately exposed for the solution of different forms of the Navier–Stokes equations by various researchers.

Various forms of finite-element formulations are available in literature for the solution of incompressible viscous flows. As the most commonly used Galerkin formulation is not able to cope with the convective effects efficiently, other forms like Petrov–Galerkin formulation [7] and Taylor–Galerkin [8] schemes were developed. Based on Taylor–Galerkin schemes, Jiang and Kawahara [9] recently developed a three-step finite-element scheme for the unsteady incompressible viscous flows. Different forms of boundary element method like direct BEM, indirect BEM [6] and dual reciprocity BEM [10] are in use for the solution of fluid-dynamics problems. In the present study, a coupled BEM–FEM scheme, in combination with other techniques is used for the solution of incompressible viscous flows.

The use of Lagrangian and Eulerian methods in combination with various numerical methods, are prominent in various applications of fluid dynamics problems. As Lagrangian method does not handle satisfactorily the material distortions and Eulerian method has got drawback in handling convective effect [11], combinations of Lagrangian–Eulerian methods with different modifications are in common use. One of the most efficient Lagrangian–Eulerian methods in practice is arbitrary Lagrangian–Eulerian (ALE) technique, based on the arbitrary movement of the reference frame, which is continuously rezoned in order to allow a precise description of moving interfaces. ALE technique was first developed in FDM by Hirt *et al.* [12] among others and then in FEM by Hughes *et al.* [13].

In the present study, a new computational procedure is developed to solve the incompressible viscous flow problems in external flow fields. The model is based on the pressure projection method of the Navier–Stokes equations in primitive variables. A three-step explicit FEM is used to solve the momentum equation of the flow domain. The pressure Poisson equation for the external flow field is treated by the boundary element method. The arbitrary Lagrangian–Eulerian scheme is employed to deal with the moving boundary, such as the motion of an impulsively moving circular cylinder in a viscous fluid.

Using the present model, by coupling of BEM and three-step FEM and by using ALE scheme for the moving boundary, a variety of external flow problems such as flow over an immersed body, movement of a body in a still fluid and other fluid structure interaction problems can be solved. Use of BEM for the solution of the pressure Poisson equation helps to handle the infinite domain of the external flow problem from a finite discrete domain

Copyright © 2001 John Wiley & Sons, Ltd. 

efficiently, as the fundamental solutions used in the BEM formulations automatically satisfy the conditions at infinity. The use of three-step FEM for the solution of the Navier–Stokes equations helps to deal with the convective effects efficiently. By the implementation of the ALE concept, moving boundary problems are effectively handled in the model.

Different external flow problems are simulated using the present model. The feasibility and accuracy of the developed numerical scheme has been verified, by comparing with other numerical schemes available in literature. After presenting the governing equations, the numerical formulation using coupled BEM and arbitrary Lagrangian–Eulerian FEM are briefly described. Then the solution procedure and numerical results for various two-dimensional laminar flow problems in external flow field are described, followed by a few concluding remarks.

## 2. GOVERNING EQUATIONS AND METHODOLOGY

### 2.1. *Fluid flow equations*

The basic equations describing laminar incompressible flow in two dimensions are the Navier–Stokes equations. They may be expressed in non-dimensional form as [14]:

*Continuity*

$$\frac{\partial u}{\partial x}+\frac{\partial v}{\partial y}=0 \tag{1}$$

*Momentum*

$$\frac{\partial u}{\partial t}+u\frac{\partial u}{\partial x}+v\frac{\partial u}{\partial y}=-\frac{\partial p}{\partial x}+\frac{1}{Re}\left(\frac{\partial^2 u}{\partial x^2}+\frac{\partial^2 u}{\partial y^2}\right) \tag{2}$$

$$\frac{\partial v}{\partial t}+u\frac{\partial v}{\partial x}+v\frac{\partial v}{\partial y}=-\frac{\partial p}{\partial y}+\frac{1}{Re}\left(\frac{\partial^2 v}{\partial x^2}+\frac{\partial^2 v}{\partial y^2}\right) \tag{3}$$

where the following non-dimensional variables are defined:

$$\begin{aligned} &x=x^*/D, \quad y=y^*/D, \quad u=u^*/u_0, \quad v=v^*/u_0 \\ &t=t^*u_0/D, \quad p=p^*/\rho u_0^2, \quad Re=u_0 D/\upsilon \end{aligned} \tag{4}$$

The $*$ denotes a dimensional variable, $u$ is the velocity in the $x$-direction and $v$ is the velocity in the $y$-direction, $p$ is the pressure, $\upsilon$ is the kinematic viscosity, $t$ is the time, $\rho$ is the mass density, $Re$ is the Reynolds number, $D$ is characteristic length used to normalize the variables and $u_0$ is the uniform velocity of the flow field.

For the solution of transient external flow problems, appropriate initial and boundary conditions should be prescribed. The initial conditions for the Navier–Stokes problem consist of specifying the values of velocity at the initial time:

$$u(x,y,0)=\bar{u}_0(x,y) \quad v(x,y,0)=\bar{v}_0(x,y) \tag{5}$$

Copyright © 2001 John Wiley & Sons, Ltd. 

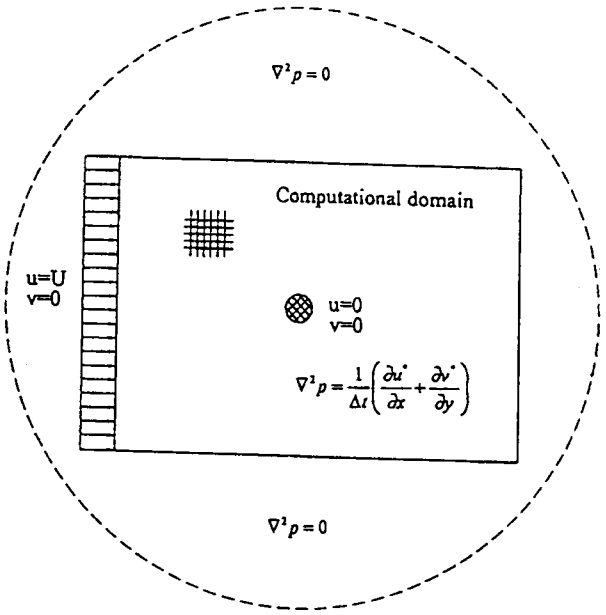


Figure 1. Computational domain and boundary conditions.

As shown in Figure 1, for the external flow problem considered in the present study, non-slip boundary conditions are imposed on the solid wall surface, that is,

$$u = 0 \quad v = 0 \tag{6}$$

At the inlet plane of the finite-flow domain, a uniform-flow profile was fixed as

$$u = U \quad v = 0 \tag{7}$$

On the other boundaries of the finite domain, no flow boundary or a fixed flow gradient can be assumed which is not essential in the present model.

As far as external flows are concerned, the outer boundaries are located at the infinity and the pressure at infinity is assumed to be zero. In numerical computations, due to the limitations of computational facilities, it is assumed that the computational domain is limited to the finite region. Outside the finite region, we assume that flow is uniform (constant velocity), continuity equation is valid, convective acceleration can be neglected and the pressure gradient in the flow direction as zero [15]. Hence we assume that

$$\nabla^2 p = 0 \tag{8}$$

is valid out of the finite computational domain where the fluid is assumed undisturbed. As a consequence, it is found to automatically satisfies the radiation boundary condition and hence only the inflow boundary condition is needed as the boundary requirement of the computational domain. In the present model, outflow boundary conditions are not necessary to be specified, as it will be automatically satisfied by the estimated pressure gradient. A sample computational domain for the type of problems that will be considered in the present study is shown in Figure 1, with boundary conditions.

Copyright © 2001 John Wiley & Sons, Ltd. 

### 2.2. *Arbitrary Lagrangian–Eulerian description*

The arbitrary Lagrangian–Eulerian scheme, originally developed by Hughes *et al.* [13], describes the fundamental kinematical relations derived by defining three domains in space called, the spatial domain, the material domain and the referential domain, and mapping between the domains. The spatial domain, regarded as generally in motion because of the moving interface to the adjoining structures, is the domain on which the fluid mechanics problem is considered. The material domain is the domain occupied at time $t=0$ by the material particles which occupy the spatial domain at $t$ and is considered in motion. The referential domain is the image of spatial domain at $t$ under prescribed mapping and is considered as fixed always. If the spatial domain coincides with the referential domain, then the description is Eulerian scheme. Similarly, if the material domain coincides with the spatial domain, the description is Lagrangian scheme.

In ALE, let $\Omega(X_i,t)$ represents the material domain (Lagrangian), $\Omega(x_i,t)$ represents the spatial domain (Eulerian) and $\Omega(\xi_i,t)$ represents the referential domain. Then the Lagrangian–Eulerian mapping can be described by $x_i=x_i(X_i,t)$ and the Eulerian-referential mapping can be described by $x_i=x_i(\xi_i,t)$. Consider a physical property $f(x_i,t)$ expressed in a spatial domain. Then owing to arbitrary Lagrangian–Eulerian scheme described by Hughes *et al.* [13] and Huerta and Liu [11], we can write the time derivative of $f$ as

$$\frac{\partial f}{\partial t}(X_i,t)\bigg|_{X_i}=\frac{\partial f}{\partial t}(\xi_i,t)\bigg|_{\xi_i}+c_i\frac{\partial f}{\partial x}(x_i,t) \tag{9}$$

$c_i$ is the convective velocity described as

$$c_i=u_i-\tilde{u}_i \tag{10}$$

where $u_i$ is the material velocity and $\tilde{u}_i$ is the mesh velocity. In the Eulerian description, the mesh velocity $\tilde{u}_i=0$, and in the Lagrangian description, $\tilde{u}_i=u_i$.

From the above-described ALE scheme, we can rewrite the governing equations (1)–(3) as

$$\frac{\partial u}{\partial x}+\frac{\partial v}{\partial y}=0 \tag{11}$$

$$\frac{\partial u}{\partial t}\bigg|_{\xi_i}+(u-\tilde{u})\frac{\partial u}{\partial x}+(v-\tilde{v})\frac{\partial u}{\partial y}=-\frac{\partial p}{\partial x}+\frac{1}{Re}\left(\frac{\partial^2 u}{\partial x^2}+\frac{\partial^2 u}{\partial y^2}\right) \tag{12}$$

$$\frac{\partial v}{\partial t}\bigg|_{\xi_i}+(u-\tilde{u})\frac{\partial v}{\partial x}+(v-\tilde{v})\frac{\partial v}{\partial y}=-\frac{\partial p}{\partial y}+\frac{1}{Re}\left(\frac{\partial^2 v}{\partial x^2}+\frac{\partial^2 v}{\partial y^2}\right) \tag{13}$$

where $\tilde{u},\tilde{v}$ are the mesh velocities in the $x$- and $y$-directions.

The boundary condition of the fixed body in the flow is set as no-slip boundary. Depending on the ALE description employed, the boundary of the moving body is specified as the velocity of flow equal to that of the body.

### 2.3. *Fluid and solid interaction*

The de-coupled method is used for the computation of the fluid and solid interaction. First the flow conditions are solved and then the force on the solid is calculated, which is produced

Copyright © 2001 John Wiley & Sons, Ltd. 

by the flow, so that the solid moving information can be obtained. Then the solid position, mesh velocity and flow boundary condition at the next time step are estimated. This recursive procedure is used in the present model.

For the structural model, the motion of a rigid circular cylinder mounted on an elastic dashpot-spring system is considered as an example. The governing equation of motion of the rigid-body structure can be written in a matrix form as [16]

$$m_{ij}\ddot{\delta}_j + c_{ij}\dot{\delta}_j + k_{ij}\delta_j = f_i \tag{14}$$

where $\delta_j, \dot{\delta}_j$ and $\ddot{\delta}_j$ are the vectors of nodal displacement, velocity and acceleration components in the $x_j$ direction defined at the centre of gravity, $f_i$ is the concentrated force components in the $x_i$-direction, $m_{ij}$ is the mass matrix, $c_{ij}$ is the damping matrix and $k_{ij}$ is the stiffness matrix. The displacement of the rigid body is included in the solution procedure, using de-couple method.

The coefficient of drag and the coefficient of lift on the solid body and the Strauhal number $S_t$ are found from the following equations:

$$C_d = \frac{F_d}{1/2\rho u_0^2 D}, \quad C_\ell = \frac{F_\ell}{1/2\rho u_0^2 D}, \quad S_t = \frac{fD}{u_0} \tag{15}$$

$$F_d = \oint_s p_s n_y \, ds - \oint_s \tau_s n_x \, ds \tag{16}$$

$$F_\ell = \oint_s p_s n_x \, ds + \oint_s \tau_s n_y \, ds \tag{17}$$

where $u_0$ is the characteristic fluid velocity, $F_d$ is the drag force, $\rho$ is the mass density, $D$ is the characteristic dimension, $F_\ell$ is the lift force, $f$ is the frequency of the oscillation, $\tau_s$ is the shear force acting on the body and $p_s$ is the pressure acting on the body.

## 3. NUMERICAL FORMULATION

As mentioned earlier, in the present model, a coupled BEM–FEM approach is used in the solution of the governing differential equations and the moving boundaries in the problem are treated with the arbitrary Lagrangian–Eulerian (ALE) scheme. In this section, the numerical formulation is briefly described.

### *3.1. ALE mesh velocity*

While using the ALE concept in FEM, spatial domain is the moving mesh and referential domain is the reference state of moving mesh. In the present study, the boundaries ($\Gamma_D$) of the finite discrete domain (see Figure 1) are assumed to be fixed in space and hence the mesh velocity $\tilde{u}_i = 0$ on $\Gamma_D$. On the moving interface $\Gamma_i$, due to non-slip condition, the velocity component ($u_i$) should be equal to the mesh velocity $\tilde{u}_i$. Hence it seems to be natural that $\tilde{u}_i$ decays to zero with distance from the body. In the present model, we have used a simple linear function of the distance from $\Gamma_i$ for the mesh velocity $\tilde{u}_i$ as proposed by Nomura and Hughes [16]. Suppose that a node $K$ outside the rigid body moves as if it is located in the

Copyright © 2001 John Wiley & Sons, Ltd. 

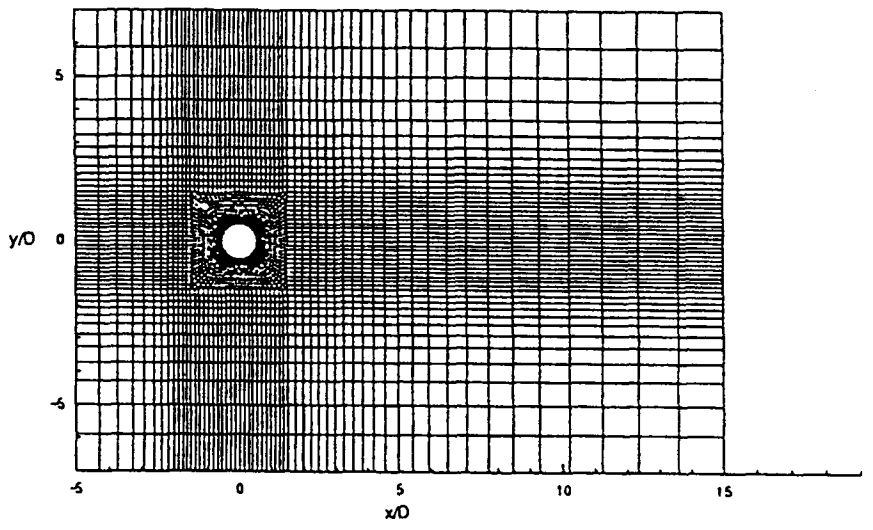


Figure 2. Mesh for the computational domain.

rigid body. Let $\delta^k$ and $u_i^k$ represent the imaginary displacements and velocities of $K$. Now the mesh displacements and velocities of the node can be expressed as

$$\tilde{\delta}^k = \lambda^k \delta^k, \quad \tilde{u}_i^k = \lambda^k u_i^k \tag{18}$$

where $\lambda^k$ $(0 \leqslant \lambda^k \leqslant 1)$ is an assigned constant coefficient to each node. In the case studies presented in Section 5, each node in the deformable region of the mesh is located on a straight line in the radial direction from the center of a circular cylinder (see Figure 2). Hence $\lambda^k$ is linearly distributed from 1 (on the cylinder surface) to 0 (on the outer boundary of the deformable region).

### *3.2. Three-step FEM formulation for Navier–Stokes equations*

In the present model, the mass–momentum Navier–Stokes equations are approximated using an explicit three-step finite-element method based on a Taylor series expansion in time [9]. From Taylor's series, a function $f$ in time can be represented as

$$f(t+\Delta t) = f(t) + \Delta t \frac{\partial f(t)}{\partial t} + \frac{\Delta t^2}{2}\frac{\partial^2 f(t)}{\partial t^2} + \frac{\Delta t^3}{6}\frac{\partial^3 f(t)}{\partial t^3} + O(\Delta t^4) \tag{19}$$

Approximating Equation (19) up to third-order accuracy, the three-step formulation can be written as

$$f\left(t+\frac{\Delta t}{3}\right) = f(t) + \frac{\Delta t}{3}\frac{\partial f(t)}{\partial t} \quad f\left(t+\frac{\Delta t}{2}\right) = f(t) + \frac{\Delta t}{2}\frac{\partial f(t+\Delta t/3)}{\partial t}$$
$$f(t+\Delta t) = f(t) + \Delta t \frac{\partial f(t+\Delta t/2)}{\partial t} \tag{20}$$

The Equations (20) are equivalent to Equation (19) and the method is referred to as three-step Taylor–Galerkin FEM. The standard Galerkin FEM can be used to obtain the finite-element

Copyright © 2001 John Wiley & Sons, Ltd. 

equation. This method has all the advantages of Taylor–Galerkin method such as third-order accuracy and the uniform CFL condition of numerical stability [9].

Applying the above procedure to the Navier–Stokes equations and using a pressure projection method [17–19], the three-step scheme can be obtained in two phases. In the first phase, the viscous and convective terms are obtained and in the second phase, the pressure terms are derived. In the first phase, from Equations (12) and (13), the following equations are obtained.

*Step 1*:

$$\frac{u^{n+1/3}-u^n}{\Delta t/3} = -\left[(u^n-\tilde{u}^n)\frac{\partial u^n}{\partial x}+(v^n-\tilde{v}^n)\frac{\partial u^n}{\partial y}\right]-\frac{\partial p^n}{\partial x}+\frac{1}{Re}\nabla^2 u^n \tag{21}$$

$$\frac{v^{n+1/3}-v^n}{\Delta t/3} = -\left[(u^n-\tilde{u}^n)\frac{\partial v^n}{\partial x}+(v^n-\tilde{v}^n)\frac{\partial v^n}{\partial y}\right]-\frac{\partial p^n}{\partial y}+\frac{1}{Re}\nabla^2 v^n \tag{22}$$

*Step 2*:

$$\frac{u^{n+1/2}-u^n}{\Delta t/2} = -\left[(u^{n+1/3}-\tilde{u}^n)\frac{\partial u^{n+1/3}}{\partial x}+(v^{n+1/3}-\tilde{v}^n)\frac{\partial u^{n+1/3}}{\partial y}\right]-\frac{\partial p^n}{\partial x}+\frac{1}{Re}\nabla^2 u^{n+1/3} \tag{23}$$

$$\frac{v^{n+1/2}-v^n}{\Delta t/2} = -\left[(u^{n+1/3}-\tilde{u}^n)\frac{\partial v^{n+1/3}}{\partial x}+(v^{n+1/3}-\tilde{v}^n)\frac{\partial v^{n+1/3}}{\partial y}\right]-\frac{\partial p^n}{\partial y}+\frac{1}{Re}\nabla^2 v^{n+1/3} \tag{24}$$

*Step 3*:

$$\frac{u^*-u^n}{\Delta t} = -\left[(u^{n+1/2}-\tilde{u}^n)\frac{\partial u^{n+1/2}}{\partial x}+(v^{n+1/2}-\tilde{v}^n)\frac{\partial u^{n+1/2}}{\partial y}\right]+\frac{1}{Re}\nabla^2 u^{n+1/2} \tag{25}$$

$$\frac{v^*-v^n}{\Delta t} = -\left[(u^{n+1/2}-\tilde{u}^n)\frac{\partial v^{n+1/2}}{\partial x}+(v^{n+1/2}-\tilde{v}^n)\frac{\partial v^{n+1/2}}{\partial y}\right]+\frac{1}{Re}\nabla^2 v^{n+1/2} \tag{26}$$

where $u^*$ and $v^*$ are the apparent velocities in which the pressure gradients are included, and the velocities in the present time step can be derived as

$$u^{n+1} = u^* - \Delta t\frac{\partial p^{n+1}}{\partial x} \tag{27}$$

$$v^{n+1} = v^* - \Delta t\frac{\partial p^{n+1}}{\partial y} \tag{28}$$

Spatial discretization of Equations (21)–(26) are performed by the standard Galerkin method using four-point bilinear elements [20]. The resulting finite element equations can be expressed as:

*For step 1*,

$$M_{ij}\frac{u_j^{n+1/3}-u_j^n}{\Delta t/3} = -A_{ij}^n u_j^n - B_{ij}p_j^n - \frac{1}{Re}S_{ij}u_j^n + \int_{\partial\Omega} N_i\frac{1}{Re}\left(\frac{\partial u^n}{\partial n}\right)\mathrm{d}S \tag{29}$$

$$M_{ij}\frac{v_j^{n+1/3}-v_j^n}{\Delta t/3} = -A_{ij}^n v_j^n - D_{ij}p_j^n - \frac{1}{Re}S_{ij}v_j^n + \int_{\partial\Omega} N_i\frac{1}{Re}\left(\frac{\partial v^n}{\partial n}\right)\mathrm{d}S \tag{30}$$

Copyright © 2001 John Wiley & Sons, Ltd. 

*For step 2,*

$$M_{ij}\frac{u_j^{n+1/2}-u_j^n}{\Delta t/2} = -A_{ij}^{n+1/3}u_j^{n+1/3} - B_{ij}p_j^n - \frac{1}{Re}S_{ij}u_j^{n+1/3} + \int_{\partial\Omega}\frac{N_i}{Re}\left(\frac{\partial u^{n+1/3}}{\partial n}\right)\mathrm{d}S \tag{31}$$

$$M_{ij}\frac{v_j^{n+1/2}-v_j^n}{\Delta t/2} = -A_{ij}^{n+1/3}v_j^{n+1/3} - D_{ij}p_j^n - \frac{1}{Re}S_{ij}v_j^{n+1/3} + \int_{\partial\Omega}\frac{N_i}{Re}\left(\frac{\partial v^{n+1/3}}{\partial n}\right)\mathrm{d}S \tag{32}$$

*For step 3*

$$M_{ij}\frac{u_j^*-u_j^n}{\Delta t} = -A_{ij}^{n+1/2}u_j^{n+1/2} - \frac{1}{Re}S_{ij}u_j^{n+1/2} + \int_{\partial\Omega}\frac{N_i}{Re}\left(\frac{\partial u^{n+1/2}}{\partial n}\right)\mathrm{d}S \tag{33}$$

$$M_{ij}\frac{v_j^*-v_j^n}{\Delta t} = -A_{ij}^{n+1/2}v_j^{n+1/2} - \frac{1}{Re}S_{ij}v_j^{n+1/2} + \int_{\partial\Omega}\frac{N_i}{Re}\left(\frac{\partial v^{n+1/2}}{\partial n}\right)\mathrm{d}S \tag{34}$$

Equations (27) and (28) can be discretized as

$$M_{ij}u_j^{n+1} = M_{ij}u_j^* - \Delta t B_{ij}p_j^{n+1} \tag{35}$$

$$M_{ij}v_j^{n+1} = M_{ij}v_j^* - \Delta t D_{ij}p_j^{n+1} \tag{36}$$

where

$$M_{ij} = \int_\Omega N_i N_j\,\mathrm{d}\Omega \quad A_{ij}^n = \int_\Omega N_i\left(N_k u_k^n\frac{\partial N_j}{\partial x} + N_k v_k^n\frac{\partial N_j}{\partial y}\right)\mathrm{d}\Omega$$

$$B_{ij} = \int_\Omega N_i\frac{\partial N_j}{\partial x}\,\mathrm{d}\Omega \quad D_{ij} = \int_\Omega N_i\frac{\partial N_j}{\partial y}\,\mathrm{d}\Omega \quad S_{ij} = \int_\Omega\left(\frac{\partial N_i}{\partial x}\frac{\partial N_j}{\partial x} + \frac{\partial N_i}{\partial y}\frac{\partial N_j}{\partial y}\right)\mathrm{d}\Omega$$

in which $N_i$ and $N_j$ are the shape functions.

After assembling the system and applying the initial and boundary conditions described in Equations (5)–(7), the system of equations is solved using the Jacobi iterations. In Jacobi iteration we initially assume some values for unknown variables and solve the linear system of equations iteratively using the values from the previous iteration. If a linear system of equations of the form $MX = R$ is to be solved, the system is transformed as

$$\bar{M}X^{k+1} = R - (M - \bar{M})X^k \tag{37}$$

where $M$ is the consistent coefficient matrix, $X$ is the unknown vector, $R$ is the known vector, $k$ is the iteration number and $\bar{M}$ is a lumped matrix. Generally, three iterations can achieve satisfactory accuracy [9]. More details of the Jacobi iteration can be found in most of the standard text books on numerical methods (e.g. Baker and Pepper [21]) which is not repeated here.

Before calculating the velocity in the present time step using Equations (27) and (28), the pressure and its derivatives are to be solved, in the second phase. Combining the continuity Equation (11) and taking gradient of Equations (25) and (26), the following pressure Poisson equation is derived to correct the velocity equation as,

$$\nabla^2 p^{n+1} = \frac{1}{\Delta t}\left(\frac{\partial u^*}{\partial x} + \frac{\partial v^*}{\partial y}\right) \tag{38}$$

Copyright © 2001 John Wiley & Sons, Ltd. 

In the present model, the pressure Poisson equation is solved using the BEM formulation, given in the following section using the boundary conditions derived from the solution of Equation (8) on the infinite domain from the finite discrete domain. The boundary conditions for the solid surface are obtained from Equations (27) and (28) for a fixed body. As obvious, the second phase being necessarily implicit obtained from the first phase and hence an iterative procedure is necessary between the solutions of $u^{n+1}$, $v^{n+1}$ and $p^{n+1}$.

### 3.3. *BEM formulation for pressure Poisson equation*

Consider the Poisson type pressure equation in $p$, $u^*$ and $v^*$ (Equation (38)),

$$\nabla^2 p = \frac{1}{\Delta t}\left(\frac{\partial u^*}{\partial x} + \frac{\partial v^*}{\partial y}\right) = b \tag{39}$$

with pressure boundary conditions as

$$\bar{p} = p_0 \quad \text{on } \Gamma_1 \quad \bar{q} = \frac{\partial p_0}{\partial n} \quad \text{on } \Gamma_2 \tag{40}$$

where $n$ is the unit outward normal vector. In the present model, an iterative scheme is used such that the velocity $u^*$ and $v^*$ are known in the current iteration and time step from the previous step by solving Equations (33) and (34).

Let $p^*$ be the fundamental solution of the Laplace equation in two dimensions, represented as $p^* = (-\ln r)/2\pi$. From Green's theorem, the boundary integral equation for Equation (39) can be written as [22]

$$C_i p_i + \int_\Gamma p q^* \, \mathrm{d}\Gamma + \int_\Omega b p^* \, \mathrm{d}\Omega = \int_\Gamma q p^* \, \mathrm{d}\Gamma \tag{41}$$

where $C_i$ is the Green's constant, $q = \partial p/\partial n$, $q^* = \partial p^*/\partial n$ and $r$ is the distance from the collocation point $(k)$ to other field point $(i)$ defined as

$$r = \sqrt{(x_k - x_i)^2 + (y_k - y_i)^2} \tag{42}$$

In Equation (41), we have boundary integrals and domain integrals. In the present model, the domain integration is carried out by subdividing the domain into a series of internal cells, on each of which a numerical integration is performed. Here linear elements are used for the boundary discretization and two-dimensional isoparametric quadrilateral cells are used for the internal discretization. The details of the element properties, shape functions, co-ordinate transformation and numerical integration used here are described in Brebbia *et al.* [22] which is not repeated here.

If the domain is discretized into $M$ internal cells, then the domain integral can be written as,

$$D_i = \int_\Omega b p^* \, \mathrm{d}\Omega = \sum_{e=1}^{M} \left[ \sum_{k=1}^{NI} w_k (b p^*)_k \right] \Omega_e \tag{43}$$

where the integral has been approximated by a summation over different cells ($e$ varies from 1 to $M$), $w_k$ are the Gauss integration weights, the function $(bp^*)_k$ needs to be evaluated at integration points $k$ on each cell ($k$ varies from 1 to $NI$, where $NI$ is the total number of integration points on each cell) and $\Omega_e$ is the area of cell $e$. The term $D_i$ is the result of the numerical integration and is different for each position $i$ of the boundary nodes.

Copyright © 2001 John Wiley & Sons, Ltd. 

Assuming that the boundary of the domain is discretized into $NE$ linear elements with $N$ nodes, Equation (41) can be discretized and written in matrix form as,

$$C_i p_i + \sum_{j=1}^{N} \bar{H}_{ij} p_j + D_i = \sum_{j=1}^{N} G_{ij} q_j \tag{44}$$

Combining the effect of the constant term $C$ with the $\bar{H}$ matrix, we can write the system of matrix as

$$Hp + D = Gq \tag{45}$$

In Equation (45), the boundary conditions are introduced and the known values are taken to the right-hand side to form a system of linear equations, which are solved using Gauss elimination scheme to find the boundary unknowns. Once this is done, it is possible to calculate internal values of $p$ or its derivatives from Equation (41).

It should be noted that the same BEM formulation without any domain integral given above (Equation (41)) is valid for the solution of the Laplace equation given in Equation (8). Equation (8) is solved for the infinite domain using the same discretization from the discrete finite domain.

The main advantage of using BEM in the solution of the pressure Poisson equation, is the effectiveness of BEM to deal with the infinite domain of the external flow problem from a finite discrete domain. Here only the boundary condition of pressure on the finite computational domain is known which is used to solve the infinite domain problem. Other numerical methods like FDM or FEM cannot be used to solve the pressure Poisson equation in infinite domain from a finite discrete domain as efficiently as BEM. In BEM, the fundamental solutions used in the formulations automatically satisfy the conditions at infinity and hence very efficient to solve the infinite domain problem from the finite discrete domain [22].

## 4. SOLUTION PROCEDURE

As mentioned earlier, here an iterative scheme is used in the solution of the Navier–Stokes equations. In most of the incompressible viscous flow problems solved using Navier–Stokes equations, the most natural boundary condition arises when the velocity is prescribed all over the boundaries of the problem. As shown in Figure 1, the boundary condition of the body in the flow is set as non-slip boundary. Based on the ALE description, the boundary of the moving body is specified as the velocity of flow equal to that of the body. The normal pressure gradient is assumed equal to zero because of the influence of acceleration of the body has been estimated by the mesh velocity. The computational procedure adopted here includes the following iterative steps:

*For the time step* $n = 1$:

(1) Assume at infinite domain, pressure $p = 0$ and solve the pressure Laplace equation (Equation (8)) outside the computational domain and pressure Poisson equation (Equation (38)) inside the computational domain and then get the pressure boundary conditions on the boundaries of the computational domain. These equations are solved simultaneously by utilizing the compatibility and equilibrium conditions of continuity of pressure and flux at the common boundary as described in Brebbia *et al.* [22].

Copyright © 2001 John Wiley & Sons, Ltd. 

(2) Solution of the Navier–Stokes equations using three-step FEM and pressure projection method.

- Solve for the unknown apparent velocity values (Equations (25) and (26)).
- Calculate the pressure distribution for the current time step from the pressure Poisson equation (Equation (38)) using BEM or FEM.
- Determine the new velocity values by solving Equations (27) and (28).

(3) Check for convergence of the velocity and pressure components in the present iteration, for example,

$$\frac{|u_{k+1}^n - u_k^n|}{|u_k^n|} \leqslant 0.001$$

If convergence criterion is satisfied, then proceed to the next step, otherwise go to step 1.

(4) From de-couple method, calculate the force on the solid and obtain the solid moving information.

- Estimate the solid position (for moving solid case) and apply the ALE to get the mesh velocity and the new flow boundary conditions.

(5) In the successive time step, use the velocity and pressure components from the previous time step as initial conditions and the new flow boundary conditions and use the iterative procedure, steps 1–4. The procedure is repeated until the prescribed time step is reached.

Detailed numerical investigations showed that the present model with the three-step FEM for the momentum equations is more stable than other FEM schemes like two-step scheme or Lax–Wendroff schemes due to the third-order accuracy and uniform CFL condition of the scheme. Various numerical experiments on two-dimensional incompressible viscous flow problem showed that the model is stable for $0 \leqslant C_r \leqslant 1$ ($C_r = \text{Courant number} = u\Delta t/\Delta x$) and hence a large time step can be used. A detailed stability analysis for the three-step FEM scheme, used in the present study can be found in Jiang and Kawahara [9].

Here it should be noted that, the solution of the pressure Poisson Equation (38) using BEM includes domain integrals. While finding out the internal pressure distribution using BEM with a fine mesh, we have to solve a large system of equations. This would increase the computational costs, as the system matrices are fully populated. Numerical investigations showed that the computing efficiency could be considerably increased by solving the boundary pressure values on the computational domain using the BEM while the FEM is used to get the internal pressure values. Both the system matrices of BEM and FEM are coupled using the compatibility and equilibrium conditions as described in Brebbia *et al.* [22].

## 5. MODEL APPLICATIONS

The developed BEM–FEM model has been applied on three test problems to verify the accuracy and feasibility of the model. The present model has been used to simulate various external flow problems like flow across circular cylinder, acceleration and deceleration of a moving circular cylinder in still fluid and vibration of the circular cylinder induced by the vortex shedding.

Copyright © 2001 John Wiley & Sons, Ltd. 

Table I. Comparison of numerical results for the flow across a circular cylinder.

| *Re* | Grid | $C_d$ | *St* | Author |
|---|---|---|---|---|
| 100 | 13 530 | 1.28 | 0.16 | Braza *et al.* [3] |
| | 1852 | 1.76 | 0.18 | Gresho *et al.* [23] |
| | 826 | 1.33 | 0.163 | Li *et al.* [24] |
| | 3564 | 1.29 | 0.168 | Present |
| | 1802 | 1.25 | 0.165 | Present |

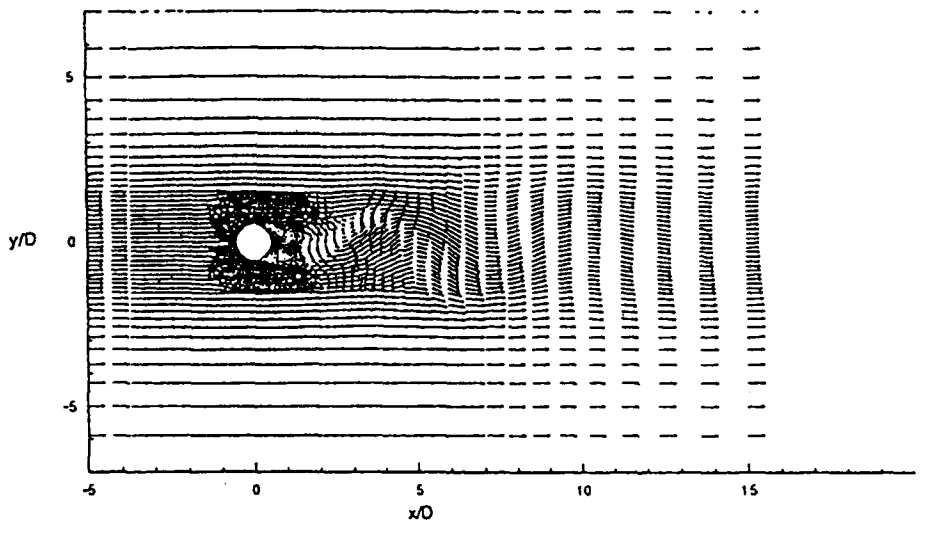


Figure 3. Velocity field for flow across a circular cylinder, $Re = 100$.

### *5.1. Flow across a fixed circular cylinder*

A large number of experimental and numerical studies have been carried out on the vortex shedding flow that is produced by the flow across a fixed cylinder [3, 23, 24]. The flow across a cylinder phenomenon has been simulated here to compare the results with the existing studies. The present model was tested by simulating flow past a circular cylinder for $Re = 100$. Figure 1 shows the computational domain with boundary conditions. It was 20 units long (cylinder diameter is unit) and 14 units wide approximately. The discretization of the domain using 3416 elements and 3564 nodes is shown in Figure 2. The domain of computation was wide enough to encompass the range of the vortex shedding. A time step of 0.025 (non-dimensional) is used in the computation. The boundary conditions were chosen as $u = 1$, $v = 0$ at the inlet and a non-slip boundary $u = 0$, $v = 0$ on the cylinder surface.

The model was run in unsteady condition and the coefficient of drag and Strauhal number, were calculated using the Equation (15). Table I shows a comparison of the coefficient of drag and Strauhal number at $Re = 100$, between the results of Braza *et al.* [3], Gresho *et al.* [23] and Li *et al.* [24]. Good agreement is observed between the results. Figure 3 shows the velocity

Copyright © 2001 John Wiley & Sons, Ltd. 

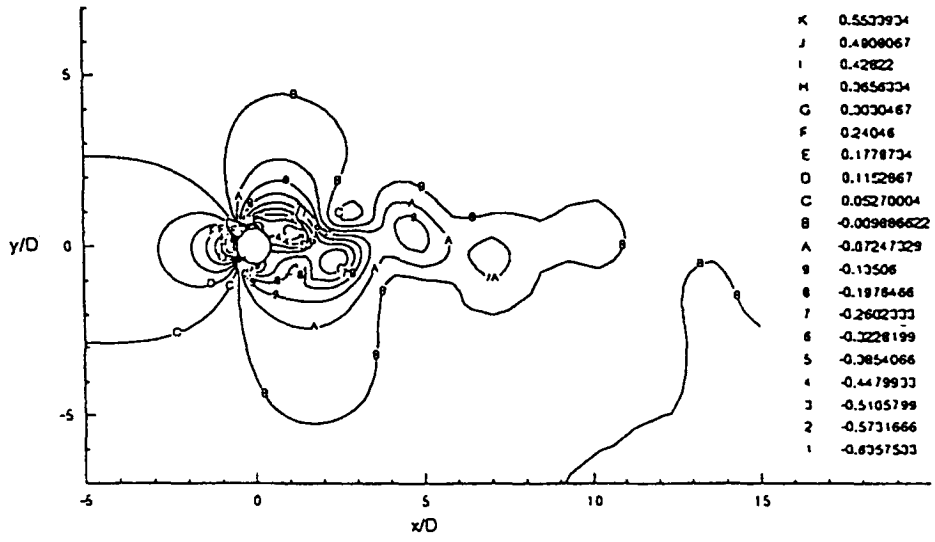


Figure 4. Pressure field for flow across a circular cylinder, $Re = 100$.

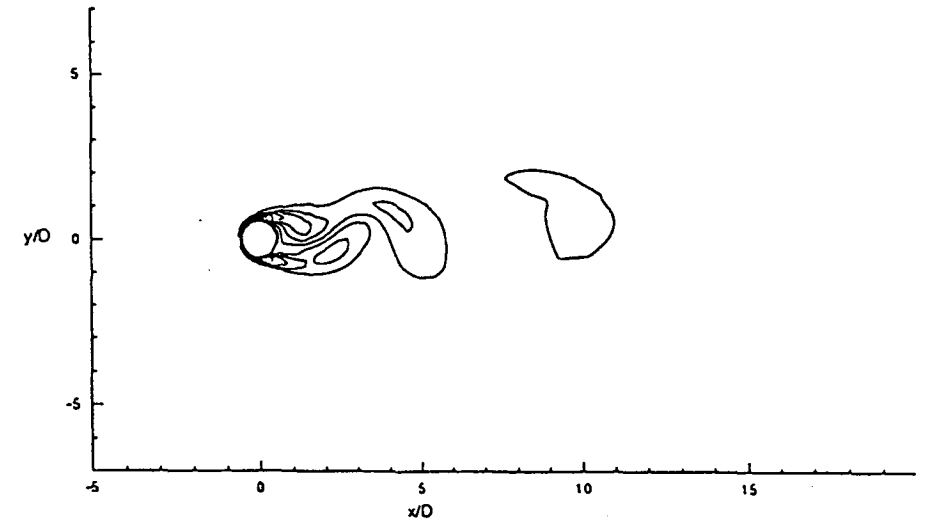


Figure 5. Vorticity distribution for flow across a circular cylinder, $Re = 100$.

field and Figure 4 shows the pressure field for the Reynolds number 100 at time equal to 107.5. The vorticity distribution around the cylinder is depicted in Figure 5. Figure 6 shows the streamlines for the circular cylinder for $Re = 100$. These figures show the salient features of the flow across the cylinder problem. As the above figures depict, the numerical simulation with the present model have rendered very reasonable and satisfactory results in comparison with the previous numerical studies [3, 23, 24].

Copyright © 2001 John Wiley & Sons, Ltd. 

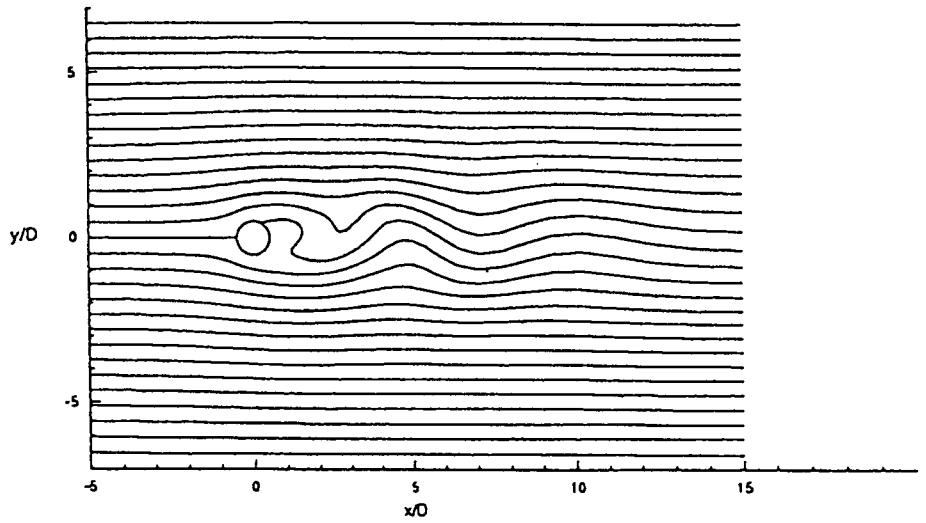


Figure 6. Streamline distribution for flow across a circular cylinder, $Re = 100$.

### 5.2. *Flow across a moving circular cylinder*

In this case study, the model is applied to simulate the motion of a circular cylinder, mentioned in the first case study (Section 5.1), with a unit diameter in still infinite fluid of unit density. The cylinder is setting into motion impulsively, from the rest to a constant acceleration and finally to a constant velocity. The velocity of the moving cylinder is then equal to the mesh velocity in the ALE description. In the present analysis Reynolds number is assumed to be 1000. The computational domain is discretized with 3416 elements and 3564 nodes (as in Figure 2). Three cases of accelerations, $a = 2.5, 5.0$ and 10.0 (non-dimensional) are considered and a time step of 0.025 is used in the simulation.

The time evolution of the drag force with various accelerations is shown in Figure 7. The drag forces are dependent on the magnitude of the acceleration. For example, for the case $a = 10.0$, the drag force for the moving cylinder in the first time step is equal to 7.856 which is very close to the value 7.854, derived from the added mass concept of the ideal flow theory. This value is reached independently on the time interval chosen. Figure 8 shows that the magnitude of 7.856 is obtained for the first time step, for all the three different time steps of 0.005, 0.01 and 0.025. Therefore, it can be concluded that for the impulsive motion of an accelerating cylinder in a viscous fluid, the drag force imposed on the cylinder can be treated as in the case of ideal fluid, at the moment of impulsive acceleration.

Figures 9, 10, 11, and 12 illustrate the local velocity field, vorticity distribution, pressure field and streamlines, respectively, at the first time step of the accelerated moment. After stopping the acceleration impulsively and maintaining at a constant velocity with zero acceleration, the drag force drops immediately for all three cases, as seeing from Figure 7. The drag forces vary for all three cases depending on the final constant velocity. Then finally the three cases are decelerated impulsively to the same constant velocity. The drag force for all three cases asymptotically approaches the value of 0.393, as predicted by using the drag

Copyright © 2001 John Wiley & Sons, Ltd. 

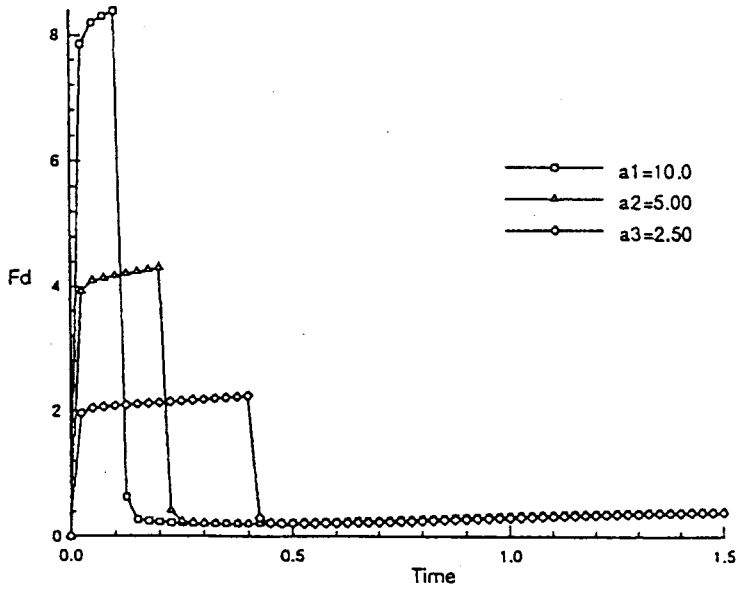


Figure 7. Time evolution of drag force with various accelerations for moving circular cylinder problem, $Re = 1000$.

coefficient as a function of Reynolds number for a smooth circular cylinder from the viscous flow theory [25]. As comparing with drag force due to the added mass, the drag force for a uniformly moving cylinder experiences $\frac{1}{20}$ of that of the uniform acceleration of a=10.0. The corresponding distributions of local velocity field and pressure distribution at the time step for the decelerated moment are shown in Figures 13 and 14, respectively.

From Figure 10, it is vivid to see that the vorticity is generated and confined around the moving cylinder only. Due to the confinement of vorticity around the cylinder, as well as the low values of drag coefficient for high Reynolds number flow for uniformly moving cylinder, it can be concluded to a first approximation that the viscosity plays only a minor role in the impulsive motion of a moving circular cylinder in a viscous flow.

### *5.3. Oscillation of a spring supported circular cylinder in a uniform flow*

The developed computational model is used to study the vortex-induced cross-flow oscillations of a circular cylinder mounted on an elastic spring in a water channel [16]. Figure 15 shows the problem set up, boundary conditions and material properties of the system. The domain is discretized using 1802 nodes and 1704 elements. Only vibration in the cross-flow direction is allowed. The other two degrees of freedom in other directions are fixed. In low Reynolds number (to the range of 100) flow regime, the wake behind the circular cylinder will be fully laminar. The *lock-in* phenomenon, in similar studies has been investigated experimentally by Anagnostopoulos and Bearman [26] and numerically by Nomura [27].

In the present study, three cases of flow regimes with Reynolds numbers, $Re = 100, 106$ and 110 were simulated, which represent before, near and after lock-in scenarios respectively. The natural frequency of the cylinder-spring system is found to be 7.0165 Hz. If we use the

Copyright © 2001 John Wiley & Sons, Ltd. 

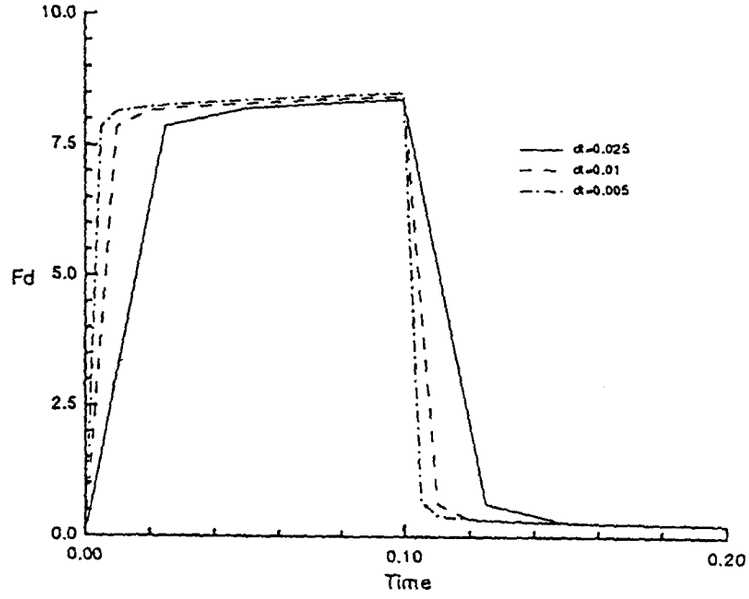


Figure 8. Variation of drag force with different time steps for moving circular cylinder problem, $Re = 1000, a = 10$.

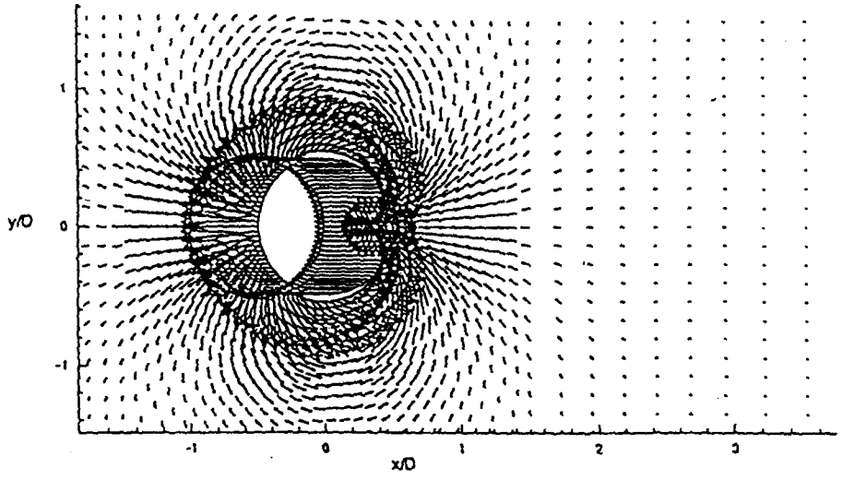


Figure 9. Local-velocity field for accelerated circular cylinder problem, $Re = 1000$.

Copyright © 2001 John Wiley & Sons, Ltd. 

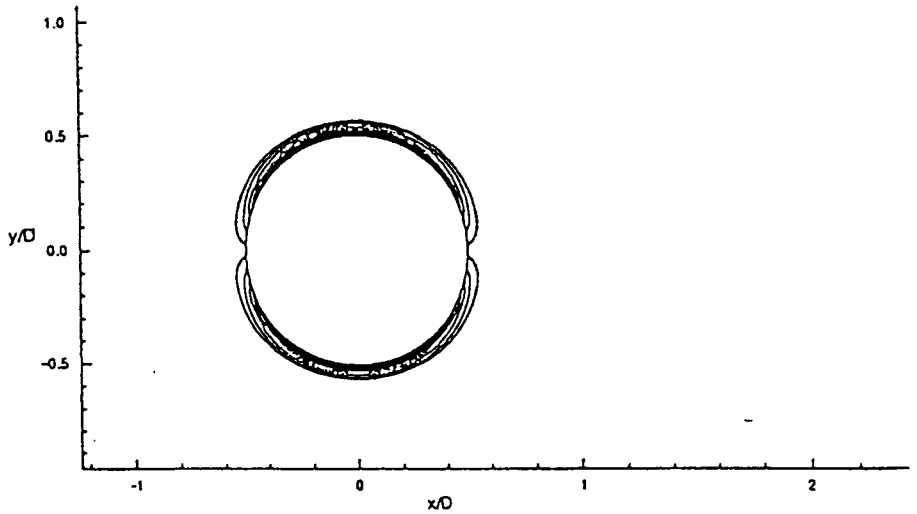


Figure 10. Vorticity distribution for accelerated circular cylinder problem, $Re = 1000$.

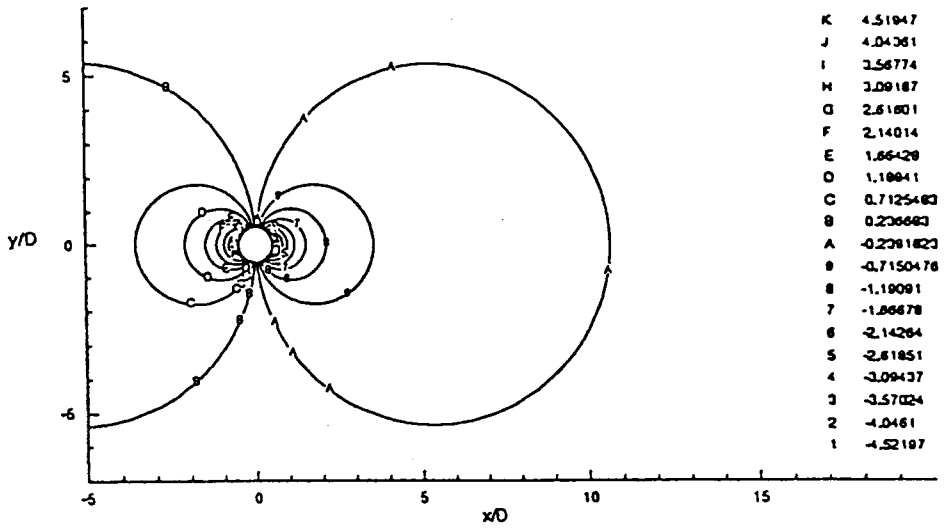


Figure 11. Pressure field for accelerated circular cylinder problem, $Re = 1000$.

Roshko's [28] experimental formula to estimate the shedding frequency for $Re = 100, 106$ and 110, the corresponding shedding frequencies are 6.92, 7.021 and 7.08 Hz respectively. It was found that in the case of $Re = 106$, the flow corresponds to the resonance of shedding and natural frequency or near the frequency locking. Figures 16–18 show the evolution of the non-dimensional displacement with time for $Re = 100, 106$ and 110, respectively.

Copyright © 2001 John Wiley & Sons, Ltd. 

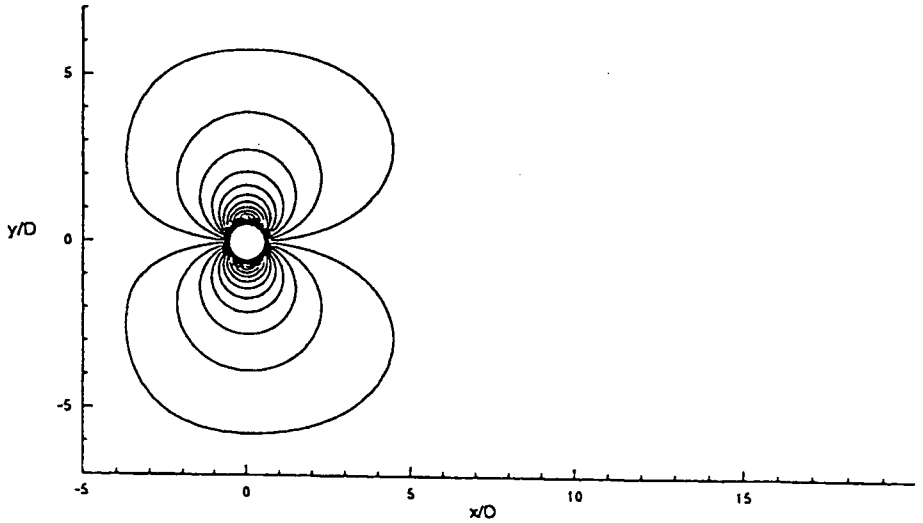


Figure 12. Streamlines for accelerated circular cylinder, $Re = 1000$.

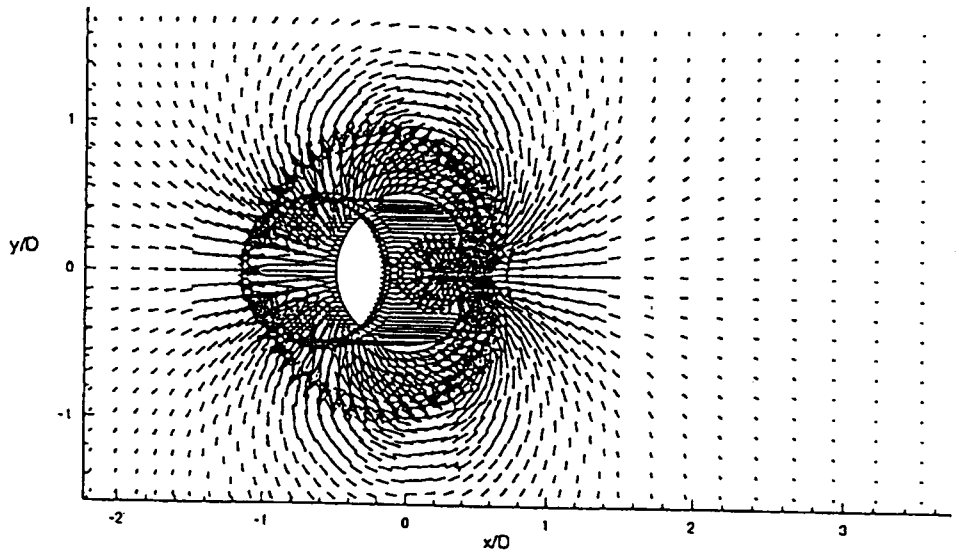


Figure 13. Local-velocity field for decelerated circular cylinder problem, $Re = 1000$.

As can be seen in Figure 17 for $Re = 106$, the amplitude is increasing conspicuously with time and the frequency of its driving force is approximated to the natural frequency. The *lock-in* mechanism is well known as the synchronization of the cylinder motion and the vortex shedding over a certain range of free stream velocity around the resonant velocity. As far as the free-stream velocity is lower or higher than that of the *lock-in*, the *beat* phenomenon is

Copyright © 2001 John Wiley & Sons, Ltd. 

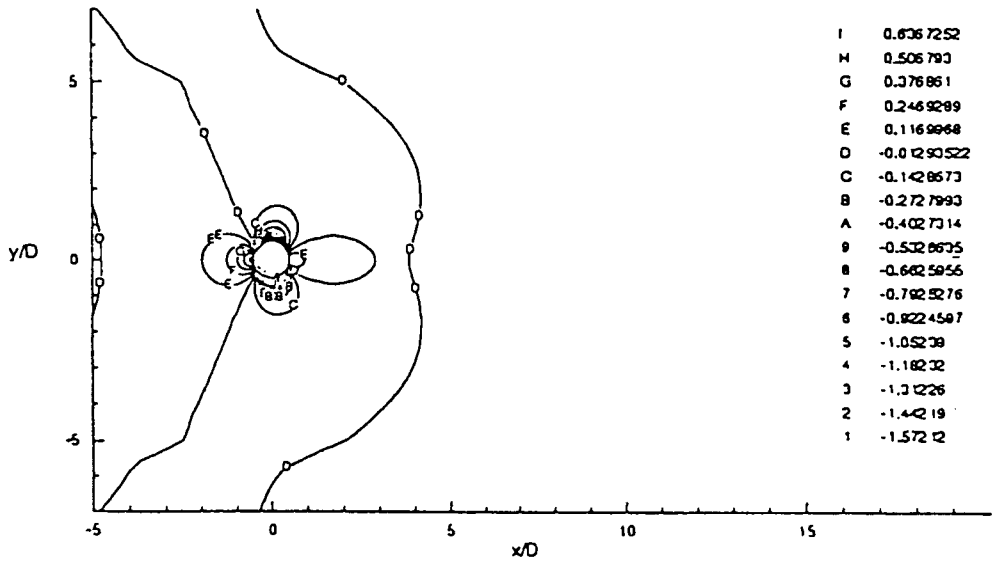


Figure 14. Pressure field for decelerated circular cylinder problem, $Re = 1000$.

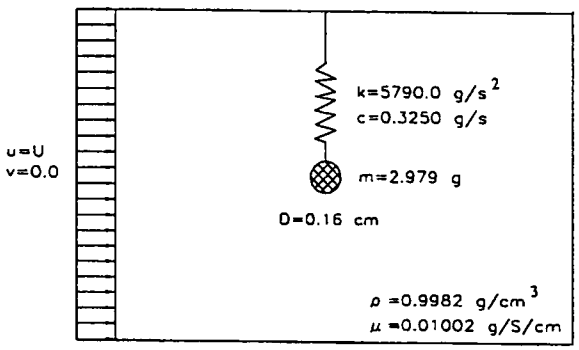


Figure 15. Transverse oscillation of a circular cylinder–spring system in a uniform flow field.

observed, which is accompanied by considerably small amplitude than that of the lock-in. As can be seen in Figure 16 for $Re = 100$, before the *lock-in* case, the small amplitude is limited to a certain region of the beat oscillation. After the frequency locking, the beat phenomenon reappears, as shown in Figure 18, for $Re = 110$. Studies of Anagnostopoulos and Bearman [26] and Nomura [27] suggest the *lock-in* region in the range of $Re = 106$–$115$. However the present study renders a narrower range of the lock-in mechanism. The small differences with the previous studies are probably due to the different meshes adopted for the studies and the difference in the approaches to model the infinite domain.

Figure 19 shows the local velocity field and Figure 20 shows the vorticity distribution for the Reynolds number 106 at time equal to 1000. The pressure field around the oscillating

Copyright © 2001 John Wiley & Sons, Ltd. 

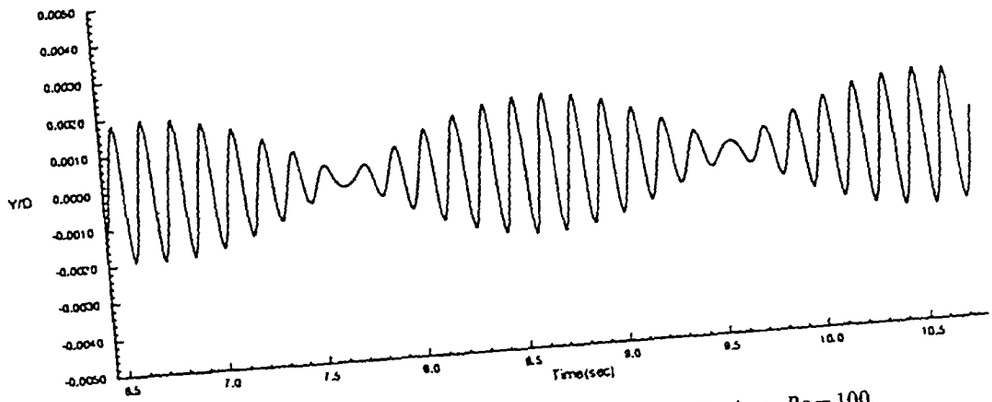


Figure 16. Evolution of non-dimensional displacement with time, $Re = 100$.

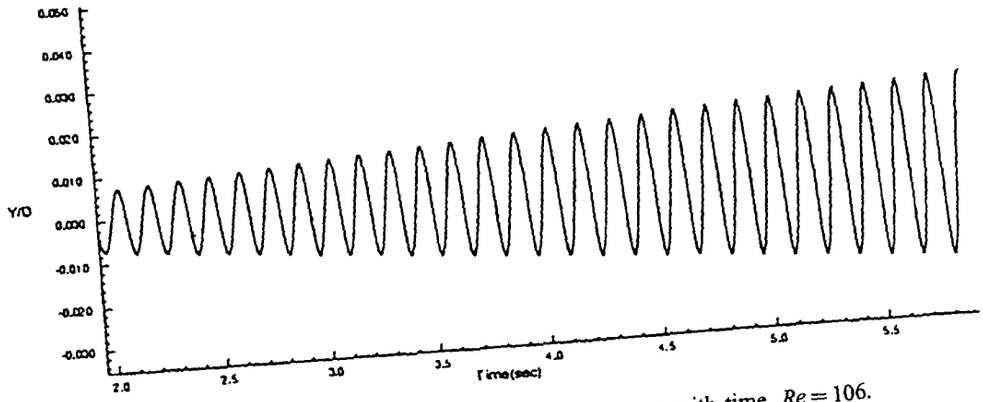


Figure 17. Evolution of non-dimensional displacement with time, $Re = 106$.

cylinder is depicted in Figure 21. Figure 22 shows the streamlines for the oscillation of the circular cylinder–spring system for $Re = 106$. These figures show the salient features of the lock-in phenomenon as the free stream approaches the resonant velocity. As the above figures depict, the numerical simulations with the present model have rendered very reasonable and satisfactory results in comparison with the previous experimental and numerical studies [26, 27].

Copyright © 2001 John Wiley & Sons, Ltd.

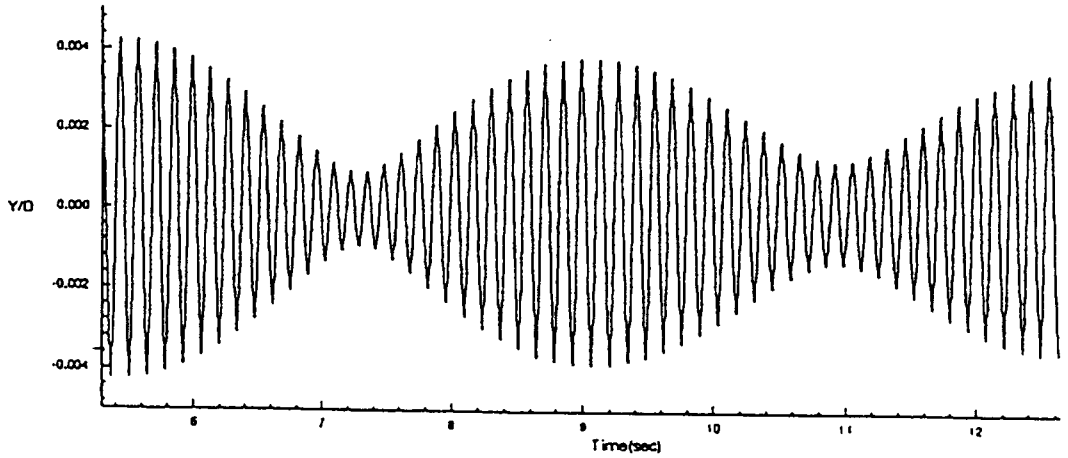


Figure 18. Evolution of non-dimensional displacement with time, $Re = 110$.

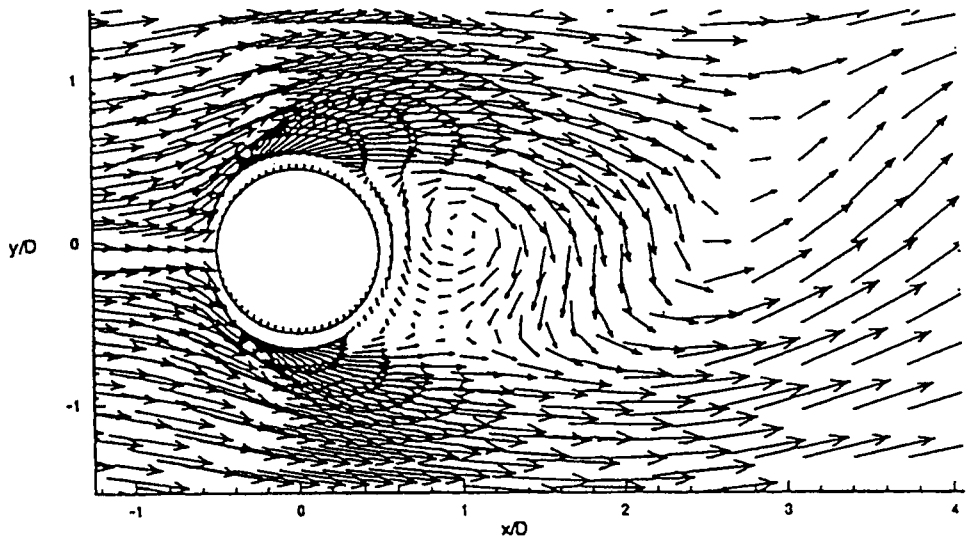


Figure 19. Local-velocity field for oscillation of circular cylinder–spring system in a uniform flow, $Re = 106$.

## 6. CONCLUDING REMARKS

A new computational model has been developed to solve two-dimensional incompressible viscous flow problems by the coupling of arbitrary Lagrangian–Eulerian FEM and BEM. The model based on the Navier–Stokes equations in primitive variables is able to solve the infinite boundary-value problems by extracting the boundary effects on a specified finite computation domain, using the pressure projection method. In the model, the Navier–Stokes equations are

Copyright © 2001 John Wiley & Sons, Ltd. 

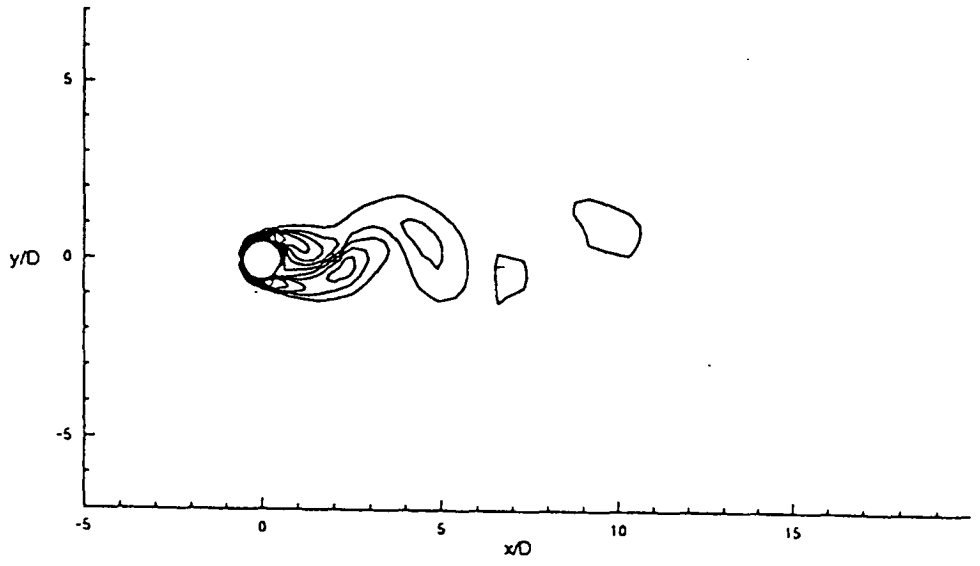


Figure 20. Vorticity distribution for oscillation of circular cylinder–spring system in a uniform flow, $Re = 106$.

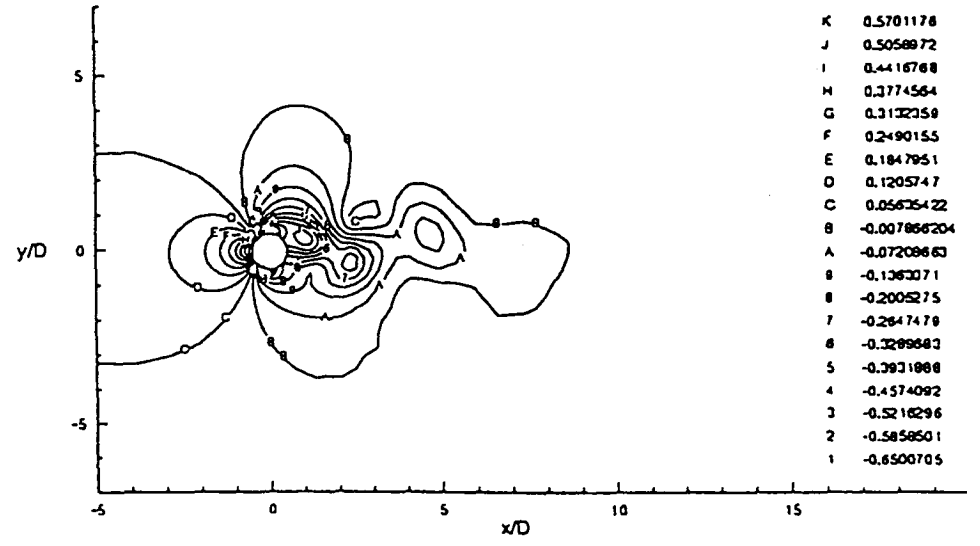


Figure 21. Pressure field for oscillation of circular cylinder–spring system in a uniform flow, $Re = 106$.

Copyright © 2001 John Wiley & Sons, Ltd. 

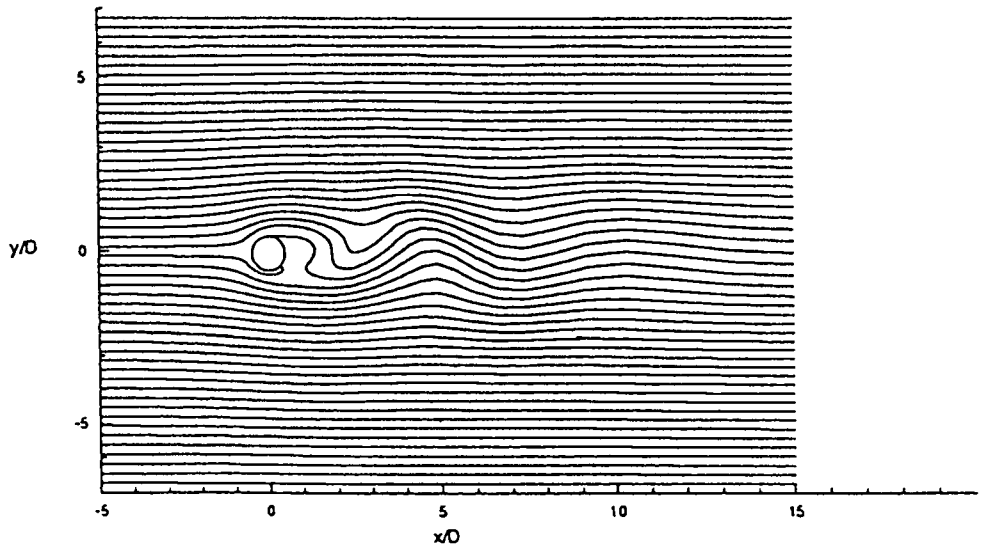


Figure 22. Streamlines for oscillation of circular cylinder–spring system in a uniform flow, $Re = 106$.

solved using a three-step FEM and the Poisson type pressure equations are solved using BEM. By coupling the FEM and BEM, the model is able to handle infinite-domain problems efficiently. The arbitrary Lagrangian–Eulerian method is used to incorporate the moving boundary problems. The model has been efficiently applied to solve various external flow problems such as flow across a cylinder, acceleration and deceleration of a moving circular cylinder in a still fluid and the vibration of the circular cylinder induced by the vortex shedding. All the applications gave reasonable and satisfactory results and show the feasibility and accuracy of the present model in dealing with external flow problems with infinite domain and moving boundaries.

## ACKNOWLEDGEMENTS

The work reported in this paper was supported by the National Science Council of Taiwan. It is greatly appreciated.

## REFERENCES

1. Peyret R, Taylor TD. *Computational Methods for Fluid Flow*, Springer Physics in Computational Physics. Springer: New York, 1983.
2. Jordan SK, Fromm JE. Oscillatory drag, lift, and torque on a circular cylinder in a uniform flow. *The Physics of Fluids* 1972; **15**:371–376.
3. Braza M, Chassaing P, Minh HH. Numerical study and physical analysis of the pressure and velocity fields in the near wake of a circular cylinder. *Journal of Fluid Mechanics* 1986; **165**:79–139.
4. Taylor C, Hughes TG. *Finite Element Programming of The Navier–Stokes Equations*. Pineridge Press Limited: Swansea, 1981.
5. Reddy JN, Gartling DK. *The Finite Element Method in Heat Transfer and Fluid Dynamics*. CRC Press: London, 1992.
6. Power H, Wrobel LC. *Boundary Integral Methods in Fluid Mechanics*. Computational Mechanics Publications: Southampton, 1995.

Copyright © 2001 John Wiley & Sons, Ltd. 

7. Tezduyar TE, Ganjoo DK. Petrov–Galerkin formulations with weighting functions dependent upon spatial and temporal discretization: applications to transient convection–diffusion problems. *Computer Methods in Applied Mechanics and Engineering* 1985; **59**:249–271.
8. Donea J. A Taylor–Galerkin method for convective transport problems. *International Journal for Numerical Methods in Engineering* 1984; **20**:101–119.
9. Jiang CB, Kawahara M. The analysis of unsteady incompressible flows by a three-step finite element method. *International Journal for Numerical Methods in Fluids* 1993; **16**:793–811.
10. Partridge PW, Brebbia CA, Wrobel LC. *The Dual Reciprocity Boundary Element Method.* Computational Mechanics Publications and Elsevier Applied Science: Southampton, 1992.
11. Huerta A, Liu WK. Viscous flow with large free surface motion. *Computer Methods in Applied Mechanics and Engineering* 1988; **69**:277–324.
12. Hirt CW, Amsden AA, Cook JL. An arbitrary Lagrangian–Eulerian computing method for all flow speeds. *Journal of Computational Physics* 1974: **14**:227–253.
13. Hughes TJR, Liu WK, Zimmermann TK. Lagrangian–Eulerian finite element formulation for incompressible viscous flows. *Computer Methods in Applied Mechanics and Engineering* 1981; **29**:329–349.
14. Liggett JA. *Fluid Mechanics.* McGraw-Hill Inc.: New York, 1994.
15. Debler WA. *Fluid Mechanics Fundamentals.* Prentice-Hall: Englewood Cliffs, NJ, 1990.
16. Nomura T, Hughes TJR. An arbitrary Lagrangian–Eulerian finite element method for interaction of fluid and rigid body. *Computer Methods in Applied Mechanics and Engineering* 1992; **95**:115–138.
17. Chorin AJ. Numerical solution of Navier–Stokes equations. *Mathematics of Computation* 1968; **22**:745–762.
18. Temam R. *The Navier–Stokes Equations.* Elsevier: Amsterdam, 1984.
19. Young DL, Liao CB, Sheen HJ. Computations of recirculation zones of a confined annular swirling flow. *International Journal for Numerical Methods in Fluids* 1999; **29**:791–810.
20. Reddy JN. *Finite Element Method.* McGraw-Hill Inc.: New York, 1993.
21. Baker AJ, Pepper DW. *Finite Elements 1.2.3.* McGraw-Hill Inc.: New York, 1991.
22. Brebbia CA, Telles JCF, Wrobel LC. *Boundary Element Techniques—Theory and Applications in Engineering.* Springer: Berlin, 1984.
23. Gresho PM, Chan ST, Lee RL, Upson CD. A modified finite element method for solving the time-dependent, incompressible Navier–Stokes equations, Part 2: application. *International Journal for Numerical Methods in Fluids* 1984; **4**:619–640.
24. Li J, Chambarel M, Donneaud M, Martin R. Numerical study of laminar flow past one and two circular cylinders. *Computers and Fluids* 1991; **19**(2):155–170.
25. Schlichting H. *Boundary-Layer Theory* (6th edn). McGraw-Hill: New York, 1968.
26. Anagnostopoulos P, Bearman PW. Response characteristics of a vortex-excited cylinder at low Reynolds number. *Journal of Fluids and Structures* 1992; **6**:115–138.
27. Nomura T. Finite element analysis of vortex-induced vibrations of bluff cylinders. *Journal of Wind Engineering and Industrial Aerodynamics* 1993; **46/47**:587–594.
28. Roshko A. On the wake and drag of bluff bodies. *Journal of Aeronautical Science* 1955; **22**:124–135.

Copyright © 2001 John Wiley & Sons, Ltd. 

ELSEVIER

Engineering Analysis with Boundary Elements 24 (2000) 449–457

ENGINEERING ANALYSIS *with* BOUNDARY ELEMENTS

www.elsevier.com/locate/enganabound

# Solution of the advection–diffusion equation using the Eulerian–Lagrangian boundary element method

D.L. Young*, Y.F. Wang, T.I. Eldho

*Department of Civil Engineering and Hydrotech Research Institute, National Taiwan University, Taipei 10617, Taiwan, ROC*

Received 14 September 1999; received in revised form 5 May 2000; accepted 19 May 2000

**Abstract**

In this paper, an Eulerian–Lagrangian boundary element method (ELBEM) is proposed by the combination of the Eulerian–Lagrangian method and boundary element method for the solution of advection–diffusion problems. Based on the concept of Eulerian–Lagrangian method (ELM), the formulation of ELBEM and its associated fundamental solution is obtained for the advection–diffusion equation. Combining ELM and BEM makes it easier to handle the variable velocity field. The ELBEM model performs well for both advection-dominated and diffusion-dominated flow fields. To verify the feasibility and accuracy of the ELBEM, the model is applied to different case studies of advection–diffusion problems and the analytical solutions are compared. Fairly accurate results are obtained in all the case studies for the entire range of Peclet numbers, from very small to infinite with less oscillations, numerical dispersion and diffusion problems. © 2000 Elsevier Science Ltd. All rights reserved.

*Keywords*: Eulerian–Lagrangian method; BEM; Advection–diffusion problem

## 1. Introduction

In general, the advection–diffusion equations are solved using numerical models based on the finite difference method (FDM), finite element method (FEM) and boundary element methods (BEM). Developments of numerical models based on these methods have shown that numerical diffusion and dispersion are the two major problems of concern. Popular methods like the upwind FDM [1,2] and upwind FEM [3,4] work well only for problems in which the diffusion effect dominates. In general, the high-order upwind schemes produce numerical oscillations in the results, while the lower-order upwind schemes cannot avoid the numerical diffusion. To improve stability, Ikeuchi et al. [5] used a high-order finite element to establish a stable transport model. However, the resulting stability criteria required very high-order finite elements, as the Peclet number is increased.

The Eulerian–Lagrangian method (ELM) is a widely used scheme for transport modeling. It is a combination of the Eulerian method, in which the equation is solved on a fixed grid in space, and Lagrangian method that utilizes either a deforming grid or a fixed grid in deforming coordinates. The (ELM) combines aspects of both approaches: so as to merge the simplicity of a fixed Eulerian grid with the computational power of the Lagrangian method [6]. In the transport model using ELM, the advection part is solved by the Lagrangian method that can be computed independently at each time step by the method of characteristics applied to a grid fixed domain. The remaining diffusion part can be solved by FEM [6–9] or FDM [10,11], on a separate grid. The influence of the advection is projected from one grid to another by local interpolation. The sharp front of the concentration is easier to trace since the system matrix becomes symmetric and diagonal. Nevertheless, numerical smearing is still observed especially for the diffusion-dominated low Peclet number problems.

In recent years, BEM has been used successfully to analyze various types of potential, diffusion and solid mechanics problems. Besides the forementioned domain-type FDM and FEM transport models, the BEM has been applied in recent times for the analysis of transport phenomena. In the earlier works of transport modeling using BEM [12–15], only the constant velocity distribution is permitted. To avoid this limitation and extend the applicability of BEM, Taigbenu and Liggett [16], Tanaka et al. [17], treated the convection term as an inhomogeneous source to

* Corresponding author. Tel./fax: +886-2-2362-6114.
*E-mail address:* dlyoung@hy.ntu.edu.tw (D.L. Young).

0955-7997/00/$ - see front matter © 2000 Elsevier Science Ltd. All rights reserved.
PII: S0955-7997(00)00026-6

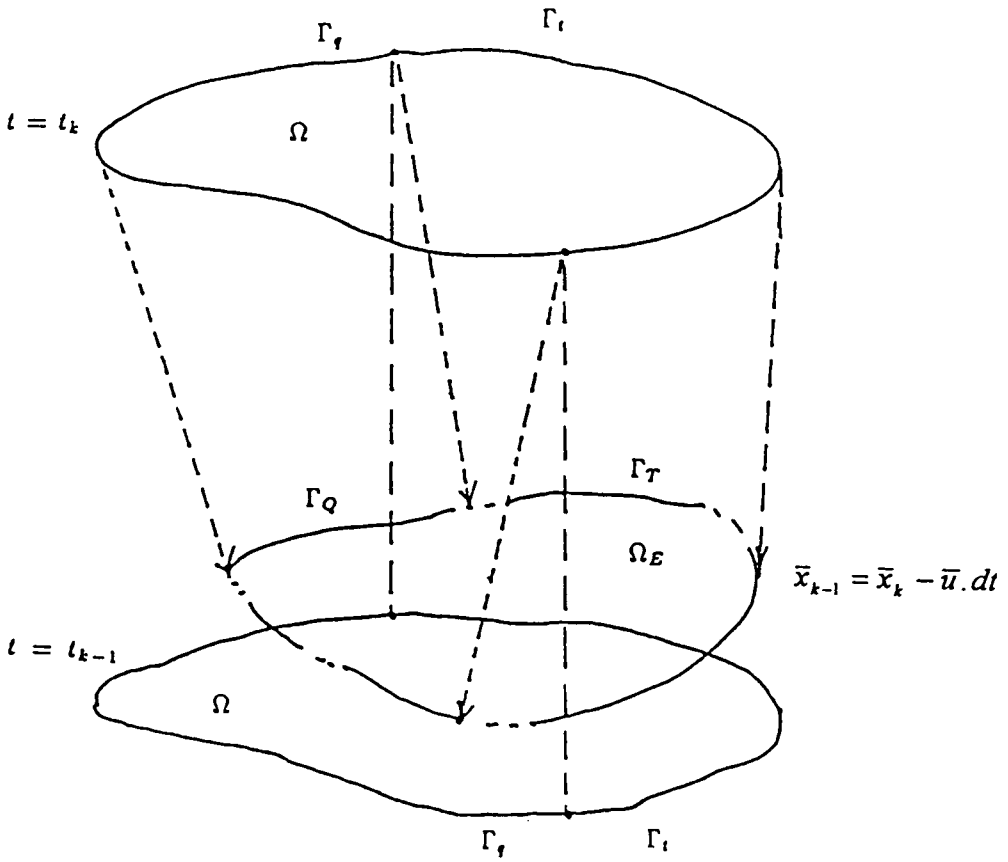


Fig. 1. Characteristic domain $\Omega_E$ and boundaries $\Gamma_T$, $\Gamma_Q$.

consider velocity fields that are more general. Numerical experiments showed that, with large Peclet numbers the relative error became exponential and the efficiency of BEM reduced, as in other domain type formulations [17].

Ikeuchi and Sakakihara [18] and Okamoto [19] presented a transformed BEM without inhomogeneous sources. Although the model has been found to be stable and accurate for all tested Peclet numbers, the velocity profile is required to satisfy the transform conditions of the transformed boundary element model. Based on the concept of time splitting or fractional steps method, Kakuda and Tosaka [20] and Sakakihara [21] proposed the BEM models for advection–diffusion and viscous fluid flows. Arbitrary velocity profiles were allowed for these models. Numerical dispersion has occurred for the simulated examples of the time splitting method, and the finite difference formulation was needed for the fractional step method.

In the present study, an ELBEM is proposed. Based on the concept of ELM, the formulation of ELBEM and its associated fundamental solution has been obtained for an advection–diffusion equation. The ELBEM is capable of handling the variable velocity field. The ELBEM performed well for both the advection- and diffusion-dominated flow fields. The interpolation procedure for the ELM computation of the convection part has been replaced by a more accurate BEM interior point evaluation, and hence the interpolation error is avoided. Compared to other numerical methods, some of the advantages of the ELBEM model include: less numerical diffusion and dispersion problems, direct flux solution at boundaries, and easiness in discretization and data preparation. The numerical examples provided verify the accuracy and feasibility of ELBEM models.

## 2. Governing equation and boundary conditions

The general governing equation for transport phenomena describing the unsteady convection–diffusion problem can be expressed as [22]:

$$\frac{\partial C}{\partial t} + \bar{u}\nabla C = +K\nabla^2 C + Q_s \text{ in } \Omega \tag{1}$$

where $\Omega$ is the flow domain with a boundary $\Gamma$, $\bar{u}(\bar{x}, t) = +(u, v, w)$ a given velocity field, $C$ is the pollutant concentration or temperature or salinity, $K$ is the diffusivity, $Q_s$ is the source or sink term of concentration and $t$ is the time.

For convection–diffusion problems, the initial and boundary conditions should be prescribed. The initial condition, usually a prescribed concentration, is described throughout the domain at some initial time as

$$C = C_i(\bar{x}) \text{ in } \Omega, \ t = 0 \tag{2}$$

Two common types of boundary conditions prescribed are

$$C = C_o(t) \text{ on } \Gamma_t,\ 0 < t \tag{3}$$

$$q = -K\frac{\partial C}{\partial n} + (\bar{u}C)\cdot\bar{n} = q_o(t) \text{ on } \Gamma_q,\ 0 < t \tag{4}$$

where $q$ is the normal flux, $-K(\partial C/\partial n)$ is the diffusive flux and the $(\bar{u}C)\cdot\bar{n}$ is the convective flux.

## 3. Numerical formulation

Owing to the Eulerian–Lagrangian concept, the computational domain is now chosen along the characteristic domain, as shown in Fig. 1, and the convection diffusion equation is rewritten by a hydrodynamic derivative within this new domain as

$$\frac{DC}{Dt} = K\nabla^2 C + Q_s \text{ in } \Omega_E \tag{5}$$

where the hydrodynamic derivative is defined as

$$\frac{D}{Dt} = \frac{\partial}{\partial t} + \bar{u}\cdot\nabla \tag{6}$$

The initial and boundary conditions are now defined as,

$$C = C_i(\bar{x}) \text{ in } \Omega_E,\ t = 0 \tag{7}$$

$$C = C_o(t) \text{ on } \Gamma_T,\ 0 < t \tag{8}$$

$$q = -K\frac{\partial C}{\partial n} = +q_o(t) \text{ on } \Gamma_Q,\ 0 < t \tag{9}$$

where $\Omega_E$ is the characteristic domain with a boundary $\Gamma_E(=\Gamma_T \cup \Gamma_Q)$.

Now, using Green's second identity, the boundary integral equations can be derived on the characteristic domain as,

$$\begin{aligned}\alpha(\bar{x}_i, t_k)C(\bar{x}_i, t_k) = &\int_{\Omega_E} \hat{C}(\bar{x}_i, t_k; \bar{x}, t_{k-1})C(\bar{x}, t_{k-1})\,d\Omega_E \\ &- \int_{tk-1}^{tk}\int_{\Gamma_E} \hat{C}(\bar{x}_i, t_k; \bar{x}, t)q(\bar{x}, t)\,d\Gamma_E\,dt \\ &+ \int_{tk-1}^{tk}\int_{\Gamma_E} \hat{q}(\bar{x}_i, t_k; \bar{x}, t)C(\bar{x}, t)\,d\Gamma_E\,dt \\ &+ \int_{tk-1}^{tk}\int_{\Omega_E} \hat{C}(\bar{x}_i, t_k; \bar{x}, t)Q_s(\bar{x}, t)\,d\Omega_E\,dt\end{aligned} \tag{10}$$

in which $\alpha$ is the Cauchy principal value, $k$ is the current time step, $\bar{x}_i$ is the position vector of base point, $\bar{x}$ is any field point and $q$,$\hat{q}$ are the flux terms defined in the following equations:

$$q(\bar{x}, t) = -K\frac{\partial C}{\partial n} \tag{11}$$

$$\hat{q}(\bar{x}, t) = -K\frac{\partial \hat{C}}{\partial n} \tag{12}$$

The associated fundamental solution $\hat{C}$ satisfying the source varying formally adjoint operator of the governing Eq. (5) can be derived from the following equation.

$$\frac{D\hat{C}}{Dt} - K\nabla^2\hat{C} = \delta(\bar{x} - \bar{x}_i)\delta(t - t_k) \tag{13}$$

Now, the fundamental solutions can be derived for the 1D, 2D and 3D problems [23,24],

$$\hat{C}(\bar{x}, t; \bar{x}_i, t_k) = \left[\frac{1}{[4\pi K(t - t_k)]^{n/2}}\exp[-r^2/4K(t - t_k)]\right] \tag{14}$$

where $r = |\bar{x} - \bar{x}_i|$ is the Cartesian distance between the base point and any field point. For 1D, 2D and 3D problems, $n$ is equal to 1, 2 and 3, respectively.

The integral Eq. (10) implies that the boundary conditions and initial condition are treated as a continuous distribution of the impulse, acting on the domain surface. The first term on the right-hand side of the integral Eq. (10), which is in the form of a volume integral, represents the initial influence. The second and third terms of the right-hand side, which are in the form of boundary integrals, express the responses of the boundary conditions. The last integral term is the sink or source effect.

As shown in Fig. 1, for each time step $t_k$, the computational domain $\Omega_E$ coincides with the physical domain $\Omega$ only at $t = t_k$, and the boundary conditions and initial condition are given on the physical boundary $\Gamma$, and the physical domain $\Omega$ of time step $t = t_{k-1}$. However, the boundary and initial values are required to be imposed in the integral terms of Eq. (10) on the computational characteristics boundary $\Gamma_E$ ($\Gamma_T U \Gamma_Q$), and the domain $\Omega_E$ of time step $t = t_{k-1}$. Without using the traditional backward-tracking interpolation procedure, a forward-tracking method is used to evaluate the prescribed boundary condition and the last time step solutions for the characteristic domain in this study. Thus, since the important information of the flow field can be transferred from the last time step, the error arising from the interpolation procedure can be reduced. The region of the characteristic domain is determined by the method of characteristics as

$$\frac{d\bar{x}}{dt} = +\bar{u} \tag{15}$$

$$\bar{x}_{k-1} = \bar{x}_k - \bar{u}\cdot dt \tag{16}$$

The fractional step technique or the Runge–Kutta scheme could be used to improve the accuracy of the integration with respect to the time domain.

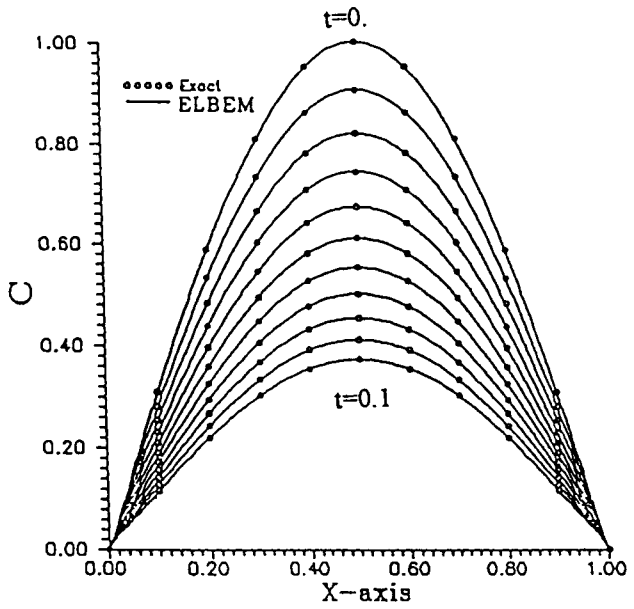


Fig. 2. Concentration profile for every 10 time steps: comparison of ELBEM and exact solutions, Example 1.

The boundary element approach [24] is used to solve the boundary integral Eq. (10) and its associated boundary and initial conditions. Constant, linear or quadratic shape functions [24] can be used to discretize the temporal and spatial domain as

$$C(\bar{x},t) = F(t)C(\bar{x},t_k) \qquad F(t) = 1,$$

$$\text{at } t_{k-1} \le t \le t_k \text{ on } \Gamma_T \text{ and } \Gamma_Q \tag{17}$$

$$q(\bar{x},t) = F(t)q(\bar{x},t_k) \qquad F(t) = 1,$$

$$\text{at } t_{k-1} \le t \le t_k \text{ on } \Gamma_T \text{ and } \Gamma_Q \tag{18}$$

$$C(\bar{x},t_k) = \sum_{j=1}^{N} G_j(\bar{x})C(\bar{x}_j,t_k) \quad \text{at } t = t_k \text{ on } \Gamma_T \text{ and } \Gamma_Q \tag{19}$$

$$q(\bar{x},t_k) = \sum_{j=1}^{N} G_j(\bar{x})q(\bar{x}_j,t_k) \quad \text{at } t = t_k \text{ on } \Gamma_T \text{ and } \Gamma_Q \tag{20}$$

$$C(\bar{x},t_k) = \sum_{l=1}^{M} H_l(\bar{x})C(\bar{x}_l,t_k) \quad \text{at } t_{k-1} \le t \le t_k \text{ on } \Gamma_T \text{ and } \Gamma_Q \tag{21}$$

where $G_j(\bar{x})$ and $H_l(\bar{x})$ are the space interpolation functions defined over the boundary and the domain, respectively, $N$ is the number of the boundary nodes and $M$ is the number of nodes of discretization for the volume integral. The use of constant elements for the temporal domain allows the analytical integration of time in Eq. (10) [24].

In integral Eq. (10), after approaching the base point to the boundary nodes on $\Omega_E$ at $t = t_k$, and imposing the boundary conditions and initial conditions, a simultaneous equation system can be written in a matrix form as,

$$[A]_{NxL1}\{C\}_{L1x1} + [B]_{NxL2}\{q\}_{L2x1} = \{\text{R.H.S}\}_{Nx1} \tag{22}$$

in which $L_1 + L_2 = N$. The element matrices $[A]$ and $[B]$ are defined as

$$A_{ij} = \int_{tk-1}^{tk} \int_{\Gamma Q} \hat{q}(\bar{x}_i,t_k;\bar{x}_j,t)G_j(\bar{x})\,d\Gamma_Q\,dt;$$

$$B_{ij} = -\int_{tk-1}^{tk} \int_{\Gamma T} \hat{C}(\bar{x}_i,t_k;\bar{x}_j,t)G_j(\bar{x})\,d\Gamma_T\,dt \tag{23}$$

In Eq. (22), {R.H.S} represents the known values after the application of the initial conditions, boundary conditions and the effect of source or sinks. If the time interval used is the same, the elements included in the matrices $[A]$ and

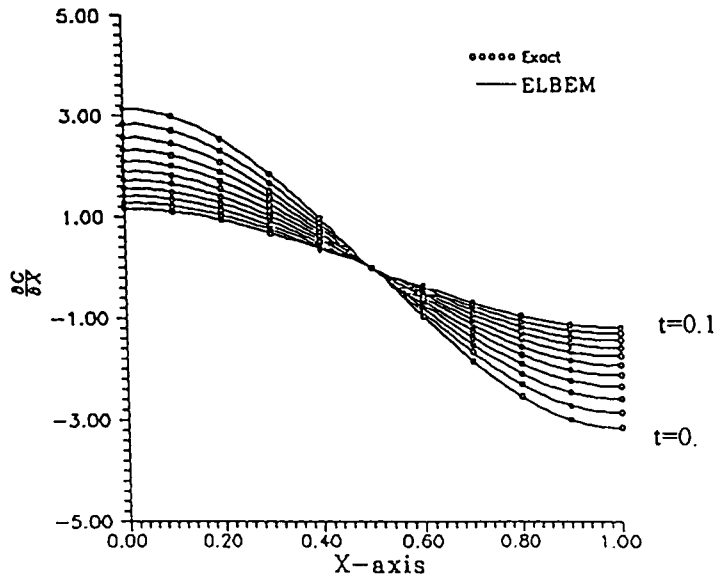


Fig. 3. Concentration gradient profile for every 10 time steps: comparison of ELBEM and exact solutions, Example 1.

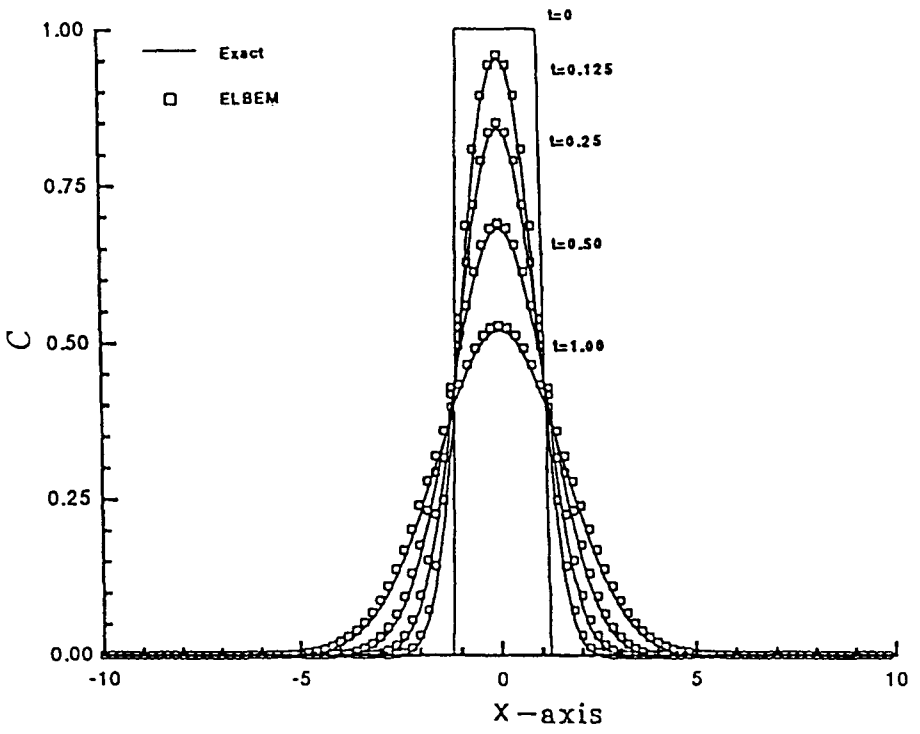


Fig. 4. Concentration distribution for an unbounded domain with $M = 200$ for various time steps, Example 2.

$[B]$ will not be changed for every time step. Only the right-hand side vector {R.H.S} should be evaluated for each time step due to the changes of the time dependent boundary conditions and the integration of the previous time step solutions. More details of the element properties, interpolation functions, time integration and equation system formation used in this paper are described in Brebbia et al. [24], therefore it is not repeated here.

## 4. Numerical examples

The following numerical examples are analyzed to verify the accuracy of the proposed ELBEM model, and show the advantages of the model for the unbounded domain problem and the forward-tracking procedure for evaluating the last time step solution on the characteristic domain. Numerical examples are presented for 1D, 2D and 3D advection–diffusion problems.

### 4.1. Example 1

The first numerical example is a 1D pure diffusion problem. The domain considered is a bounded domain $x \in [0,1]$. The diffusivity $K = 1.0$, time step $\delta t = 0.001$ and 81 constant elements are used for the volume discretization. The initial distribution is given by,

$$C(x,0) = \sin(\pi x) \tag{24}$$

For 100 time step simulations, the time histories of the concentration distributions are compared with the exact solution,

$$C(x,t) = \sin(\pi x)\,\mathrm{Exp}\,(-K\pi^2 t) \tag{25}$$

Fig. 2 shows the concentration distribution and Fig. 3 shows the concentration gradient for a time step interval of 10, in comparison with the analytical solutions. Good agreement is observed between the ELBEM solution and the exact solution.

### 4.2. Example 2

Here, the ELBEM is used to solve the 1D advection–diffusion problem with an unbounded domain. A uniform distribution of concentration with unit magnitude is given between $x \in [-1,1]$ as the initial condition. The boundary condition is placed at the $x \to \pm\infty$, the diffusivity $K = 1$, the Courant number $Cr = 0.5$ and 200 constant elements are used for the volume discretization. The time histories of the concentration are compared with the exact solutions,

$$C(x,t) = \frac{1}{2}\left\{\mathrm{erf}\left(\frac{1-x'}{2K\sqrt{t}}\right) - \mathrm{erf}\left(\frac{-1+x'}{2K\sqrt{t}}\right)\right\} \quad x' \le -1$$

$$= \frac{1}{2}\left\{\mathrm{erf}\left(\frac{1-x'}{2K\sqrt{t}}\right) + \mathrm{erf}\left(\frac{1+x'}{2K\sqrt{t}}\right)\right\} \quad -1 < x' < 1$$

$$= \frac{1}{2}\left\{\mathrm{erf}\left(\frac{1+x'}{2K\sqrt{t}}\right) - \mathrm{erf}\left(\frac{-1+x'}{2K\sqrt{t}}\right)\right\} \quad x' \ge 1;$$

$$x' = x + \mathrm{u.t} \tag{26}$$

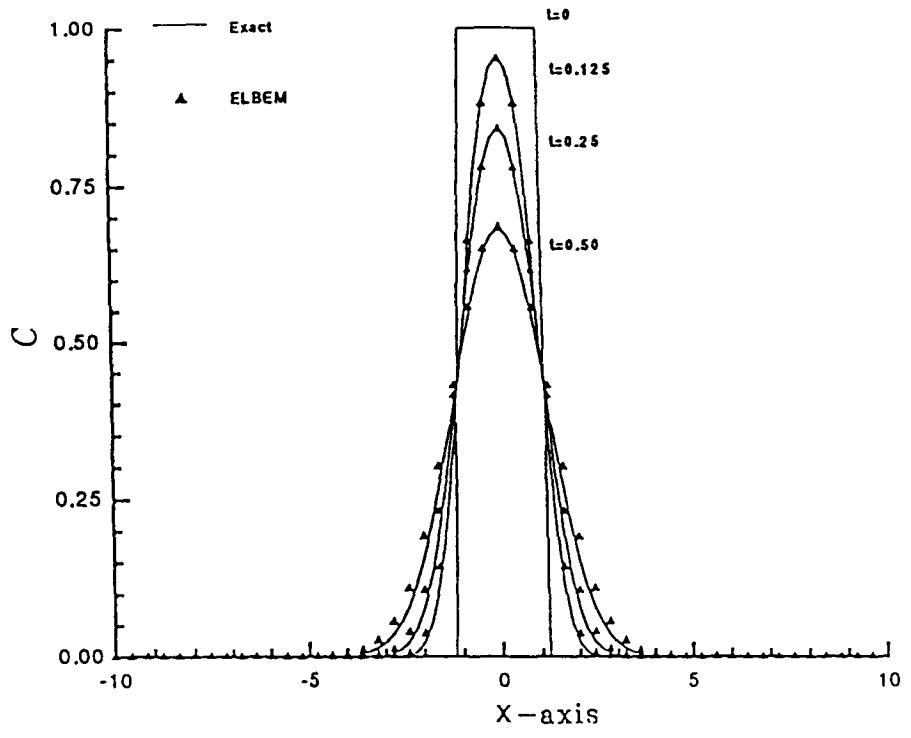


Fig. 5. Concentration distribution for an unbounded domain with $M = 100$ for various time steps (with forward-tracking), Example 2.

Fig. 4 shows the concentration distribution in comparison with the exact solution, and a good agreement is observed between the solutions. Numerical experiments carried out with various discretizations ($M = 50$, 100 and 200) showed that, the accuracy of the solution decreases with a coarse mesh. In order to achieve good accuracy for coarse mesh, a forward-tracking procedure is proposed to simulate the advection effects. Fig. 5 shows the concentration distribution in comparison with the exact solution for $M = 100$, using the forward-tracking procedure. Reasonably good

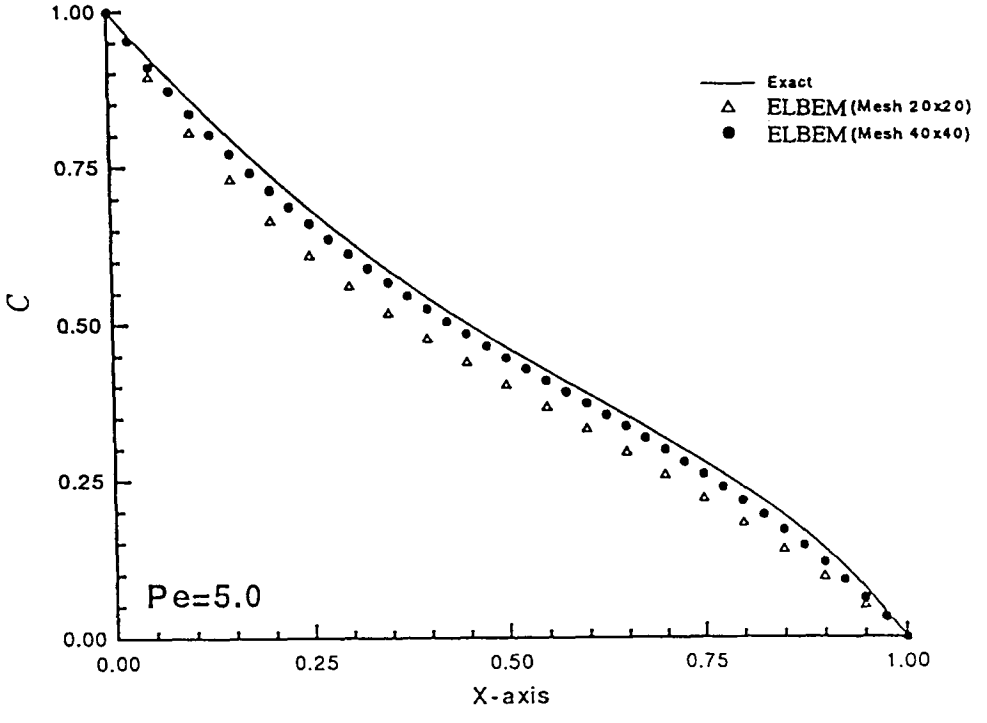


Fig. 6. Concentration profile for Example 3: comparison of ELBEM and the exact solution.

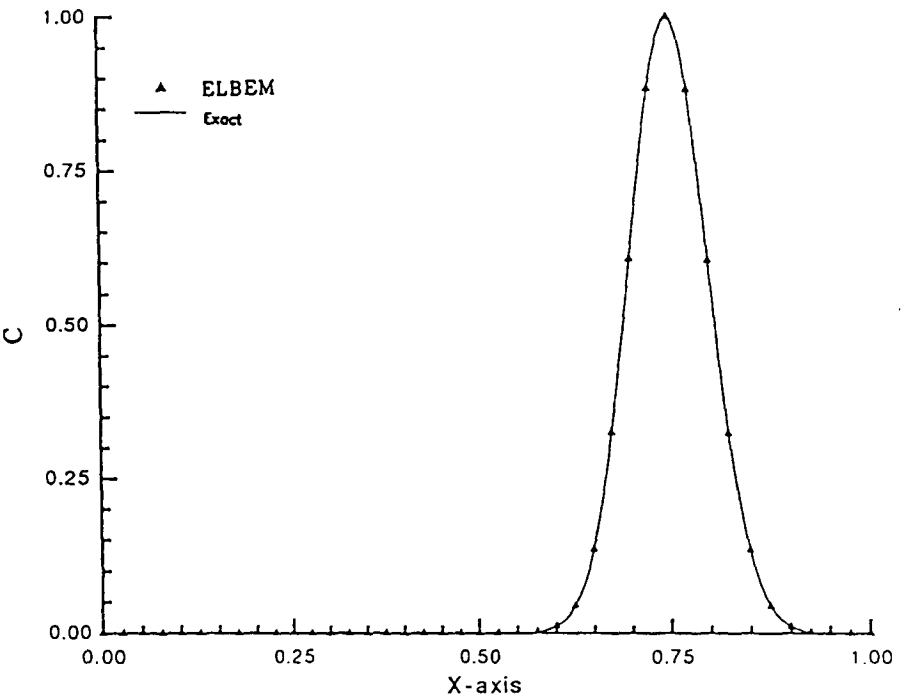


Fig. 7. Concentration distribution at $t = 2\pi$ for a rotating cone: comparison of ELBEM and the exact solution, Example 4.

agreement is observed for the coarse mesh with the forward-tracking technique. This problem shows the feasibility of ELBEM for the unbounded domain and the exterior problem.

### 4.3. Example 3

Here, we consider an advection–diffusion problem in the 2D domain. The problem is a bounded rectangular domain. The initial concentration is assumed to be zero. A boundary condition with $\sin(\pi y)$ concentration profile is imposed on the boundary $(0,y)$, and zero concentration is assumed on all other boundaries. The diffusivity is assumed to be unity and a time step of 0.01 is used (dimensionless). The 2D ELBEM simulates the flow field with constant $u = u_o$, $v = 0$ till steady state is achieved. Two types of domain discretizations are used with meshes ($20 \times 20$) and ($40 \times 40$). The computations are carried out for Peclet numbers of 0.0, 0.1, 0.5, 1.0 and 5 (with various flow velocities $u$). For all the Peclet numbers, very stable and comparable results with analytical solutions are obtained. Here we present the results for Peclet number 5. Fig. 6 shows the concentration along $(x,0.5)$ at steady state and compared with the exact solution for Peclet number 5. A good agreement is observed between the solutions, especially for the finer mesh. This case study shows the effectiveness of the ELBEM model for the 2D advection–diffusion problems and also shows the mesh sensitivity.

### 4.4. Example 4

Here, we consider a pure advection problem (the Peclet number is infinite) in a 2D domain. This example is the classic rotating cone problem [25,26]. In order to compare the ELBEM solution for the 2D hyperbolic case, we followed the precedent and placed a 'concentration cone' in a pure rotation velocity field [25,26]. The exact solution is simply a solid body rotation of the initial field. The radius of the cone is four grid units ($4\Delta x$) and the grid employs $40 \times 40$ uniform square elements. The (prescribed) velocity field is one of pure (solid body) rotation, $u = -(y - y_0)$, $v = (x - x_0)$ and physical diffusion is absent. As described in Pironneau [25], initially a normal distribution of concentration is assumed and the concentration on the boundaries is assumed to be zero. After a cycle, the rotating cone is moves back to the initial position. The results from this pure advection problem at various time periods are found and compared with the results of Pironneau [25] and Orszag [26]. Fig. 7 shows the concentration distribution at time $t = 2\pi$ in comparison with the analytical solution [25,26]. The ELBEM solution is in good agreement with the exact solution and proves the feasibility of the model for pure advection problems.

### 4.5. Example 5

In this example, a 3D diffusion problem is solved using the ELBEM model, and the results are compared with the derived exact solutions. Here, a unit cubic domain with a unit concentration on one side and zero concentration on the opposite side is considered for analysis. The concentration flux is assumed to be zero on all other faces. Initially, zero concentration is assumed throughout the domain. A mesh of

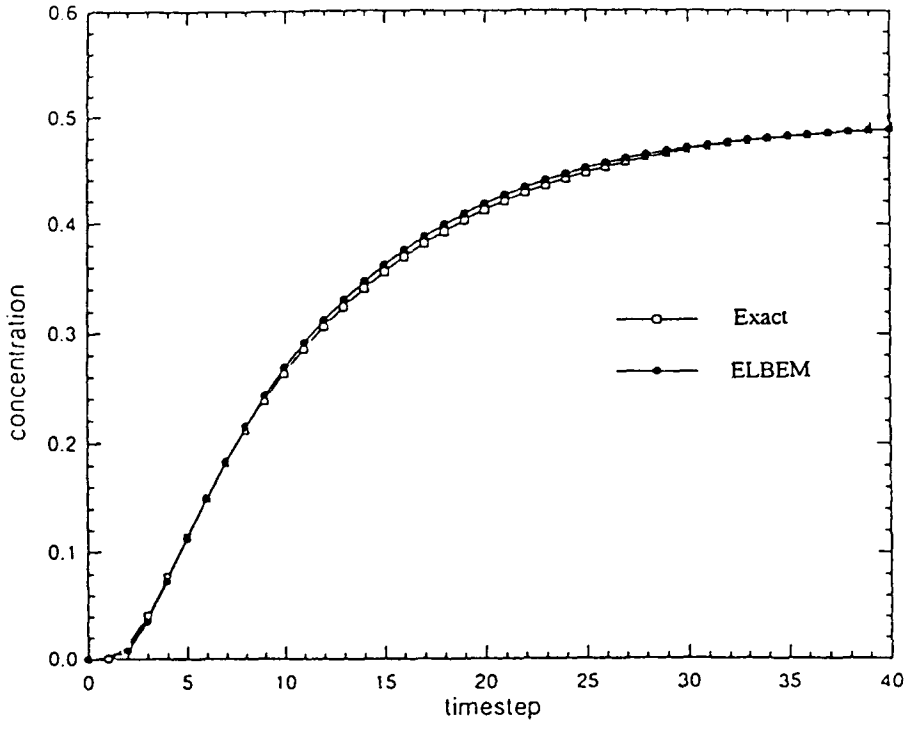


Fig. 8. Concentration distribution for various time steps: comparison of ELBEM and the exact solution, Example 5.

$6 \times 6 \times 6$ has been used for discretization. Here, the diffusivity coefficient is assumed as unity. Fig. 8 shows the concentration variation for various time steps in comparison with the derived exact solution and the ELBEM solutions for the diffusion case (no advection), at the center of the domain ($x = 0.5$, $y = 0.5$ and $z = 0.5$). The results show a good agreement with the exact solutions and demonstrate the 3D capability of the model. A further detailed verification of the presented ELBEM model for the 3D advection–diffusion problems with analytical solutions and other numerical models are described in Young et al. [27,28].

In the present study, we have described most problems with a constant velocity field. However, the present ELBEM model could easily handle the variable velocity field as described in Young et al. [27,28] and the model performs well for both the advection- and diffusion-dominated flow fields. Even though domain integration is necessary for transport simulation, it retains all the advantages of the BEM including lesser numerical dispersion and diffusion problems compared to other domain-oriented numerical techniques. The presented numerical examples in 1D, 2D and 3D show the applicability of ELBEM for the entire range of Peclet numbers from very small to infinity, with less oscillations and numerical smearing.

## 5. Concluding remarks

An Eulerian–Lagrangian boundary element method (ELBEM) is developed by the combination of the Eulerian–Lagrangian method and BEM. With ELBEM, it is easy to handle the variable velocity field, and the model performs well for both the advection- and diffusion-dominated flow fields. The interpolation procedure for the Eulerian–Lagrangian computation of the advection part has been improved by the process of BEM interior point evaluation. Even though domain integration is necessary, the ELBEM model has got all the advantages of the BEM including less numerical diffusion and dispersion problems. The simulations of various numerical examples presented in 1D, 2D and 3D demonstrated the accuracy and feasibility of ELBEM model. The numerical dispersion caused by the backward tracking of the characteristics is improved by the forward tracking and suitable interpolation techniques shall be imposed to improve the computations.

## Acknowledgements

The work reported in this paper was supported by the National Science Council, Taiwan. It is greatly appreciated.

## References

[1] Sharif MAR, Busnainam AA. Assessment of finite difference approximations for the advection terms in the simulation of practical flow problems. J Comp Phys 1988;74:143–76.

[2] Busnania AA, Zheng X, Sharif MAR. A modified skew upwind scheme for fluid flow and heat transfer computations. Appl Math Modelling 1991;15:425–32.

[3] Heinrich JC, Huyakorn PS, Zienkiewics OC, Mitchell AR. An upwind

finite element scheme for two-dimensional convective transport equation. Int J Numer Methods Engng 1977;11:131–43.
[4] Sun NZ, Yeh WWG. A proposed upstream weight numerical method for simulating pollutant transport in groundwater. Water Res Res 1983;19(6):1489–500.
[5] Ikeuchi M, Sakakihara M, Niki H. Stability of finite element solutions for steady-state convective diffusion equations. Trans IECE Jpn 1982;E65(11):684–5.
[6] Neuman SP. A Eulerian–Lagrangian numerical scheme for the dispersion–convective equation using conjugate space–time grids. J Comp Phys 1981;41:270–94.
[7] Neuman SP. Adaptive Eulerian–Lagrangian finite element method for advection–dispersion. Int J Numer Methods Engng 1984;20:321–37.
[8] Cady R, Neuman SP. Three-dimensional adaptive Eulerian–Lagrangian finite element method for advection–dispersion, Computational methods in water resources, vol. 2. Numerical methods for transport and hydrologic processes. Proceedings of the VII International Conference, MIT, USA, 1988, p. 183–93.
[9] Szymkiewics R. Solution of the avection–diffusion equation using the spline function and finite elements. Commun Numer Methods Engng 1993;9:197–206.
[10] Li CW. Advective–dispersion simulation by minimisation characteristics and alternate direction-explicit methods. Appl Math Modelling 1991;15:616–23.
[11] Hong LD, Akiyama J, Ura M. A Eulerian–Lagrangian method with monotonic interpolation function for transport equation. Proceedings of the 25th IAHR Congress, vol. V, Tokyo, Japan, 1993, p. 47–54.
[12] Ikeuchi M. Transient solution of convective diffusion problem by boundary element method. Trans IECE Jpn 1985;E68(7):435–40.
[13] Tanaka Y, Honma T, Kaji I. Mixed boundary element solutions using both of constant and linear elements for a steady-state convective diffusion problem in three dimensions. Trans IECE Jpn 1984;E67(8):445–6.
[14] Tanaka Y, Honma T, Kaji I. On mixed boundary element solutions of convection–diffusion problems in three dimensions. Appl Math Modelling 1986;10:170–5.
[15] Chan CL, Chandra A. An algorithm for handling corners in the boundary element method: application to conduction–convection equations. Appl Math Modelling 1991;15:244–55.
[16] Taigbenu A, Liggett JA. An integral solution for the diffusion–advection equation. Water Resour Res 1986;22(8):1237–46.
[17] Tanaka Y, Honma T, Kaji I. Mixed boundary element solutions for three-dimensional convection–diffusion problem with a velocity profile. Appl Math Modelling 1987;11:402–10.
[18] Ikeuchi M, Sakakihara M. Boundary elements in steady convective diffusion problems. J Comput Appl Math 1985;12&13:381–9.
[19] Okamoto N. Analysis of convective diffusion problem with first-order chemical reaction by boundary element method. Int J Numer Methods Fluids 1988;8:55–64.
[20] Kakauda K, Tosaka N. Boundary element analysis of viscous flow problems using the time splitting method. In: Brebbia CA, editor. Boundary element methods in engineering, Berlin: Springer, 1990. p. 87–93.
[21] Sakakihara M. Fractional step boundary element method for convection diffusion problems. In: Tanaka M, editor. Applications in stress analysis, potential and diffusion, Boundary elements XII, vol. 1. Berlin: Springer, 1990. p. 192–9.
[22] Liggett JA. Fluid mechanics. New York: McGraw-Hill, 1994.
[23] Carslaw HS, Jaegar JC. Conduction of heat in solids. 2nd ed. Oxford: Clarendon Press, 1959.
[24] Brebbia CA, Telles JCF, Wrobel LC. Boundary element techniques — theory and applications in engineering. Berlin: Springer, 1984.
[25] Pironneau O. Finite element methods for fluids. New York: Wiley, 1989. p. 81.
[26] Orzag S. Numerical simulation of incompressible flows with simple boundaries: accuracy. J Fluid Mech 1971;49:75–112.
[27] Young DL, Her BC, Wang YF. Three-dimensional mathematical modeling of pollutant transport in stratified estuaries. In: Lee JH et al., editors. Environmental hydraulics. Rotterdam: Balkema, 1999. p. 93–7.
[28] Young DL, Her BC, Eldho TI. BIEM modeling of 3D circulation and transport in stratified estuaries. J Engng Mech, ASCE, in press.

ELSEVIER

Engineering Analysis with Boundary Elements 24 (2000) 549–557

ENGINEERING ANALYSIS *with* BOUNDARY ELEMENTS

www.elsevier.com/locate/enganabound

# Solution of Poisson's equation by iterative DRBEM using compactly supported, positive definite radial basis function

A.H.-D. Cheng[a,*], D.-L. Young[b], C.-C. Tsai[b]

[a]*Department of Civil and Environmental Engineering, University of Delaware, Newark, DE 19716, USA*
[b]*Department of Civil Engineering, National Taiwan University, Taipei, Taiwan, R.O.C.*

**Abstract**

In the numerical solution of three-dimensional boundary value problems, the matrix size can be so large that it is beyond a computer's capacity to solve it. To overcome this difficulty, an iterative dual reciprocity boundary element method (DRBEM) is developed to solve Poisson's equation without the need of assembling a matrix. The DRBEM procedure requires that the right hand side of Poisson's equation be approximated by a radial basis function interpolation. In the iterative solution, it is found that only compactly supported, positive definite radial basis functions lead to converged results. © 2000 Elsevier Science Ltd. All rights reserved.

*Keywords*: Boundary element method; Dual reciprocity boundary element method; Radial basis function; Iterative method; Poisson's equation

## 1. Introduction

In the numerical solution of complex three-dimensional problems, a large number of discrete unknowns are required to accurately represent the geometry and the solution variation. When the matrix representing the linear or nonlinear system of equations is assembled, its size can be so large such that it poses difficulty for the computer to store it in the random access memory and to solve it by elimination. Consequently, the matrix size becomes the limiting factor that defines the largest problem a given computer can solve.

In the finite difference method (FDM), the need for assembling a solution matrix can be circumvented by using the so-called relaxation technique pioneered by Southwell [1,2]. To apply this technique, an initial trial solution is assigned to a solution grid. The discrete values at each node is corrected in an iterative manner, until convergence is achieved. No matrix or matrix solution is needed. Because of this advantage, large size fluid dynamic problems are typically solved by the finite difference method, not by the finite element method (FEM). It appears that this iterative solution idea can be extended to the boundary element method (BEM).

A search in the literature finds a number of BEM solutions that utilize iterative techniques [3–7]. However, matrices were assembled in those implementations. Iterative techniques were used only to invert the matrices. These methods do not meet our definition.

Iterative BEMs that do not assemble solution matrices do exist. To our knowledge, the first such attempt was made by Cahan, et al. [8] for solving Laplace's equation based on the direct BEM formulation. Later, an improved version was presented by Cahan and Lafe [9]. An iterative BEM based on the indirect formulation was devised for solving the governing equations of stochastic boundary value problems [10,11]. In those stochastic problems, not only the mean, but also the covariances are obtained. For a boundary geometry discretized into $N$ nodes, the number of unknown covariances is $N^2$. The matrix, if assembled, would be of the size $N^2 \times N^2$. These unusually large sizes have necessitated the use of an iterative technique.

In this paper, we shall revisit the iterative BEM with the goal of solving Poisson's equation. The inhomogeneous right-hand side is treated by the dual reciprocity boundary element method (DRBEM) [12]. The underlying reason for the current practice is to construct an efficient algorithm to solve three-dimensional fluid dynamics problems governed by Navier–Stokes equations. By a velocity–vorticity formulation and a time-marching scheme, Navier–Stokes equations can be transformed into a number of Poisson's and Helmholtz-type equations. The iterative DRBEM can then be implemented for these equations. In this paper, however, only two-dimensional Poisson's equations are solved as a demonstration of the methodology.

* Corresponding author. Tel.: +1-302-831-2442; fax: +1-302-831-3640.
*E-mail address:* cheng@chaos.ce.udel.edu (A.H.-D. Cheng).

0955-7997/00/$ - see front matter © 2000 Elsevier Science Ltd. All rights reserved.
PII: S0955-7997(00)00035-7

As a part of the DRBEM solution process, the right hand side of Poisson's equation is approximated by an interpolation using radial basis functions. The coefficients of the interpolation are determined by collocation. Iterative methods are developed to avoid the assemblage of matrices. However, it is discovered that when conventional radial basis functions are used, none of the iterative methods tested converges. In fact, only the recently derived compactly supported, positive definite radial basis functions [13] can achieve convergence. These and other findings are reported in this paper.

## 2. Formulation of DRBEM

The governing equation investigated is Poisson's equation,

$$\nabla^2\phi(\mathbf{x}) = f(\mathbf{x}) \tag{1}$$

In a DRBEM formulation, the right-hand side of Eq. (1) is interpolated using a combination of monomials and radial basis functions: [14]

$$f(\mathbf{x}) = \sum_{i=1}^{n_r} \alpha_i \varphi(r_i) + \sum_{i=1}^{n_p} \beta_i p_i(\mathbf{x}) \tag{2}$$

where $\varphi(r)$ is a radial basis function, $r_i = \|\mathbf{x}_i - \mathbf{x}\|$ is the Euclidean distance between a field point $\mathbf{x}$ and the $i$th collocation point $\mathbf{x}_i$, $p_i(\mathbf{x})$ is a multi-variate monomial, $\alpha_i$ and $\beta_i$ are coefficients to be determined by collocation and constraint equations, $n_r$ is the number of collocation nodes, and $n_p$ is the number of monomial terms needed to support the convergence and stability of the approximation scheme [14]. The collocation nodes are distributed in the interior as well as on the boundary, hence their number is relatively large. $\alpha_i$ and $\beta_i$ need to be solved from Eq. (2) prior to the implementation of the BEM. In addition, we need to find the particular solutions of the following Poisson's equations using the radial and monomial basis functions as the right hand side:

$$\nabla^2\psi = \varphi(r) \tag{3}$$

$$\nabla^2 q_i = p_i; \qquad i = 1, \ldots, n_p \tag{4}$$

The analytical expressions for $\psi$ and $q_i$ can be found in the literature [14,15], hence is not repeated here. We shall return to more details of the RBF in Section 4.

Given a radial-basis-function interpolation, a 'boundary-only' integral equation that solves Poisson's Eq. (1) can be found as [12]

$$c(\mathbf{x})\phi(\mathbf{x}) = c(\mathbf{x})\left[\sum_{i=1}^{n_r} \alpha_i \psi(\mathbf{x} - \mathbf{x}_i) + \sum_{i=1}^{n_p} \beta_i q_i(\mathbf{x})\right] + \int_\Gamma G(\chi - \mathbf{x})\left[\frac{\partial\phi(\chi)}{\partial n(\chi)} - \sum_{i=1}^{n_r} \alpha_i \frac{\partial\psi(\chi - \mathbf{x}_i)}{\partial n(\chi)} - \sum_{i=1}^{n_p} \beta_i \frac{\partial q_i(\chi)}{\partial n(\chi)}\right] \mathrm{d}\chi - \int_\Gamma \frac{\partial G(\chi - \mathbf{x})}{\partial n(\chi)}\left[\phi(\chi) - \sum_{i=1}^{n_r} \alpha_i \psi(\chi - \mathbf{x}_i) - \sum_{i=1}^{n_p} \beta_i q_i(\chi)\right] \mathrm{d}\chi \tag{5}$$

where $\mathbf{x}$ is the base point, $\chi \in \Gamma$ is a field point, $\mathbf{x}_i \in \Omega$ is a collocation point, $\Gamma$ denotes the solution boundary, and $\Omega$ the solution domain, $c$ is a geometric factor equal to 0, 1/2, or 1, depending on the location of $\mathbf{x}$, $n$ is the outward normal direction of $\Gamma$, and $G$ is the free-space Green's function given by

$$G = -\frac{\ln r}{2\pi} \tag{6}$$

for two-dimensional problems, with $r = \|\chi - \mathbf{x}\|$. We note that the second integral in Eq. (5) is strongly (Cauchy) singular when $\mathbf{x} \in \Gamma$, due to the presence of the kernel $\partial G/\partial n$. The integration is performed in the Cauchy principal value sense and is denoted by $\int$.

We observe that Eq. (5) is in a natural form for an iteration procedure. Similar to the relaxation method, we can assign a set of initial trial values to all boundary nodes. We then apply Eq. (5) by placing the base point on a boundary node where $\phi$ is an unknown. Performing the integration and summation according to the right hand side of Eq. (5), we obtain an updated value of $\phi$ at that node. We then move on to the next node and repeat the procedure.

In a mixed boundary value problem, there exist nodes on which $\partial\phi/\partial n$, instead of $\phi$, is the unknown. To have a formula for this situation, the dual integral equation approach [16] is taken. Eq. (5) can be differentiated at a boundary point $\mathbf{x} \in \Gamma$ in the direction of boundary normal $n$. The resultant equation is a hypersingular equation containing Hadamard finite part integrals denoted by $\oint$ :

$$c(\mathbf{x})\frac{\partial\phi(\mathbf{x})}{\partial n(\mathbf{x})} = c(\mathbf{x})\left[\sum_{i=1}^{n_r} \alpha_i \frac{\partial\psi(\mathbf{x} - \mathbf{x}_i)}{\partial n(\mathbf{x})} + \sum_{i=1}^{n_p} \beta_i \frac{\partial q_i(\mathbf{x})}{\partial n(\mathbf{x})}\right] + \int_\Gamma \frac{\partial G(\chi - \mathbf{x})}{\partial n(\mathbf{x})}\left[\frac{\partial\phi(\chi)}{\partial n(\chi)} - \sum_{i=1}^{n_r} \alpha_i \frac{\partial\psi(\chi - \mathbf{x}_i)}{\partial n(\chi)} - \sum_{i=1}^{n_p} \beta_i \frac{\partial q_i(\chi)}{\partial n(\chi)}\right] \mathrm{d}\chi - \oint_\Gamma \frac{\partial^2 G(\chi - \mathbf{x})}{\partial n(\chi)\,\partial n(\mathbf{x})}\left[\phi(\chi) - \sum_{i=1}^{n_r} \alpha_i \psi(\chi - \mathbf{x}_i) - \sum_{i=1}^{n_p} \beta_i q_i(\chi)\right] \mathrm{d}\chi \tag{7}$$

The pair of integral Eqs. (5) and (7), can be alternately used in Neumann and Dirichlet type boundary conditions to update the missing boundary values. The process continues until convergence is reached.

The hypersingular Eq. (7), however, adds to the complexity of the solution. The hypersingularity needs to be regularized before its finite part can be evaluated. Several techniques exist [16]. In this paper we choose to avoid this issue by using only the Cauchy singular Eq. (5). To overcome the difficulty of solving mixed boundary value problems, the iterative scheme suggested by Cahan and Lafe [9] is adopted. Details of the method are presented in the next section.

## 3. Iterative scheme

To devise a scheme that uses only Eq. (5), we seek its discretized form, which can be expressed as follows:

$$\sum_{k=1}^{N} a_{jk}\phi^k - \sum_{k=1}^{N} b_{jk}\phi_n^k = c_j, \qquad j = 1,\ldots,N \tag{8}$$

where $\phi^k$ is the discrete value of $\phi$ at node $k$, $\phi_n^k$ is the discrete value of $\partial\phi/\partial n$ at node $k$, coefficients $a_{jk}$, $b_{jk}$, and $c_j$ are constants obtained by integration over the elements. Given either a Dirichlet or a Neumann type condition, we can extract the corresponding unknown variable $\partial\phi/\partial n$ and $\phi$, respectively, to form the following iterative formulae

$$\phi_n^j = \frac{1}{b_{jj}}\left[-c_j + \sum_{k=1}^{N} a_{jk}\phi^k - \sum_{\substack{k=1\\k\neq j}}^{N} b_{jk}\phi_n^k\right], \qquad \text{if } \phi^j \text{ is given} \tag{9}$$

$$\phi^j = \frac{1}{a_{jj}}\left[c_j - \sum_{\substack{k=1\\k\neq j}}^{N} a_{jk}\phi^k - \sum_{k=1}^{N} b_{jk}\phi_n^k\right], \qquad \text{if } \phi_n^j \text{ is given} \tag{10}$$

Hence the pair of Eqs. (9) and (10) forms the basis of an iterative scheme. Particularly, a procedure similar to the Gauss–Seidel scheme, in which an updated datum is immediately put into use in the evaluation of next datum, can be applied.

The above equations differ from a typical FDM relaxation formula in that the solution at a given node is dependent on values on all nodes of the boundary, not just a few neighboring nodes. An advantage of this property is that in the summation of Eqs. (9) and (10) half of the data are already correct, supplied by the known boundary conditions. This allows zero initial trial values be assigned to all the unknowns. The first correction can already bring the solution into a reasonable range of the true solution. Hence a stable scheme is expected.

In a standard BEM, Eqs. (9) and (10) are assembled into a matrix system

$$[\mathbf{A}]\{\mathbf{x}\} = \{\mathbf{b}\} \tag{11}$$

where $[\mathbf{A}]$ is an $N \times N$ matrix. In the current iterative scheme, $[\mathbf{A}]$ is not assembled. Its elements are calculated on the fly and immediately discarded. Hence only column matrices of size $N$ are needed. We also notice that all quantities under the summation signs in Eqs. (5) and (6) are known quantities that do not change from iteration to iteration. These parts are computed only once and stored in an array of size $N$.

The need for regenerating elements in the coefficient matrix over and over is a major disadvantage of the iterative method as the cost of numerical integration can be high. This problem is alleviated by the use of low-order elements, over which exact integration is available. For the current implementation, constant elements and their exact integrations are used. Hence the cost of integration is minimized.

## 4. Radial basis functions

The theoretical basis of radial basis function (RBF) and its application in DRBEM have been well explored by Golberg, Chen, and co-workers in a series of articles. See, for example, Golberg et al. [14] for a recent review. There exist a number of RBFs, such as the conical, spline, Gaussian, and multiquadric types. The conical type is given by

$$\varphi(r) = r^{2n-1}, \qquad n = 1,2,3,\ldots \tag{12}$$

The polyharmonic spline functions typically give better performance [17] and are given by

$$\varphi(r) = r^{2n}\ln r, \qquad n = 1,2,3,\ldots \tag{13}$$

The case $n = 1$ is known as the thin-plate spline. As indicated in Eq. (2), these RBFs need to be supplemented by a monomial family

$$p_i = \{1, x, y, x^2, y^2, xy, x^3, \ldots\} \tag{14}$$

to ensure proper convergence and stability of the scheme. Take for example, for the thin-plate spline $r^2 \ln r$, terms up to linear order, $\{1, x, y\}$, need to be included. For higher order splines $r^{2n}\ln r$, terms up to $n$th order must be incorporated.

The interpolation of the function $f(\mathbf{x})$ in Eq. (2) is accomplished by solving a set of collocation equations

$$\sum_{i=1}^{n_r} \alpha_i \varphi(r_{ij}) + \sum_{i=1}^{n_p} \beta_i p_i(\mathbf{x}_j) = f(\mathbf{x}_j), \qquad j = 1,2,\ldots,n_r \tag{15}$$

where $r_{ij} = \|\mathbf{x}_i - \mathbf{x}_j\|$, $n_r$ is the number of collocation nodes, and $n_p$ is the number of monomial terms needed. To determine the additional coefficients associated with the monomial terms, the following constraint equations are imposed:

$$\sum_{i=1}^{n_r} \alpha_i p_j(\mathbf{x}_i) = 0, \qquad \text{for } j = 1,2,\ldots,n_p \tag{16}$$

Eqs. (15) and (16) form a linear system of $n_r + n_p$ equations, solving for the $n_r + n_p$ unknowns, $\alpha_i$ and $\beta_i$. As

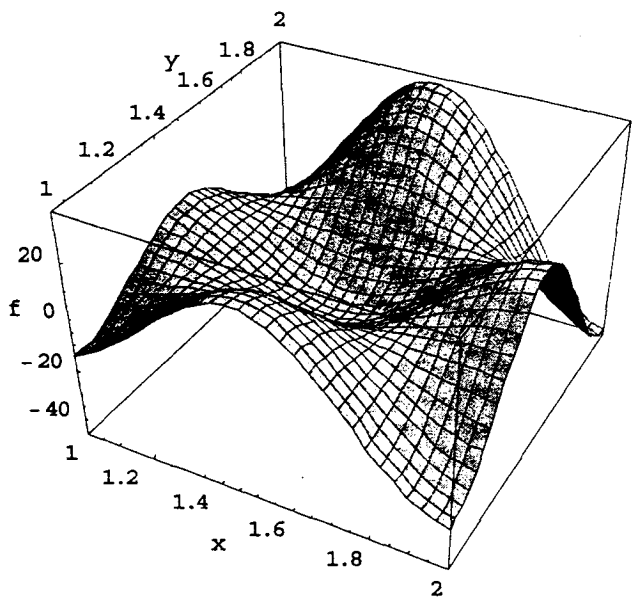


Fig. 1. The right hand side of Poisson's Eq. (23).

mentioned above, the number of monomial terms needed is dependent on the order of the RBF.

In an iterative scheme, the matrix corresponding to the linear systems (15) and (16) is not assembled. The matrix elements given as $\varphi(r_{ij})$, $1, x_i, y_i$, etc. are instantly generated. Because of their simple form, the computation time is minimal.

Several standard iterative techniques, such as the Gauss–Seidel method and the conjugate gradient method, have been employed to perform the iteration. However, to our surprise, none of the iterative schemes worked! Replacing the RBF from spline types to conical types makes no difference. For the Gauss–Seidel method, a check of convergence condition shows that the spectral radius is greater than 1, hence the solution diverges as expected. For the conjugate gradient method, a check of the matrices shows that they are not positive definite. Convergence is not guaranteed.

Indeed, as commented by Chen, et al. [18] all of the above-mentioned RBFs are globally defined. The resulting interpolation matrix is dense and can be highly ill-conditioned, especially for a large number of interpolation points. This can cause serious stability problems. It was suggested [19] that the difficulty can be overcome by the use of a compactly supported, positive definite RBF (CS-PD-RBF) [13].

CS-PD-RBFs became available only recently. It was demonstrated by Wendland [13] that for a given dimension $d$ and smoothness $C^{2k}$, a positive definite radial basis function in the form of a univariate polynomial of minimal degree always exists, and is unique within a constant factor. Results were given for $d = 1, 3, 5$. For the current two-dimensional problems, we choose two of the CS-PD-RBFs [13,18]: for $d = 3$ and $k = 0$

$$\varphi(r)\begin{cases}\left(1-\frac{r}{a}\right)^2, & \text{for } 0 \le r \le a\\ 0, & \text{for } r > a\end{cases} \tag{17}$$

and for $d = 3$ and $k = 1$

$$\varphi(r)\begin{cases}\left(1-\frac{r}{a}\right)^4\left(1+\frac{4r}{a}\right), & \text{for } 0 \le r \le a\\ 0, & \text{for } r > a.\end{cases} \tag{18}$$

Although $d = 3$ is used in the above, the corresponding CS-PD-RBF is valid for any lower dimension, which is a consequence of positive definiteness. Hence they are valid for the current two-dimensional problems. In the above, $a$ is an influence radius beyond which the function is truncated to zero. The influence radius controls the density of the matrix. If $a$ is larger than the largest span of the domain, the matrix is fully populated. If $a$ is smaller than the smallest distance between two collocation nodes, the matrix becomes diagonal. A proper $a$ value should fall between these two limits.

The interpolation equation for CS-PD-RBF is given by

$$f(\mathbf{x}) = \sum_{i=1}^{n_r} \alpha_i \varphi(r_i) \tag{19}$$

As compared to Eq. (15), we notice that polynomial terms are not needed for the CS-PD-RBF, for its positive definiteness. The coefficients $\alpha_i$ are determined from the collocation equations

$$\sum_{i=1}^{n_r} \alpha_i \varphi(r_{ij}) = f(\mathbf{x}_j), \qquad j = 1, 2, \ldots, n_r \tag{20}$$

The implementation of an iterative scheme solving the above system will be discussed in Section 5.

For the purpose of DRBEM implementation, the particular solution satisfying Eq. (3) with the CS-PD-RBF as the right hand side is needed. This has been found by Chen, et al. [18] The particular solution corresponding to Eq. (17) is

$$\psi = \begin{cases}\frac{r^2}{4} - \frac{2r^3}{9a} + \frac{r^4}{16a^2}, & \text{for } 0 \le r \le a\\ \frac{13a^2}{144} + \frac{a^2}{12}\ln\left(\frac{r}{a}\right), & \text{for } r > a.\end{cases} \tag{21}$$

In the second line of the above equation, we have corrected an error that exists (see Table 2 in Ref. [18]). For Eq. (18), the corresponding particular solution is

$$\psi = \begin{cases}\frac{r^2}{4} - \frac{5r^4}{8a^2} + \frac{4r^5}{5a^3} - \frac{5r^6}{12a^4} + \frac{4r^7}{49a^5}, & \text{for } 0 \le r \le a\\ \frac{529a^2}{5880} + \frac{a^2}{14}\ln\left(\frac{r}{a}\right), & \text{for } r > a\end{cases} \tag{22}$$

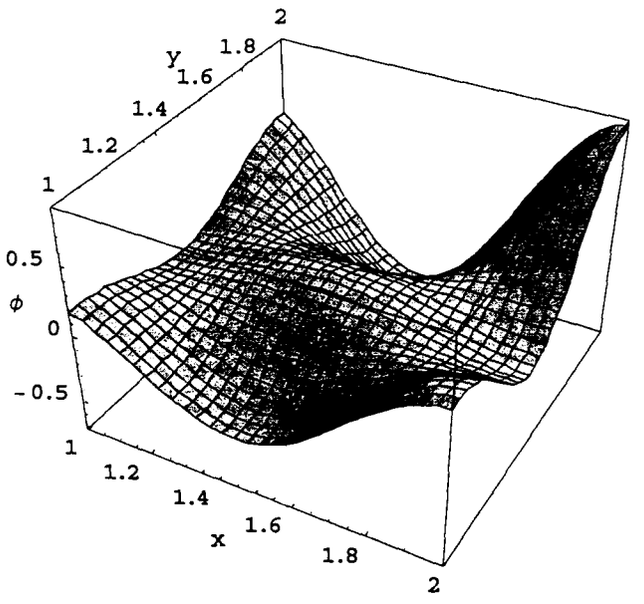


Fig. 2. The solution of Poisson's Eq. (23).

## 5. Example

To test the algorithm, an example with a known exact solution is investigated [15]. The problem is governed by the following Poisson's equation

$$\nabla^2\phi = -\frac{751\pi^2}{144}\sin\frac{\pi x}{6}\sin\frac{7\pi x}{4}\sin\frac{3\pi y}{4}\sin\frac{5\pi y}{4} + \frac{7\pi^2}{12}\cos\frac{\pi x}{6}\cos\frac{7\pi x}{4}\sin\frac{3\pi y}{4}\sin\frac{5\pi y}{4} + \frac{15\pi^2}{8}\sin\frac{\pi x}{6}\sin\frac{7\pi x}{4}\cos\frac{3\pi y}{4}\cos\frac{5\pi y}{4} \quad (23)$$

in the domain of $1 \le x \le 2$ and $1 \le y \le 2$. The right hand side function is plotted in Fig. 1. We observe that it has a relatively large variability. Eq. (23) is subject to the boundary conditions

$$\begin{aligned}
\phi(x,1) &= -\frac{1}{2}\sin\frac{\pi x}{6}\sin\frac{7\pi x}{4}\\
\phi(1,y) &= -\frac{1}{2\sqrt{2}}\sin\frac{3\pi y}{4}\sin\frac{5\pi y}{4}\\
\phi(x,2) &= -\sin\frac{\pi x}{6}\sin\frac{7\pi x}{4}\\
\phi(2,y) &= -\frac{\sqrt{3}}{2}\sin\frac{3\pi y}{4}\sin\frac{5\pi y}{4}
\end{aligned} \quad (24)$$

The exact solution of this problems is

$$\phi = \sin\frac{\pi x}{6}\sin\frac{7\pi x}{4}\sin\frac{3\pi y}{4}\sin\frac{5\pi y}{4} \quad (25)$$

which is plotted as Fig. 2.

The first step of solving this boundary value problem by DRBEM is to approximate the right hand side by a RBF interpolation. A uniform grid of $11 \times 11$ is laid over the domain for collocation. For the iterative solution of the linear system (20), a subroutine *linbcg* found in *Numerical Recipes* [20], based on the iterative bi-conjugate gradient method, is used. The subroutine requires a user-supplied matrix in compacted form. Since the present method does not assemble a matrix, the subroutine needs to be modified. This is easily accomplished by changing a few lines in the subroutine *atimes*, which performs matrix multiplication, called by subroutine *lincbg*.

The iterative method requires an initialization of the solution. By noticing that the diagonal terms of the CS-PD-RBF collocation matrix are all equal to unity, we can simply assign the initial trial values as

$$\alpha_i = f(\mathbf{x}_i), \qquad i = 1, 2, \ldots, n_r \quad (26)$$

For the influence radius, two cases are chosen: $a = 0.5$ and 1.5, which cover about 35 and 100% of the maximum linear dimension of the solution domain, respectively. The first-order CS-PD-RBF defined in Eq. (17) is adopted. The solution converges rapidly. For the case of $a = 0.5$, it takes 8 iterations for the solution to converge to a relative tolerance of $10^{-2}$, and 17 iterations to a tolerance of $10^{-4}$. The iterative scheme is highly efficient.

To investigate the effect of the influence radius and the order of CS-PD-RBF on the rate of convergence, cases are run with different combinations of these factors. The result is presented in Fig. 3. The two lower curves correspond to the first-order CS-PD-RBF defined in Eq. (17). It shows that the use of a larger influence radius that produces a full matrix only slightly increases the number of iterations. The upper two curves correspond to the second-order CS-PD-RBF defined in Eq. (18). The number of iterations has significantly increased, particularly for the larger influence radius case.

We next investigate the effect of the number of nodes, i.e. the size of the system, on the convergence rate. The results presented so far are based on an $11 \times 11$ mesh. We now vary the mesh size. The first-order CS-PD-RBF with the influence radius 0.5 is used in these cases. The tolerance is fixed at $10^{-3}$. Fig. 4 plots the number of iterations versus the number of collocation nodes in log–log scale. The result indicates a relation

$$\text{iteration number} \sim \text{node number}^{1/2} \quad (27)$$

This convergence rate is the same as the successive-over-relaxation (SOR) method of the FDM [20].

The accuracy of the approximation is examined next. We plot in Fig. 5 the relative error, defined as the error normalized by the maximum absolute value of the solution, using the $11 \times 11$ grid and the first-order CS-PD-RBF with $a = 0.5$. The maximum error is found to be 2.8%, located near the corner (2,2). If we use the second-order CS-PD-RBF, the accuracy is only slightly improved, with a maximum error of −2.5%. If the influence radius for the first-order

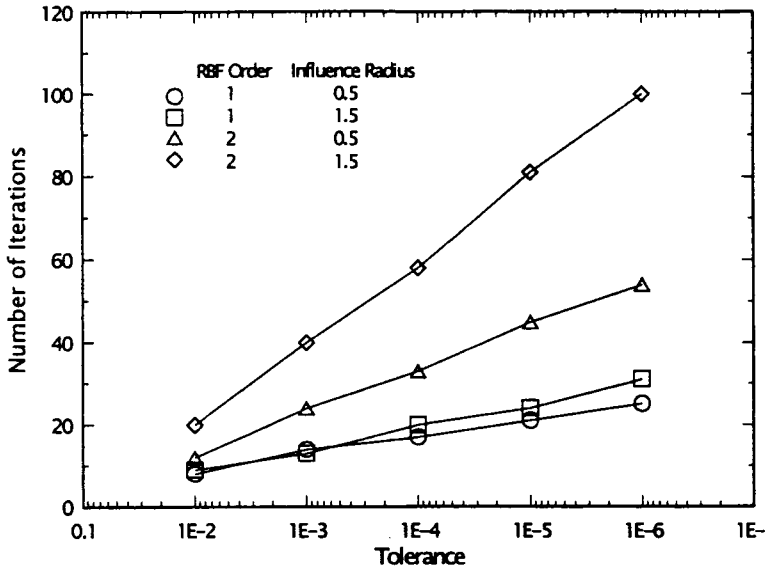


Fig. 3. Iterations needed for solution convergence as a function of tolerance, for different order CS-PD-RBFs and different scaling factors.

CS-PD-RBF is increased to $a = 1.5$, we also see very little improvement, with a maximum error of 2.5% observed. Judging from the performance of accuracy and efficiency, the first-order CS-PD-RBF with $a = 0.5$ will be used in the BEM solution below.

To compare the accuracy of the CS-PD-RBF with other RBFs, the same function on the right hand side of Eq. (23) was approximated by the thin-plate spline RBF using the same $11 \times 11$ collocation nodes. Fig. 6 shows the relative error. We observe that the thin-plate spline RBF, which gives an maximum error of 1.7%, performs better. The same case is also tested for the first-order conical RBF. The maximum error is around 2.6%, comparable to the CS-PD-RBF case. We should comment, however, that both the spline and the conical RBF collocations diverge in the iterative procedure, and have to be obtained by matrix elimination.

The next step is to find the BEM solution using the iterative procedure described in Section 3. The solution boundary is subdivided into 40 constant elements (nodes) with 10 on each side. The $11 \times 11$ collocation mesh is used for RBF interpolation. Fig. 7 plot the relative error of the solution. The maximum error is found to be 2%.

It is of interest to examine the rate of convergence of the iterative DRBEM under different element sizes and accuracy requirements. The problem is solved using four

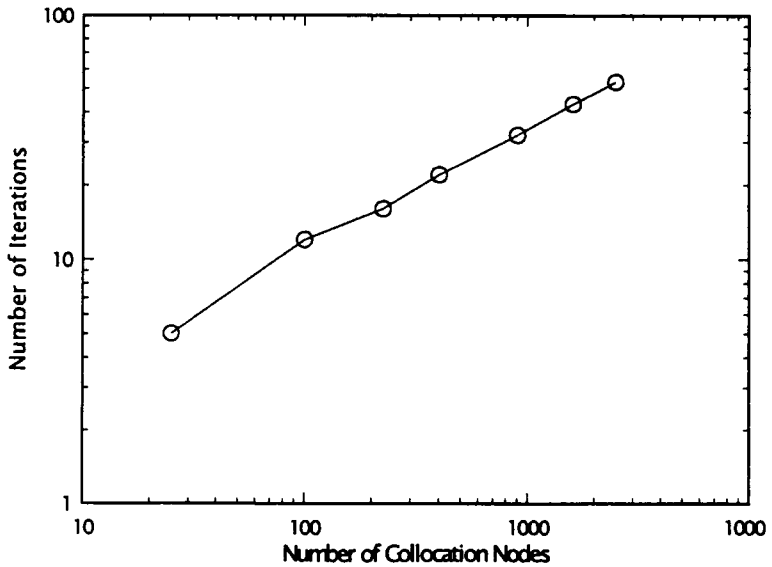


Fig. 4. Number of iterations as a function of the number of collocation nodes.

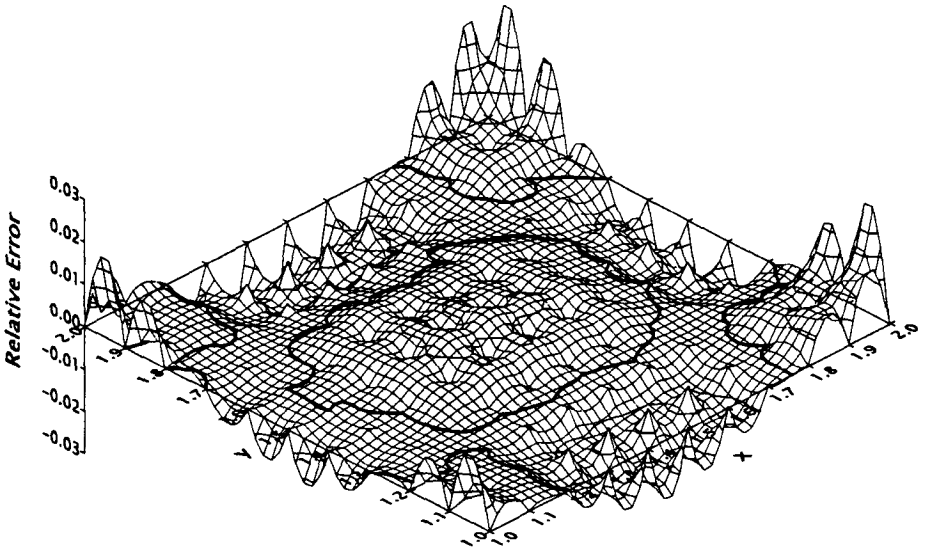


Fig. 5. Relative error of a first-order CS-PD-RBF interpolation. Thick contour lines mark zero error.

different meshes, involving 20, 40, 80, and 160 constant elements. A relative tolerance is defined as

$$\text{tol} = \max\left\{\left|\frac{\text{solution at iteration } \ell - \text{solution at iteration } \ell + 1}{\text{solution at iteration } \ell}\right|\right\} \tag{28}$$

Fig. 8 plots the number of iterations needed for the solution to converge to a specified tolerance versus the number of nodes, in log–log scale. We observe the relation

$$\text{iteration number} \sim \text{node number}^{3/4} \tag{29}$$

This rate of convergence is better than that of the Gauss–Seidel iterative scheme used in FDM, which has a rate proportional to the first power of the node number. It is however, worse than the SOR scheme, which converges at the rate of 1/2 power. We note that the current scheme is not accelerated, hence is equivalent to a Gauss–Seidel scheme. Acceleration should further improve the efficiency of the scheme. Furthermore, we should note that the comparison of efficiency with FDM is made with node number, not mesh size. As the linear dimension of the element size decreases, the node number for the BEM increases linearly for two dimensional problems. For the FDM, the node number increases by a power of 2. Hence the BEM should be highly competitive in solving large size problems.

Fig. 9 presents the number of iterations versus tolerance, in semi-log scale. The relation is roughly a straight line, suggesting

$$\text{iteration number} \sim \log(\text{tol}) \tag{30}$$

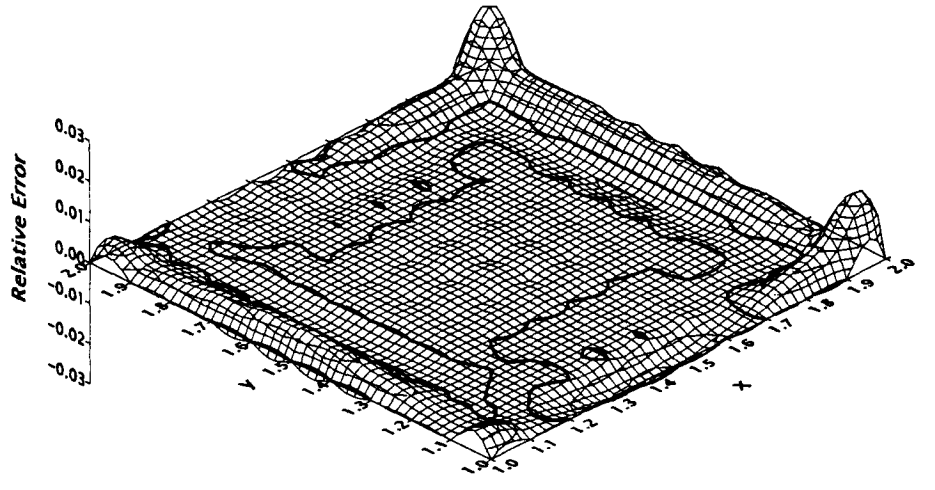


Fig. 6. Relative error of a thin-plate spline RBF interpolation. Thick contour lines mark zero error.

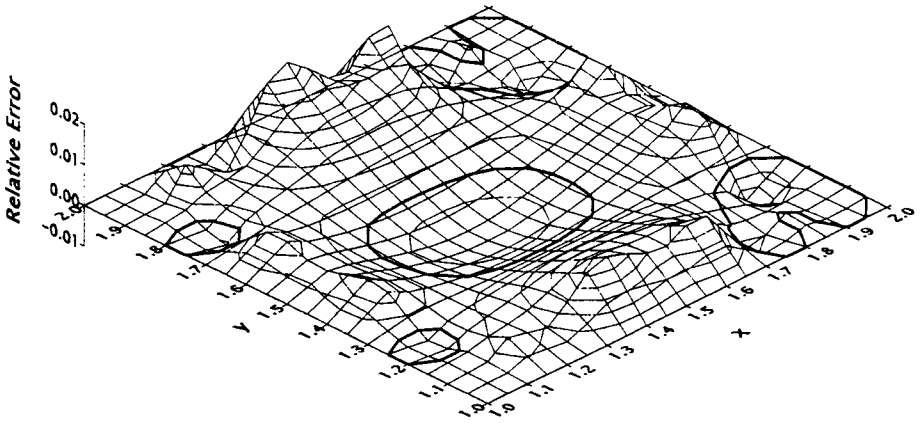


Fig. 7. Relative error of the boundary element solution. Thick contour lines mark zero error.

This behavior is the same as the Gauss–Seidel and the SOR schemes.

## 6. Conclusions

We have conducted a preliminary study in which an iterative DRBEM is constructed to solve problems governed by Poisson's equations. In the application of DRBEM, there are two linear systems to be solved — one involves the RBF interpolation of the right hand side of the Poisson's equation, and the other concerns the boundary integral equation solution. For both systems, they are solved by iterative schemes that do not assemble solution matrix. In the case of the collocation system for the RBF interpolation, it is found that only the compactly supported, positive definite radial basis functions lead to converged results. The accuracy and the convergence rate are investigated and compared with other methods. Although only a two-dimensional problem is solved in the current effort, the findings clearly indicate that the iterative DRBEM is a promising technique for solving large-size three-dimensional problems. This part of study, particularly relating to the solution of Navier–Stokes equations, is underway.

## Acknowledgements

The work reported herein is supported by the National Science Council of the Republic of China (Taiwan), Grant no. NSC 88-2811-E-002-0008, during the first author's sabbatical leave at the National Taiwan University. The discussion with Michael Golberg and C.S. Chen brought our attention to the existence of the CS-PD-RBF. Their assistance is deeply appreciated.

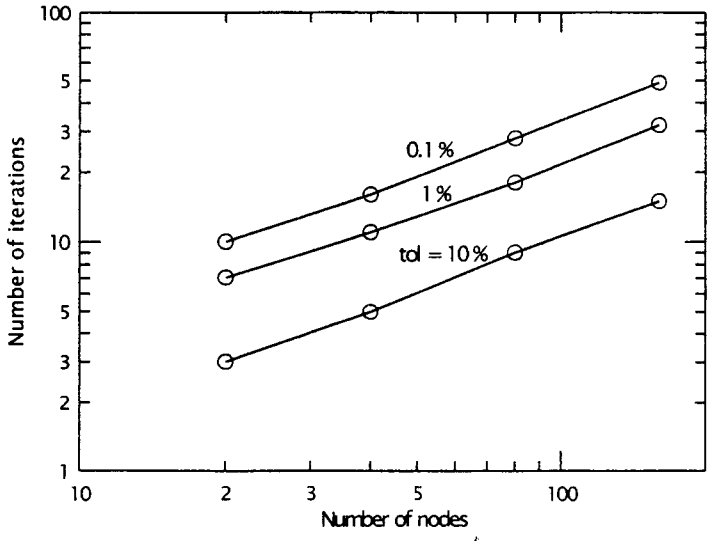


Fig. 8. Convergence rate shown as the number of iterations versus the number of nodes.

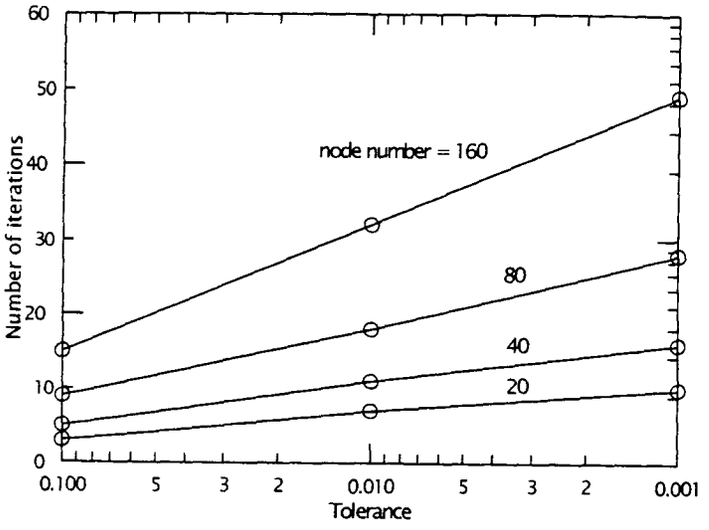


Fig. 9. Convergence rate shown as the number of iterations versus tolerance.

## References


[1] Southwell RV. Relaxation methods in engineering science, A treatise on approximate computation. Oxford: Oxford University Press, 1940.

[2] Southwell RV. Relaxation methods in theoretical physics. Oxford University Press, 1946.

[3] Yang LS, Machidori H, Shirakawa T. BEM and BEM with SOR on the parallel computer QCDPAX. Engng Anal Bound Elem 1996;18:231–7.

[4] Lesnic D, Elliott L, Ingham DB. An iterative boundary element method for solving numerically the Cauchy problem for the Laplace equation. Engng Anal Bound Elem 1997;20:123–33.

[5] Mai-Duy N, Nguyen-Hong P, Tran-Cong T. A fast convergent iterative boundary element method on PVM cluster. Engng Anal Bound Elem 1998;22:307–16.

[6] Merkel M, Bulgakov V, Bialecki R, Kuhn G. Iterative solution of large-scale 3D-BEM industrial problems. Engng Anal Bound Elem 1998;22:183–97.

[7] Valente FP, Pina HLG. Iterative solvers for BEM algebraic systems of equations. Engng Anal Bound Elem 1998;22:117–24.

[8] Cahan BD, Scherson D, Reid MA. I-BIEM. An iterative boundary integral equation method for computer solutions of current distribution problems with complex boundaries-A new algorithm. J Electrochem Soc 1988;135:285–93.

[9] Cahan BD, Lafe OE. On the iterative boundary element method. In: Cheng AH-D, Brebbia CA, Grilli S, editors. Computational engineering with boundary elements, 2: solid and computational problems, Computational Mechanics, 1990. p. 199–209 BETECH90, University of Delaware.

[10] Cheng AH-D, Lafe OE. Boundary element solution for stochastic groundwater flow: random boundary condition and recharge. Water Resour Res 1991;27:231–42.

[11] Cheng AH-D, Abousleiman Y, Ruan F, Lafe OE. Boundary element solution for stochastic groundwater flow:temporal weakly stationary problems. Water Resour Res 1993;29:2893–908.

[12] Partridge PW, Brebbia CA, Wrobel LC. The dual reciprocity boundary element method. Amsterdam: CMP/Elsevier, 1992.

[13] Wendland H. Piecewise polynomial, positive definite and compactly supported radial functions of minimal degree. Adv Comput Math 1995;4:389–96.

[14] Golberg MA, Chen CS, Bowman H. Some recent results and proposals for the use of radial basis functions in the BEM. Engng Anal Bound Elem 1999;23:285–96.

[15] Cheng AH-D, Lafe O, Grilli S. Dual reciprocity BEM based on global interpolation functions. Engng Anal Bound Elem 1994;13:303–11.

[16] Chen JT, Hong H-K. Review of dual boundary element methods with emphasis on hypersingular integrals and divergent series. Appl Mech Rev, ASME 1999;52:17–33.

[17] Partridge P.W. Towards criteria for selection approximation functions in the Dual Reciprocity Method. Engng Anal Bound Elem 2000;24:519–29.

[18] Chen CS, Brebbia CA, Power H. Dual reciprocity method using compactly supported radial basis functions. Commun Numer Meth Engng 1999;15:137–50.

[19] Golberg MA, Chen CS. Private communication, 1999.

[20] Press WH, Teukolsky SA, Vetterling WT, Flannery BP. Numerical recipes in Fortran, the art of scientific computing. 2nd ed. Cambridge: Cambridge University Press, 1992.

# FEM-BEM ANALYSIS OF VORTEX-INDUCED OSCILLATION OF A CIRCULAR CYLINDER

D.L. Young
*Department of Civil Engineering and Hydrotech Research Institute, National Taiwan University, Taipei, Taiwan.*
*dlyoung@hy.ntu.edu.tw*

**Abstract**

This paper describes an innovative computational model developed to solve two-dimensional incompressible viscous flow problems in external flow fields. The model based on the Navier-Stokes equations in primitive variables is able to solve the infinite boundary value problems by extracting the boundary effects on a specified finite computational domain, using the pressure projection method. The external flow field is simulated using the boundary element method by solving a pressure Poisson equation that assumes the pressure as zero at the infinite boundary. The momentum equation of the flow motion is solved using the three-step finite element method. The arbitrary Lagrangian-Eulerian (ALE) method is incorporated into the model, to solve the moving boundary problems. For illustration of the present numerical code, a vortex-induced cross-flow oscillations of a circular cylinder mounted on an elastic dashpot-spring system is considered. The phenomena of the beat, lock-in, and resonance are revealed in the Reynolds number range between 100 and 110, which are much narrower than the previous results by experimental and numerical studies.

**Keywords** : Navier-Stokes equations, external flow, arbitrary Lagrangian-Eulerian method, boundary elements, finite elements, vortex-induced oscillations

## Introduction

Wind-structure interaction is always an interesting subject in the wind engineering from both the academic as well as the industrial points of views. The flow-induced vibration by vortex shedding is vital to the safety design of elastic structures, such as high-rise buildings, bridges in particular (Blevins, 1990). For example, the response characteristic of vortex-induced oscillations of bluff cylinders has drawn a lot of experimental and computational investigations in the literature. In the experimental studies, vortex-excited cross-flow vibrations of a circular cylinder mounted elastically in a water or air channel have been conducted by Griffin and Ramberg (1982), Anagnostopoulos and Bearman (1992), among others. As far as numerical modeling is concerned, Anagnostopoulos (1989) used the finite element technique to solve the unsteady two-dimensional Navier-Stokes equations, while Nomura (1993) adopted the arbitrary Lagrangian-Eulerian (ALE) finite element formulation to incorporate the interface conditions on the moving boundary of the fluid-structure system. Cheng and Liu (2000) studied the effects of after body shape on flow around prismatic cylinders, and Cheng *et al.* (2001) extended to flow past a rotationally oscillating cylinder to investigate the characteristics of the intensive vortex shedding, the look-on frequency, and coalescence process.

In this study, we will develop an innovative computational procedure to solve the nonlinear interaction between a two-dimensional viscous incompressible fluid flow and motion of a rigid circular cylinder mounted on an elastic spring. This is a good case study for the simulation of the beat, lock-in and resonance phenomena. Lock-in mechanism is well known as the synchronization of the cylinder motion and the vortex shedding over a certain range of free stream velocities around the resonant frequency of the cylinder-spring system. The fluid-induced vibration is characterized by the natural frequency of the cylinder-spring system and Strouhal number of the fluids. The beat phenomenon is observed at a free stream velocity lower or higher than that of the lock-in and is accompanied by considerably small amplitudes than that of the lock-in. To simulate the 'beat', 'lock-in', and 'resonance' phenomena, a series of calculations over the Reynolds number range between 100 and 110 were carried out. The numerical code is based on the ALE finite element and boundary element approaches, which enable us to treat the infinite boundary effects coming from the finite computational domain with the consideration of moving boundary. The experimental results by Anagnostopoulos and Bearman (1992) as well as the numerical computations by Nomura (1993) are used for comparison. A more sensitivity of the range of lock-in is revealed at the present study, as compared with the previous works.

**Wind-Structure Model**

The motion of an incompressible viscous fluid flow is governed by the following ALE description of the Navier-Stokes equations and continuity equation in a non-dimensional form:

$$\frac{\partial u_i}{\partial x_i} = 0 \tag{1}$$

$$\frac{\partial u_i}{\partial t} + (u_i - \tilde{u}_i)\frac{\partial u_i}{\partial x_j} = -\frac{\partial p}{\partial x_i} + \frac{1}{\mathrm{Re}}\frac{\partial^2 u_i}{\partial x_j \partial x_j} \tag{2}$$

where t = time; $x_i$ = Cartesian coordinates , p = pressure , $u_i$ = velocity components in the $x_i$-direction , $\tilde{u}_i$=mesh velocity in the $x_i$-direction , Re = Reynolds number $= U_0 D/\upsilon$, $U_0$ =characteristic velocity , D = characteristic length , $\upsilon$ = kinematic viscosity.

For the structural model, the motion of a rigid circular cylinder mounted on an elastic dashpot-spring system is considered. The governing equations of motion of the rigid body are written as

$$m_{ij}\ddot{\delta}_j + c_{ij}\dot{\delta}_j + k_{ij}\delta_j = f_i \tag{3}$$

where $\delta_i$ = displacement components in the $x_i$-direction defined at the center of gravity , $f_i$ = concentrated force components in the $x_i$-direction, $m_{ij}$ = mass matrix , $c_{ij}$ = damping matrix , $k_{ij}$ = stiffness matrix .

In the external flow field, its outer boundary is situated at the infinity. Limitation of our resource of the computer capacity, forces us to assume a finite computational domain to replace the infinite domain problem. Depending on our computational method, two assumptions are introduced, i.e., the pressure equals to zero on the infinite boundary and $\nabla^2 p = 0$ is satisfied out of the finite computational domain. Therefore, only inflow boundary condition is needed for the boundary requirement of the computational domain. The computational domain and the boundary conditions are shown in Figure 1. The boundary condition of the fixed body in the flow is set as no-slip boundary and the normal pressure gradient is equal to zero. Depending on the ALE description, the boundary of the moving body is specified as the velocity of flow equal to that of the body. The normal pressure gradient is assumed equal to zero because the mesh velocity has estimated the influence of the acceleration of the body.

The numerical method of the primitive variables to solve the incompressible viscous fluid flow was developed. Based on the projection method (Chorin, 1967) three-step explicit method is used in the time direction, while the finite element method is employed for space (Chung and Kawahara, 1993). As far as the pressure Poisson equation is concerned, the boundary element method is used to solve the boundary pressure values on the computational domain, while the finite element method is used to get the internal pressure values because it can increase the computing efficiency. The algorithms are given below.

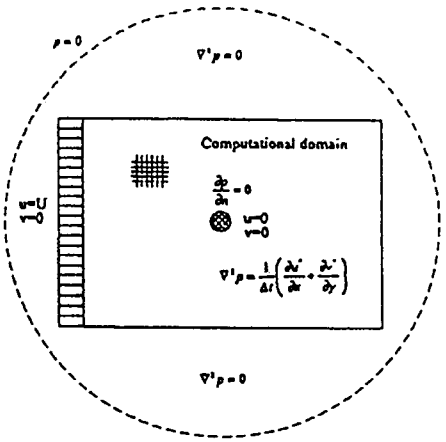


Fig. 1 Computational domain and boundary conditions

Three-step explicit method based on the Taylor series expansion in time can be written as follows:

$$f(t+\frac{\Delta t}{3}) = f(t) + \frac{\Delta t}{3}\frac{\partial f(t)}{\partial t} \tag{4.1}$$

$$f(t+\frac{\Delta t}{2}) = f(t) + \frac{\Delta t}{2}\frac{\partial f(t+\Delta t/3)}{\partial t} \tag{4.2}$$

$$f(t+\Delta t) = f(t) + \Delta t\frac{\partial f(t+\Delta t/2)}{\partial t} \tag{4.3}$$

By using equation (2) into equation (4), we obtain the parabolic equations (5), (6), (7) of velocity. Combining continuity equation (1) and taking the gradient of (7), the pressure Poisson equation is derived to correct the velocity. The procedures are stated as follows:

Step 1

$$\frac{u_i^{n+1/3}-u_i^n}{\Delta t}=-(u_j^n-\tilde{u}_j^n)\frac{\partial u_i^n}{\partial x_j}-\frac{\partial p^n}{\partial x_i}+\frac{1}{\mathrm{Re}}\frac{\partial^2 u_i^n}{\partial x_j \partial x_j} \tag{5}$$

Step 2

$$\frac{u_i^{n+1/2}-u_i^n}{\Delta t}=-(u_j^{n+1/3}-\tilde{u}_j^n)\frac{\partial u_i^{n+1/3}}{\partial x_j}-\frac{\partial p^n}{\partial x_i}+\frac{1}{\mathrm{Re}}\frac{\partial^2 u_i^{n+1/3}}{\partial x_j \partial x_j} \tag{6}$$

Step 3

$$\frac{u_i^{*}-u_i^n}{\Delta t}=-(u_j^{n+1/2}-\tilde{u}_j^n)\frac{\partial u_i^{n+1/2}}{\partial x_j}+\frac{1}{\mathrm{Re}}\frac{\partial^2 u_i^{n+1/2}}{\partial x_j \partial x_j} \tag{7}$$

Step 4

$$\frac{\partial^2 p^{n+1}}{\partial x_j \partial x_j}=\frac{1}{\Delta t}\frac{\partial \dot{u}_i}{\partial x_i} \tag{8}$$

Step 5

$$u_i^{n+1}=u_i^{*}-\Delta t\frac{\partial p^{n+1}}{\partial x_i} \tag{9}$$

All of the above step equations except the equation (8) are discretized by using standard Galerkin finite element method via the four points bilinear element. The resulting form of the consistent mass matrix is solved by the Jacobian iteration method. The equation (8) is solved by the standard boundary element method for the boundary and the finite element method for the domain (refer Young and Chang, 1995 and Young *et al.*, 2001 for details).

**Numerical Simulations**

The computational model is used to study the vortex induced cross-flow oscillations of a circular cylinder mounted on an elastic spring in a water channel. The 'lock-in' phenomenon over the Reynolds number range of 106~126 has been investigated experimentally by Anagnostopoulous and Bearman (1992), as well as numerically over the Reynolds number range of 100~130 by Nomura (1993). At such lower Reynolds number, the wake behind the circular cylinder is fully laminar. Figure 2 shows the material properties of the fluid, the parameters and boundary conditions of cylinder-spring system. Only vibrations in the cross-flow direction are allowed. The other two degrees of freedom in other directions are fixed.

Three cases of Reynolds number (Re=100, 106, 110) were simulated in this

investigation, which represent before, near and after 'lock-in' scenarios respectively. The natural frequency of the cylinder-spring system is found to be 7.0165 Hz. However, if we used the Roshko (1995) experimental formula to estimate the shedding frequency for Re=100, 106 and 110, the corresponding shedding frequencies are 6.92Hz, 7.021Hz, and 7.08Hz, respectively. We found that the case of Re = 106 corresponds to the resonance of the shedding and natural frequency or near the locking frequency. As shown in Figure 4, the amplitude is increasing conspicuously with time and frequency of its driving force is approximated to the natural frequency. The 'lock-in' mechanism is well known as the synchronization of the cylinder motion and the vortex shedding over a certain range of free stream velocity around the resonant velocity. As far as the free stream velocity is lower or higher than that of the 'lock-in', the 'beat' phenomenon is observed, which is accompanied by considerably small amplitudes than that of the 'lock-in'. Before the 'lock-in' case, the time history of displacement is depicted in Figure 3 for Re = 100. The small amplitude is limited to a certain region of the 'beat' oscillation. After the frequency locking, the 'beat' phenomenon appears again as shown in Figure 5 for Re=110.

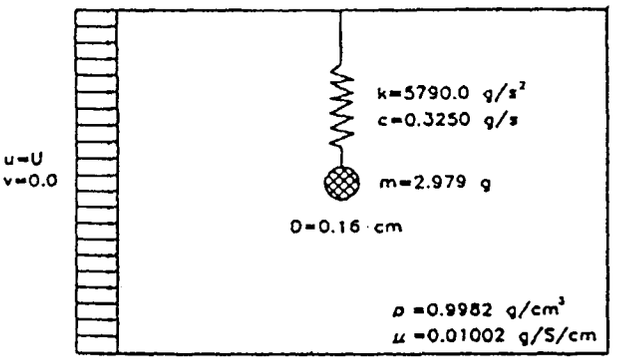


Fig. 2 Transverse oscillation of a circular cylinder-spring system in a uniform flow

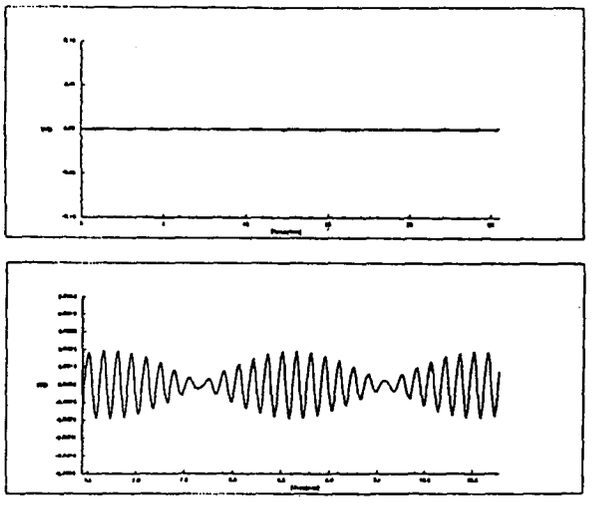

Fig. 3 Evolution with time of non-dimensional displacement, Re=100

According to the experimental studies by Anagnostopoulos and Bearman (1992), they observed that the range of the lock-in region lies within Re=106~115, while Re=103 is below the lock-in region; and Re = 135 is above the lock-in region. Similar results were also confirmed by the numerical simulation as performed by Nomura (1993). However, the present study renders a narrower range of the lock-in mechanism, as compared to the previous investigators.

Comparing with these results, we conjecture that some differences may lie in our simulation methods and procedures; such as (a) our numerical model is more stable than others; (b) the meshes of adjacent cylinder are not fine enough, so that we can not estimate the accurate shear force; (c) the procedures of simulation have differences, we independently simulate the different Re number flow field that the cylinder is fixed in the beginning, but Nomura's procedure (1993) is continuously to simulate the case that firstly simulates Re = 100 , then raises the Re number to 110 , 120,130; and (d) our numerical simulation is in the infinite domain as far as treatment of pressure boundary condition is concerned. Figure 6 displays the distribution of the structure of the local velocity vector, pressure, streamlines, as well as the vorticity for the oscillation of a circular cylinder-spring system in a uniform flow of Re = 106 at time equal to 1000. These figures show the salient features of the lock-in phenomenon as the free stream approaches the resonant velocity.

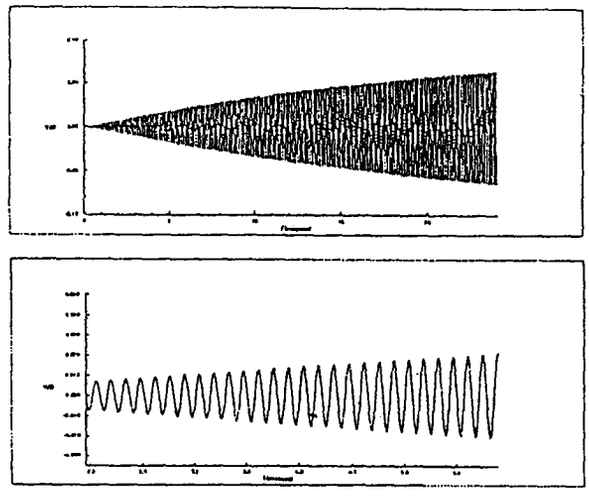

Fig. 4 Evolution with time of non-dimensional displacement, Re=106

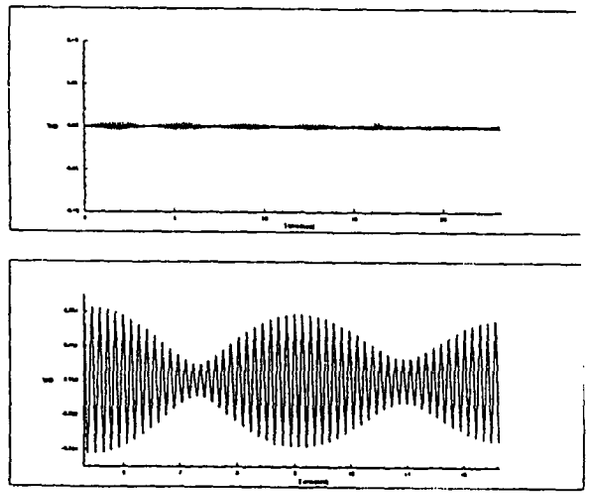

Fig. 5 Evolution with time of non-dimensional displacement, Re=110

**Conclusions**

The present numerical method is applied to simulate the flow across a circular cylinder, which is mounted on an elastic spring in the perpendicular direction of the main flow in the infinite domain. This is a typical problem for some flow-induced vibration studies, such as the "lock-in" or the "beat" phenomenon. The numerical simulations have rendered very reasonable and satisfactory results, as compared to those obtained by experimental or other numerical investigations, as far as the studies

of 'beat', 'lock-in', and 'resonance' phenomena are concerned. This method may be extended to deal with the more complicated wind-structure interaction programs.

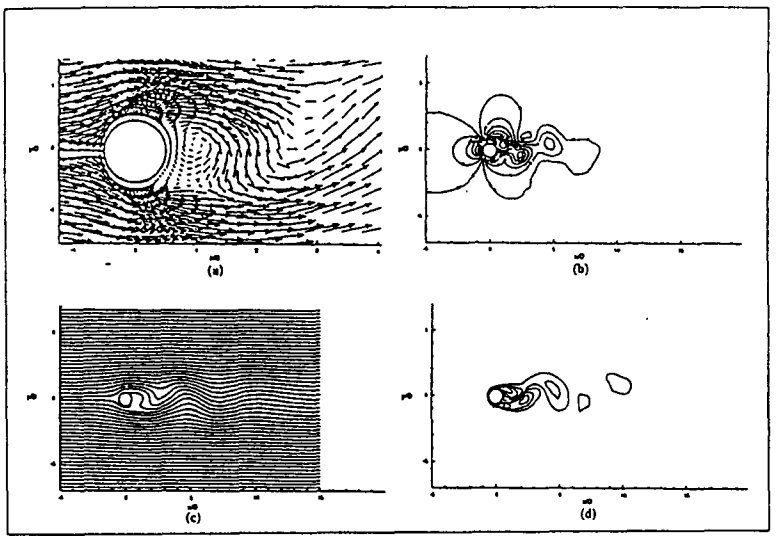

Fig. 6 Oscillation of circular cylinder-spring system in uniform flow, Re=106,t=1000,(a) local velocity vector . (b) pressure, (c) streamline, (d) vorticity

**Acknowledgements**

This work was supported by the National Science Council, the Republic of China, through the grant No. NSC 84-2215-E-002-041. It is greatly appreciated. The computational work was carried out in part by IBM 9000 Supercomputer, in the National Center for High-performance Computing, it is also highly acknowledged.

**References**

Anagnostopoulos , P. (1989) , "Numerical solution for laminar two-dimensional flow about a fixed and transversely oscillating cylinder in a uniform stream," *Journal of Computational Physics* , 85 , 434-456 .

Anagnostopoulos , P. and Bearman , P.W. (1992), "Response characteristics of a vortex-excited cylinder at low Reynolds number ," *Journal of Fluids and Structures* , 6 , 115-138 .

Blevins , R. D. (1990) . *Flow-induced vibration , second edition* , Van Nostrand Reinhold Company .

Cheng , M and Liu , G.R. (2000) , "Effects of afterbody shape on flow around prismatic cylinders," *Journal of Wind Engineering and Industrial Aerodynamics* , 84 , 181-196.

Cheng , M ., Liu , G.R , and Lam , K.Y.(2001), "Numerical simulation of flow past a rotationally oscillating cylinder," *Computers and Fluids* , 30 , 365-392.

Chorin , A. J. (1967) , "A numerical method for solving incompressible viscous flow problems," *Journal of Computational Physics* , 2 , 12-26 .

Chung , B. J. and Kawahara , M. (1993) , "The analysis of unsteady incompressible flows by a

three-step finite element method," *International Journal for Numerical Methods in Fluids* , 16 ,793-811 .

Griffin , O. M. and Ramberg , S. E. (1982) , "Some recent studies of vortex shedding with application to marine tubulars and risers ," *ASME Journal of Energy Resources Technology* , 104 , 2-13 .

Nomura , T. (1993) , "Finite element analysis of vortex-induced vibrations of bluff cylinders," *Journal of Wind Engineering and Industrial Aerodynamics* , 46/47 , 587-594.

Roshko , A. (1955) , "On the wake and drag of bluff bodies," *Journal of Aeronautical Science* , 22 , 124-135 .

Young , D. L., and Chang , J. D. (1995) , "Numerical simulation for two-dimensional laminar flow about the fixed and moving circular cylinder in the external flow field," *Proceedings of High-performance Computing , (HPC)* ASIA , 1995 , Taipei , Taiwan , ROC , FH046 , 1-14 .

Young, D. L., Chang, J.T., and Eldho, T.I. (2001), "A coupled BEM and arbitrary Lagrangian-Eulerian FEM model for the solution of two-dimensional laminar flows in external flow fields", *International Journal for Numerical Methods in Engineering*, 51, 1053-1077.

# Analysis of the Stokes Flow by the NSBIE for the Laplace Equation and the Biot-Savart Law

Chia-Ming Fan , Der-Liang Young

Department of Civil Engineering & Hydrotech Research Institute
National Taiwan University
Taipei, Taiwan, Republic of China

## ABSTRACT

The non-singular boundary integral equation for the Laplace (Poisson) equation , the Biot-Savart law and the velocity-vorticity formulation will be used to solve the typical problem , such as the 2D Stokes flow in a square cavity and a circular cavity . The Stokes flow problems can be considered as a subproblem of the Navier-Stokes flow problems , in which the non-linear convective terms are very small or neglected . The results will be presented and compared with the exact solutions and those of other numerical methods .

**Key Words** : the non-singular boundary integral equation, the Laplace (Poisson) equation, the Biot-Savart law, the velocity-vorticity formulation,

## INTROCUCTION

In computational mechanics field , several numerical methods are utilized , such as the Finite Difference Method (FDM) , Finite Element Method (FEM) , Boundary Element Method (BEM) , and so on . With the development of the equipments of computers , these numerical methods are widely developed and used by researchers , scientists and engineers .

In BEM , only the boundary should be discretized and the domain integration is not required . In two dimensional problems in particular , only the contour integration is considered , and the flux term is obtained directly . These advantages make BEM more suitable for solving some engineering problems . Although the field of computational science was developed widely and quickly , there still exist some problems in these numerical methods . The errors in FDM , the storage of huge data in FEM , the singularities in BEM , and so on still confused many researchers .

Boundary integral equation method is a powerful technique for the solution of boundary value problems . Originally the singularities in boundary integral equation method should be evaluated in a very careful way . It needs huge numerical calculations in general . One general way of treating the non-singular boundary integral equation is to consider the singular points which are still on the boundary but the singular behavior is removed by a mathematical technique via the Gauss flux theorem and other analytic scheme . The non-singular boundary equation method in this paper belongs to this method .

The viscous incompressible flow is governed by the Navier-Stokes equations . There are three general

formulations for numerical analysis of the viscous flow which is governed by the Navier-Stokes equations . They are the primitive variable approach , the vorticity-stream function approach and the velocity-vorticity approach . The primitive variable approach and the vorticity-stream function approach have been investigated by many researchers such as Anderson et al. (1984)[1] . The velocity-vorticity also has been implemented in numerical calculations by many researchers like Giannatasio and Napolitano (1996)[2] . The most advantage of the velocity-vorticity formulation is to separate the kinematic and kinetic aspects of the fluid flow from the pressure computation .

The Stokes flow problem is a subproblem of the Navier-Stokes flow problems . The non-linear convective terms are very small or neglected . The governing equations of the Stokes flow are changed to a linear equation system of the Laplace equation and the Poisson equation . According to the Biot-Savart law , the governing equations are transformed to the Laplace equation and the velocity field can be determined by the vortivity field . Liang (2000)[3] used the BEM and the Biot-Savart Law to simulate the Stokes flow in a circular cavity and a square cavity .

## MATHEMATICAL MODELS

### 1.Derivation of the Velocity-Vorticity Formulation

The non-dimensional Navier-Stokes equations which are the governing equations for incompressible Newtonian fluid can be written as

$$\frac{\partial \vec{u}}{\partial t} + (\vec{u} \bullet \nabla)\vec{u} = -\nabla p + \frac{1}{\mathrm{Re}}\nabla^2 \vec{u} \qquad (1)$$

where $\vec{u}$ is the velocity vector . $p$ is the pressure . Re is the Reynolds number and $t$ is the time .

Another governing equation is the continuity equation .

$$\nabla \bullet \vec{u} = 0 \qquad (2)$$

The vorticity vector can be expressed as

$$\vec{\omega} = \nabla \times \vec{u} \qquad (3)$$

By taking the curl of both sides of eq(1) and using eq(2) and eq(3) , we can obtain the vorticity transport equation as

$$\frac{\partial \vec{\omega}}{\partial t} + (\vec{u} \bullet \nabla)\vec{\omega} = (\vec{\omega} \bullet \nabla)\vec{u} + \frac{1}{\mathrm{Re}}\nabla^2 \vec{\omega} \qquad (4)$$

By taking the curl of eq(3) and using eq(2) , we can get a vector form of the poisson equation for velocity .

$$\nabla^2 \vec{u} = -\nabla \times \vec{\omega} \qquad (5)$$

For two-dimensional problems , the governing equations , eq(4) and eq(5) , can be written as

$$\frac{\partial \omega}{\partial t} + u\frac{\partial \omega}{\partial x} + v\frac{\partial \omega}{\partial y} = \frac{1}{\mathrm{Re}}\nabla^2 \omega \qquad (6)$$

$$\nabla^2 u = -\frac{\partial \omega}{\partial y} \qquad (7)$$

$$\nabla^2 v = \frac{\partial \omega}{\partial x} \tag{8}$$

When the Reynolds number approach to zero , the flow field is the so-called Stokes flow . The eq(6) will become the form of the Laplace equation .

$$\nabla^2 \omega = 0 \tag{9}$$

## 2.The Biot-Savart Law

In 1820 , the French scientist Jean-Baptiste Biot and Fe'lix Savart derived the Biot-Savart Law based on experiments . By the Biot-Savart law and the principle of superposition , the poisson equation , eq(7) and eq(8) , can be simplified .

$$(u_p)_i = \iint_{\Omega} \frac{-\omega}{2\pi} \frac{y_i - y}{(x_i - x)^2 + (y_i - y)^2} d\Omega \tag{10}$$

$$(v_p)_i = \iint_{\Omega} \frac{\omega}{2\pi} \frac{x_i - x}{(x_i - x)^2 + (y_i - y)^2} d\Omega \tag{11}$$

$$u = u_h + u_p \tag{12}$$

$$v = v_h + v_p \tag{13}$$

$$\nabla^2 u_h = 0 \tag{14}$$

$$\nabla^2 v_h = 0 \tag{15}$$

where $u_p$ and $v_p$ are the particular solutions of eq(7) and eq(8) . $u_h$ and $v_h$ are the homogeneous solutions of eq(7) and eq(8) . $\omega$ is the vorticity in a small area which is centered at $(x, y)$ .

Eq(10) and eq(11) can be discretized as

$$(u_p)_i = \sum_{\substack{j=1 \\ i \neq j}}^{N} \frac{-\omega_j}{2\pi} \frac{y_i - y_j}{(x_i - x_j)^2 + (y_i - y_j)^2} a_j \tag{16}$$

$$(v_p)_i = \sum_{\substack{j-1 \\ i \neq j}}^{N} \frac{\omega_j}{2\pi} \frac{x_i - x_j}{(x_i - x_j)^2 + (y_i - y_j)^2} a_j \tag{17}$$

## 3.The Formulation of the Non-Singular Boundary Integral Equation for the Laplace Equation

The vorticity transport equation in the Stokes flow is the Laplace equation. If we want to find the solutions of this kind of problems by boundary integral equation method , we need to derive the

non-singular boundary integral equation first . It is well known that the implementation needs to involve the Green's second identity as ,

$$\iint_D \left(f\nabla^2 g - g\nabla^2 f\right)dD = \oint_\Gamma \left( f\frac{\partial g}{\partial n} - g\frac{\partial f}{\partial n}\right)d\Gamma \qquad (18)$$

where $f(\vec{x})$ and $g(\vec{x})$ are scalar functions and also continuous in domain $D$ which is covered by smooth boundary $\Gamma$ . The normal vector $\vec{n}$ points outwards the domain $D$ .

The Green's function $G(\vec{x},\ \vec{x}')$ indicates the potential at the field point $\vec{x}$ induced by the base point $\vec{x}'$ , satisfies the following governing equation in domain $D$ .

$$\nabla^2 G = -\delta(\vec{x}'-\vec{x}) \quad (19)$$

In two dimensional domain , the fundamental solution of the Laplace equation $G(\vec{x},\ \vec{x}')$ can be written as

$$G(\vec{x},\ \vec{x}') = \frac{-1}{2\pi}\ln(r) \quad (20)$$

in which $r$ of the above equations is the distances between field point $\vec{x}$ and base point $\vec{x}'$ .

$$r = \sqrt{(x'-x)^2 + (y'-y)^2} \quad (21)$$

Replacing $g(\vec{x})$ in eq(18) by physical quantity $\phi$ , and $f(\vec{x})$ by fundamental solution $G(\vec{x},\ \vec{x}')$ , we obtain

$$\iint_D \left(G\nabla^2\phi - \phi\nabla^2 G\right)dD = \oint_\Gamma \left( G\frac{\partial\phi}{\partial n} - \phi\frac{\partial G}{\partial n}\right)d\Gamma \quad (22)$$

Finally the boundary integral equation for the Laplace equation can be expressed as

$$\varepsilon(\vec{x})\phi(\vec{x}) = \oint_\Gamma \left( G\frac{\partial\phi(\vec{x}')}{\partial n_{\vec{x}'}} - \phi(\vec{x}')\frac{\partial G}{\partial n_{\vec{x}'}}\right)d\Gamma(\vec{x}') \quad (23)$$

The coefficient $\varepsilon(\vec{x})$ is equal to $1/2$ when $\vec{x}$ is on the smooth boundary . The coefficient $\varepsilon(\vec{x})$ is equal to 1 when $\vec{x}$ is inside the domain , and 0 when $\vec{x}$ is outside the domain .

The eq(23) then can be written as

$$\varepsilon(\vec{x})\phi(\vec{x}) + \oint_\Gamma [\phi(\vec{x}') - \phi(\vec{x})]\frac{\partial G}{\partial n_{\vec{x}'}}d\Gamma(\vec{x}') + \oint_\Gamma \phi(\vec{x})\frac{\partial G}{\partial n_{\vec{x}'}}d\Gamma(\vec{x}')$$

$$= \oint_\Gamma \left( \frac{\partial\phi(\vec{x}')}{\partial n_{\vec{x}'}} - \frac{\partial\phi(\vec{x})}{\partial n_{\vec{x}}}\frac{\sigma(\vec{x}')}{\sigma(\vec{x})}\right)Gd\Gamma(\vec{x}') + \frac{\partial\phi(\vec{x})}{\partial n_{\vec{x}}}\frac{1}{\sigma(\vec{x})}\oint_\Gamma \sigma(\vec{x}')Gd\Gamma(\vec{x}') \quad (24)$$

where $\sigma(\vec{x})$ and $\sigma(\vec{x}')$ are the source functions at $\vec{x}$ and $\vec{x}'$ .

The source function satisfies a homogeneous boundary integral equation and the derivation can be referenced in Jason and Symm [4] . The source function can be found by

$$0 = \int_{\Gamma}\left[\sigma(\vec{x}')\frac{\partial G}{\partial n_{\vec{x}}} - \sigma(\vec{x})\frac{\partial G}{\partial n_{\vec{x}'}}\right]ds \quad (25)$$

The source function cannot be determined uniquely and needs to give a fixed value at some points on the surface . By using the iterative method , one obtains

$$\sigma^{m+1}(\vec{x}) = \sigma^{m}(\vec{x}) - \int_{\Gamma}\left[\sigma^{m}(\vec{x}')\frac{\partial G}{\partial n_{\vec{x}}} - \sigma^{m}(\vec{x})\frac{\partial G}{\partial n_{\vec{x}'}}\right]ds \quad (26)$$

The Gauss Flux theorem in potential theory will reduce the normal derivative type singularities in integral equations . The Gauss Flux theorem can be written as

$$-\varepsilon(\vec{x}) = \oint_{\Gamma}\frac{\partial G}{\partial n_{\vec{x}'}}d\Gamma(\vec{x}') \quad (27)$$

The concept of equipotential function $\Phi_e$ should be introduced to solve the singular kernel of $\ln(r)$ . The $\Phi_e$ can be defined by

$$\Phi_e = \oint_{\Gamma}\sigma(\vec{x}')G d\Gamma(\vec{x}') \quad (28)$$

$\Phi_e$ is a constant in the interior of an equipotential surface .

By substituting eq(27) and eq(28) into eq(24) , the eq(24) will become

$$\oint_{\Gamma}[\phi(\vec{x}') - \phi(\vec{x})]\frac{\partial G}{\partial n_{\vec{x}'}}d\Gamma(\vec{x}') = \oint_{\Gamma}\left(\frac{\partial \phi(\vec{x}')}{\partial n_{\vec{x}'}} - \frac{\partial \phi(\vec{x})}{\partial n_{\vec{x}}}\frac{\sigma(\vec{x}')}{\sigma(\vec{x})}\right)G d\Gamma(\vec{x}') + \frac{\partial \phi(\vec{x})}{\partial n_{\vec{x}}}\frac{\Phi_e}{\sigma(\vec{x})} \quad (29)$$

The eq(29) is the Non-Singular Boundary Integral Equation for the Laplace equation . The numerical singularities will be eliminated when $r$ approach to zero .

## NUMERICAL RESULTS

The first test problem is the 2-D circular cavity . The velocity $v_\theta = 1$ and $v_r = 0$ on upper half side and $v_\theta = v_r = 0$ on the others are imposed . The radius $R$ is equal to 10 .Figure 1 illustrates the geometry of the circular cavity . Figure 2 , 3 and 4 are the distributions of vorticity ($\omega$) and velocity ($u$) and ($v$) . The numerical solutions are symmetric and the same with those of Liang(2000)[3] and Lu(2000)[5] .The no-slip boundary condition and the viscosity induce the velocity gradient near the boundaries . According to the principle of superposition , figure 3 is the combination of the particular solution and the homogeneous solution in eq(7). Figure 4 is the combination of the particular solution and the homogeneous solution in eq(8). Figure 5 is the profile of velocity component ($u$) along $x = 0$ and figure 6 is the profile of velocity component ($v$) along $y = 0$ . The numerical solutions with 80 , 160 and 400 boundary nodes are compared with the exact solution which is derived by Hwu et al [6] . The direction of velocity along the upper surface is counterclockwise . So that the motion of the Stokes flow

in a circular cavity is counterclockwise . The velocity component ($u$) is negative on the upper half side and positive in the other half side . It means that the fluid moves to the left in the upper half side and to the right in the other side is equal by continuity .

Figure 7 is the geometry of the square cavity . Figure 8 is the distributions of vorticity ($\omega$).According to figure 8 , the distributions of vorticity are symmetric . The distributions of vorticity and velocity are the same with those of Lo(2000)[7] which is computed by FEM . The singularities which are on the upper two corners can be found in Figure 8 . This kind of singularity is due to the discontinuous boundary conditions of $u$ velocity . Figure 9 is the profile of velocity component $u$ along $x = 0.5$ . The motion of fluid in a square cavity is clockwise . The profile of velocity component $u$ along $x = 0.5$ is compared with those of Burggraf [8] .

## CONCLUSIONS

The numerical solutions of the Stokes flow in a square cavity are almost identical in comparing with those by other numerical methods , and comparing with analytic solutions for a circular cavity . Both circular and square cavities show the efficiency of the non-singular boundary integral equation and the reliability of the velocity-vorticity formulation . It also demonstrates that the Biot-Savart law can be used together with the principle of superposition .The fact that the vorticity induces the velocity is obviously confirmed .

## ACKNOWLEDGEMENTS

This work is supported by the grant from the National Science Council , NSC89-2211-E-002-138 . It is greatly appreciated and acknowledged .

## REFERENCES

1. Anderson D.A. , Tannehill J.C. and Fletcher R.H. , Computational Fluid Mechanics and Heat Transfer , McGraw-Hill , New York , 1984 .
2. Giannattasio P. and Napolitano M. , "Optimal Vorticity Conditions for the Node-Centered Finite-Difference Discretization of the Second-Order Velocity-Vorticity Equations" , J. Comput. Phy. ,127,208-217,2000.
3. Liang E. W., "Velocity-Vorticity Formulation for the 2D Stokes Flows by Biot-Savart Law and Boundary Element Method", MS Thesis , National Taiwan University, 2000.
4. Jason M.A. and Symm G.T. , Integral Equation Methods in Potential Theory and Elastostatics , Academic , London ,1977.
5. Lu H.L., "The Non-Singular Boundary Integral Equation Analysis to the Stokes Flow" MS Thesis , National Taiwan University, 2000.
6. Hwu T. Y. , Young D. L. and Chen Y. Y. "Chaotic Advections for Stokes Flows in Circular Cavity", J. Engineering Mech. ,ASCE, Vol. 123, pp.774-782,1997.

7. Lo D. C., "Two-Dimensional Velocity-Vorticity Formulation for Incompressible Flows with Free Surfaces by the Finite Element Method", MS Thesis , National Taiwan University, 2000.
8. Burggraf O.R. ,"Analytic and Numerical Studies of Structure of Steady Separated Flows" , J. Fluid Mechanics, 24 , pp.131-151 , 1966.

## FIGURES AND TABLES

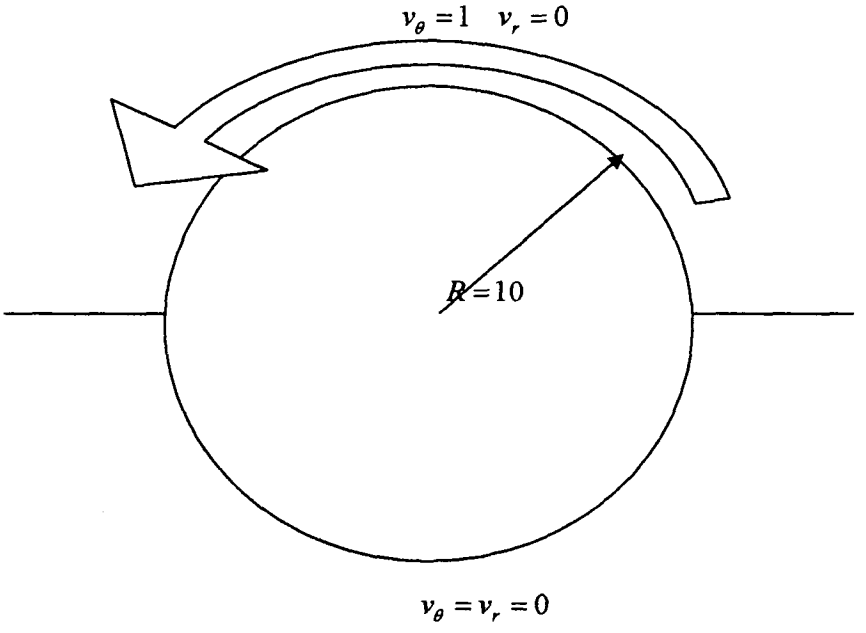


Fig 1 Schematic diagram of a circular cavity

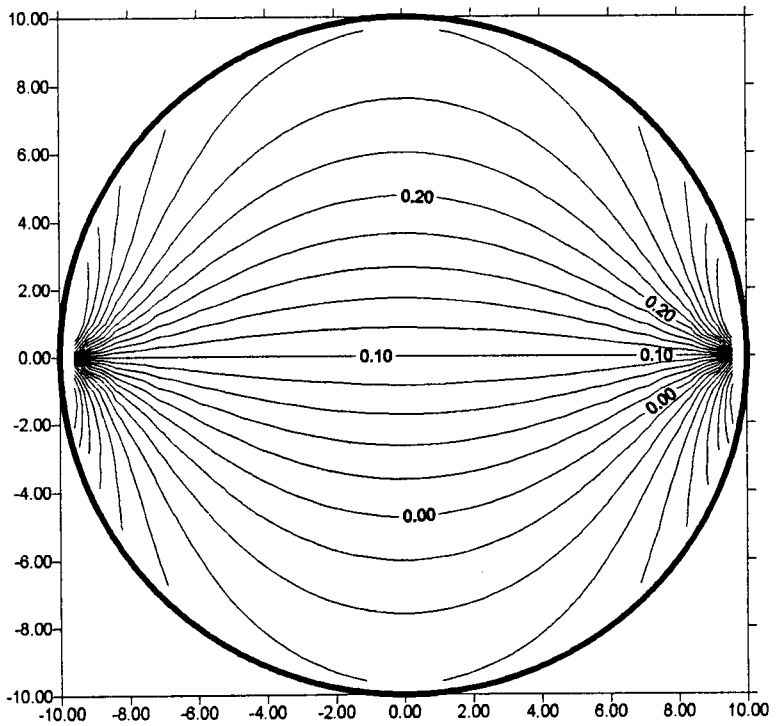


Fig 2 Vorticity $\omega$ contour for a circular cavity

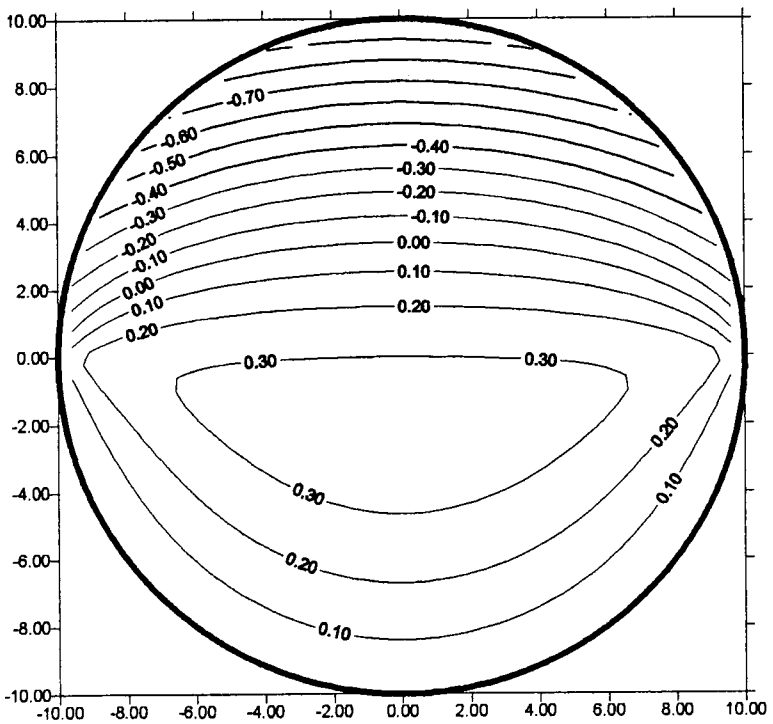


Fig 3 Velocity $u$ contour for a circular cavity

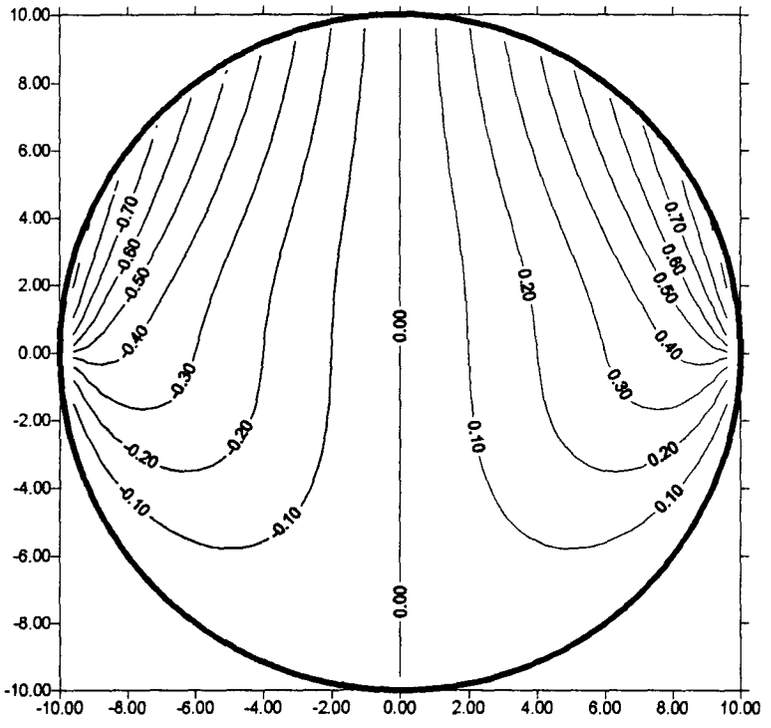


Fig 4 Velocity $v$ contour for a circular cavity

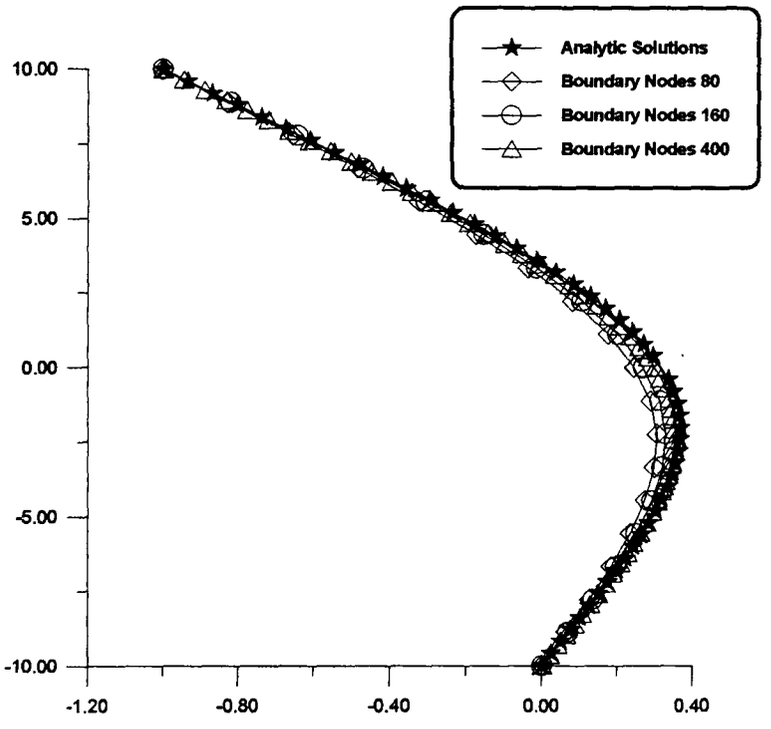


Fig 5 Comparison of $u$ velocity profiles along $x = 0$ at different mesh for a circular cavity

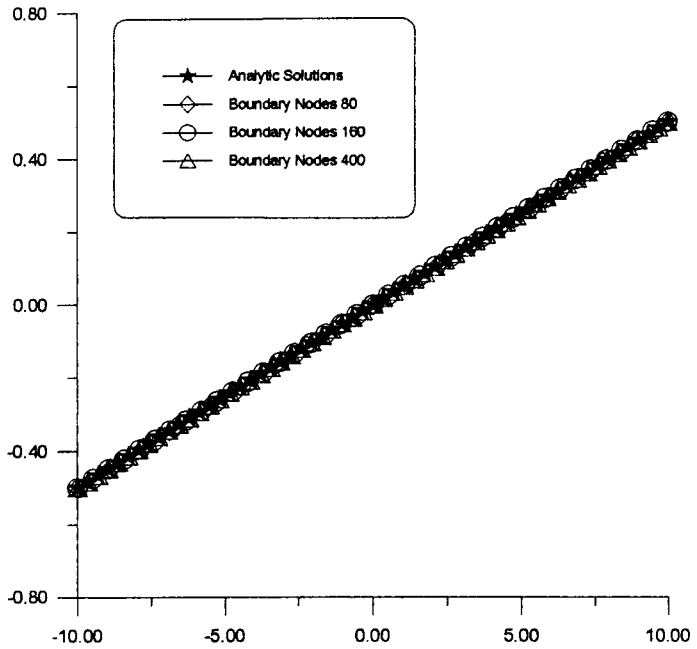


Fig 6 Comparison of $v$ velocity profiles along $y = 0$ at different mesh for a circular cavity

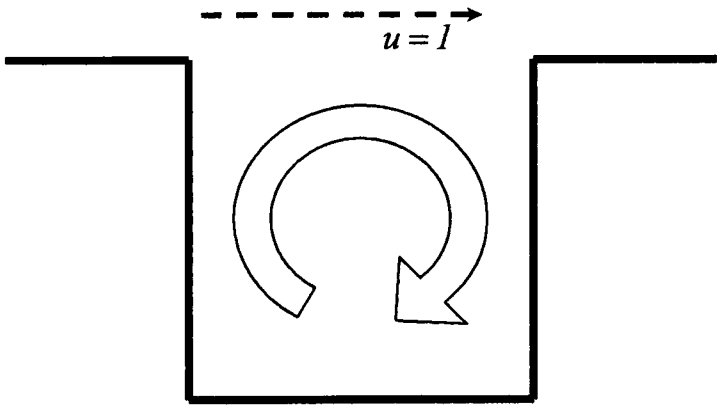


Fig 7 Schematic diagram of a square cavity

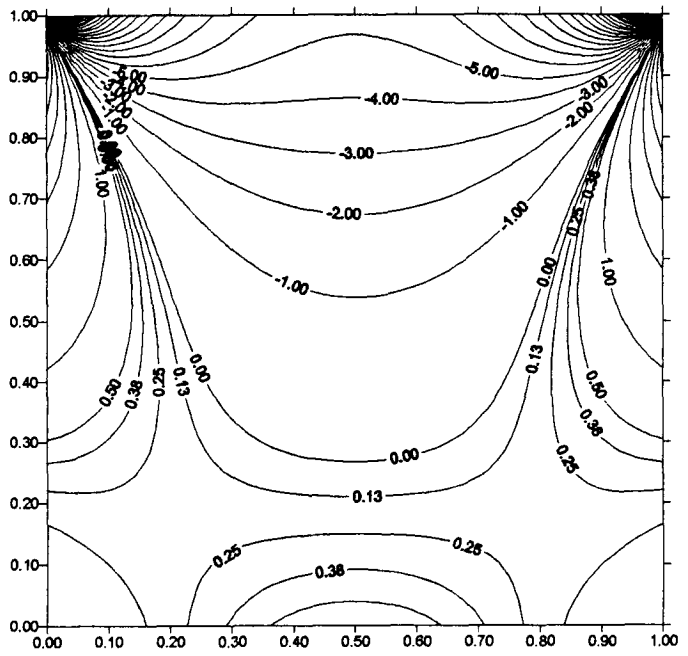


Fig 8 Vorticity $\omega$ contour for a square cavity

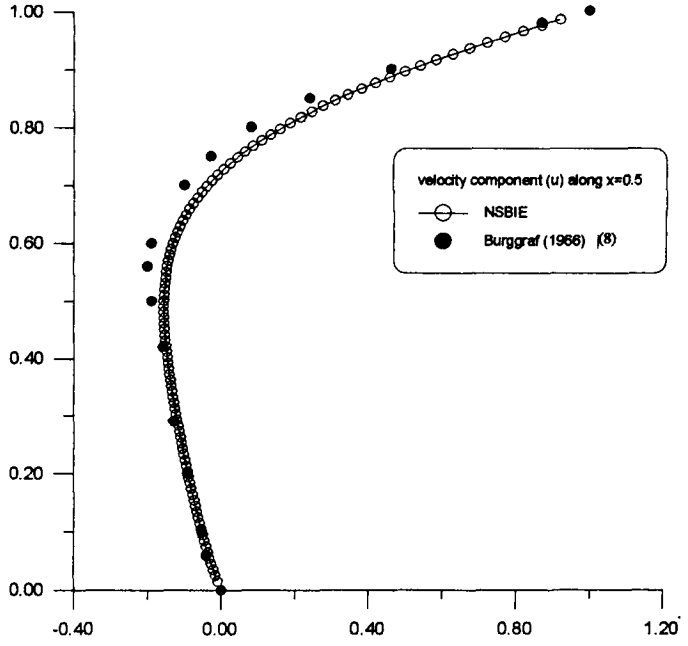


Fig 9 Comparison of $u$ velocity profiles along $x = 0.5$ for a square cavity

# 以非奇異性邊界積分方程式與必歐沙伐定理解析二維史托克斯流場

范佳銘[1]　楊德良[2]

[1]台灣大學土木工程學系碩士班研究生
[2]台灣大學土木工程學系教授

## 摘要

本文旨在探討改進傳統邊界元素法的數值奇異性。利用非奇異性邊界積分方程式及必歐沙伐定理解析二維不可壓縮史托克斯流場。首先，由高斯通量定理及等勢能理論推導出拉普拉斯方程式的非奇異性邊界積分方程式，接著利用速度渦度法及必歐沙伐定理將速度分解成齊性解及特解，速度的特解部分由必歐沙伐定理配合渦度可求出，速度的齊性解部分則由拉普拉斯方程式的非奇異性邊界積分方程式求出。在圓形穴室流場及方形穴室流場中，利用非奇異性邊界元素法及必歐沙伐定理求解二維史托克斯流場，並與解析解及其他數值方法的結果比較。

**關鍵字**：非奇異性邊界積分方程式，必歐沙伐定理，史托克斯流場，高斯通量定理，等勢能理論，拉普拉斯方程式，速度渦度法，

# An iterative DRBEM for three-dimensional Poisson's equation

C.C. Tsai[1], D.L. Young[1], A.H.-D. Cheng[2]

[1] *Department of Civil Engineering & Hydrotech Research Institute, National Taiwan University, Taiwan*

[2] *Department of Civil & Environmental Engineering, University of Delaware, USA*

## Abstract

In the numerical solution of three-dimensional boundary value problems, the large matrix size can pose memory and computational problems. To overcome this difficulty, an iterative dual reciprocity boundary element method is developed to solve Poisson's equation without the need of assembling a matrix. The compactly supported, positive-definite radial basis functions are used to approximate the right hand side of Poisson's equation. Suitable iterative method is then used to solve both the radial basis function collocation matrix and the linear system of the BEM.

## 1 Introduction

In the numerical solution of complex three-dimensional problems, a large number of discrete unknowns are required to accurately represent the geometry and the solution variation. A large memory may be required to store the matrix, which can become the limiting factor that the largest problem can be solved by a given computer. In this paper we continue the development of an iterative boundary element method (BEM) that does not assemble the matrix. In this case, the largest matrix size is not $N \times N$, but $N \times 1$. In particular, we develop the method to work with the dual reciprocity boundary element method (DRBEM) for the solution of Poisson's equation in three dimensions.

Literature survey finds a number of BEM solutions that utilize iterative techniques [1-6]. However, matrices were assembled in these implementations. The iterative BEM that does not assemble the matrix, resembling the relaxation technique used in the finite difference method, was pioneered by Cahan et al. [7]

for solving Laplace's equation based on the direct BEM formulation. An improved version was presented by Cahan and Lafe [8]. An iterative BEM based on the indirect formulation was devised to solve the governing equations of stochastic boundary value problems [9, 10]. Recently, the iterative method was applied to the DRBEM for the solution of Poisson's equation [11] and the Stokes flow equations [12]. In the iterative DRBEM solution, there are two iterative procedures involved: one related to the boundary integral equation, and the other with the radial basis function collocation.

The above efforts, however, are limited to the solution of two-dimensional problems. In present paper, we extend the work in Cheng et al. [11] to solve three-dimensional problems.

## 2 DRBEM

The governing equation to be solved is the 3D Poisson's equation

$$\nabla^2\Phi(\bar{x}) = b(\bar{x}) \tag{1}$$

with boundary conditions

$$\Phi = \Phi_\Gamma \quad \text{on } \Gamma_1; \quad \frac{\partial\Phi}{\partial n} = q_\Gamma \quad \text{on } \Gamma_2 \tag{2}$$

To derive the DRBEM formula, we split the solution into two parts: the homogenous solution and the particular solution:

$$\Phi(\bar{x}) = \Phi_h(\bar{x}) + \Phi_p(\bar{x}) \tag{3}$$

where the particular solution $\Phi_p(\bar{x})$ satisfies

$$\nabla^2\Phi_p(\bar{x}) = b(\bar{x}) \tag{4}$$

without boundary condition, and the homogenous solution $\Phi_h(\bar{x})$ satisfies

$$\nabla^2\Phi_h(\bar{x}) = 0 \tag{5}$$

with the boundary conditions

$$\Phi_h = \Phi_\Gamma - \Phi_p \quad \text{on } \Gamma_1; \quad \frac{\partial\Phi_h}{\partial n} = q_\Gamma - \frac{\partial\Phi_p}{\partial n} \quad \text{on } \Gamma_2 \tag{6}$$

Using the standard BEM for Laplace operator, the homogeneous solution can be solved from the boundary integral equation:

$$c\Phi_h(\bar{x}) = \int_\Gamma [G(\bar{\chi} - \bar{x})\frac{\partial\Phi_h(\bar{\chi})}{\partial n(\bar{\chi})} - \Phi_h(\bar{\chi})\frac{\partial G(\bar{\chi} - \bar{x})}{\partial n(\bar{\chi})}]\, d\Gamma(\bar{\chi}) \tag{7}$$

where c is the solid angle at $\bar{x}$ and

$$G(\bar{\chi} - \bar{x}) = \frac{1}{4\pi r(\bar{x}, \bar{\chi})} \tag{8}$$

is the fundamental solution of Laplacian operator in 3D.

To find the particular solution, we first approximate the right hand side of (1) by a radial basis function (RBF) interpolation:

$$\sum_{i=1}^{n_d} \alpha_i f(r_i) = b(\bar{x}) \tag{9}$$

where $f(r)$ is a radial basis function, $r_i = |\bar{x}_i - \bar{x}|$ is the radial distance between the center of the RBF $\bar{x}_i$ and the field point $\bar{x}$, $n_d$ is the number of terms of the approximation, and $\alpha_i$ are coefficients to be determined from collocation. The collocation nodes typically coincide with the centers of the RBF and are distributed in the interior as well as on the boundary. By collocating at the $n_d$ points, a linear system is formed that can be used to solve for the $\alpha$'s.

If we find the particular solution of $f(r)$

$$\nabla^2 F(r) = f(r) \tag{10}$$

in close form, the particular solution of (4) can be approximated as

$$\Phi_p(\bar{x}) = \sum_{i=1}^{n_d} \alpha_i F(r_i) \tag{11}$$

This then defines the boundary conditions in (6). Equation (7) can now be discretized using a standard BEM procedure to produce a linear equation system as

$$[H]\{\Phi\} = [G]\{\partial\Phi / \partial n\} \tag{12}$$

We note, however, the matrices $H$ and $G$ are written here only symbolically. In the iterative solution, these two matrices are not assembled.

## 3 Radial Basis Functions

The theoretical basis of radial basis function (RBF) and its application in DRBEM has been well explored by Golberg, Chen and collaborators in a series of articles; see, for example, Golberg et al. [13] for a recent review. There exist a number of RBFs, such as the conical, spline, Gaussian, and multiquadric types. The collocation matrix, however, is often ill conditioned, particularly for large system of equations. In our previous studies [11, 12], we find that iterative schemes failed to converge for the collocation matrices based on the above-mentioned conventional RBFs. In fact, only the compactly supported, positive-definite RBF (CS-PD-RBF) developed by Wendland [14] gives convergent result. Hence only this type of RBF will be used in the iterative DRBEM solution.

For the current three-dimensional problems, we choose the following CS-PD-RBF:

$$f(r)=\begin{cases}(1-\frac{r}{a})^2, & r\le a\\ 0, & r>a\end{cases} \tag{13}$$

where $a$ is the influence radius, beyond which the function is truncated to zero. The influence radius controls the density of the matrix. If $a$ is larger than the largest span of the domain, the matrix is fully populated; if $a$ is smaller than the smallest distance between two collocation nodes, the matrix becomes diagonal. A proper value of $a$ should fall between these two limits. In this study, various influence radii are tested. The corresponding convergence efficiency will be shown later.

For the purpose of DRBEM implementation, the particular solution $F(r)$ as defined in (10) is needed. It has been found by Chen, et al [15]:

$$F(r)=\begin{cases}\dfrac{r^2(10a^2-10ar+3ar^2)}{60a^2}, & r\le a\\ \dfrac{a^2}{12}-\dfrac{a^3}{30r}, & r>a\end{cases} \tag{14}$$

## 4 Iterative schemes

There are two parts of iteration solution involved. The first part is the BEM part based on (12), resulting from the discretization of (7). The second part is the RBF collocation matrix, expressed as

$$[A]\{X\}=\{B\} \tag{15}$$

The iterative scheme for the BEM equations has been described in detail elsewhere [11, 12], and will not be repeated here. Only the iterative solution of the RBF system is discussed.

Depending on the property of matrix $[A]$, various iterative schemes, such as the Gauss-Seidel scheme and conjugate gradient method, can be used. The Gauss-Seidel method is based on the following iterative formula:

$$x_i^{(k)}=\frac{-\sum_{j=1}^{i-1}a_{ij}x_j^{(k)}-\sum_{j=i+1}^{n}a_{ij}x_j^{(k-1)}+b_i}{a_{ii}} \tag{16}$$

The sufficient and necessary condition for the convergence of matrix $A$ is that the spectrum radius must be less than one. It is shown that the scheme will converge if

$$\max\sum_{\substack{j=1\\ j\neq i}}^{N}\frac{|a_{ij}|}{|a_{ii}|}<1 \tag{17}$$

This condition is easy to check since only a simple operation is involved.

The conjugate gradient method requires that the system matrix $A$ be positive-definite. Since the collocation matrix based on CS-PD-RBF has been

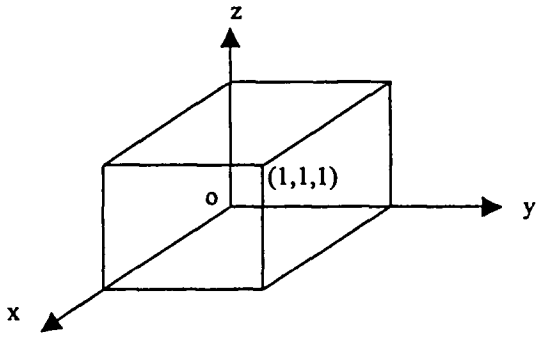


Figure 1: Geometry of the test problem

proven to be positive-definite, this method can be adopted. The conjugate gradient method is based on the following formula:

$$x_i^{(k)} = x_i^{(k-1)} - v\sum_{j=1}^{n} a_{ij}x_j^{(k-1)} + vb_i \tag{18}$$

where $v$ is some selected positive real number that makes the spectrum radius of matrix $(I - vA)$ less than unity. This criteria is equivalent to saying that the matrix $A$ is positive definite. The method will be convergent more efficiently if larger value of $v$ is used. But there exists some upper bound criteria for v.

## 5 Illustrated examples

To test the feasibility of the scheme, two examples with known exact solutions are investigated.

*Ex1:*

Governing equation:

$$\nabla^2\Phi = x + 2 + z^2 \quad \text{in} \quad 0 \le x \le 1, \quad 0 \le y \le 1, \quad 0 \le z \le 1 \tag{19}$$

with B.C.

$$\begin{cases} \Phi(0,y,z) = y^2 + \dfrac{z^4}{12}; \quad \Phi(1,y,z) = \dfrac{1}{6} + y^2 + \dfrac{z^4}{12}; \quad \Phi(x,0,z) = \dfrac{x^3}{6} + \dfrac{z^4}{12}; \\ \Phi(x,1,z) = \dfrac{x^3}{6} + 1 + \dfrac{z^4}{12}; \quad \Phi(x,y,0) = \dfrac{x^3}{6} + y^2; \quad \Phi(x,y,1) = \dfrac{x^3}{6} + y^2 + \dfrac{1}{12} \end{cases} \tag{20}$$

The exact solution is

$$\Phi(x,y,z) = \frac{x^3}{6} + y^3 + \frac{z^4}{12} \tag{21}$$

*Ex2:*

Same as example 1, except that the boundary conditions are changed to mixed type:

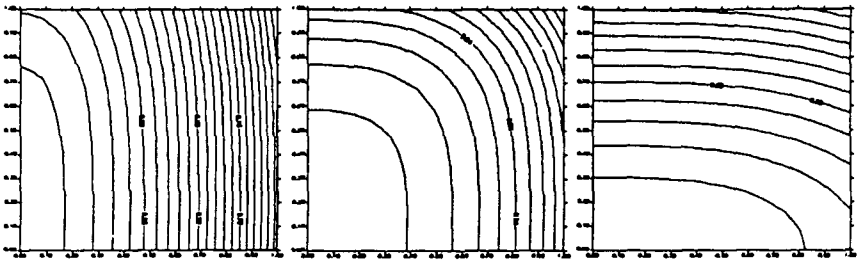

Figure 2: Exact solution profiles (Left: Profile I. Middle: Profile II. Right: Profile III)

$$\begin{cases} \Phi(0,y,z) = y^2 + \dfrac{z^4}{12}; \quad \Phi(1,y,z) = \dfrac{1}{6} + y^2 + \dfrac{z^4}{12}; \quad \Phi(x,0,z) = \dfrac{x^3}{6} + \dfrac{z^4}{12}; \\ \Phi(x,1,z) = \dfrac{x^3}{6} + 1 + \dfrac{z^4}{12}; \quad \Phi(x,y,0) = \dfrac{x^3}{6} + y^2; \quad \dfrac{\partial \Phi}{\partial n}(x,y,1) = \dfrac{z^3}{3} \end{cases} \tag{22}$$

The exact solution is also the same.

The computational domain is shown in Figure1, and the solution profiles are shown in Figure 2, where profile I is the contour at $x = 0.5$, profile II at $y = 0.5$, and profile III at $z = 0.5$. Since the geometry is a simple cube, we adopt a uniform computational mesh. That means if the mesh size is 11×11×11, there are 11×11×11 collocation points and 6×10×10 boundary elements.

In the RBF iteration, we adopted the conjugate gradient method using all zero values as the initial guess, and the tolerance condition is defined as

$$Max\left|Xnew_i - Xold_i\right| < 0.00001 \tag{23}$$

where $Xold_i$'s are the unknown variables before updating, and $Xnew_i$'s are after updating. Here, we use an arbitrarily chosen value 0.00001 as a convergence criterion. In practical problems, it should be chosen as a function of dimensionless variables. For example, we should choose 0.00001 times the Reynolds number in the solution of incompressible fluid flow.

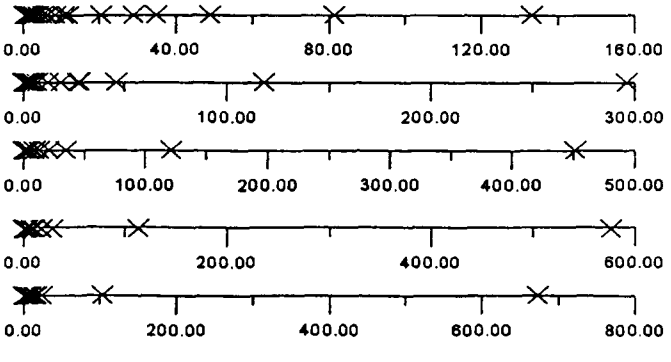


Figure 3: Spectrum distributions for $a$ = 0.8, 1.2, 1.6, 2.0, 2.4, respectively.

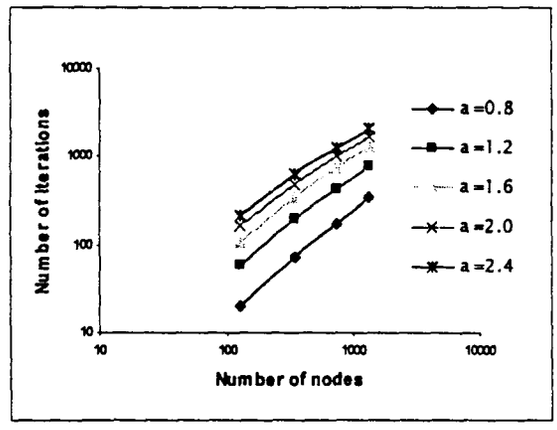


Figure 4: Number of iteration for various mesh sizes and different compact radius.

The step coefficient of the conjugate gradient method $\nu$ in (18) is set to be the reciprocal of the maximum eigenvalue of the system matrix. In a practical problem, this value can be initially set to a small number, and changed to progressively larger ones to be more efficient, unless it diverges. A fixed value can be used if the matrix structure is unchanged. The matrix spectra corresponding to $a = 0.8, 1.2, 1.6, 2.0, 2.4$ are depicted in Figure 3. In the figures, it is observed that these matrices are all positive definite as expected, and the maximum eigenvalue increases as the compact radius increases. It is known that a matrix with larger maximum eigenvalue results in a smaller step coefficient, $\nu$, and this smaller step coefficient will result in a larger number of iterations.

Figure 4 shows the relation among iteration number, mesh size, and compact radius in log-log scale. The relation shows

$$[\textit{number of nodes}] \propto [\textit{number of iterations}] \tag{24}$$

It is clear from the figure that either larger number of collocation nodes or smaller value of compact radius will result in a larger number of iterations. From Figures 3 and 4, we find that there is a tradeoff between the efficiency and the accuracy by using various compact radii.

After approximating the right hand side of the Poisson equation, we need to solve the linear equation system (12), resulting from the integral equation. For different boundary conditions, the matrix structure will be different. Numerical experiments are needed to investigate the convergence. Two examples, respectively corresponding to boundary conditions (20) and (22), are tested. Although no mathematical proof is attempted, numerical experiments show that the iterative schemes are feasible for various mixed type boundary conditions. In our numerical experiments, the accelerated Gauss-Seidel method is adopted. We use 1.1 as the acceleration coefficient. The selection of 1.1 is

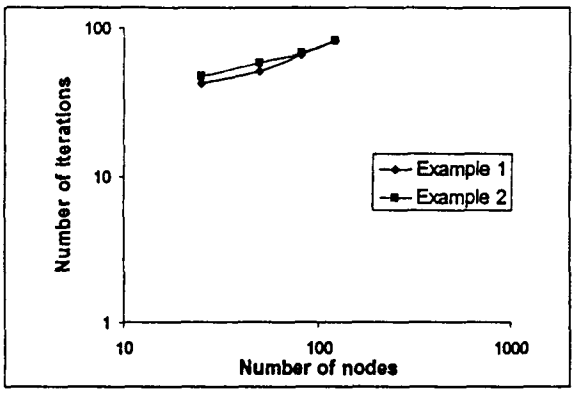


Figure 5: Number of iteration for various mesh sizes

somewhat arbitrary as larger values are possible and will result in a more convergence, until it diverges. Also, (23) is used as the tolerance criterion.

In Figure 5, the relation between the number of iterations and the number of nodes is shown for the two problems with different boundary conditions. Equation (17) has been checked to ensure the convergence of the scheme. The figure shows that the two examples exhibit very similar convergence behavior.

For checking the accuracy of the schemes, we define the relative error in percentage as

$$\frac{\text{numerical solution} - \text{exact solution}}{\text{Max of exact solution}} \times 100 \qquad (25)$$

The relative error on profiles I, II and III are plotted in Figures 6 and 7, respectively for example 1 and 2. In the figures, the bold lines mark the zero contours. For example 2, we find some relatively large errors near the corners where the two types of boundary conditions meet, due to the inexact treatment of corner nodes. They are nevertheless within 0.1% error. Otherwise, the overall accuracy is excellent.

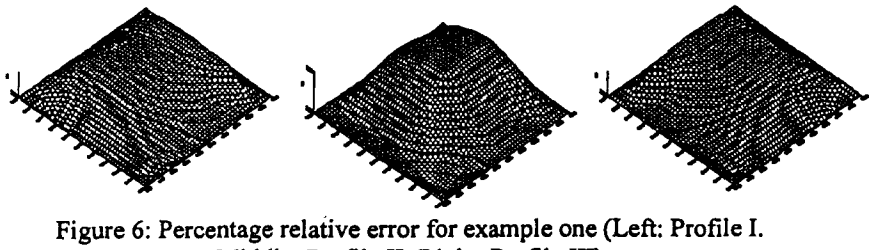

Figure 6: Percentage relative error for example one (Left: Profile I. Middle: Profile II. Right: Profile III)

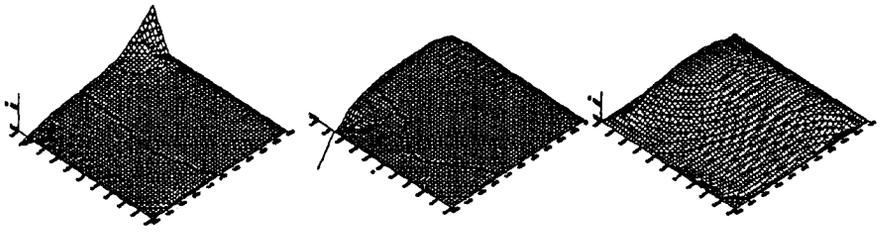

Figure 7: Percentage relative error for example two (Left: Profile I. Middle: Profile II. Right: Profile III)

## 6 Conclusions

We have conducted a preliminary study in which an iterative DRBEM is constructed to solve problems governed by 3-D Poisson's equations. In the application of DRBEM, there are two linear systems to be solved: one involves the RBF interpolation of the right hand side of the Poisson's equation, and the other concerns the boundary integral equation solution. For both systems, they are solved by iterative schemes that do not assemble matrices. In the case of the collocation system for the RBF interpolation, it is found that only the compactly supported, positive-definite radial basis functions lead to converged results. The accuracy and the convergence rate are also investigated. The result shows that the iterative DRBEM is a promising technique for solving large-size three-dimensional problems. Our goal is the apply the technique to solve large-scale engineering problems such as Navier-Stokes equations in fluid mechanics using the vorticity-velocity formulation.

## References

1. Yang LS, Machidori H, Shirakawa T., *BEM and BEM with SOR on the parallel computer QCDPAX,* Engng Anal Bound Elem. p231-237, 1996.
2. Lesnic D, Elliott L, Ingham DB, *An iterative boundary element method for solving numerically the Cauchy problem for the Laplace equation,* Engng Anal Bound Elem 1997. p123-133, 1997.
3. Mai-Duy N, Nguyen-Hong P, Tran-Cong T, *A fast convergent iterative boundary element method on PVM cluster,* Engng Anal Bound Elem. p307-316, 1998.
4. Merkel M, Bulgakov V, Bialecki R, Kuhn G, *Iterative solution of large-scale 3D-BEM industrial problems,* Engng Anal Bound Elem. p183-197, 1998.
5. Bulgakov V, Sarler B, Kuhn G, *Iterative solution of systems of equations in the dual reciprocity boundary element method for the diffusion equation,* Engng Anal Bound Elem. p713-732, 1998.

6. Valente FP, Pina HLG, *Iterative solvers for BEM algebraic systems of equations*, Engng Anal Bound Elem. p22:117-124, 1998.
7. Cahan BD, Scherson D, Reid MA, *An iterative boundary integral equation method for computer solutions of current distribution problems with complex boundaries-A new algorithm*, J. Electrochemical Soc. p285-293, 1988.
8. Cahan BD, Lafe OE, *On the iterative boundary element method*, In: Cheng AH-D, Brebbia CA, Grilli S, editors. Computational engineering with boundary element, 2: solid and computational problems, Computational Mechanics, 1990. p. 199-209 BEYECH90, University of Delaware.
9. Cheng AH-D, Lafe OE, *Boundary element solution for stochastic groundwater flow: random boundary condition and recharge*, Water Resour Res. p231-242, 1991.
10. Cheng AH-D, Abousleiman Y, Ruan F, Lafe OE, *Boundary element solution for stochastic groundwater flow: temporal weakly stationary problems*, Water Resour Res. p2893-2908, 1993.
11. Cheng AH-D, Young DL, Tsai CC, *Solution of Poisson's equation by iterative DRBEM using compactly supported, positive definite radial basis function*, Engng Anal Bound Elem. p549-557, 2000.
12. Young DL, Tsai CC, Eldho TI, Cheng AH-D, *Solution of Stokes flow using an iterative DRBEM based on compactly-supported, positive-definite radial basis function*, to appear in Computers and Mathematics with Applications.
13. Golberg MA, Chen CS, Bowman H, *Some recent result and proposals for the use of radial basis functions in the BEM*, Engng Anal Bound Elem. p285-296, 1999.
14. Wendland H., *Piecewise polynomial, positive definite and compactly supported radial basis functions of minimal degree.* Adv. Comp. Math., p389-396,1995.
15. Chen C.S., Brebbia C.A., and Power H., *Dual reciprocity method using compactly supported radial basis functions*, Commun Numer Meth Engng, p137-150, 1999.

# Meshless BEM for Steady Three-dimensional Stokes Flows

C.C. Tsai[1], D.L. Young[1], A.H.-D. Cheng[2]

[1]*Department of Civil Engineering & Hydrotech Research Institute*

*National Taiwan University, Taipei, Taiwan 10617.*

[2] *Department of Civil & Environmental Engineering,*

*University of Delaware, Newark, DE 19716, USA.*

## Abstract

This paper describes a combination of the dual reciprocity method (DRM) and the method of fundamental solution (MFS) as a meshless BEM (DRM-MFS) to solve steady three-dimensional Stokes flow problems by the velocity-vorticity formulation, where the DRM is based on the compactly supported, positive definite radial basis function. In the velocity-vorticity formulation, both of the Laplace type vorticity equations and the Poisson type velocity equations are solved by DRM-MFS. Here a typical cubic cavity flow is presented. Furthermore, this paper provides a preliminary work for applications to the three-dimensional Navier-Stokes equations.

**Keywords:** Velocity-vorticity formulation, Stokes flow, meshless, boundary element method, radial basis function, dual reciprocity method, method of fundamental solution

## 1. Introduction

In the past years, there has been an increasing interest in the idea of meshless numerical methods for solving partial differential equations (PDEs). Generally speaking, such methods can be divided into two types. The first one is the so-called DRM-MFS, which combines the dual reciprocity method and the method of fundamental solution, and the second one is the so-called Kansa's method [1]. In this paper, we will adopt the DRM-MFS method to solve the 3D Stokes flow problems.

The dual reciprocity method (DRM) was introduced by Nardini and Brebbia to approximate the particular solution of the equation in their 1982 pioneer work [2]. Since then, many ideas of meshless numerical methods have been tried based on the radial basis functions (RBFs). Furthermore, the method of fundamental solution (MFS) is used to approximate the homogenous solution of the equation. More details about MFS can be found in the excellent review papers [3,4]. The meshless BEM, which combines the DRM and MFS, has been used to solve many PDEs in different areas successfully [1,3,5,6]. In the paper, we use the DRM-MFS to solve the three-dimensional Stokes flow problems.

There are three well-known formulations for the solution of the incompressible Navier-Stokes equations in terms of: primitive variables of pressure and velocity, velocity-stream function and velocity-vorticity. The first two formulations have been thoroughly investigated by various researchers for two and three-dimensional problems by using various numerical methods such as finite difference methods (FDM) [7], finite element methods (FEM) [8], and boundary element methods (BEM) [9]. The third formulation in terms of velocity and vorticity also has been explained in the last decade in two and three dimensions using various numerical schemes [10-12,16].

Stokes flow problems can be considered as a subset of the Navier-Stokes flow problems, in which the nonlinear convective terms are very small, thus neglected. For the solution of steady Stokes flows using the velocity-vorticity formulation, the governing equations have been written as a system of Laplace and Poisson-type equations for the components the vorticity and velocity fields, respectively. The main advantage of this formulation is the numerical separation of the kinematic and kinetic aspects of the fluid flow.

In this paper, a numerical experiment of steady Stokes flow in a cubic cavity is investigated by using DRM-MFS. For further application to the three dimensional Navier-Stokes equations, this paper really provides a preliminary work. The advantage of mesh free can be used for large-scale industrial problems. The disadvantages of full matrix can be circumvented by using compactly-support RBFs and some iterative schemes which could result in an iterative scheme without the assembling of matrix[13].

## 2. Governing Equations

The governing equations of steady Stokes flow for the velocity-vorticity formulation can be derived from the Navier-Stokes equations and written as:

$$\begin{cases} \nabla^2 \vec{\omega} = \vec{0} \\ \nabla^2 \vec{u} = -\nabla \times \vec{\omega} \end{cases} \quad \text{in } \Omega \qquad (1a)\text{、}(1b)$$

$$\vec{u} = \vec{U} \text{ on } \Gamma \qquad (2)$$

where $\vec{u} = \vec{U}$ is the velocity vector, $\vec{\omega}$ is the vorticity vector, $\vec{U}$ is the known boundary velocity, and $\Omega$ as well as $\Gamma$ are the domain and boundary, respectively. The vorticity vector $\vec{\omega}$ can be expressed as:

$$\vec{\omega} = \nabla \times \vec{u} \qquad (3)$$

In equation (1), they are the Laplace and Poisson equations and can be solved by DRM-MFS to be described below.

## 3. Numerical Formulation

The governing equations (1) to be solved is of the type:

$$\nabla^2 \Phi(\vec{x}) = b(\vec{x}) \qquad (4)$$

where $\Gamma$ is the boundary of the problem. We decompose the solution into

$$\Phi(\vec{x}) = \Phi_h(\vec{x}) + \Phi_p(\vec{x}) \tag{5}$$

where the particular solution, $\Phi_p(\vec{x})$, satisfies

$$\nabla^2 \Phi_p(\vec{x}) = b(\vec{x}) \tag{6}$$

and the homogenous solution, $\Phi_h(\vec{x})$, satisfies

$$\nabla^2 \Phi_h(\vec{x}) = 0 \text{ and } \Phi_h(\vec{x}) = BC(\vec{x}) - \Phi_p(\vec{x}) \text{ on } \Gamma \tag{7}$$

The particular solution corresponding to equation (6) can be approximation by the DRM. Let the right hand side of the Poisson's equation take the form

$$\sum_{i=1}^{n_d} \alpha_i f(r_{ij}) = b(\vec{x}_j) \tag{8}$$

where $f(r)$ is a radial basis function, $r_{ij} = \left|\vec{x}_i - \vec{x}_j\right|$ is the radial distance between a field point $\vec{x}_j$ and the i-th collocation point $\vec{x}_i$, and $n_d$ is the number of collocation nodes. The collocation nodes are typically distributed in the interior as well as on the boundary. And $\alpha_i$ are the collocation coefficients to be determined. If we let the function values be equal at $n_d$ collocation points, we result in a linear system with $n_d$ unknowns, $\alpha_i$, and $n_d$ equations, which can be solved if the system is nonsingular. After $\alpha$ 's have been solved, we can find the particular solution which is of the form:

$$\Phi_p(\vec{x}_j) = \sum_{i=1}^{n_d} \alpha_i F(r_{ij}) \tag{9}$$

where $F(r)$ is the inverse Laplacian of the radial basis function $f(r)$, i.e. $\nabla^2 F(r) = f(r)$.

For the current three-dimensional problems, we choose the following CS-PD-RBF:

$$f(r) = \begin{cases} (1 - \frac{r}{a})^2 & r \le a \\ 0 & r > a \end{cases}, \tag{10}$$

This has been found by Chen, et al [5]. The particular solution corresponding to equation (10) is

$$F(r) = \begin{cases} \dfrac{r^2(10a^2 - 10ar + 3ar^2)}{60a^2} & r \le a \\ \dfrac{a^2}{12} - \dfrac{a^3}{30r} & r > a \end{cases} \tag{11}$$

Furthermore, the homogeneous solution corresponding to equation (7) can be solved by the MFS. Let the homogeneous solution to be the linear combination of the fundamental solution of the Laplace operator, i.e.:

$$\sum_{i=1}^{m_d} \beta_i g(r_{ij}) = \Phi_h(\vec{x}_j) \tag{12}$$

where $g(r) = -\frac{1}{4\pi r}$ is the fundamental solution of the Laplace operator, $r_{ij} = \left|\vec{x}_i - \vec{x}_j\right|$ is the distance between a field point $\vec{x}_j$ and the i-th source point $\vec{x}_i$, and $m_d$ is the number of source nodes. The source nodes are typically distributed in small distance away from the boundary to avoid the coincidence of $\vec{x}_j$ and $\vec{x}_i$ to avoid the singularity. And $\beta_j$ are the coefficients to be determined. If we let the function values be equal at $m_d$ boundary points, we result in a linear system with $m_d$ unknowns, $\beta_j$, and $m_d$ equations, which can be solved if the system is nonsingular. After $\beta_j$'s have been solved, we can find the homogeneous solution.

After the homogeneous solution $\Phi_h$ and the particular solution $\Phi_p$ have been solved, we can apply the superposition principle (equation (5)) to get the solution.

## 4. Solution procedures

As mentioned earlier, an iterative scheme is used in the solution of the velocity and vorticity equations. The computational procedure adopted here includes the following iterative steps:

1. Solve the homogeneous velocity equation (1b) with the know boundary velocity condition. (Laplace equation)
2. Get the vorticity at boundary by $\vec{\omega} = \nabla \times \vec{u}$
3. Solve the vorticity equation (1a) with the boundary condition in step 2.
4. Solve the velocity equation (1b) with the know boundary, where the source term is the derivative of the vorticity components got from step 3.
5. Repeat 2~4 until solutions are convergent

## 5. Results and conclusions

The three-dimensional cubic cavity flow has the configuration shown in the diagram, where a uniform velocity drives the top face to the right. Using the method described above, we can get the following results. The figures are the velocity field in the plane of x=0.5, y=0.5, and z=0.5, respectively. Also, the vorticity components at x=0.5, y=0.5 and z=0.5 are shown below. The result is compared to other

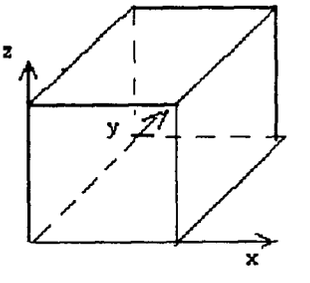

paper [16] and shows satisfactory accuracy.

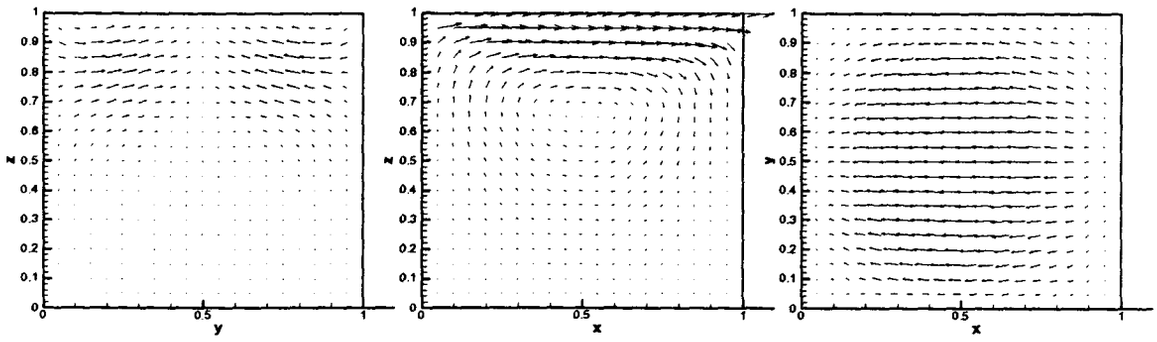


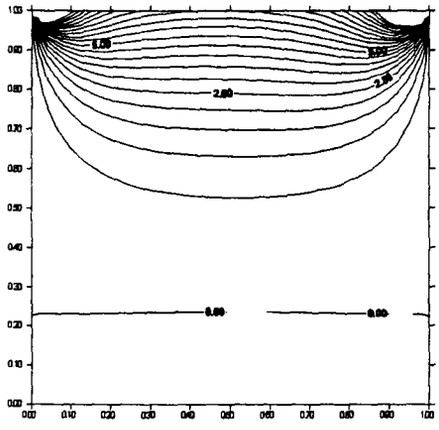

Vorticity component z at x=0.5

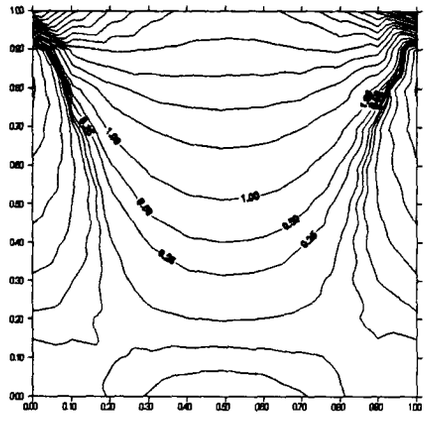

Vorticity component y at y=0.5

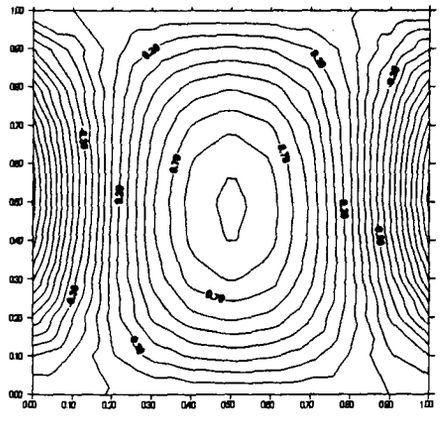

Vorticity component y at z=0.5

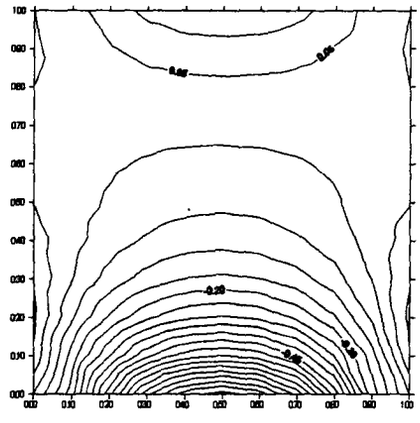

Vorticity component z at z=0.5

Fig 1: velocity and vorticity distributions of a cubic cavity flow

## References


[1] C.S. Chen, Jichun Li and Y.C. Hon. Numerical Comparisons between Two Meshless Methods using Radial Basis Function. (personal communications)

[2] D. Nardini and C.A. Brebbia, A new approach to free vibration analysis using boundary elements, in Boundary Element Methods in Engineering, C.A. Brebbia (Ed.), Springer-Verlag, Berlin, 1982.

[3] M.A. Golberg and C.S. Chen, The method of fundamental solutions for potential, Helmholtz and diffusion problems, in Boundary Integral Methods – Numerical and Mathematical Aspects, M.A. Golberg (Ed.), Computational Mechanics Publication, 99. 103-176, 1998.

[4] G. Fairweather and A. Karageorghis, The method of fundamental solutions for elliptic boundary value problems, Adv. Comput. Math. 9, 69-95, 1998.

[5] C.S. Chen, C.A. Brebia and H. Power, Dual reciprocity method using compactly supported radial basis functions, Commun. Numer. Mech. Engrg., 15, 137-150, 1999.

[6] A.S. Muleshkov, M.A. Golberg and C.S. Chen, Particular solutions of Helmholtz-type operators using higher order polyharmonic splines, Computational Mechanics, 23, 411-419, 1999.

[7] D.A. Anderson, J.C. Tannehill, and R.H. Pletcher, Computational fluid mechanics and heat transfer, New York: McGraw-Hill, 1984.

[8] M.D. Gunzaburger, Finite element theory and application, in D.L. Dwoyer, M.Y. Hussaini, R.G. Voigt (Ed.) Proceedings of the ICASE/NASA Langly Workshop, New York: Springer, 1987.

[9] H. Power, and L.C. Wrobel, Boundary integral methods in fluid mechanics, Southampton: Computational Mechanics Publication, 1995.

[10] S.C.R. Dennis, D.B. Ingham, and R.N. Cook, Finite-difference methods for calculating steady incompressible flows in three dimensions, J. Comput. Phys. 33, 325-339, 1979.

[11] M.D. Gunzaburger, and J.S. Peterson, On finite element approximations of the stream funcition-vorticity and velocity-vorticity equations, Int. J. Numer. Meth. Fluids 8, 1229-1240, 1988.

[12] L. Skerget, and Z. Rek , Boundary-domain integral method using a velocity-vorticity formulation. Engng. Anal. Bound. Elem. 15, 359-370, 1995.

[13] D.L. Young, C.C. Tsai, T.I. Eldho, and A.H.-D. Cheng, "Solution of Stokes flow using an iterative DRBEM based on compactly-supported, positive-definite radial basis function", International Journal of Computer and Mathematics with Applications (in press).

[14] A.H.-D. Cheng, D.L. Young, and C.C. Tsai, " Solution of Poisson's equation by iterative DRBEM using compactly supported, positive definite radial basis function", Engng. Anal. Bound. Elem. 24, 549-557, 2000.

[15] C.C. Tsai, D.L. Young, and A.H.-D. Cheng, "An Iterative DRBEM for Three-Dimensional Poisson's Equation", Boundary Element Technology XIV, 323-332.

[16] D.L. Young, Y.H. Liu, and T.I. Eldho, A combined BEM-FEM model for the velocity-vorticity formulation of the Navier-Stokes equations in three dimensions, Eng. Analysis Boundary Elements 24, 309-316, 2000.

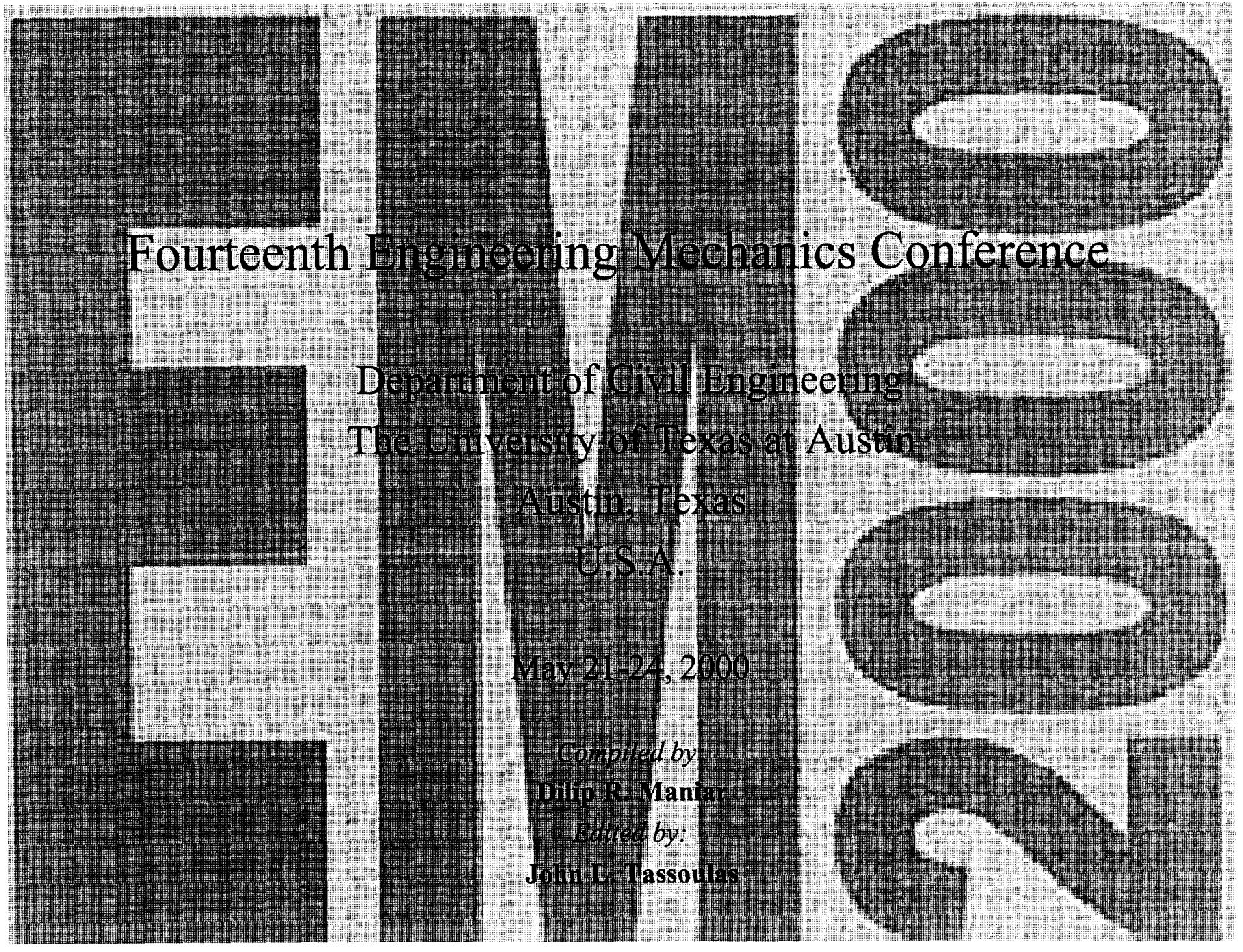

# Fourteenth Engineering Mechanics Conference

Department of Civil Engineering

The University of Texas at Austin

Austin, Texas

U.S.A.

May 21-24, 2000

*Compiled by:*

**Dilip R. Maniar**

*Edited by:*

**John L. Tassoulas**

# Solution of the Velocity-Vorticity Navier-Stokes Equations Using Dual Reciprocity Boundary Element Method

**T. I. Eldho, D.L. Young**
*Department of Civil Engineering & Hydrotech Research Institute*
*National Taiwan University, Taipei, Taiwan 10617*
*Email: eldho@hy.ntu.edu.tw; dlyoung@hy.ntu.edu.tw*

## SUMMARY

This paper describes the use of dual reciprocity boundary element method (DRBEM) for the solution of incompressible viscous flow problems using velocity-vorticity variables. The model involves the solution of vorticity transport equation for vorticity whose solenoidal vorticity components are obtained by solving Poisson equations involving the velocity and vorticity components. Both the Poisson equations and the vorticity transport equation are solved iteratively using DRBEM and combined to determine the velocity and vorticity vectors. Here the results of 2-dimensional Navier- Stokes problems with low Reynolds number in a typical cavity flow are obtained and compared with other models. The DRBEM model has been found to be satisfactory.

## KEY WORDS

Navier-Stokes equations, velocity-vorticity, dual reciprocity boundary element method

## 1. INTRODUCTION

For the solution of incompressible viscous flow problems, the velocity-vorticity form of Navier-Stokes equations has been established as an effective formulation. The main advantage of this formulation includes the numerical separation of the kinematic and kinetic aspects of the fluid flow from the pressure computation, which is determined afterwards from the known velocity and vorticity fields. Boundary Element Method (BEM) has been established as a powerful numerical tool in the solution of various fluid flow problems (Power and Wrobel, 1995). The main advantages of BEM are: reduction in computational dimensions, easiness in discretization and data preparation and direct solution to flux term at the boundaries. The major problems in using the general BEM techniques to solve the incompressible viscous flows are the difficulties in dealing with the convective and time dependent terms unless internal cells are defined (Brebbia et al. 1984).

Dual reciprocity boundary element method (DRBEM) employs a fundamental solution corresponding to a simpler equation and treat the remaining terms, through a procedure which involve a series expansion using global approximating functions and the applications of the reciprocity principle (Partridge et. al,1992) so that a boundary only solution is possible.

To solve the incompressible viscous flow problems, here DRBEM is used. In the DRBEM solution of Navier-Stokes equations, the fundamental solution of Laplace equation is used. The vorticity boundary conditions are got by the DRBEM solution of the Poisson equations. An iterative scheme is used to solve the system of equations after the numerical discretization by DRBEM. The feasibility of the DRBEM model has been demonstrated using the model problem of flow in a driven square cavity.

## 2. GOVERNING EQUATIONS

For two-dimensional incompressible viscous flow problems, if $(u,v)$ are the velocity vectors ( $\bar{u}$ ) and ? is the corresponding vorticity, the governing Navier-Stokes equations in the velocity-vorticity formulation can be written as:

$$\frac{\omega}{} + \bar{u} \bullet \nabla \omega = \frac{1}{\mathrm{Re}} \nabla^2 \omega \tag{1}$$

$$\nabla^2 u = -\frac{\omega}{\partial y}; \quad \nabla^2 v = \frac{\omega}{\partial x} \tag{2}$$

The vorticity vector $\bar{\omega}$ can be expressed as, $\bar{\omega} = \nabla \times \bar{u}$ . A solution is sought in the domain satisfying the initial conditions, $\bar{u} = \bar{u}_0$ , $\bar{\omega} = \nabla \times \bar{u}_0$ at initial time and the boundary conditions, $\bar{u} = \bar{u}_\Gamma ; \bar{\omega} \quad (\nabla \times \bar{u})|_\Gamma \; at \; t \geq 0$ .

The solution of vorticity-transport equation (1), in combination with the velocity Poisson equations (2), with reference to initial and boundary conditions, gives the velocity and vorticity distribution all over the domain at the concerned time step.

## 3. NUMERICAL FORMULATION

### 3.1. DRBEM Formulation of Velocity Poisson Equations

Consider the Poisson type velocity equation in $u$ and ? , say

$$\nabla^2 u = -\frac{\omega}{\partial y} = b \tag{3}$$

with velocity boundary conditions as, $u = \bar{u}_0 on \; \Gamma_1 ; \bar{q} \quad \partial \bar{u}_0 / \partial n \; on \; \Gamma_2$ , where n is the unit outward normal vector. Here, an iterative algorithm is used such that the right hand side of equation (3) is known from the previous step by solving (1).

Solution to equation (3) can be expressed as the sum of the solution of a homogeneous Laplace equation ( $\tilde{u}$ ) and a particular solution ( $\hat{u}$ ) as, $u \quad \tilde{u} \quad \hat{u}$ , such that, $\nabla^2 \hat{u} = b$ . The DRBEM proposes the use of a series of particular solution $\hat{u}_j$ instead of a single $\hat{u}$ . The number of $\hat{u}_j$ used is equal to the total number (N+L, N= boundary nodes, L= internal nodes) of nodes in the problem. Following approximation of b is then proposed,

$$b \approx \sum_{j=1}^{N+L} \alpha_j f_j \approx \sum_{j=1}^{N+L} \alpha_j \nabla^2 \hat{u}_j$$

(4)

where the $\alpha_j$ - are a set of initially unknown coefficients and the $f_j$ are approximating function which is geometrically dependent. Using (4) in (3) gives,

$$\nabla^2 u \quad \sum_{j=1}^{N+L} \alpha_j (\nabla^2 \hat{u}_j)$$

(5)

The procedure for developing the boundary element method for the Laplace equation (Brebbia et al.,1984) will now be applied. Equation (5) can be multiplied by the fundamental solution u* (for 2-D problems u*=ln r/(2p ), where r is the distance from the collocation point (k) to other field points (i)) and integrating over the domain producing,

$$\int_\Omega (\nabla^2 u) u^* d\Omega = \sum_{j=1}^{N+L} \alpha_j \int_\Omega (\nabla^2 \hat{u}_j) u^* d\Omega$$

(6)

Applying Green's second identity, (Brebbia et al. 1984) produces the following integral equation for each source node i,

$$C_i u_i + \int_\Gamma q^* u \, d\Gamma - \int_\Gamma u^* q \, d\Gamma = \sum_{j=1}^{N+L} \alpha_j \left( C_i \hat{u}_{ij} + \int_\Gamma q^* \hat{u}_j \, d\Gamma - \int_\Gamma u^* \hat{q}_j \, d\Gamma \right)$$

(7)

where $C_i$ is the Green's constant, $\hat{q}_j = \partial \hat{u}_j / \partial n$ and q*= $\partial u^* / \partial n$. Note that equation (7) involves no domain integrals. The source term b in (3) has been substituted by equivalent boundary integrals. After introducing the interpolation functions and integrating over each boundary element, the above equation can be written in the discretized matrix form as:

$$C_i u_i + \sum_{k=1}^{N} H_{ik} u_k - \sum_{k=1}^{N} G_{ik} q_k = \sum_{j=1}^{N+L} \alpha_j \left( C_i \hat{u}_{ij} + \sum_{k=1}^{N} H_{ik} \hat{u}_{kj} - \sum_{k=1}^{N} G_{ik} \hat{q}_{kj} \right)$$

(8)

Applying to all boundary nodes using a collocation technique, and each of the vector $\hat{u}_j$ and $\hat{q}_j$ is considered to be one column of the matrices $U$ *and* $Q$ respectively, equation (8) can be expressed in matrix form as,

$$H u - G q = (H U - G Q)\alpha$$

(9)

Equation (9) is the basis for the application of the DRBEM and involves discretization of the boundary only. Internal nodes may be defined in the number and the location desired by the user. From equation (3), taking the value of b at (N+L) points and expressing in a matrix form, $b = F \alpha$; $\alpha = F^{-1} b$, where each column of $F$ consists of vectors $f_j$ containing the values of the function $f_j$ at the (N+L) collocation points. Thus the right hand side vector of (9) is a known vector. Applying the boundary conditions to (9) gives a linear system of equations which are solved using Gauss elimination scheme to get the boundary unknowns. After finding the boundary unknowns, the internal values can be found from equation (9).

The particular solution $\hat{u}$, its normal derivative and the corresponding approximating function $f$ used in DRBEM analysis are limited by the formulation except that the resulting $F$ matrix, should be non-singular. Here the $f$ function used is: $f = 1 + r + r^2 + .... + r^m$. Correspondingly,

$$\hat{u} = \frac{r^2}{6} + \frac{r^3}{12} + .. + \frac{r^{m+2}}{(m+2)^2 + (m+2)}; \hat{q} = \left( r_x \frac{\partial x}{\partial n} + r_y \frac{\partial y}{\partial n} \right) \left( \frac{1}{3} + \frac{r}{4} + .. + \frac{r^m}{m+3} \right) \quad (10)$$

Other than the boundary only solution, the main advantage of using DRBEM in the solution of the velocity Poisson equations is the exact determination of the vorticity boundary conditions which are obtained as the velocity normal derivative from the solution of (9) together with the no-slip boundary conditions.

### 3.2. DRBEM Formulation of Vorticity Transport Equation

Consider the advection-diffusion type vorticity transport equation (1),

$$\nabla^2 \omega = R_e \left( \frac{\partial \omega}{\partial t} + \bar{u} \bullet \nabla \omega \right) = R_e \, b(x, y, \omega, t)$$

(11)

As mentioned earlier, an iterative procedure is used to solve equation (11). In the current iteration it will be assumed that the values of ($u$, $v$) are known from the previous iteration. The fundamental solution of Laplace equation is used in the solution (11). Appropriate boundary conditions ? or q ( $\omega$ $n$) and initial conditions should be prescribed.

As in section 3.1, using the DRBEM, solution to equation (11) can be expressed as the sum of the solution of a homogeneous Laplace equation $\tilde{\omega}$ and a particular solution $\hat{\omega}$ as, $\omega$ $\tilde{\omega}$ $\hat{\omega}$ such that, $\nabla^2 \hat{\omega} = b$. The DRBEM proposes the use of a series of N+L

particular solution $\hat{\omega}_j$. Following approximation of b is then proposed,

$$b \approx \sum_{j=1}^{N+L} \alpha_j f_j$$

(12)

where the $\alpha_j$ are a set of initially unknown coefficients and the $f_j$ are approximating function. As explained in section 3.1, we can finally write equation (12) as:

$$\nabla^2 \omega = R_e \sum_{j=1}^{N+L} \alpha_j (\nabla^2 \hat{\omega}_j)$$

(13)

Similar to the procedure in section 3.1, using the 2D fundamental solution of Laplace equation ln r/(2p), using the BEM procedure and after the boundary discretization and integration, the final system of equations in matrix form is obtained as:

$$H\omega - Gq = R_e (H\hat{\omega} - G\hat{Q})\alpha$$

(14)

Similar in section 3.1, $b =$ $\alpha$ or $\alpha = F^{-1} b$ and putting $S = -H\hat{\omega} - G\hat{Q}\ F^{-1}$ and substituting for b, equation (14) can be written as:

$$H\omega - Gq = S\left[R_e\left(\frac{\partial \omega}{\partial t} + u\frac{\partial \omega}{\partial x} + v\frac{\partial \omega}{\partial y}\right)\right]$$

(15)

Setting, $\omega = F\beta$ or $\beta = F^{-1}\omega$. Differentiating ? with respect to x and y,

$$\frac{\omega}{\partial x} = \frac{F}{\partial x} F^{-1}\omega; \frac{\omega}{\partial y} = \frac{F}{\partial y} F^{-1}\omega$$

(16)

Therefore equation (15) can be written as,

$$H\omega - Gq = R_e S\left[\frac{\partial \omega}{\partial t} + \left(u\frac{\partial F}{\partial x} \quad v\frac{\partial F}{\partial y}\right)F^{-1}\omega\right]$$

(17)

Putting $\omega = \partial\omega/\partial t$; $E = u\,\partial F/\partial x + v\,\partial F/\partial y$, we can write equation (17) as,

$$H\omega - Gq = R_e S[\omega' + E F^{-1}\omega]$$

(18)

Now substituting, $M = R_e S E F^{-1}$; $N = -R_e S$, we can write the final system as:

$$N\omega + (H \qquad)\omega = q$$

(19)

Using a two level time integration for ? and q and a difference scheme for $\omega$

$$\omega = (1-\theta_u)\omega^m + \theta_u \omega^{m+1}; q = (1-\theta_q)q^m + \theta_q q^{m+1}; \omega' = \frac{1}{t}(\omega^{m+1} - \omega^m)$$

(20)

where $?_u$ and $?_q$ are weighting factors which position the values of u and q , respectively, between time levels m and m+1. Substituting (20) into (19) gives:

$$\left(\frac{N}{\Delta t} + \theta_u(H - M)\right)\omega^{m+1} - \theta_q G q^{m+1} = \left[\frac{N}{\Delta t} - (1-\theta_u)(H - M)\right]\omega^m + (1-\theta_q) G q^m$$

(21) The right hand side of (21) is known at time (m+1)? t, since it involves values which have been specified as initial conditions or calculated previously. Upon imposing the boundary conditions at time (m+1)? t, we can form a linear system, which are solved using the Gauss elimination scheme to find the unknown function values initially over the boundary and then at the internal nodes considered. The approximating functions $f$ ' given

in section 3.1 and corresponding particular solutions and derivatives given in equation (10) are used here also. Here an iterative scheme is used and the derivatives of the vorticity ? in $x$- and $y$- direction are determined using (16) before the velocity Poisson equations are solved.

## 4. MODEL RESULTS AND DISCUSSIONS

The proposed DRBEM model has been applied on the classical 'driven flow in a square cavity' problem for which many numerical model results are available in literature. Present model results are compared with a series solution, FDM, FEM and BEM models in 2-D.

The model problem consists of a square cavity with a moving top lid with constant velocity, totally filled with an incompressible viscous fluid. The flow inside the cavity is initially at rest. No slip and impermeability conditions were imposed on all walls, with the velocity at the upper wall set equal to unity. Due to the computational limitations (we used an IBM Pentium II PC with 64 MB RAM), the present analysis is limited to a maximum of computational mesh points of 21x21 (on the boundary and internal nodes). One analysis is presented here, for a Reynolds number of 100.

Figures 1 and 2 show the u and v velocity profiles along the vertical and horizontal centerlines of the cavity, respectively. The velocity variations are compared with a series solution of Burgraff (1966), FDM solution of Ghia et al. (1982), FEM solution of Young and Lin (1986) and BEM solution of Young et al. (2000). The results mostly agree with all the model results, considering the coarse nature of the mesh used in the present analysis. Figure 3 shows the vorticity distribution along the domain and Fig. 4 shows the velocity vector field.

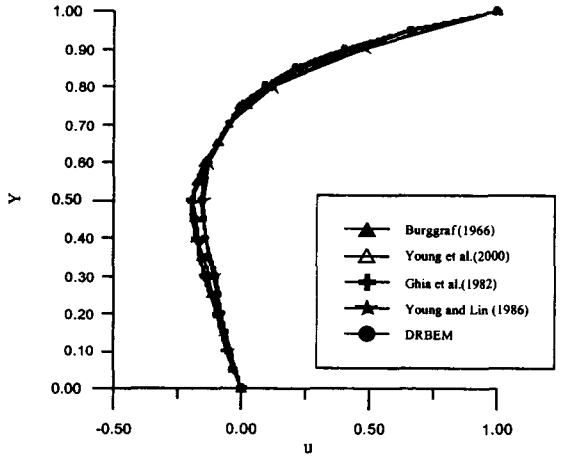


Fig. 1. u- velocity profile along vertical centerline for Re=100

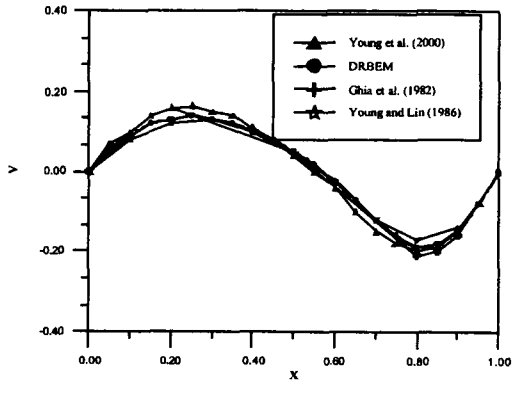

Fig. 2. v- velocity profile along horizontal centerline for Re=100

DRBEM has been proved to be a feasible method to solve advective-diffusion equation like vorticity transport equation. The necessary vorticity boundary conditions are determined by the DRBEM solution of the velocity Poisson equations together with the no-slip boundary conditions. Hence the present model in which the velocity Poisson equations and vorticity transport equation are solved using DRBEM, and the iterative scheme combining both models provides the best way to treat the velocity-vorticity formulation for two-dimensional incompressible viscous flow problems.

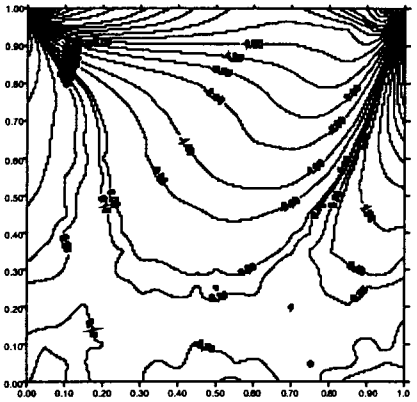

Fig. 3. Vorticity distribution for Re=100

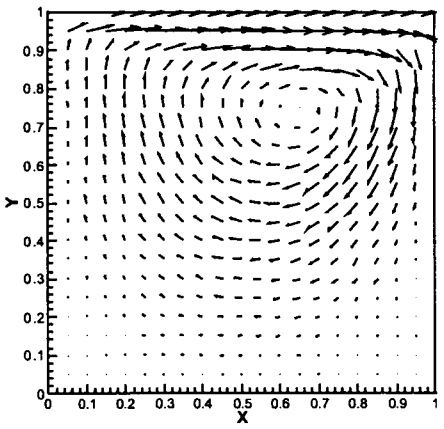


Fig. 4. Profile of the flow vectors for Re=100

## 5. CONCLUDING REMARKS

Here a dual reciprocity boundary element method for solving the velocity-vorticity Navier-Stokes equations is presented. The Poisson type velocity equations and the vorticity transport equation are solved using DRBEM. The vorticity boundary conditions

for the solution of vorticity transport equation are exactly obtained from the DRBEM solution of velocity Poisson equations. The use of DRBEM enables one to have a boundary only solution for the problem. Here the results of 2-D Navier-Stokes problems with low Reynolds number in a typical square cavity are presented. A comparison with other models demonstrates the feasibility of the DRBEM model.

**ACKNOWLEDGEMENTS**

The work reported in this paper was supported by the National Science Council of Taiwan. It is greatly appreciated.

**REFERENCES**

Brebbia, C.A., Telles, J.C.F., and Wrobel, L.C. (1984). *Boundary Element Techniques Theory and Applications in Engineering*. Springer-Verlag, Berlin.

Burgraff, O.R. (1966). Analytic and numerical studies of structure of steady separated flows. *J. Fluid Mech*. 24, 131-151.

Ghia, U., Ghia, K.N., Shin, C.T. (1982) High-Re solutions for incompressible flow using the Navier–Stokes equations and a multigrid method. *J. Comput. Phys*.48,387-411.

Partridge, P.W., Brebbia, C.A., and Wrobel, L.C.(1992). *The Dual Reciprocity Boundary Element Method*, Computational Mechanics Publications, Southampton.

Power, H., Wrobel, L.C.(1995) *Boundary Integral Methods in Fluid Mechanics.* Computational Mechanics Publications, Southampton.

Young, D.L., Lin, Q.H. (1986) Application of finite element method to 2-D flows. *Proc. 3rd National Conf. On Hydraulic Engineering*, Taipei, pp.223-242.

Young, D.L., Yang, S.K., Eldho T.I. (2000). The solution of the Navier-Stokes equations in velocity-vorticty form using Eulerian-Lagrangian boundary element method. *Int. J. Numer. Meth. Fluids* (in press).

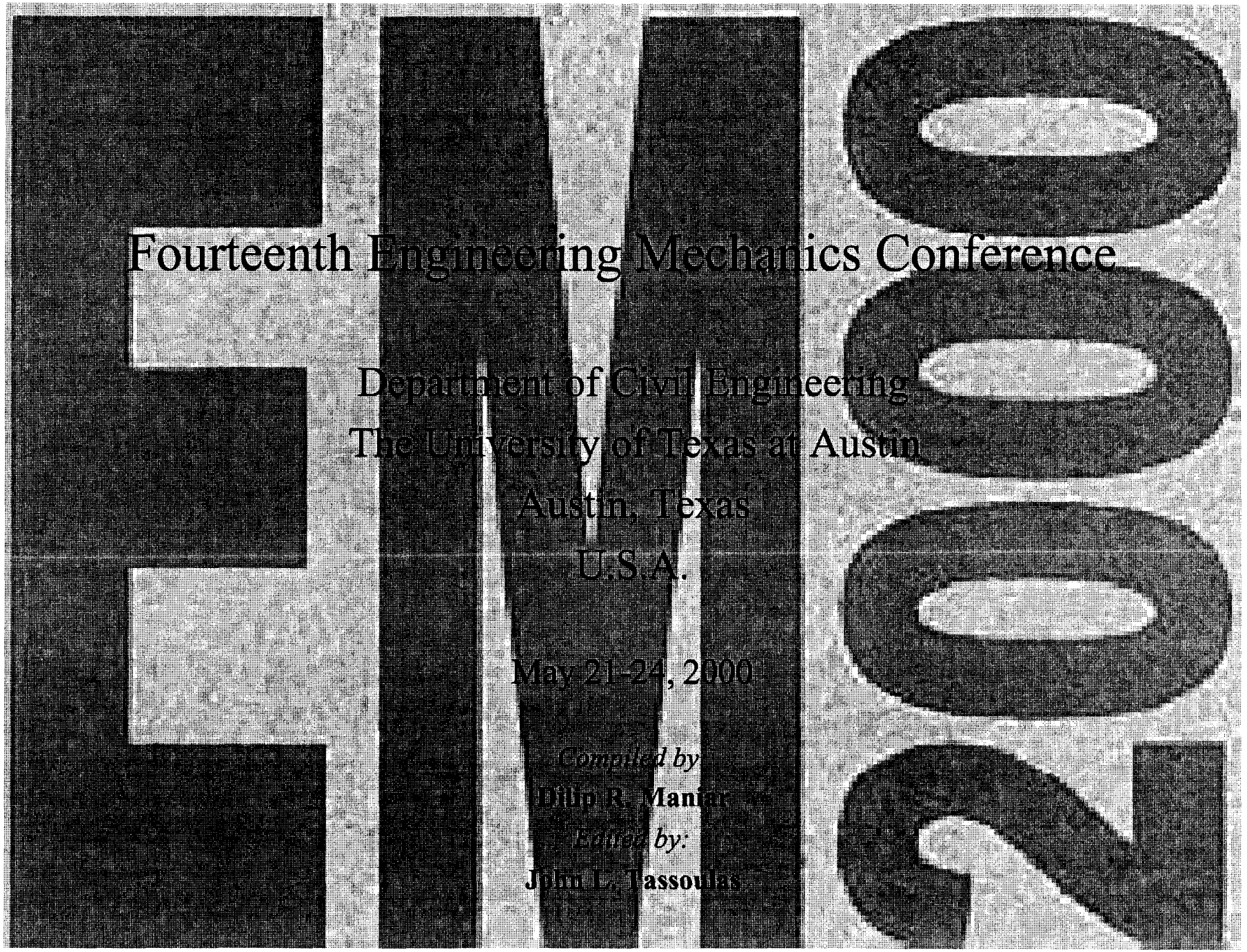

# Fourteenth Engineering Mechanics Conference

Department of Civil Engineering

The University of Texas at Austin

Austin, Texas

U.S.A.

May 21-24, 2000

*Compiled by:*

**Dilip R. Maniar**

*Edited by:*

**John L. Tassoulas**

# Radial Basis Functions, Polynomial Basis Functions, Particular Solutions, and DRBEM

Alexander H.-D. Cheng, Member ASCE
*Department of Civil & Environmental Engineering, University of Delaware*
*cheng@ce.udel.edu*

C. S. Chen
*Department of Mathematical Sciences, University of Nevada, Las Vegas*
*chen@nevada.edu*

M. A. Golberg
*2025 University Circle, Las Vegas, Nevada*
*mag741@aol.com*

D.-L. Young
*Department of Civil Engineering, National Taiwan University, Taiwan, R.O.C.*
*dlyoung@hy.ntu.edu.tw*

## Introduction

Since its introduction in 1982 by Nardini and Brebbia [1], the dual reciprocity boundary element method (DRBEM) has been applied to a wide range of engineering problems involving linear and nonlinear partial differential operators [2]. To eliminate the domain integration, an ad-hoc trial basis $(1 + r)$ was used to approximate the body force term.

A decade later, Golberg and Chen [3] pointed out that the basis $r$ is but a special case in the larger family of the so-called radial basis functions (RBFs) [4]. Several variations of the RBFs, such as the higher order conical types, the polyharmonic splines, the multiquadrics, and the Gaussians, have been introduced [5]. Some of the functions have been carefully tested in the DRBEM procedure [6].

All of the above-mentioned RBFs are globally defined. The resulting interpolation matrix is dense and can be highly ill conditioned, especially for a large number of interpolation points. This can cause serious stability problems. As a remedy, the compactly supported, positive definite radial basis functions (CS-PD-RBFs) have been derived [7] and implemented in DRBEM [8]. It was further demonstrated that in an iterative solution scheme, only the matrices based on CS-PD-RBF led to converged results. All other matrices diverged [9].

Not only radial bases, but also polynomials can be used as interpolants. Atkinson in 1985 [10] used harmonic polynomials as interpolants for the solution of Poisson's equation. Cheng, et al. [11] introduced the complete set monomial bases for the DRBEM. The collocation system, however, was ill-conditioned. Singular value decomposition had to be employed to solve the linear system. To overcome the difficulty, recently the Chebyshev polynomials, the optimal polynomials for interpolation, were revived. The scheme was found to be stable and highly accurate when used in conjunction with the method of fundamental solutions [12].

Initially, the DRBEM was developed for the Navier operator in elasticity [1]. Later applications were focused mainly on the Laplacian operator. Only recently the

capability of the DRBEM was expanded to include Helmholtz-type [13, 14] and polyharmonic [15] operators. Particularly, the ability to treat Helmholtz-type operators opened the gateway for solving transient problems by way of time differencing.

For the extension to new operators and new basis functions, particular solutions of the operators corresponding to the various basis functions need to be found. Take for example, the elasticity operator. Traditionally, $1 + r$ has been used as the trial base. Bridges and Wrobel in 1996 [16] and Partridge and Sensale in 1997 [17] extended the DRBEM capability for solving elasticity problems in 2-D to include the use of augmented thin-plate spline. Further extension to higher order splines in both 2-D and 3-D problems was accomplished by Cheng, et al. [18] for elasticity as well as for thermoelasticity. However, work still needs to be completed for the CS-PD-RBF and the polynomial bases. In this paper, we report some recently derived results as another step towards the completion of the work.

## DRBEM

A brief derivation of the DRBEM is given below. We assume that a governing equation can be arranged into the following form

$$\mathbb{L}\{u\} = f\left(\mathbf{x}, u, \frac{\partial u}{\partial x_i}, u^2, \ldots\right) \tag{1}$$

where $\mathbb{L}$ is a linear operator whose boundary integral equation is available. For simplicity, we shall assume that an iterative method is used for the right hand side such that it contains only known values, $f = f(\mathbf{x})$. The dependent variable $u$ can be decomposed into a particular solution $u_p$ and a complementary solution $u_c$:

$$u = u_p + u_c \tag{2}$$

The complementary part satisfies the homogeneous governing equation, hence can be solved from the boundary integral equation without a domain integral

$$u_c = \int_\Gamma \left[G\,\mathbb{N}\{u_c\} - u_c\,\mathbb{N}\{G\}\right]\, d\mathbf{x} \tag{3}$$

where $G$ is the fundamental solution, and $\mathbb{N}$ is the operator corresponding to the generalized normal derivative. Assuming that the particular solution can be found explicitly, we can substitute (2) into (3) to obtain a "boundary-only" formulation solving for $u$, despite the presence of an inhomogeneous right hand side:

$$u - u_p = \int_\Gamma \left[G\,\mathbb{N}\{u - u_p\} - (u - u_p)\,\mathbb{N}\{G\}\right]\, d\mathbf{x} \tag{4}$$

## Particular Solutions

We assume that the function $f$ can be approximated as

$$f \simeq \sum_{i=1}^{n} \alpha_i \varphi_i \tag{5}$$

where $\varphi_i$ are basis functions, and $\alpha_i$ are coefficients to be determined from collocation. If we can find the particular solution $\psi_i$ governed by

$$\mathbb{L}\{\psi_i\} = \varphi_i \tag{6}$$

then $u_p$ is explicitly found as

$$u_p \simeq \sum_{i=1}^{n} \alpha_i \psi_i \tag{7}$$

Hence the success of the DRBEM hinges on our ability to find $\psi_i$ corresponding to the various operators and the assorted radial and polynomial basis functions.

**Test Functions**

A few of the test functions are listed below.
*Polyharmonic splines*

$$\begin{aligned} \varphi &= r^{2n} \ln r; \qquad n = 1, 2, \ldots; \quad \text{in } \mathbb{R}^2 \\ \varphi &= r^{2n-1}; \qquad n = 1, 2, \ldots; \quad \text{in } \mathbb{R}^3 \end{aligned} \tag{8}$$

*CS-PD-RBFs*, for $d = 3$ and $k = 0$ [7]

$$\varphi = \left(1 - \frac{r}{a}\right)_+^2; \qquad \text{in } \mathbb{R}^2 \text{ and } \mathbb{R}^3 \tag{9}$$

and for $d = 3$ and $k = 1$

$$\varphi = \left(1 - \frac{r}{a}\right)_+^4 \left(1 + \frac{4r}{a}\right); \qquad \text{in } \mathbb{R}^2 \text{ and } \mathbb{R}^3 \tag{10}$$

*Monomials*

$$\begin{aligned} \varphi &= x^i y^j; \qquad i, j = 0, 1, 2, \ldots; \quad \text{in } \mathbb{R}^2 \\ \varphi &= x^i y^j z^k; \quad i, j, k = 0, 1, 2, \ldots; \quad \text{in } \mathbb{R}^3 \end{aligned} \tag{11}$$

*Chebyshev polynomials*

$$\begin{aligned} \varphi &= T_i(x) T_j(y); \qquad i, j = 0, 1, 2, \ldots; \quad \text{in } \mathbb{R}^2 \\ \varphi &= T_i(x) T_j(y) T_k(z); \quad i, j, k = 0, 1, 2, \ldots; \quad \text{in } \mathbb{R}^3 \end{aligned} \tag{12}$$

where $T_i(x)$ is the Chebyshev polynomial of degree $i$.

**Some New Results**

Here we present some new results. Assume that $\mathbb{L} = \nabla^2$ and $\varphi$ is given by the monomials in (11). Hence the particular solution of

$$\nabla^2 \psi = x^i y^j z^k; \quad i, j, k = 0, 1, 2, \ldots; \quad \text{in } \mathbb{R}^3 \tag{13}$$

The particular solution is even longer. It, however, can be generated by the computer without much effort:

$$\begin{aligned}\psi \;=\; & \frac{-5\,x^3\,z}{2}-\frac{16\,x^7\,z}{21}-\frac{8\,x^9\,z}{63}-\frac{16\,x^{11}\,z}{693}-\frac{64\,x^{13}\,z}{15015}+20\,x^3\,y^2\,z-4\,x^5\,y^2\,z \\ & +\frac{16\,x^7\,y^2\,z}{7}+\frac{64\,x^9\,y^2\,z}{63}+\frac{256\,x^{11}\,y^2\,z}{1155}-20\,x^3\,y^4\,z+16\,x^5\,y^4\,z-\frac{32\,x^7\,y^4\,z}{7} \\ & -\frac{64\,x^9\,y^4\,z}{63}+\frac{10\,x^3\,z^3}{3}-\frac{4\,x^5\,z^3}{3}+\frac{16\,x^7\,z^3}{21}+\frac{16\,x^9\,z^3}{189}+\frac{128\,x^{11}\,z^3}{3465} \\ & -\frac{80\,x^3\,y^2\,z^3}{3}+16\,x^5\,y^2\,z^3-\frac{64\,x^7\,y^2\,z^3}{21}-\frac{128\,x^9\,y^2\,z^3}{63}+\frac{80\,x^3\,y^4\,z^3}{3} \\ & -32\,x^5\,y^4\,z^3+\frac{256\,x^7\,y^4\,z^3}{21} \end{aligned} \tag{19}$$

Fortran code of these expressions can be automatically generated using the *Mathematica* program.

**Example**

As a demonstration, we solve the following problem

$$\nabla^2 u = 2e^{x-y} \tag{20}$$

defined in the domain $[-1,1]\times[-1,1]$ in $\mathbb{R}^2$, with the Dirichlet boundary condition

$$u = e^{x-y}+e^x\cos y \tag{21}$$

A $5\times5$ grid is used for the Chebyshev polynomial interpolation of the right hand side of (20). The method of fundamental solutions (MFS) is used to solve the boundary value problem, and 32 source points are used. The numerical result, when compared with the exact solution, is accurate up to 5 to 6 decimal places. When the interpolation grid of the Chebyshev polynomials is increased to $8\times8$, the accuracy of the numerical solution is up to 10 to 11 decimal places. The performance is excellent.

**Acknowledgment**

The first and the last author were partially supported by the grant NSC 88-2811-E-002-0008 from the National Science Council of the Republic of China (Taiwan), during the first author's sabbatical leave at the National Taiwan University. This generous support that makes this collaboration possible is deeply appreciated.

**References**

1. Nardini, D. and Brebbia, C. A., "A new approach to free vibration analysis using boundary elements," In: *Boundary Element Methods in Engineering*, Proc. 4th Int. Seminar, Southampton, ed. C.A. Brebbia, Springer-Verlag, 312-326, 1982.
2. Partridge, P.W., Brebbia, C.A. and Wrobel, L.C., *The Dual Reciprocity Boundary Element Method*, CMP/Elsevier, 1992.
3. Golberg, M.A. and Chen, C.S., "The theory of radial basis functions applied to the BEM for inhomogeneous partial differential equations," *Boundary Elements Commun.*, **5**, 57-61, 1994.

4. Powell, M.J.D., "The theory of radial basis function approximation in 1990," In: *Advances in Numerical Analysis, v. II: Wavelets, Subdivision Algorithms, and Radial Basis Functions*, (ed.) W. Light, Clarendon Press, 105-210, 1992.
5. Golberg, M.A., Chen, C.S. and Bowman, H., "Some recent results and proposals for the use of radial basis functions in the BEM," *Eng. Analy. Boundary Elements*, **23**, 285-296, 1999.
6. Partridge, P.W., "Towards criteria for selection approximation functions in the dual reciprocity method," to appear in *Engng. Analy. Boundary Elements.*
7. Wendland, H., "Piecewise polynomial, positive definite and compactly supported radial functions of minimal degree," *Adv. Comp. Math.*, **4**, 389-396, 1995.
8. Chen, C.S., Brebbia, C.A., and Power, H., "Dual reciprocity method using compactly supported radial basis functions," *Commun. Numer. Meth. Engng.*, **15**, 137-150, 1999.
9. Cheng, A.H.-D., Young, D.-L. and Tsai, J.-J., "Solution of Poisson's equation by iterative DRBEM using compactly-supported, positive-definite radial basis function," to appear in *Eng. Analy. Boundary Elements.*
10. Atkinson, K.E., "The numerical evaluation of particular solutions for Poisson's equation," *J. Numer. Analy.*, **5**, 319-338, 1985.
11. Cheng, A.H.-D., Lafe, O. and Grilli, S., "Dual reciprocity BEM based on global interpolation functions," *Eng. Analy. Boundary Elements*, **13**, 303-311, 1994.
12. Chen, C.S., Golberg, M.A., Muleshkov, A.S. and Cheng, A.H.-D., "Dual reciprocity method using Chebyshev polynomials," in preparation.
13. Golberg, M.A., Chen, C.S. and Rashed, Y.F., "The annihilator method for computing particular solutions to partial differential equations," *Engng. Analy. Boundary Elements*, **23**, 275-279, 1999.
14. Muleshkov, A.S., Golberg, M.A. and Chen, C.S., "Particular solutions of Helmholtz-type operators using higher order polyharmonic splines," *Comp. Mech.*, **23**, 411-419, 1999.
15. Cheng, A.H.-D., "Particular solutions of Laplacian, Helmholtz-type, and polyharmonic operators involving higher order radial basis functions," to appear in *Eng. Anal. Boundary Elements.*
16. Bridges, T.R. and Wrobel, L.C., "A dual reciprocity formulation for elasticity problems with body forces using augmented thin plate splines," *Comm. Numer. Meth. Eng.*, **12**, 209-220, 1996.
17. Partridge, P.W. and Sensale, R., "Hybrid approximation functions in the dual reciprocity boundary element method," *Comm. Numer. Meth. Eng.*, **13**, 83-94, 1997.
18. Cheng, A.H.-D., Chen, C.S., Golberg, M.A. and Rashed, Y.F., "BEM for thermoelasticity and elasticity with body force—A revisit," submitted to *Eng. Anal. Boundary Elements.*